2016

Production of Dual-Phase and Transformation-Induced Plasticity Steels by Strip Casting

Zhiping Xiong
University of Wollongong

UNIVERSITY OF WOLLONGONG

School of Mechanical, Materials and Mechatronic Engineering

Production of Dual-Phase and Transformation-Induced Plasticity Steels by Strip Casting

Zhiping Xiong

This thesis is presented as part of the requirements for the award of the Degree of the Doctor of Philosophy

University of Wollongong, Australia

November, 2016

Dedicated to my dear father (24.05.1962-22.01. 2013)

THESIS CERTIFICATION

I, Zhiping Xiong, declare that this thesis, submitted in fulfilment of the requirements for the award of Doctor of Philosophy, in the school of Mechanical, Material and Mechatronic Engineering, University of Wollongong, is wholly my own work unless otherwise referenced or acknowledged. The document has not been submitted for qualifications at any other academic institution.

Zhiping Xiong

30th November, 2016

ABSTRACT

Dual phase (DP) and transformation-induced plasticity (TRIP) steels have received a significant attention in automotive industry due to their high strength and good ductility. At present, they are industrially manufactured using hot rolling and cold rolling followed by intercritical annealing. Alternatively, strip casting is another potential way to produce these steels, which will significantly reduce energy consumption. Thus, for the first time, an investigation into the possibility of production of DP and TRIP steels using strip casting was carried out in this work on the laboratory scale.

For DP and TRIP steels, the processing parameters for simulated strip casting technique were determined based on prior austenite microstructures and continuous cooling transformation diagrams. The effects of interrupted cooling temperature, the amount of deformation and deformation temperature on microstructure evolution and tensile properties were studied in depth. The influence of isothermal bainite transformation (IBT) temperature on microstructure and mechanical behaviours of the TRIP steel was also investigated. Typical microstructures of DP and TRIP steels were obtained in strip cast steels, which were characterised using X-ray diffraction, energy dispersive spectrometry, scanning and transmission electron microscopy (TEM), electron backscattering diffraction (EBSD) and atom probe tomography (APT). The strain hardening behaviour after tensile tests was analysed using modified Crussard – Jaoul model. The strengthening after deformation was predominantly ascribed to grain refinement and dislocation strengthening. The mechanical properties of strip cast DP and TRIP steels outperformed industrially produced DP 600 and TRIP 690 steels, respectively, indicating the feasibility to produce these two steels using strip casting.

For DP steel, the average ferrite grain size was significantly refined from ~ 25 to ~ 3 μm by the triggering of strain-induced ferrite (SIF) formation when the samples were deformed between 700 and 800 °C at a reduction of ~ 0.41. The EBSD maps were segmented into polygonal ferrite, SIF and second phase regions using mean angular deviation and grain size. A diffusional mode for SIF formation was suggested based

on the similarity in dislocation substructure features, misorientation angle distribution and the deviation from theoretical orientation relationships between polygonal ferrite and SIF. The contribution to strain hardening from every microstructure constituent was analysed using modified iso-work modelling.

The effects of neighbouring phases, retained austenite (RA) size and morphology on its carbon content were studied using site-specific APT correlated with EBSD. The results highlighted the dominant role of neighbouring phases on the carbon content in the RA. The analysis of C and Mn partitioning across the interfaces between the RA and ferrite in bainite showed that it could be explained using either diffusional mechanism of bainite formation and/or diffusionless one followed by tempering.

ACKNOWLEDGEMENTS

I would like to express my deepest gratitude to my supervisors, Prof. Elena Pereloma and Dr. Andrew Koshtryzhev. The successful completion of this thesis is due to their continuous support and well directed guidance. Elena always responded back at her earliest possibility whenever I sent any draft for corrections. The discussions with Elena always broadened my knowledge and boosted my creativity. Being my daily supervisor, Andrew helped me obtain a good start point at the University of Wollongong. He always encouraged me to work hard and live a positive life, which really helped me overcome the academic difficulties. He was always ready to give corrections and comments on my drafts whenever I needed his input.

I am also very grateful to Dr. Ahmed Saleh's help with the X-ray diffraction training and electron backscattering diffraction mapping as well as data processing training along with some analysis, Dr. Gilberto Casillas's training with transmission electron microscopy, Dr. Liang Chen's help with the training for dilatometer and support with Gleeble, and Greg Tillman's help in the metallographic laboratory.

A/Prof. Nicole Stanford, formerly at Deakin University and now at Monash University, is gratefully acknowledged for providing the dip cast samples. Drs. Ross Marceau and Adam Taylor, Deakin University, are also very gratefully acknowledged for atom probe data acquisition and FIB site-specific lift-outs, respectively.

I would like to thank all my friends for the happy times we had in the university and outdoors.

Finally, I would like to acknowledge my family for their support and unconditional love.

DECLARATION ON PULICATIONS

This thesis includes the following chapters that have been written as the journal articles:

Chapter 2: Z.P. Xiong, A.G. Kostryzhev, N.E. Stanford, E.V. Pereloma, "Microstructures and mechanical properties of dual phase steel produced by laboratory simulated strip casting", Materials & Design 88 (2015) 537-549.

Chapter 3: Z.P. Xiong, A.G. Kostryzhev, N.E. Stanford, E.V. Pereloma, "Effect of deformation on microstructure and mechanical properties of dual phase steel produced via strip casting simulation", Materials Science and Engineering A 651 (2016) 291-305.

Chapter 4: Z.P. Xiong, A.A. Saleh, A.G. Kostryzhev, E.V. Pereloma, "Strain-induced ferrite formation and its effect on mechanical properties of a strip cast dual phase steel" under review for publication in the Acta Materialia.

Chapter 5: Z.P. Xiong, A.G. Kostryzhev, A.A. Saleh, L. Chen, E.V. Pereloma, Microstructures and mechanical properties of TRIP steel produced by strip casting simulated in the laboratory, Materials Science and Engineering A 664 (2016) 26-42.

Chapter 6: Z.P. Xiong, A.G. Kostryzhev, A.A. Saleh, L. Chen, E.V. Pereloma, "Microstructure and mechanical properties of strip cast TRIP steel subjected to thermo-mechanical simulation", Materials Science and Engineering A 667 (2016) 356-366.

Chapter 7: Z.P. Xiong, A.A. Saleh, R.K.W. Marceau, A.S. Taylor, N.E. Stanford, A.G. Kostryzhev, E.V. Pereloma, "Site-specific atomic scale characterisation of retained austenite in a strip cast TRIP steel" in preparation for submission to the Acta Materialia.

I, Prof. Elena V. Pereloma, as the principal supervisor declare that the candidate, Mr Zhiping Xiong, has reviewed the relevant literature, conducted most of experiments and preliminary data analysis, and wrote the first draft of each manuscript (Chapters 2 – 7). Following the additional data interpretation from the co-authors and their editorial suggestions, Zhiping was responsible for submitting each manuscript for publication to the relevant peer-reviewed journals. In all publications, the candidate has responded to the comments raised by editors and reviewers with the assistance of his supervisors. In particular, the following contributions were made by the candidate to each chapter:

Chapter 2, 3, 5, and 6: The source materials were dip cast by A/Prof. Nicole E. Stanford at Deakin University. The picric etching was carried out with the help of Dr. Liang Chen for chemical solution preparation and etching. All heat treatments were carried out by Zhiping. Gleeble tests were assisted by Dr. Liang Chen for machine operation. Optical microscopy was carried out by Zhiping.

All corresponding experiments involving scanning electron microscopy (SEM), transmission electron microscopy (TEM), X-ray diffraction, hardness and tensile testing, as well as subsequent analysis, were conducted by Zhiping.

Chapter 4: The electron backscattering diffraction (EBSD) maps, as well as guidance for data analysis and interpretations were provided by Dr. Ahmed Saleh. However, Zhiping was responsible for the analysis after his training on the Oxford Instruments Channel-5 software package. SEM, TEM and tensile tests were conducted by Zhiping. The modified iso-work modelling was carried out by Zhiping.

Chapter 7: EBSD mapping was done by Dr. Ahemd Saleh with Zhiping's presence and participation. Site-specific preparation of atom probe samples using focused ion beam and atom probe tomography (APT) experiments were respectively undertaken by Drs. Adam Taylor and Ross Marceau, Deakin University. The complete APT data analysis was performed by Zhiping after he received training for IVAS 3.6.8 software (Cameca Instruments) by Prof. Elena Pereloma. Methodology for interface determination using Gibbsian interfacial excess was explained by Dr. Anna. V. Ceguerra, the University of Sydney, AMMRF. Drs. Gilberto Casillas and David R.G. Mitchell, the University of Wollongong, helped with high resolution TEM and

electron energy loss spectroscopy. Zhiping carried out data interpretation and together with Prof. Elena Pereloma provided the explanations.

Zhiping Xiong	Prof. Elena V. Pereloma	Dr. Andrew G. Kostryzhev
Candidate	Principal Supervisor	Co-Supervisor
30th November, 2016	30th November, 2016	30th November, 2016

TABLE OF CONTENTS

LIST OF FIGURES

LIST OF TABLES

CHAPTER 1 INTRODUCTION

1.1 Motivation

Advanced high strength steels (AHSSs) are being developed for automotive industry due to the increasing requirements for passenger safety, fuel economy and vehicle performance. Different grades of AHSSs have been produced such as dual phase steels (DP) [1], transformation-induced plasticity steels (TRIP) [2], twinning-induced plasticity (TWIP) steels [3], complex phase steels [4] and martensitic steels [5].

In recent decades, DP and TRIP steels have received significant attention in science and engineering, especially in relation to automotive industry. So far, DP and TRIP steels have been used in car bodies, such as pillars, body structure, closures and suspensions [6, 7]. Compared to mild steels, interstitial free steels and high strength low-alloyed (HSLA) steels, DP and TRIP steels combine high strength and good ductility (Fig. 1.1 [8]), which are required for car bodies [6, 8, 9]. These excellent mechanical properties are derived from their multiphase microstructures. In addition, DP steel exhibits good formability, continuous yielding behaviour, low yield-tensile strength ratio and high work hardening rate [7, 10]. Compared to DP steel, TRIP steel has a better combination of strength and formability in terms of both elongation and strain hardening exponent [11].

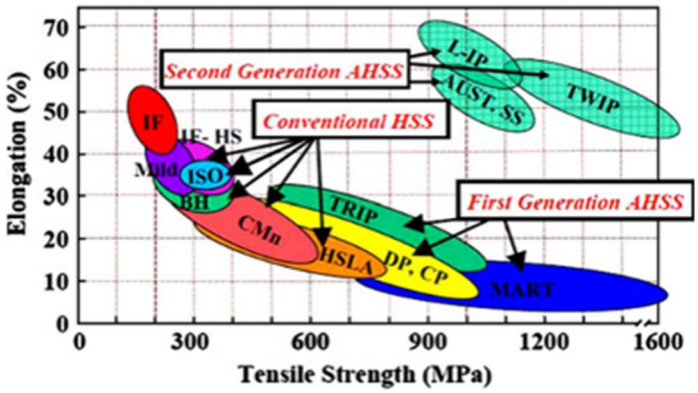

Figure 1.1 Conventional high strength steels (HSS), first generation advanced high strength steels (AHSSs) and second generation AHSSs [8].

At present, there are two processing paths to produce DP and TRIP steels in industry, which are shown in Fig. 1.2 [6, 11]. One is through controlling the cooling process after hot rolling (Figs. 1.2 (a, c)). The other one is through the heat treatment conducted for cold rolled steels (Figs.1.2 (b, d)).

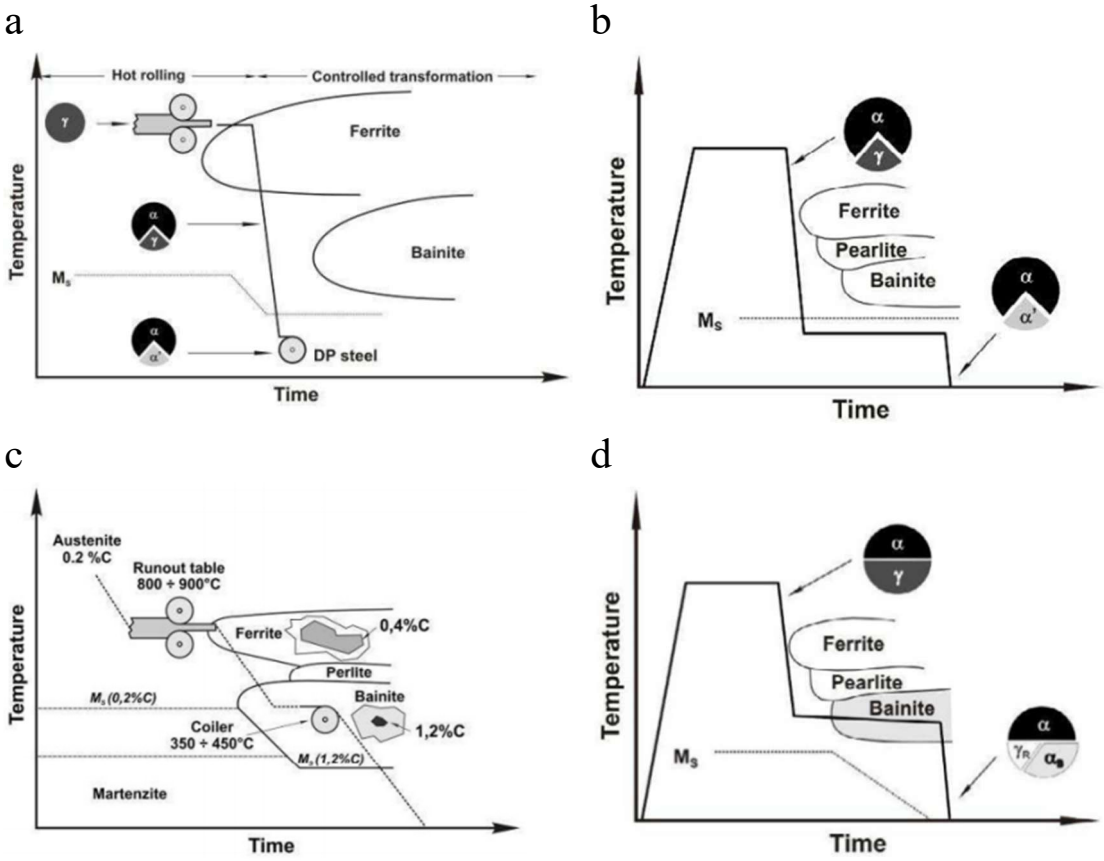

Figure 1.2 Industrial processing schedules for DP and TRIP steels: hot rolling for (a) DP steel and (c) TRIP steel; heat treatments after cold rolling for (b) DP steel and (d) TRIP steel [6]. γ is austenite, α is polygonal ferrite, α' is martensite, α_B is bainite and γ_R is retained austenite.

However, another economic and environmental way for DP and TRIP steels production could be the strip casting, which has already found application for carbon steels, silicon steels and stainless steels [12, 13]. So far, a very limited research has been focused on this processing path for DP and TRIP steels [14]. Thus, this study is aimed to investigate the microstructure development mechanisms during thermo-mechanical processing used for the simulated strip casting to produce DP and TRIP steels, which would assure obtaining the mechanical properties comparable to those of DP and TRIP steels after hot rolling and cold rolling.

1.2 Background

1.2.1 Strip casting process

Strip casting process is defined as a production of strip metals through direct casting from molten condition in a single process, which may combine subsequent inline hot rolling by a micro-mill [12]. Strip casting includes different technologies, such as single roll casting, twin roll casting, single belt casting and twin belt casting. Due to the elimination of many subsequent hot rolling stages compared to the conventional continuous casting (CCC) and thin slab casting (TSC), strip casting process has many advantages, such as energy saving and emission reduction, lower capital and operating costs, a smaller and more flexible operating regime, a higher tolerance to high residual scrap (due to reduced number of steel production stages), and easy adjustment for different steel grades [12, 13, 15, 16]. Noticeably, strip casting is more efficient by decreasing cast thickness down to 1 – 15 mm compared to ~ 200 and 50 mm produced by CCC and TSC, respectively [13].

CASTRIP is the twin roll casting process which has been commercialised since 1990s. As can be seen in Fig. 1.3 [12], the strips are produced directly from liquid metal using twin rolls and a hot rolling stand. CASTRIP can not only produce carbon steels, microalloyed steels, silicon steels and stainless steels, but also lead, aluminium and brass strips [12, 13, 17]. In the following, microstructures and mechanical properties of carbon and microalloyed steels produced by CASTRIP are introduced.

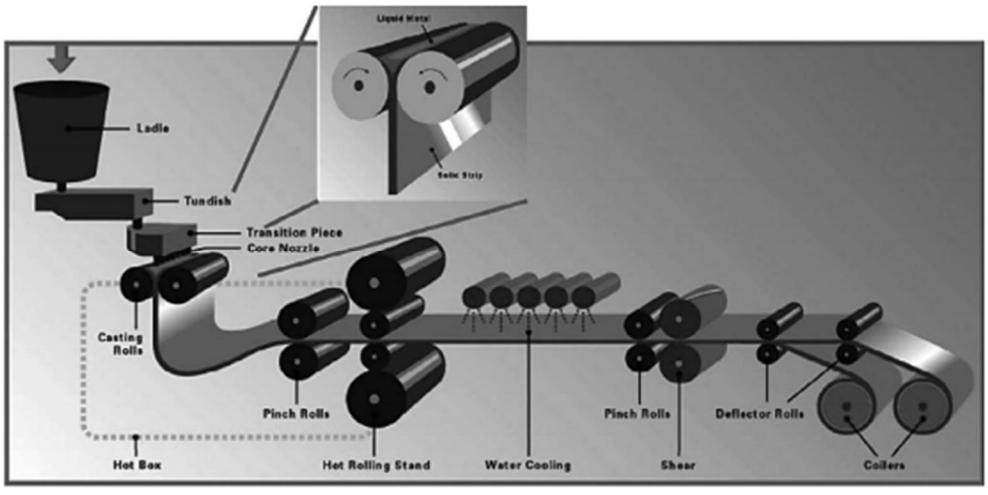

Figure 1.3 The design and components of the CASTRIP caster [12].

Strip casting has a typical coarse austenite microstructure with grain length and width larger than 0.45 and 0.2 mm respectively, which raises a challenge for engineers to control austenite transformation to low temperature phases [17]. The prior austenite microstructure consists of columnar grains growing from the surface to the centre and equiaxed grains in the centre (Fig. 1.4) [18], which corresponds to conventional casting microstructures. Due to the rapid cooling rate during solidification, a pronounced microsegregation exits in strip casting, leading to an inhomogenous microstructures [19, 20]. This microsegregation could be eleminated by subsequent annealing [19].

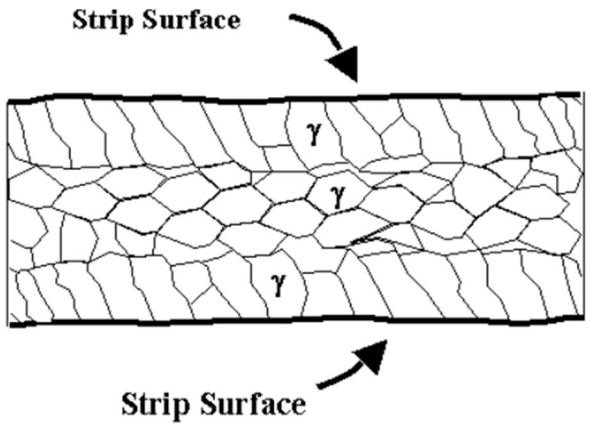

Figure 1.4 Illustration of as-cast austenite grain structure of the ultra-thin cast strip produced by CASTRIP [18]. γ is austenite.

The final microstructure phase balance of strip-cast steels varies with steel compositions and processing schedules. The microstructure of the steel containing 0.03C-0.9Mn-0.2Si (wt. %) produced by strip casting, consisted of polygonal ferrite, Widmanstätten ferrite and bainite (Figs. 1.5 (a, b)) [21]. Microalloying with Nb resulted in the final microstructure consisting of fine Widmanstätten ferrite and bainite as illustrated in Figs. 1.5 (c, d) because austenite decomposition shifted towards low temperature reaction due to its enhancement of austenite stability [22]. Through hot rolling with ~ 28% reduction, microstructures were refined in Nb-free and 0.084% Nb steels [21]. Produced by laboratory simulations, the strip cast steel (Fe-0.11C-0.59Mn-0.16Si-0.16Nb, wt. %) comprised pearlite, polygonal ferrite or bainite depending on the coiling temperature (600, 700 and 850 °C) [23]. In addition

to carbon and microalloyed steels, a Fe-29Mn-0.3C (wt. %) TWIP steel consisting of austenite was laboratory produced using strip casting [20].

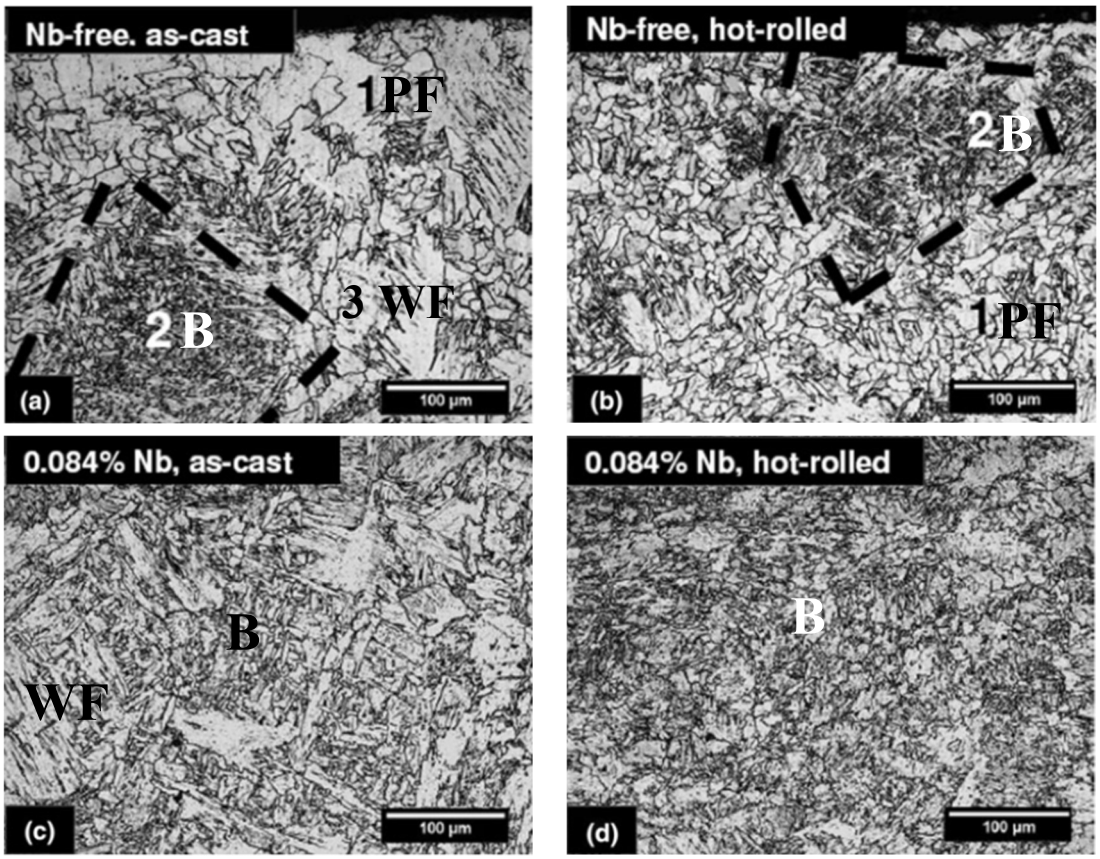

Figure 1.5 Cross-sectional optical microstructures of (a) as-cast and (b) hot-rolled Nb-free steel (28% reduction), and (c) as-cast and (d) hot-rolled 0.084 wt% Nb steel (28% reduction) [21]. *PF* is polygonal ferrite, *WF* is Widmanstätten ferrite, *B* is bainite.

The mechanical properties of ultra-thin cast strip (UCS) products (manufactured by CASTRIP) and conventional products (manufactured by hot rolling and cold rolling) are listed in Table 1.1. It can be seen that the mechanical properties of UCS products are comparable to conventional products. Besides, stretch flange-ability, biaxial stretch, normal anisotropy, limiting draw ratio and forming limit diagram are also found to be comparable to the hot rolled and cold rolled strip grades with similar thickness having the yield stress in the range of 275 – 380 MPa [18]. In addition, the thin high strength strip with the yield strength in the range of 380 – 550 MPa was developed by microalloying with Nb [17]. Importantly, proper continuous heat treatments carried out by a continuous annealing line and a continuous galvanizing line result in a wide range of UCS mechanical properties and thus enlarge the UCS

product utilisation scope [14]. As a conclusion, UCS products manufactured by strip casting can substitute cold rolled and hot rolled steel strips in some cases because of comparable mechanical properties.

Table 1.1 Comparison of mechanical properties of ultra-thin cast strip (UCS) products with conventional hot rolled (HR) and cold rolled & continuously annealed (CR & CA) products [13, 18, 24].

Grade	Yield strength, MPa	Tensile strength, MPa	Elongation, %
275 UCS	325	430	28
340 UCS	375	475	21
300 UCS	315	416	36
380 UCS	440	530	18
550 UCS	--	850	4.5
SS Grade 275 [a]	275	380	15
SS Grade 310 [a]	310	410	13
SS Grade 340 [a]	340	450	11
SS Grade 380 [a]	380	480	9
SS Grade 550 [a]	550	620	6
200 HR	297	380	34
300 HR	370	480	28
360 HR	415	510	22
300 CR & CA	340	400	30
350 CR & CA	369	468	34

[a] SS Grade with reference to ASTM A 1011M.

1.2.2 Role of alloying elements in DP and TRIP steels

The chemical compositions of DP and TRIP steels are important in governing microstructure constituents through different heat treatments. Carbon and manganese are principal alloying elements while silicon, aluminium, niobium, nickel, molybdenum, chromium, copper and phosphorus may be also incorporated to adjust microstructures and mechanical properties.

1.2.2.1 Carbon

Carbon (C) enhances austenite stability and acts as solid solution strengthening element [25]. In addition, C can increase stacking fault energy and play an important role in strain hardening [26]. However, it deteriorates weldability and formability [7]. When carbon concentration increases, low temperature transformation products (bainite and martensite) are promoted; austenite-to-martensite transformation temperature is lowered (depending on the C content it can be below room temperature) [26]. Martensite forms during quenching to room temperature [1, 27]. Besides, increasing the C content in retained austenite (RA) tends to increase the elongation values (as a result of TRIP effect; namely, RA transforming to martensite during deformation leads to the delay of local necking) because carbon enhances austenite stability [28].

1.2.2.2 Manganese

Manganese (Mn) is one of austenite stabilising elements, which decreases austenite-to-ferrite transformation start temperature (Ar_3) leading to enlarged austenite domain. Mn also improves hardenability [29]. In DP steels, when Mn content increases, less austenite will transform to ferrite, resulting in more austenite remaining for martensite transformation [30, 31]. In TRIP steels, increasing Mn content in RA enhances its stability, resulting in improved tensile elongation [32]. However, when the Mn segregation across the interface between RA and ferrite in bainitic ferrite/granular bainite exists, the strain resulted from the substitution of Fe for Mn will reduce the RA stability [33].

1.2.2.3 Silicon

Silicon (Si) is a non-carbide-forming element and ferrite stabilising element because it promotes carbon rejection from ferrite to austenite. In addition, Si can retard

pearlite formation and accelerate ferrite formation [34]. However, significant alloying with Si induces surface defects, like red scale and tiger strips [35]; high Si content also leads to galvanizing problems and difficulties in welding [36]. In TRIP steels, Si, which is the critical solute, is typically added in the amount of about 1.5 wt. % in order to prevent cementite precipitation during isothermal bainite transformation (IBT) [28, 37, 38].

1.2.2.4 Aluminium

Aluminium (Al) is a ferrite stabiliser similar to Si [10, 37, 39]. It accelerates ferrite formation [35, 40] and retards pearlite formation as well [34, 35]. By promoting AlN precipitation it can inhibit austenite grain growth, resulting in a fine microstructure [39]. Addition of Al to DP steels can make the temperature range wider for successful production in industry by elevating pearlite transformation finish temperature (which results in the shrinkage of pearlite formation temperature region) and lowering bainite formation temperature [35]. Similar to Si in TRIP steels, Al assists the formation of carbide-free bainite morphologies by the prevention of cementite precipitation during IBT holding [37]. Besides, Al refines bainitic microstructure [41] and accelerates bainite formation [37].

1.2.2.5 Phosphorus

Phosphorus (P) is located near Al and Si in the periodic table and thus it has some similar physical and chemical properties to those of Al and Si. Therefore, P could be used to replace Al because high Al in steel may induce casting problems [42]. P reduces carbon activity in cementite as well and then depresses cementite precipitation [42]. Besides, P enhances RA stability in TRIP steel [42]. However, P segregation along grain boundaries is harmful to mechanical properties, resulting in embrittlement fracture [31, 42].

1.2.2.6 Chromium

Chromium (Cr) is an effective element in improving austenite hardenability [27, 43, 44]. Thus, it allows a reduced cooling rate for DP steel to obtain martensite phase while it prevents ferrite transformation from austenite during cooling [27]. Cr also slows down the isothermal transformation kinetics of bainite and in turn postpones the decomposition of austenite [41].

1.2.2.7 Molybdenum

Molybdenum (Mo) has strong solute drag effect and thus retards austenite grain growth, leading to a fine microstructure [39, 45, 46]. Mo enhances martensite formation due to an increase in austenite hardenability by increasing carbon equivalent in austenite [39, 43, 44]. Besides, Mo not only can decrease bainite start and finish temperatures, but also can reduce the pearlite start temperature and increase the pearlite finish temperature [47, 48], which is undesirable for both DP and TRIP steels.

1.2.2.8 Nickel

Nickel (Ni) is an austenite stabiliser [29]. Thus, Ni can delay bainite transformation, resulting in an increase in RA fraction and a corresponding decrease in RA carbon content [44]. In addition, increasing Ni content increases film RA fraction, resulting in a decrease in plasticity and an increase in strength due to high resistance of film RA to TRIP effect [49].

1.2.2.9 Copper

Copper (Cu) extends the bainitic transformation domain in continuous cooling transformation (CCT) diagram to much slower cooling rates [50]. Similar to Cr and Ni, it also contributes to solid solution hardening in steels [51].

1.2.2.10 Boron

Increasing boron (B) content reduces austenite region, resulting in a decrease in RA fraction and an increase in carbon content [31]. However, pearlite reaction can be easily inhibited by adding B as it has a nucleation site poisoning effect on prior austenite grain boundaries [31, 52]. The addition of B increases the incubation time for bainite formation and then decreases the transformation kinetics of bainite. Besides, B retards bainite nucleation at austenite grain boundaries and promotes bainite nucleation in austenite interior, resulting in enhancement of variant selection [52].

1.2.2.11 Niobium, titanium and vanadium

Niobium (Nb) retards austenite recrystallisation both in solute form and as carbide or carbonitride precipitation [7], as well as slows down the rate of austenite-to-ferrite

and austenite-to-pearlite transformations [53]. Austenite-to-bainite transformation is suppressed to lower temperatures [7, 47]. On one hand, Nb in solid solution suppresses carbide precipitation during bainite formation, leading to an increase in the RA carbon content and its fraction [36, 53]. On the other hand, Nb also can precipitate as carbides, nitrides or carbonitrides. Although the formation of precipitate refines the microstructure, it would consume carbon, leading to a decrease in RA fraction [36, 53]. In other words, the effect of Nb on fraction and carbon content of RA should consider the combined influence of Nb solid solution, Nb precipitation and grain refinement [53].

Titanium (Ti) and vanadium (V) help refine microstructure and enhance strain hardening [54]. TiN of micron size forms in austenite and although indirectly contributes to final properties by serving heterogeneous nucleation sites for (Ti, Nb)(C, N) or NbC carbides formation, they do not contribute much to strengthening [54, 55]. On the other hand, fine submicron and nanometer size NbC, V(C, N) and VC formed in ferrite or bainite could significantly increase the strength of steel [55].

1.2.3 Microstructures and mechanical properties of DP and TRIP steels

1.2.3.1 Microstructures and thermo-mechanical processing

Typical microstructures of DP and TRIP steels produced using thermo-mechanical controlled processing (TMCP) are given in Fig. 1.6. DP steel consists of soft polygonal ferrite matrix with good ductility and hard martensite with high strength (Fig. 1.6(a)) [48, 56]. According to different processing routes and chemical compositions, a small amount of bainite and RA could be included in the final microstructure [57]. Low-carbon Si-Mn TRIP steel contains 50 – 60 % polygonal ferrite, 25 – 40 % predominantly carbide-free bainite, 5 – 15 % RA and a small amount of martensite (Fig. 1.6(b)) [58-60].

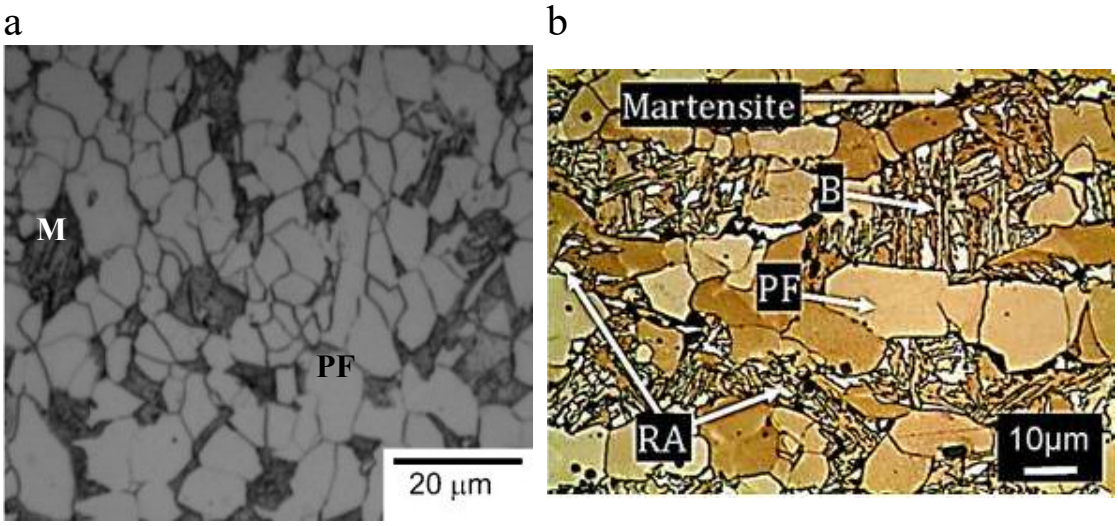

Figure 1.6 Microstructures of thermo-mechanical processed (a) DP steel containing 80% polygonal ferrite (0.06C-1.3Mn-0.10Si-0.6Cr-0.02Nb-0.005Mo, wt.%) [61] and (b) TRIP steel having ~ 50% polygonal ferrite (0.21C-1.51Mn-1.49Si-0.039Nb, wt%) [62]. *PF* is polygonal ferrite, *B* is bainite, *RA* is retained austenite and *M* is martensite.

In TMCP schedule, the initial austenite microstructure is determined by austenitisation process. Higher austenitisation temperature results in coarser and more heterogeneous final microstructure [63]. With a decrease in austenitisation holding time, a smaller austenite grain size is obtained [1].

Following austenitisation, the deformation in austenite region is divided into two stages based on the deformation temperature with respect to non-recrystallisation temperature (T_{nr}). T_{nr} is defined as the temperature, below which the static

recrystallization cannot be completed during cooling after deformation [64]. When the deformation temperature is above T_{nr}, the prior austenite grains are refined through recrystallisation and more nucleation sites along prior austenite grain boundaries are provided for the ferrite nucleation [65]. When the deformation temperature is below T_{nr}, the pancaked austenite structure is obtained, resulting in an increase in ferrite nucleation sites both along the prior austenite grain boundaries and inside the prior austenite grains on dislocations and deformation bands [66-68]. In other words, by lowering the hot rolling finishing temperature, the microstructure after hot rolling is refined; contrarily, the increasing in finish temperature coarsens the microstructure [69]. On the other hand, by increasing the amount of deformation, the number of nucleation sites increases due to an increase in amount of deformation-related defects, leading to ferrite grain size refinement [7, 70]. For example, with an increase in reduction from 0 to 60% at 800 °C, the ferrite grain size decreased from 6.0 to 2.7 μm and fractions of polygonal ferrite increased from 48% to 60% [60]. Conversely, too large reduction may cause some drawbacks, such as micro-shrinkages [63].

When the deformation temperature is in the range from Ar_3 to (Ar_3 + 100) °C, the strain-induced ferrite (SIF) formation can be stimulated [71]. A significant increase in the number of SIF nucleation sites considerably reduces ferrite grain size due to the limited time for its growth and early impingement [72, 73]. For example, a ferrite grain size of 1 – 3 μm was obtained in carbon steels (0.0022 – 0.17 wt. % C) with fine-grained SIF [74-76]. DP steels with an average ferrite grain size of ~ 1.5 μm were also successfully produced as a result of SIF formation [71, 77]. SIF first preferentially nucleated along prior austenite grain boundaries and then the nucleation of SIF in the interior of prior austenite grains takes place with a decrease in deformation temperature and an increase in strain, resulting in more nucleation sites for SIF; an increase in strain rate also increases the number of SIF nucleation sites but reduces the time for its growth [71, 77, 78]. However, the transformation mechanism of the SIF has not been clear until now. Gosh *et al.* suggested a diffusionless transformation [79] while Zheng *et al.* simulated the SIF formation based on diffusional transformation [72].

Following deformation, polygonal ferrite forms during cooling through the austenite-to-ferrite temperature region to interrupted cooling temperature (T_{IC}) (Figs. 1.2(a, c)). Polygonal ferrite transforms from austenite in a diffusional rearrangement of the iron and solute atoms in a series of nucleation and growth steps occurring via interface migration [80], which results in a predominantly random orientation relationship with prior austenite [81]. T_{IC} means the start of fast cooling from this temperature after polygonal ferrite formation. Increasing T_{IC} leads to less amount of polygonal ferrite due to less time for its growth [61, 82]. Pereloma *et al.* [68] reported that the amount of polygonal ferrite formed from recrystallised austenite decreased from 50 – 70% to 15 – 20% when T_{IC} increased from 670 to 725 °C. With an increase in the cooling rate at the same T_{IC}, polygonal ferrite fraction decreases, because the time for its growth decreases and A_{r3} decreases with an increase in the cooling rate [61]. The effect of holding time in austenite-to-ferrite transformation temperature region on ferrite fraction has been studied in the laboratory. Longer holding time increases the ferrite fraction to the value defined by the lever rule [83]. Holding at the nose temperature of ferrite formation boosts the ferrite formation because of shorter incubation period [84]. For TRIP steel, 50 – 60% polygonal ferrite should be obtained because this ferrite fraction could maximise the quantity of RA for different original austenite grain sizes [85].

Following polygonal ferrite formation, the processing route varies for DP and TRIP steels.

(i) DP steel

For DP steel, cooling after polygonal ferrite formation should be fast enough to avoid pearlite and bainite formation and enhance martensite formation [57]. The martensite forms in a diffusionless mode by the coordinated movement of atoms relative to their neighbours without a long-range diffusion [86], which leads to Kurdjumov–Sachs ($\{110\}_{bcc}//\{111\}_{fcc}$, $\langle 111\rangle_{bcc}//\langle 110\rangle_{fcc}$) or Nishiyama–Wasserman ($\{110\}_{bcc}//\{111\}_{fcc}$, $\langle 110\rangle_{bcc}//\langle 112\rangle_{fcc}$) orientation relationships with prior austenite [87, 88]. However, if T_{IC} temperature is too high, some bainite will form instead of martensite during the quenching, because a lower ferrite fraction at higher T_{IC} results in an insufficient carbon enrichment in remaining austenite and raises the bainite and martensite formation temperatures [35]. In industrial conditions, the coiling temperature is

higher than room temperature, which is different from just quenching to room temperature in the laboratory. For example, coiling at a higher temperature (350 vs 250 °C) leads to ferrite ageing and probably martensite tempering [30].

(ii) TRIP steel

For TRIP steel, bainite will form following polygonal ferrite formation. The bainite transformation mechanism has been intensively debated: one school subscribes to a diffusional, reconstructive mechanism [89]; the other school believes the displacive, shear mode of bainite transformation [90, 91]. Classically, carbide-containing bainite is divided into upper bainite and lower bainite based on the cementite distribution. Upper bainite is characterised by cementite precipitating between the bainitic ferrite laths; lower bainite is characterised by carbide precipitating within the bainitic ferrite laths as well as between them [92]. With the development of processing routes and steels with relatively high Si contents (~ 1.5 wt. %), granular bainite and bainitic ferrite are defined according to the morphology of ferrite and the absence of carbides. Granular bainite consists of irregular-shaped ferrite grains containing dispersed martensite/austenite islands; bainitic ferrite comprises ferrite laths with interlayers of austenite and/or martensite [91, 93]. In TRIP steel, the formation of granular bainite and bainitic ferrite is encouraged because it will reject carbon atoms to austenite and increase the RA fraction following quenching to room temperature [40]. However, the formation of upper bainite and lower bainite should be avoided due to their carbon consumption, resulting in a decrease in RA fraction [94].

The cooling rate from T_{IC} to IBT temperature should be high enough to prohibit pearlite formation. Otherwise, pearlite would form and consume carbon, which would result in a decreased RA fraction and, in turn, the deterioration of mechanical properties [42, 63]. However, the control of cooling rate to IBT temperature should be careful in industry. On one hand, slow cooling rate causes pearlite formation. On the other hand, accelerated cooling rate results in residual stresses. During this cooling to IBT temperature, granular bainite forms. And then holding at this IBT temperature is carried out, leading to bainitic ferrite formation. Following carbon rejection to austenite during polygonal ferrite formation, the austenite is continuously carbon-enriched during granular bainite and bainitic ferrite formation. This process is predominately controlled by IBT temperature and holding time.

The temperature chosen for IBT must not only be lower than bainitic transformation start temperature (B_S), but also higher than martensitic transformation start temperature (M_S). Depending on steel compositions and equipment at a steelmaking plant, the IBT temperature is usually between 300 to 500 °C [42, 73]. Bainite transformation rate increases with an increase in the holding temperature [95]. The RA fraction first increases and then decreases with an increase in the IBT temperature from 300 to 500 °C [55, 68]. However, Li *et al.* [73], Seol *et al.* [40] and Zhang *et al.* [96] have found that RA fraction continuously increases with an increase in IBT temperature. This may be due to the narrow range of IBT temperatures they researched. Fig. 1.7(a) shows the maximum RA fraction is achieved at 400 °C. When the temperature increases up to 450 °C, the RA fraction decreases probably due to carbides formation which reduces the carbon enrichment in austenite, leading to the transformation of austenite to martensite during the following quenching [40, 68, 97]; when the temperature decreases down to 350 °C, more austenite is consumed by bainitic ferrite formation due to higher driving force and sometimes lower bainite formation takes up carbon, resulting in a decrease in RA fraction [97].

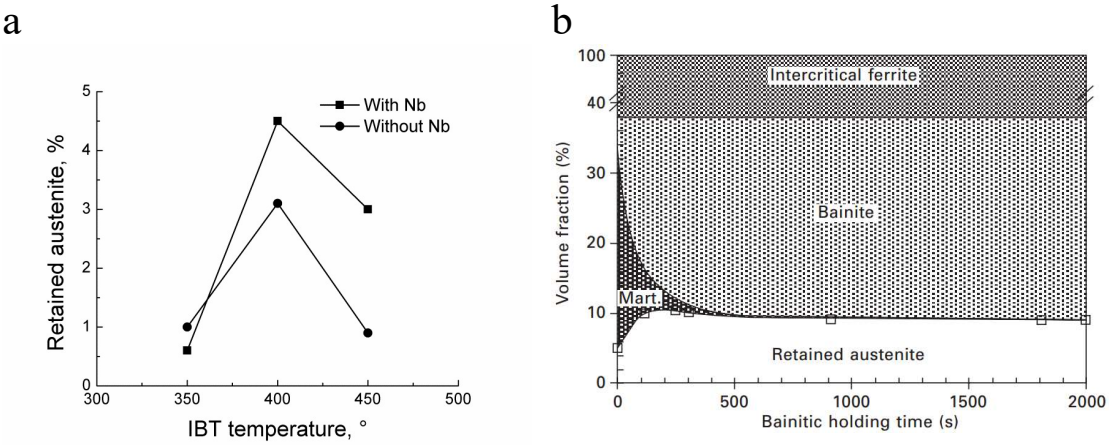

Figure 1.7. (a) The retained austenite fraction as a function of isothermal bainite transformation temperature holding for 600 s after intercritically annealed at 670 ℃ for 600 s of 0.2C-1.55Mn-1.5Si TRIP steel with or without 0.039Nb (wt. %) [68]; (b) the evolution of the room temperature microstructure with the holding time at 360 °C after intercritically annealing at 760 °C for 360 s (0.29C-1.42Mn-1.41Si-0.04Al, wt.%) [98].

On the other hand, a suitable IBT holding time for industrial process simulation should be adopted through experiments. As seen in Fig. 1.7(b), with an increase in

holding time, the RA fraction first increases and then decreases after a maximum value [25, 98, 99]. When the holding time is too short, the carbon enrichment in RA is not enough because of a small amount of bainite formed, resulting in martensite transformation during subsequent quenching [37]. When the holding time is too long, austenite will start to decompose with formation of carbides/cementite and ferrite due to high level of carbon enrichment [99, 100].

Following IBT holding, quenching to room temperature is employed in the laboratory. In industrial production, the air cooling is always chosen for strip steels in a coil. During this cooling to room temperature, martensite will form if austenite is not stable enough.

1.2.3.2 Mechanical properties

For DP steels, the martensite fraction is a key factor governing the mechanical properties [101, 102]. Ultimate tensile strength (UTS) and yield strength (YS) increase with an increase in martensite fraction [103]. When martensite fraction is less than 15%, the ductility of ferrite matrix determines the overall ductility of DP steels [56]. However, when martensite fraction is higher than 15%, the overall ductility of DP steels is determined by microstructure-level inhomogeneity of harder martensite grains in ferrite matrix [56]. For TRIP steels, the features of RA play a crucial role in the mechanical behaviour [104]. The product of UTS and total elongation (TE) tend to increase with an increase in RA fraction [105]. Thus, the RA characteristics, such as morphology, size, and carbon content, should be properly adjusted through thermo-mechanical processing. Some mechanical properties of DP and TRIP steels produced by hot rolling and cold rolling followed by intercritical annealing are plotted in Fig. 1.8. TE trends to decrease with an increase in UTS, which is pronounced for DP steel and less clear for TRIP steel due to the variations in the amount of RA formed after different processing schedules.

a b

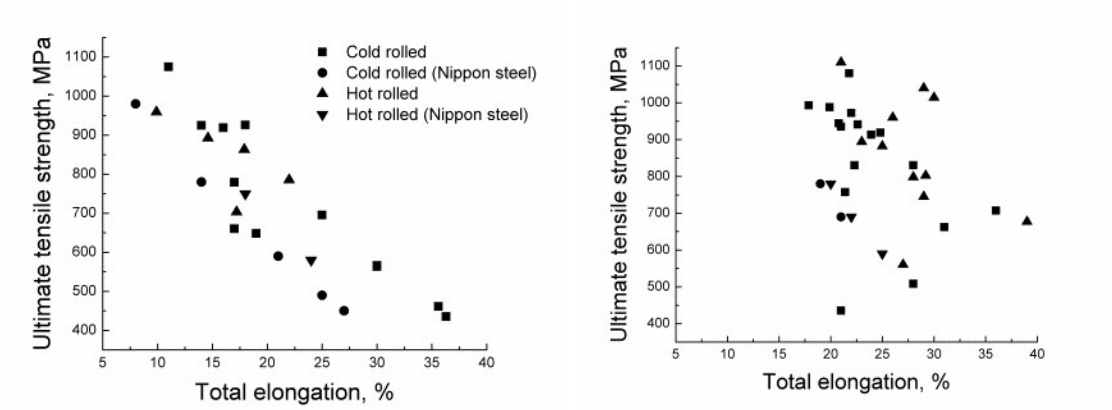

Figure 1.8 Ultimate tensile strength vs total elongation of (a) DP [43, 69, 70, 106-109] and (b) TRIP steels [36, 49, 51, 59, 62, 96, 110-114] produced by hot rolling and cold rolling followed by intercritical annealing.

Fig. 1.9(a) shows representative tensile curves of DP and TRIP steels, both of which exhibit a continuous yielding behaviour. From the curves, the YS is determined using 0.2% offset and the UTS is obtained at the maximum load. The uniform elongation (UE) at the maximum load represents the onset of plastic instability and the TE corresponds to the fracture point. The product of UTS and TE provides a simple prediction for the formability. The higher product means a better formability [115].

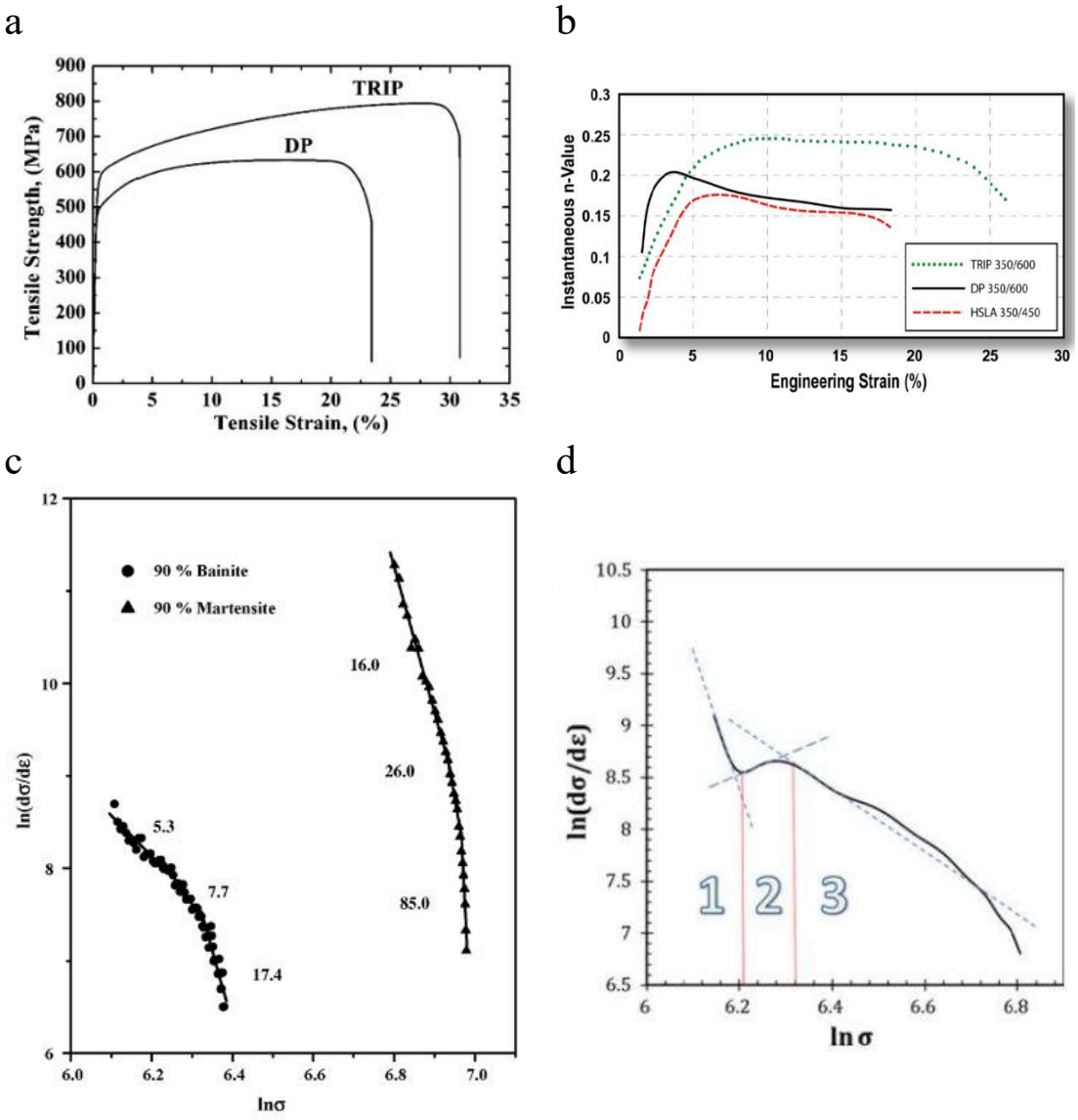

Figure 1.9 (a) Tensile curves [116] and (b) instantaneous strain hardening exponents of DP and TRIP steels [117]; (c, d) modified Crussard–Jaoul model analysis which shows three distinct stages of work hardening for (c) DP [118] and (d) TRIP steels [62].

From the tensile curves, the instantaneous strain hardening exponent n (Fig. 1.9(b)) can be calculated based the following equation [119]:

$$n = d(\ln\sigma) / d(\ln\varepsilon) \tag{1.1}$$

where σ is true stress and ε is true strain. The instantaneous strain hardening exponent also is a good indicator of formability. A higher and more sustained strain hardening exponent means a higher resistance to plastic instability and a delay of the onset of necking, leading to a higher UE and better formability [62, 104, 120]. For DP steel, a higher fraction of polygonal ferrite provides better strain hardening

capability, resulting in a more sustained strain hardening exponent and in turn a higher UE; when the fraction of polygonal ferrite is lower, the strain hardening exponent decreases faster during straining, leading to a lower UE [120, 121]. Compared to HSLA and DP steels, TRIP steel exhibits a higher and more sustainable strain hardening exponent (Fig. 1.9(b)), which results from the continuous transformation of RA to martensite during straining [62, 104].

The generally used Hollomon's equation is a power law relationship between the stress and the strain, which is expressed as follows [122]:

$$\sigma = K\varepsilon^n \tag{1.2}$$

where n is strain hardening exponent and K is strengthening co-efficient. However, the calculated Hollomon curves deviated from linearity over all the uniform strain range for the high strength steels and thus, the Hollomon parameters could not be applied to an entire curve [118, 123]. The modified Crussard–Jaoul (C–J) analysis based on the Swift formula is sensitive to the changes in the deformation behaviour, which presents as follows [123]:

$$\varepsilon = \varepsilon_0 + c\sigma^m \tag{1.3}$$

where ε_0 is the initial true strain, c is a constant and m is the strain hardening index. The modified C–J analysis is useful for the interpretation of the work-hardening behaviour. Fig.1.9(c) shows the plots of $\ln(d\sigma/d\varepsilon)$ versus $\ln\sigma$ for DP steels having 90% martensite or bainite, which clearly exhibited three deformation stages. The numbers near the curves correspond to the m values in different stages. The first stage is related to the deformation of the ferrite matrix; the second stage corresponds to the ferrite deformation restrained by martensite/bainite with dislocations piling up in the regions adjacent to martensite/bainite; the third stage was associated with uniform straining of ferrite and martensite/bainite [118, 122, 124]. Fig. 1.9(d) illustrates three distinct stages for a TRIP steel having 49% polygonal ferrite and 13% RA. As can be seen, the second stage is totally different from the second stage of DP steel, which is ascribed to the contribution of TRIP effect in this stage [62].

1.2.4 Retained austenite stability with respect to martensite transformation

The excellent combination of high strength and high ductility in TRIP steels is obtained through the RA transforming to martensite during deformation, *i.e.* TRIP effect which delays the onset of local necking and increases the elongation [125]. Thus, the stability of RA is crucial to mechanical properties. When the RA is not stable, the RA transforms early to martensite at a low strain during deformation, which makes the RA contribution to ductility of TRIP steels small; whereas, when RA is overstabilised, the TRIP effect is totally inhibited, resulting in no contribution to the mechanical properties improvement [112]. In order to contribute as much as possible to mechanical properties, the RA providing a gradual transformation to martensite during deformation should be obtained through suitable steel compositions and processing schedules [126].

1.2.4.1 Retained austenite stability

(a) Chemical stability

Chemical stability is an important operational mechanism for austenite retention. Carbon significantly enhances the austenite stability. RA containing very low carbon (< 0.6 wt. %) concentration transforms to martensite at a low strain [127] while a high carbon (> 1.8 wt. %) [128] content in RA completely inhibits austenite-to-martensite transformation. The other alloying elements, such as Mn, Si, and Al, also enhance RA stability as discussed in *Section 1.2.2*.

(b) Mechanical stability

Mechanical stability of RA mainly refers to the resistance to martensitic transformation induced by applied stress, which is affected by the load transfer from neighbouring phases. RA located among the softer ferrite, which work hardens fast, bears more strain and stress, resulting in a faster transformation to martensite. Contrarily, when RA is encompassed by harder bainite, which helps to reduce strains and stresses transferred to RA, the martensite transformation is delayed [113]. The dislocations in RA, induced by deformation, enhance the RA stability by retarding the martensite transformation [129]. The RA grain size also affects mechanical stability. The smaller grain size results in a better mechanical stability as nucleation of martensite is more difficult in a finer austenite [53]. In addition, the RA

orientation with respect to the load direction affects the stability. When the RA exhibits an orientation which helps the RA deformation, it will result in a larger driving force for austenite-to-martensite transformation and in turn the earlier transformation of RA [127]. RA could also rotate during deformation, resulting in transformation to martensite by changing the slip plane and direction [130]. Furthermore, the RA stability is also affected by the stress state. Tensile loading leads to a faster transformation of RA to martensite than compressive loading [131]; whereas, the RA is less stable under biaxial stretching than under tensile loading [132].

1.2.4.2 Factors affecting retained austenite stability

(a) Effect of morphology

There are two main types of RA morphology, namely film RA and blocky RA [55], as shown in Figs. 1.10 (a) and (b) respectively [112]. Based on prior researches [63, 93, 104, 112, 113, 126, 130, 133], film RA is much more stable than blocky RA. Two main reasons were put forward for this: (1) film RA is much smaller than the blocky type; (2) film RA contains a higher carbon concentration than the blocky type.

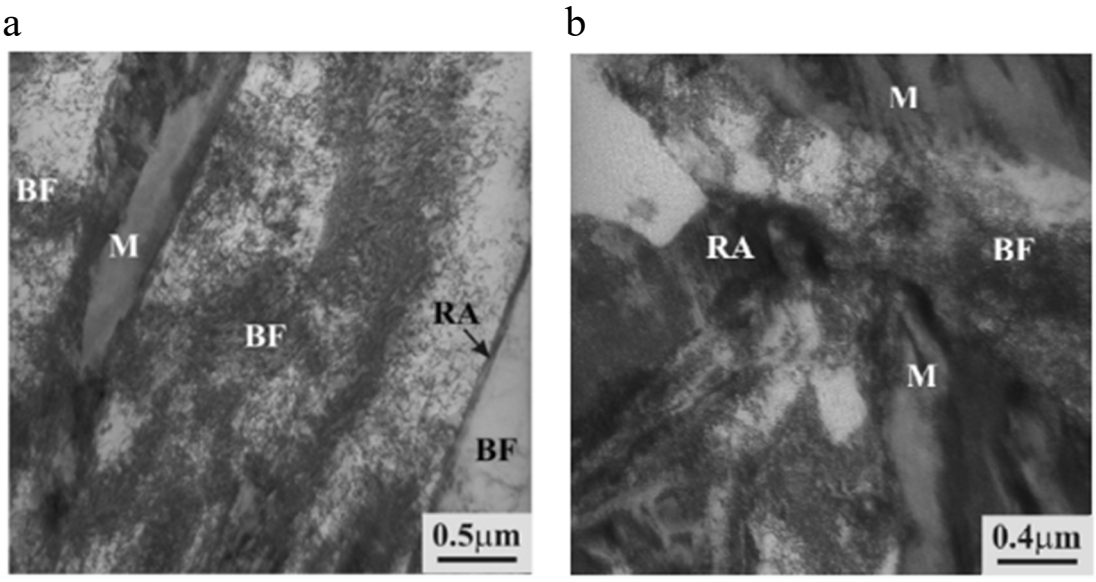

Figure 1.10 Representative transmission electron microscopy images for retained austenite: (a) film retained austenite; (b) blocky retained austenite [112]. *RA* is retained austenite, *M* is martensite and *BF* is bainitic ferrite.

(b) Effect of surrounding phases

Five different RA locations are typically as follows [113]: (1) blocky islands among polygonal ferrite grains; (2) small islands at interfaces between polygonal ferrite and bainite; (3) small islands in granular bainite; (4) layers or films between bainitic ferrite laths; (5) martensite/austenite constituent.

As mentioned in *Section 1.2.4.1* with respect to mechanical stability, the RA located among the softer ferrite bears more strains and stresses, resulting in a faster transformation to martensite; while the strains and stresses transferred to the RA encompassed by harder bainite are reduced, leading to a delayed martensite transformation [113]. Moreover, the RA located in bainite benefits from the additional carbon enrichment during bainite transformation, which enhances its stability [93, 134]. However, thin austenite is also found to more easily transform to martensite by the assistance of local stress concentration caused by slip deformation [135]. RA in granular bainite, which demonstrates the optimum stability and contributes to ductility in TRIP steels, gradually transforms to martensite during deformation [93]. Noticeably, the dependence of carbon content in the RA on its surrounding phases has not been experimentally and systematically studied so far.

(c) Effect of grain size

It is reported that austenite with a finer grain size has a higher stability [53]. A suitable grain size with proper stability is important to gain a continuous deformation-induced martensite transformation. When the grain size is smaller than 0.02 μm, RA cannot contribute to the TRIP effect because the fine RA resists forming martensite due to insufficient nucleation sites [136, 137]. When the grain size is larger than 1 μm, it is not stable and tends to transform to martensite at a low level of strain [136]. In addition, the carbon content distribution in the RA is not homogeneous and sometimes the carbon depleted zone is observed, resulting in a partial transformation to martensite during straining [138].

1.3 Objective of the thesis

With respect to the currently operating technologies (hot rolling and cold rolling) for the production of DP and TRIP steels in industry, strip casting technology is another promising way due to its lower cost and higher efficiency resulting from shorter processing line. However, the development of strip casting to manufacture these steels requires ground-breaking investigation. In addition, the effect of processing parameters in strip casting on the microstructures and mechanical properties should be studied in depth. Furthermore, the transformation mechanism of SIF has not been fully understood. Finally, a site-specific and systematic study with respect to the relationships between carbon content, and grain size, morphology and neighbouring phase for RA have not been carried out yet.

Addressing the above, the conventional 0.08C-0.81Si-1.47Mn-0.03Al DP and 0.17C-1.52Si-1.61Mn-0.03Al TRIP steels (wt. %) were chosen for this project. The aims of the present study are two-fold:

(i) To develop the processing schedules for the production of DP and TRIP steels using the strip casting technique and study their microstructures and mechanical properties;

(ii) To site-specifically investigate the dependence of RA carbon content on its grain size, morphology and neighbouring phase, and the substitutional solute segregation across the interface between RA and ferrite in bainitic ferrite/granular bainite.

With respect to the first aim, the particular objectives are:

- To study the effect of austenitisation temperature and time, deformation temperature, the amount of deformation, interrupted cooling temperature and IBT temperature on microstructure evolution.

- To develop an approach for grain refinement by SIF and understand the mechanism of SIF formation.

- To understand the relationship between microstructures and tensile properties using the strain hardening rate, instantaneous strain hardening exponent, the modified C–J model and iso-work modelling.

To achieve the second aim, the following tasks need to be undertaken for the TRIP steel:

- To characterise in detail the microstructure with particular attention to bainite and RA morphologies using correlative electron backscattering diffraction (EBSD) and transmission electron microscopy (TEM).

- To conduct correlative EBSD and atom probe tomography (APT) studies in order to determine C content in RA as a function of its location and size, and to obtain different interfaces between RA and ferrite in bainitic ferrite/granular bainite.

1.4 Materials and processing

1.4.1 Initial materials

The chemical compositions of the studied steels (Table 1.2) were chosen as typical industrial compositions for DP and TRIP steels [6]. Individual alloy stock of each element (Fe, Cr, Mn, etc.) was used for the steels production using both conventional casting and dip tester. Flat dip-cast specimens of 36 x 36 x 1.2 mm^3 size used in the present study were produced at Deakin University using a dip tester (Fig. 1.11). In the dip tester, copper substrates spot welded with R-type thermocouple were employed to simulate the initial contact conditions between the liquid metals and twin rollers in the strip casting technology [139]. In order to achieve high cooling rate up to ~ 1700 Ks^{-1} which is typical for the strip casting process [13, 16, 24], a certain time for substrates immersion into the molten metal should be controlled. After the immersion, the substrates were removed from the melt and the dip-cast specimens were obtained. In addition, 9 mm in height and 35 mm in diameter ingots were cast only for the determination of CCT diagrams, which requires hollow cylinder samples for the experiments.

Table 1.2 Chemical compositions of DP and TRIP steels (wt. %).

	C	Si	Mn	Al	Cu	Cr	P	S	B
DP steel	0.0768	0.805	1.47	0.0346	0.0126	0.233	0.0055	<0.00050	0.00091
TRIP steel	0.172	1.52	1.61	0.0266	0.0153	0.195	0.0044	<0.00050	0.00057

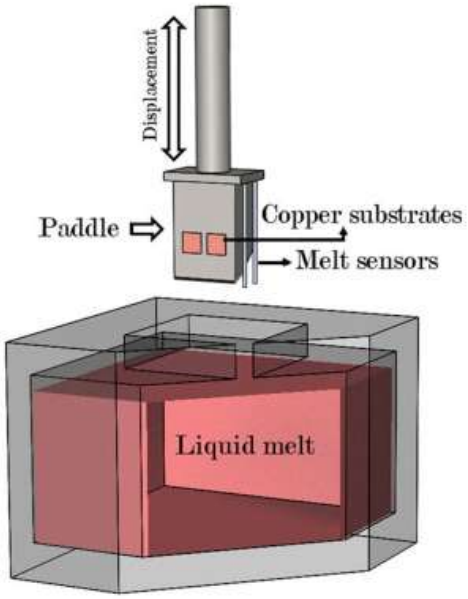

Figure 1.11 Schematic diagram of the dip tester [139].

1.4.2 Heat treatments and thermo-mechanical processing

Heat treatments were carried out using a Theta Dilatronic III Quenching and Deformation dilatometer operating under a vacuum of ~ 6.7×10^{-2} Pa. This vacuum prevented oxidation and decarburization of the samples. The temperature was monitored using an S-type thermocouple spot-welded to the surface centre of a cylindrical or flat sample. For the determination of CCT diagrams, hollow cylinder specimens (an outer diameter of 5 mm and an inner diameter of 3.5 mm with the length of 10 mm) for both steels were machined from as-cast ingot. The flat samples of 14×6 mm^2 and ~ 1 mm thickness with extension at each side (as shown in Fig. 2.2(b), for gripping the sample in the dilatometer), cut from dip-cast samples, were used for all other heat treatments. The heat treatment schedules for DP and TRIP steels are described in detail in *Chapter 2* and *Chapter 5*, respectively.

The thermo-mechanical processing was carried out using a Gleeble 3500 thermo-mechanical simulator in hydrawedge mode. The samples of $20 \times 15 \times (0.9 – 1.2)$ mm^3 size were machined from the dip-cast specimens. However, the thickness of the samples was beyond the capability of the movement control system of the Gleeble 3500 thermo-mechanical simulator. Thus, a sandwich sample was designed (Fig. 1.12), which used two dummy samples (2.5 mm thickness; made of structural microalloyed steel) to clamp the studied sample. Tantalum sheets were inserted between them in order to prevent diffusion, while carbon sheets were added on the top and bottom in order to enhance the conductivity between the sample and anvils. A K-type thermocouple for temperature monitoring was welded to the centre of cross-section of the studied sample. The sandwich sample was clamped by two Gleeble anvils. The rolling convention (Fig. 1.12) is used throughout the thesis because plain strain compression during hot rolling is simulated in our thermo-mechanical processing. Namely, the normal direction (ND) is parallel to the compression direction, the rolling direction (RD) relates to the sample extension and the transverse direction (TD) corresponds to the sample constraint. The selected thermo-mechanical processing parameters of DP and TRIP steels are listed in Table 1.3.

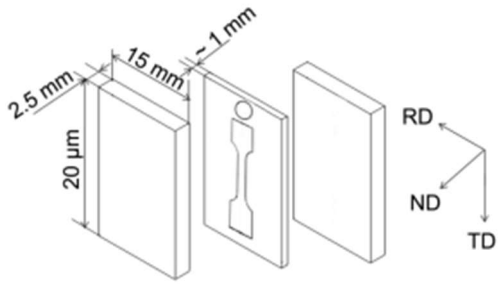

Figure 1.12 The illustration of sandwiched sample. *RD* is rolling direction, *ND* is normal direction and *TD* is transverse direction.

Table 1.3 Main thermo-mechanical processing parameters of selected schedules for DP and TRIP steels.

	Austenitisation temperature, °C /time, s	Reduction	Deformation temperature, °C	T_{IC}, °C	IBT temperature, °C
DP steel	1300/180	~ 0.17	1050	650	--
		~ 0.46	1050	650 – 690	--
		~ 0.41	700 – 1050	670	--
TRIP steel	1250/300	~ 0.41	1050	670 – 710	--
				710	350 – 500

1.5 Microstructure characterisation and mechanical testing

For deformed samples, the coordinate system of normal direction (ND), rolling direction (RD) and transverse direction (TD) is used because the plain strain compression during hot rolling was simulated in the thermo-mechanical experiments. The force direction corresponds to ND direction while the RD direction is along the width.

1.5.1 Optical microscopy

A Leica DMR research optical microscope (OM) was used to characterise the microstructures. The non-deformed samples were cut perpendicular to longitudinal direction and the deformed samples were cut parallel to RD–ND plane. The cross-sections were mounted and then mechanically polished. To reveal the prior austenite grain boundaries, the samples were etched for 15 – 20 s at 65 °C temperature in the solution of saturated picric acid in ethanol plus few drops of benzene sulfonate. To reveal ferrite, bainite and martensite, the samples were etched with 2 vol. % nital.

Colour etching was employed to distinguish polygonal ferrite, bainite, martensite and RA. The samples were mechanically polished and then electropolished using the Struers Lectropol-5 in an electrolyte of 330 ml methanol, 330 ml butoxyethanol and 40 ml perchloric acid at 50 V, ~ 1.0 mA and 17 °C for ~ 90 s. Then the samples were firstly dipped for 18 – 20 s in a solution of 4 % picral (4 gm dry picric acid in 100 ml ethanol) mixed with few drops of concentrated hydrochloric acid (1 ml per 100 ml of picral solution) and then etched for 6 – 8 s with freshly prepared 10 % aqueous sodium metabisulfite solution [140].

1.5.2 Scanning electron microscopy and electron backscattering diffraction

The microstructures from the central areas of cross-sections were characterised using a JEOL JSM-7001F field emission gun – scanning electron microscope (FEG – SEM) fitted with a Nordlys-II(S) EBSD and an 80 mm^2 X-Max energy dispersive X-ray spectroscopy (EDS) detectors interfacing with the Oxford Instruments Aztec software suite, which was operated at 15 kV accelerating voltage and 5.1 nA probe current.

EBSD is a powerful technique to study any crystalline or polycrystalline materials based on the Kikuchi bands present in the diffraction pattern. These bands are related to the crystal structure and orientation within the electron interaction volume. Bearing in mind, EBSD cannot distinguish the phases having the same crystal structure, such as polygonal ferrite, bainite and martensite [141]. In addition, the resolution of EBSD is restricted by the step size.

EBSD mapping, and simultaneous EBSD and EDS mapping were undertaken on the same machine. The EBSD maps returning an overall indexing rate of 90 – 98% were processed using the Oxford Instruments Channel-5 software package. Micro-textures were depicted via exporting the EBSD data to the JTex software [142]. For EBSD, DP steel samples were polished using standard Struers colloidal silica suspension (OP-S, 0.04 micron size) as a final step following the mechanical polishing to 1 μm, while TRIP steel samples were electropolished.

1.5.3 Transmission electron microscopy

The 3-mm discs for TEM were electrically wire cut in the centre parallel to the long axis for non-deformed samples and wire cut from RD–TD plane of deformed sample, mechanically polished to 50 – 80 μm thickness using silicon papers, and electropolished using a twin-jet Struers Tenupol-5 electropolisher in a solution of 10 vol. % perchloric acid in methanol at 30 V, 150 mA and -25 °C. The JEOL 2011 TEM and JEOL JEM-ARM200F operating at 200 kV were used to characterise the microstructures.

1.5.4 X-ray diffraction

A PANalytical X'pert-Pro MRD goniometer equipped with Ni-filtered Cu Kα radiation was employed to measure the RA fraction on the electropolished plane at mid-thickness of the non-deformed sample. It was operated at 40 kV accelerating voltage and 45 mA beam current. The X-ray diffraction (XRD) scans were conducted over the range of scattering angles $2\theta = 38 – 150°$ at a step size of 0.01° and a step time of 750 s. The direct comparison method was used to calculated RA fraction based on the integrated intensities of four austenite peaks {(111), (200), (220) and (113)} and four ferrite peaks {(110), (200), (211) and (310)} [97]. The following empirical equation was used to determine the carbon content in RA [143]:

$$a = 3.572 + 0.033 \times [C\%] + 0.0012 \times [Mn\%] - 0.00157 \times [Si\%] + 0.0056 \times [Al\%] \quad (1.4)$$

where a is austenite lattice parameter (Å) [31], and [C%], [Mn%], [Si%] and [Al%] represent the concentrations in weight percentage of carbon, manganese, silicon and aluminum, respectively. For convenience, the nominal steel's compositions (Table 1.2) of alloying elements were used in Eq. 1.1 for determination of carbon in RA for all processing conditions.

1.5.5 Atom probe tomography

APT provides both three-dimension imaging and chemical composition analysis at the atomic scale. The sample is in the form of a needle with a very sharp tip. Under a very high electrostatic field, the atom evaporation from the surface, layer by layer, is triggered via a voltage or laser pulse. According to the Cameca Instruments Inc., the detection efficiency is up to 80% in the most modern instruments. The Time of Flight of the evaporated ion allows determining the mass-over-charge ratio and in turn identifying the type of the element. The original position of the atoms can be reconstructed based on the ion impact positions on the detector and the arrival sequence [144].

Atom probe specimens were prepared by a site-specific lift-out method as illustrated in Fig. 1.13, using a dual-beam focused ion beam (FIB)/SEM instrument (FEI Quanta 3D) with the final annular FIB milling stage carried out at 8 kV and 25 pA. The procedures of this lift-out method are briefly described in the following [145, 146]. First, the region of interest (ROI) should be found based on the corresponding EBSD map (Figs. 1.13(a, b)). Second, a bar containing the ROI was cut out using stepwise patterns and an undercut (Fig. 1.13(b)). Third, a micromanipulator was used to lift-out the bar and a piece of the bar was attached to the tip of the electropolished Mo grid with ion-beam-assisted Pt deposition (Fig. 1.13(c)). Finally, a sequence of annular mill patterns was applied to the specimen post and an appropriate tip shape was obtained (Fig. 1.13(d)). Several needle-like specimens were also prepared using a standard two-stage electropolishing technique [144].

APT experiments were carried out using a local electrode atom probe (LEAP 4000HR, Cameca Instruments) operating at a pulse repetition rate of 200 kHz, 20%

pulse fraction, temperate set-point of 60 K and target evaporation rate of 0.5%. The IVAS 3.6.8 software (Cameca Instruments) was used to reconstruct and analyse the data.

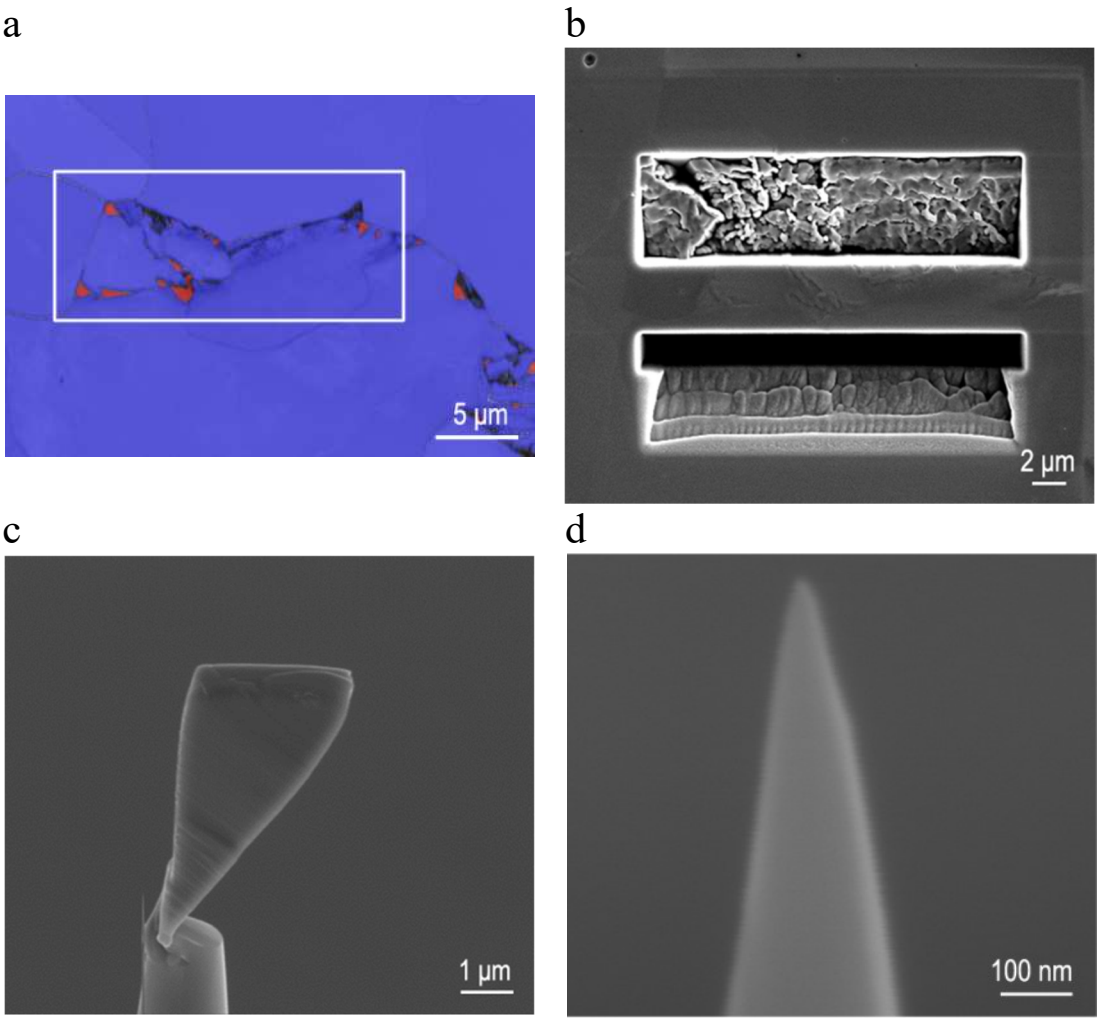

Figure 1.13 Site-specific lit-out method for preparation of APT specimens. (a) A corresponding EBSD map showing the region of interest indicated by the white rectangle (Red is fcc and blue is bcc); (b) the bar containing the region of interest was mill cut for lift-out; (c) a piece of the bar was attached to the support grid; (d) an atom probe sample was produced after annular milling.

1.5.6 Microhardness measurement

Struers Emco-Test DuraScan-70 Vickers hardness tester was employed to measure hardness using a load of 25 g and a loading time of 10 s. For both polygonal ferrite and second phase regions, the average hardness was calculated using the values from 5 areas by removing the maximum and minimum values among 7 areas.

1.5.7 Tensile tests

Tensile tests were carried out on a minimum of two dog-bone samples (gauge length × width × thickness = 4.9 × 2.1 × (0.5 – 1) mm^3) per condition at an initial strain rate of 4 $\times 10^{-4}$ s^{-1} using an in-house modified "Kammrath and Weiss GmbH" tensile stage with 5 kN load cell.

1.6 Overview of chapters 2 to 7

Chapter 2 details the design of processing route for the production of DP steel using strip casting. Prior austenite microstructure was first simulated. Based on the measured CCT diagram, the effect of cooling rate, holding temperature and time on ferrite formation was studied. A typical microstructure of DP steel was obtained and characterised using XRD, SEM, EDS and TEM. The influence of ferrite fraction on tensile properties and fracture was investigated. The strain hardening behaviour was analysed using strain hardening exponent and modified C–J model. The tensile tests results were compared with the properties of existing DP steels. The results were published in **Materials & Design** 88 (2015) 537-549.

Chapter 3 illustrates the effect of deformation (reduction = ~ 0.17 and ~ 0.46) at 1050 °C, which is above T_{nr}, and of T_{IC} on microstructure evolution and mechanical properties of the DP steel. A decrease in both ferrite grain size and the size of second phase regions occurred following the deformation as a result of static recrystallisation leading to an increase in the number of ferrite nucleation sites. The evolution of mechanical properties as a function of ferrite fraction and the amount of deformation was analysed. The dislocation density of ferrite and ferrite grain size were discussed in relation to the strengthening mechanisms. The results were published in **Materials Science and Engineering A** 651 (2016) 291-305.

Chapter 4 elucidates the influence of deformation temperatures (in the range of 700 – 1050 °C) at a reduction of ~ 0.41 on microstructure and mechanical properties of the DP steel. The dependence of ferrite formation mechanism on deformation temperature was analysed. The microstructure constituents of polygonal ferrite, SIF and second phase region were separated using EBSD and then the analysis for each constituent was carried out. Based on this analysis, a possible transformation mechanism of SIF was discussed. The modified iso-work modelling was utilised to determine the contribution to strength arising from different microstructure constituents. The obtained tensile properties outperformed the industrially produced DP 600 steel. The results have been submitted for publication in **Acta Materialia**.

Chapter 5 details the design of processing route for the production of TRIP steel using strip casting based on the prior austenite microstructure simulation and constructed CCT diagram. The dependence of ferrite formation on cooling rate, holding temperature and time was investigated. The evolution of microstructure and mechanical properties with respect to IBT temperature was studied. A typical microstructure of TRIP steel was obtained, which was characterised using XRD, colour etching, SEM, EDS, EBSD, APT and TEM. The strain hardening behaviour was studied using strain hardening rate, strain hardening exponent and C – J model, which was correlated to microstructures. The results were published in **Materials Science and Engineering A** 664 (2016) 26-42.

Chapter 6 illustrates the influence of deformation (reduction = ~ 0.41) at 1050 °C above T_{nr} and IBT temperature on microstructure evolution and mechanical properties of the TRIP steel. The variation of polygonal ferrite formation with T_{IC} was also evaluated. A decrease in the average ferrite grain size and the average size of second phase regions was resulted from the deformation, indicating a refined and more homogeneous microstructure. The RA fraction was discussed in relation to the size of second phase region and IBT temperature. The strengthening mechanisms after deformation were predominantly ascribed to dislocation strengthening and grain size refinement. The tensile properties of studied TRIP steels were comparable to the industrially manufactured TRIP 690 steel. The results were published in **Materials Science and Engineering A** 667 (2016) 356-366.

Chapter 7 addresses the site-specific characterisation of the different morphologies of RA with respect to different neighbouring phases using correlated EBSD, TEM and APT. The variation of chemical compositions in different types of RA was investigated by correlated EBSD and APT. The dependence of carbon content in RA on its neighbouring phase and grain size was discussed with respect to the carbon partitioning. The discussion on the substitutional solute segregation across the interfaces between the RA and ferrite in bainitic ferrite/granular bainite was provided. Following this, the bainite transformation mechanism was discussed. The results are in preparation for submission to **Acta Materialia**.

References

[1] T. Furukawa, Met. Prog. 116 (1979) 36-39.

[2] B.C. De Cooman, Curr. Opin. Solid State Mater. Sci. 8 (2004) 285-303.

[3] O. Bouaziz, S. Allain, C.P. Scott, P. Cugy, D. Barbier, Curr. Opin. Solid State Mater. Sci. 15 (2011) 141-168.

[4] I.Y. Pyshmintsev, C. Mesplont, S. Jacobs, B.C. De Cooman, Steel Res. 73 (2002) 392-402.

[5] V. Savic, L. Hector Jr, J. Fekete, Exp. Mech. 50 (2010) 99-110.

[6] R. Kuziak, R. Kawalla, S. Waengler, Arch. Civ. Mech. Eng. 8 (2008) 103-117.

[7] H. Niakan, A. Najafizadeh, Mater. Sci. Eng. A 527 (2010) 5410-5414.

[8] H. Aydin, E. Essadiqi, I.H. Jung, S. Yue, Mater. Sci. Eng. A 564 (2013) 501-508.

[9] A.P. Hardwick, T. Outteridge, Int. J. Life Cycle Ass. (2015) 1-8.

[10] H. Wang, W.Y. Liu, X.P. Duan, Q.S. Wu, G.L. Yuan, Ironmak. Steelmak. 36 (2009) 120-124.

[11] D. Bhattacharya, Mater. Sci. Forum 773 (2014) 325-335.

[12] S. Ge, M. Isac, R.I.L. Guthrie, ISIJ Int. 52 (2012) 2109-2122.

[13] N. Zapuskalov, ISIJ Int. 43 (2003) 1115-1127.

[14] K.H. Spitzer, F. Ruppel, R. Viscorova, R. Scholz, J. Kroos, V. Flaxa, Steel Res. Int. 74 (2003) 724-731.

[15] R. Wechsler, Scand. J. Metall. 32 (2003) 58-63.

[16] S. Ge, M. Isac, R.I.L. Guthrie, ISIJ Int. 53 (2013) 729-742.

[17] R. Nooning Jr, C. Killmore, H. Kaul, A. Phillips, D. Edelman, P. Campbell, J. Williams, International Conference on Microalloyed Steels, AIST, Pittsburgh, USA, 2007, pp. 57-69.

[18] C.R. Killmore, H. Creely, A. Phillips, H. Kaul, P. Campbell, M. Schueren, J.G. Williams, W. Blejde, Mater. Forum 32 (2007) 13-28.

[19] M. Daamen, C. Haase, J. Dierdorf, D.A. Molodov, G. Hirt, Mater. Sci. Eng. A 627 (2015) 72-81.

[20] M. Daamen, O. Güvenç, M. Bambach, G. Hirt, CIRP Ann. Manuf. Techn. 63 (2014) 265-268.

[21] K.Y. Xie, L. Yao, C. Zhu, J.M. Cairney, C.R. Killmore, F.J. Barbaro, J.G. Williams, S.P. Ringer, Metall. Mater. Trans. A 42A (2011) 2199-2206.

[22] P.J. Felfer, C.R. Killmore, J.G. Williams, K.R. Carpenter, S.P. Ringer, J.M. Cairney, Acta Mater. 60 (2012) 5049-5055.

[23] T. Dorin, K. Wood, A. Taylor, P. Hodgson, N. Stanford, Acta Mater. 115 (2016) 167-177.

[24] D.J. Sosinsky, P. Campbell, R. Mahapatra, W. Blejde, F. Fisher, Metallurgist 52 (2008) 691-699.

[25] B. Fu, W.Y. Yang, L.F. Li, Z.Q. Sun, Acta Metall. Sin. 49 (2013) 408-414.

[26] J.B. Seol, J.E. Jung, Y.W. Jang, C.G. Park, Acta Mater. 61 (2013) 558-578.

[27] T. Furukawa, M. Tanino, H. Morikawa, M. Endo, Trans. ISIJ 24 (1984) 113-121.

[28] B.S. Seong, E.J. Shin, Y.S. Han, C.H. Lee, Y.J. Kim, S.J. Kim, J. Phy. B 350 (2004) E467-E469.

[29] B. Demir, M. Erdoğan, J. Mater. Process. Technol. 208 (2008) 75-84.

[30] W. Tan, B. Han, S.Z. Wang, Y. Yang, C. Zhang, Y.K. Zhang, J. Iron Steel Res. Int. 19 (2012) 37-41.

[31] X.P. Shen, R. Priestner, Metall. Trans. A 21 (1990) 2547-2554.

[32] S.J. Kim, Mater. Sci. Forum 638-642 (2010) 3313-3318.

[33] G. Tirumalasetty, M. van Huis, C. Kwakernaak, J. Sietsma, W. Sloof, H. Zandbergen, Scripta Mater. 71 (2014) 29-32.

[34] L.J. Zhu, D. Wu, X.M. Zhao, J. Iron Steel Res. Int. 15 (2008) 68-71.

[35] A. Mein, G. Fourlaris, D. Crowther, P.J. Evans, Mater. Charact. 64 (2012) 69-78.

[36] K.I. Sugimoto, T. Muramatsu, S.I. Hashimoto, Y. Mukai, J. Mater. Process. Technol. 177 (2006) 390-395.

[37] S. Chatterjee, M. Murugananth, H.K.D.H. Bhadeshia, Mater. Sci. Technol. 23 (2007) 819-827.

[38] P. Jacques, E. Girault, T. Catlin, N. Geerlofs, T. Kop, S. van der Zwaag, F. Delannay, Mater. Sci. Eng. A 273 (1999) 475-479.

[39] J.Y. Kang, H.C. Lee, S.H. Han, Mater. Sci. Eng. A 530 (2011) 183-190.

[40] J.B. Seol, D. Raabe, P.P. Choi, Y.R. Im, C.G. Park, Acta Mater. 60 (2012) 6183-6199.

[41] T.S. Wang, M. Zhang, Y.H. Wang, J. Yang, F.C. Zhang, Scripta Mater. 68 (2013) 162-165.

[42] L. Li, B.C. De Cooman, R.D. Liu, J. Vleugels, M. Zhang, W. Shi, J. Iron Steel Res. Int. 14 (2007) 37-41.

[43] A. Huseyin, K.Z. Havva, K. Ceylan, J. Iron Steel Res. Int. 17 (2010) 73-78.

[44] J. Kobayashi, D. Ina, N. Yoshikawa, K. Sugimoto, ISIJ Int. 52 (2012) 1894-1901.

[45] H.K.D.H. Bhadeshia, J. Mater. Sci. 18 (1983) 1473-1481.

[46] H. Chen, Z. Yang, C. Zhang, K. Zhu, S. van der Zwaag, Acta Mater. 104 (2016) 62-71.

[47] C.L. Zhang, B. Liao, D.Y. Cai, T.C. Zhao, Y.C. Fan, Mater. Des. 28 (2007) 1760-1766.

[48] S. Chatterjee, A.K. Verma, V. Sharma, Scripta Mater. 58 (2008) 191-194.

[49] N. Zhu, Q. Wu, Y. He, X. Lu, L. Li, P. Hu, Steel Res. Int. (2013).

[50] S.K. Ghosh, P.P. Chattopadhyay, A. Haldar, S. Ganguly, S. Datta, ISIJ Int. 48 (2008) 649-657.

[51] L.Y. Zhang, D. Wu, Z. Li, J. Iron Steel Res. Int. 19 (2012) 42-47.

[52] T. Song, B.C. De Cooman, Metall. Mater. Trans. A 44A (2013) 1686-1705.

[53] A.Z. Hanzaki, P.D. Hodgson, S. Yue, Metall. Mater. Trans. A 28 (1997) 2405-2414.

[54] L.A. Dobrzanski, W. Borek, Arch. Civ. Mech. Eng. 12 (2012) 299-304.

[55] C.J. Wang, X.J. Sun, Q.L. Yong, Z.D. Li, X. Zhang, L. Jiang, Acta Metall. Sin. 49 (2013) 399-407.

[56] X. Sun, K.S. Choi, A. Soulami, W.N. Liu, M.A. Khaleel, Mater. Sci. Eng. A 526 (2009) 140-149.

[57] M. Dziedzic, S. Turczyn, Arch. Civ. Mech. Eng. 10 (2010) 21-30.

[58] A. Ray, S.K. Dhua, Mater. Charact. 37 (1996) 1-8.

[59] J. Zrnik, O. Muransky, O. Stejskal, P. Lukas, P. Hornak, Mater. Sci. Eng. A 483-84 (2008) 71-75.

[60] Z.Y. Tang, H. Ding, L.X. Du, H. Ding, X. Zhang, J. Iron Steel Res. Int. 14 (2007) 56-60.

[61] M. Asadi, B.C. De Cooman, H. Palkowski, Mater. Sci. Eng. A 538 (2012) 42-52.

[62] F. Alharbi, A.A. Gazder, A.G. Kostryzhev, B. Cooman, E.V. Pereloma, J. Mater. Sci. 49 (2014) 2960-2974.

[63] L. Skalova, R. Divisova, D. Jandova, J. Mater. Process. Technol. 175 (2006) 387-392.

[64] S. Vervynckt, K. Verbeken, B. Lopez, J.J. Jonas, Int. Mater. Rev. 57 (2012) 187-207.

[65] S. Ghosh, S. Mula, Mater. Sci. Eng. A 646 (2015) 218-233.

[66] M. Rakhshkhorshid, H. Monajati Zadeh, S.H. Hashemi, Int. J. Adv. Manuf. Technol. 79 (2015) 1623-1631.

[67] S. Wang, H. Yu, T. Zhou, T. Wang, Mater. Des. 88 (2015) 847-853.

[68] E.V. Pereloma, I.B. Timokhina, P.D. Hodgson, Mater. Sci. Eng. A 273 (1999) 448-452.

[69] S.H. Han, S.H. Choi, J.K. Choi, H.G. Seong, I.B. Kim, Mater. Sci. Eng. A 527 (2010) 1686-1694.

[70] E. Ahmad, T. Manzoor, N. Hussain, N.K. Qazi, Mater. Des. 29 (2008) 450-457.

[71] A. Karmakar, R. Misra, S. Neogy, D. Chakrabarti, Metall. Mater. Trans. A 44 (2013) 4106-4118.

[72] C. Zheng, N. Xiao, L. Hao, D. Li, Y. Li, Acta Mater. 57 (2009) 2956-2968.

[73] C.W. Zheng, D. Raabe, D.Z. Li, Mater. Sci. Forum 706 (2012) 1592-1597.

[74] H. Beladi, G. Kelly, A. Shokouhi, P. Hodgson, Mater. Sci. Eng. A 371 (2004) 343-352.

[75] P.J. Hurley, P. Hodgson, B. Muddle, Scripta Mater. 40 (1999) 433-438.

[76] P. Hurley, P. Hodgson, Mater. Sci. Eng. A 302 (2001) 206-214.

[77] K. Mukherjee, S. Hazra, M. Militzer, Metall. Mater. Trans. A 40 (2009) 2145-2159.

[78] S.C. Hong, K.S. Lee, Mater. Sci. Eng. A 323 (2002) 148-159.

[79] C. Ghosh, V.V. Basabe, J.J. Jonas, Y.M. Kim, I.H. Jung, S. Yue, Acta Mater. 61 (2013) 2348-2362.

[80] H. Bhadeshia, Scripta Metall. 21 (1987) 1605-1609.

[81] E. Novillo, D. Hernandez, I. Gutierrez, B. Lopez, Mater. Sci. Eng. A 385 (2004) 83-90.

[82] A.R. Salehi, S. Serajzadeh, A.K. Taheri, J. Mater. Sci. 41 (2006) 1917-1925.

[83] A. Basso, R. Martínez, J. Sikora, J. Alloys Compd. 509 (2011) 9884-9889.

[84] M. Gouné, F. Danoix, J. Ågren, Y. Bréchet, C.R. Hutchinson, M. Militzer, G. Purdy, S. van der Zwaag, H. Zurob, Mater. Sci. Eng. R 92 (2015) 1-38.

[85] A. ZareiHanzaki, S. Yue, ISIJ Int. 37 (1997) 583-589.

[86] J. Christian, G. Olson, M. Cohen, J. Phy. IV 5 (1995) C8-3-C8-10.

[87] N.Y. Zolotorevsky, S.N. Panpurin, A.A. Zisman, S.N. Petrov, Mater. Charact. 107 (2015) 278-282.
[88] L. Morsdorf, O. Jeannin, D. Barbier, M. Mitsuhara, D. Raabe, C.C. Tasan, Acta Mater. 121 (2016) 202-214.
[89] M. Hillert, L. Höglund, J. Ågren, Metall. Mater. Trans. A 35 (2004) 3693-3700.
[90] H.K.D.H. Bhadeshia, D.V. Edmonds, Acta Metall. 28 (1980) 1265-1273.
[91] M. Takahashi, H. Bhadeshia, Mater. Trans. JIM 32 (1991) 689-696.
[92] G. Thewlis, Mater. Sci. Technol. 20 (2004) 143-160.
[93] A. Mark, M. Westphal, D. Boyd, J. McDermid, D. Embury, Can. Metall. Q. 48 (2009) 237-245.
[94] S.M.K. Hosseini, A. Zaeri-Hanzaki, S. Yue, Mater. Sci. Eng. A 618 (2014) 63-70.
[95] E. Girault, P. Jacques, P. Ratchev, J. van Humbeeck, B. Verlinden, E. Aernoudt, Mater. Sci. Eng. A 273 (1999) 471-474.
[96] Z.C. Zhang, F.X. Zhu, Y.M. Li, J. Iron Steel Res. Int. 17 (2010) 44-50.
[97] R. Ranjan, H. Beladi, S.B. Singh, P.D. Hodgson, Metall. Mater. Trans. A 46 (2015) 3232-3247.
[98] P.J. Jacques, E. Girault, P. Harlet, F. Delannay, ISIJ Int. 41 (2001) 1061-1067.
[99] Y.Q. Huo, X.H. Long, Z.H. Zhou, J.G. Li, Mater. Sci. Eng. A 438 (2006) 158-161.
[100] E. Abbasi, W.M. Rainforth, Mater. Sci. Eng. A 651 (2016) 822-830.
[101] H.C. Chen, G.H. Cheng, J. Mater. Sci. 24 (1989) 1991-1994.
[102] I. Gupta, P.H. Chang, J. Met. 36 (1984) 34-34.
[103] U. Liedl, S. Traint, E.A. Werner, Comput. Mater. Sci. 25 (2002) 122-128.
[104] J. Chiang, B. Lawrence, J.D. Boyd, A.K. Pilkey, Mater. Sci. Eng. A 528 (2011) 4516-4521.
[105] O. Kawano, J. Wakita, K. Esaka, H. Abe, Tetsu-to-Hagane 82 (1996) 232-237.
[106] S. Gunduz, Mater. Lett. 63 (2009) 2381-2383.
[107] J. Lis, A.K. Lis, C. Kolan, J. Mater. Process. Technol. 162 (2005) 350-354.
[108] J. Hu, L.X. Du, J.J. Wang, C.R. Gao, T.Z. Yang, A.Y. Wang, R.D.K. Misra, Metall. Mater. Trans. A 44A (2013) 4937-4947.
[109] X.J. Xu, J.Q. Kong, J.P. Lin, R.R. Zheng, Rev. Adv. Mater. Sci. 33 (2013) 348-353.

[110] Q. Feng, L. Li, W. Yang, Z. Sun, Mater. Sci. Eng. A 605 (2014) 14-21.
[111] C. Wang, H. Ding, Z. Tang, J. Zhang, H. Di, Steel Res. Int. 85 (2014) 388-394.
[112] E.V. Pereloma, A.A. Gazder, I.B. Timokhina, Mater. Sci. Forum 738-739 (2013) 212-216.
[113] I.B. Timokhina, P.D. Hodgson, E.V. Pereloma, Metall. Mater. Trans. A 35A (2004) 2331-2341.
[114] Z. Li, D. Wu, W. Lv, M.F. Shao, Appl. Mech. Mater. 377 (2013) 123-127.
[115] Z. Zhao, T. Tong, J. Liang, H. Yin, A. Zhao, D. Tang, Mater. Sci. Eng. A 618 (2014) 182-188.
[116] I.B. Timokhina, E.V. Pereloma, P.D. Hodgson, Metall. Mater. Trans. A 45 (2014) 4247-4256.
[117] E. Opbroek. Advanced high strength steel application guidelines. Technical report, International Iron and Steel Institute, 2006.
[118] A. Kumar, S.B. Singh, K.K. Ray, Mater. Sci. Eng. A 474 (2008) 270-282.
[119] I.B. Timokhina, P.D. Hodgson, E.V. Pereloma, Metall. Mater. Trans. A 38 (2007) 2442-2454.
[120] W.J. Dan, Z.Q. Lin, S.H. Li, W.G. Zhang, Mater. Sci. Eng. A 552 (2012) 1-8.
[121] T.T. Huang, R.B. Gou, W.J. Dan, W.G. Zhang, Mater. Sci. Eng. A 672 (2016) 88-97.
[122] J.H. Hollomon, Trans. Metall. Soc. AIME 162 (1945) 268-290.
[123] Y. Tomita, K. Okabayashi, Metall. Trans. A 16 (1985) 865-872.
[124] Z. Jiang, Z. Guan, J. Lian, Mater. Sci. Eng. A 190 (1995) 55-64.
[125] F.D. Fischer, Q.P. Sun, K. Tanaka, Appl. Mech. Rev. 49 (1996) 317-364.
[126] J.R. Mcdermid, H.S. Zurob, Y. Bian, Metall. Mater. Trans. A 42A (2011) 3627-3637.
[127] G. Reisner, E.A. Werner, P. Kerschbaummayr, I. Papst, F.D. Fischer, JOM 49 (1997) 62-65.
[128] M. De Meyer, D. Vanderschueren, B.C. De Coomam, ISIJ Int. 39 (1999) 813-822.
[129] S. Chatterjee, H.S. Wang, J.R. Yang, H.K.D.H. Bhadeshia, Mater. Sci. Technol. 22 (2006) 641-644.
[130] G.K. Tirumalasetty, M.A. van Huis, C. Kwakernaak, J. Sietsma, W.G. Sloof, H.W. Zandbergen, Acta Mater. 60 (2012) 1311-1321.

[131] I.Y. Pyshmintsev, M. De Meyer, B. De Cooman, R. Savray, V. Shveykin, M. Vermeulen, Metall. Mater. Trans. A 33 (2002) 1659-1667.
[132] K. Sugimoto, M. Kobayashi, A. Nagasaka, S. Hashimoto, ISIJ Int. 35 (1995) 1407-1414.
[133] K.K. Park, S.T. Oh, S.M. Baeck, D.I. Kim, J.H. Han, H.N. Han, S.H. Park, C.G. Lee, S.J. Kim, K.H. Oh, Mater. Sci. Forum 408-412 (2002) 571-576.
[134] E.V. Pereloma, L.C. Zhang, K.D. Liss, U. Garbe, J. Almer, T. Schambron, H. Beladi, I.B. Timokhina, Solid State Phenom. 172-174 (2011) 741-746.
[135] Y. Tomota, H. Tokuda, Y. Adachi, M. Wakita, N. Minakawa, A. Moriai, Y. Morii, Acta Mater. 52 (2004) 5737-5745.
[136] D.Q. Bai, A.D. Chiro, S. Yue, Mater. Sci. Forum 284-286 (1998) 253-262.
[137] M.M. Wang, C.C. Tasan, D. Ponge, A. Kostka, D. Raabe, Acta Mater. 79 (2014) 268-281.
[138] M.X. Zhang, P.M. Kelly, Mater. Charact. 40 (1998) 159-168.
[139] M. Ramajayam, N. Stanford, Mater. Sci. Eng. A 671 (2016) 147-157.
[140] A.K. De, J.G. Speer, D.K. Matlock, Adv. Mater. Process. 161 (2003) 27-30.
[141] A.J. Schwartz, M. Kumar, B.L. Adams, D.P. Field, Electron backscatter diffraction in materials science, Springer, New York (NY), 2009.
[142] J.J. Fundenberger, B. Beausir, Université de Lorraine - Metz, 2015, JTEX - Software for Texture Analysis, http://jtex-software.eu/.
[143] T. Nakagaito, H. Matsuda, Y. Nagataki, K. Seto, Tetsu-to-Hagane 101 (2015) 426-434.
[144] M.K. Miller, Atom probe tomography: Analysis at the atomic level, Kluwer Academic/Plenum press, New York (NY), 2000.
[145] K. Thompson, D. Lawrence, D. Larson, J. Olson, T. Kelly, B. Gorman, Ultramicroscopy 107 (2007) 131-139.
[146] P.J. Felfer, T. Alam, S.P. Ringer, J.M. Cairney, Microsc. Res. Tech. 75 (2012) 484-491.

CHAPTER 2 MICROSTRUCTURES AND MECHANICAL PROPERTIES OF DUAL PHASE STEEL PRODUCED BY LABORATORY SIMULATED STRIP CASTING

Z.P. Xiong[1*], A.G. Kostryzhev[1], N.E. Stanford[3], E.V. Pereloma[1, 2]

[1]*School of Mechanical, Materials and Mechatronic Engineering, University of Wollongong, Wollongong, NSW 2522, Australia*

[2]*Electron Microscopy Centre, University of Wollongong, Wollongong, NSW 2519, Australia*

[3]*Institute of Frontier Materials, Deakin University, Geelong, Victoria 3216, Australia*

Abstract: Conventional dual phase (DP) steel (0.08C-0.81Si-1.47Mn-0.03Al wt. %) was manufactured using simulated strip casting schedule in laboratory. The average grain size of prior austenite was 117±44 μm. The continuous cooling transformation diagram was obtained. The microstructures having polygonal ferrite in the range of 40-90 %, martensite with small amount of bainite and Widmanstätten ferrite were observed, leading to an ultimate tensile strength in the range of 461 – 623 MPa and a corresponding total elongation in the range of 0.31 – 0.10. All samples exhibited three strain hardening stages. The predominant fracture mode of the studied steel was ductile, with the presence of some isolated cleavage facets, the number of which increased with an increase in martensite fraction. Compared to those of hot rolled DP steels, yield strength and ultimate tensile strength are lower due to large ferrite grain size, coarse martensite area and Widmanstätten ferrite.

Key words: Strip casting; Dual phase steel; Continuous cooling transformation diagram; Mechanical properties; Crussard-Jaoul model; Electron microscopy

2.1 Introduction

Dual phase (DP) steels are widely used in automotive industry due to a good combination of continuous yielding behaviour, high strength, high strain hardening rate, low yield stress-to-tensile strength ratio and good formability [1-3]. DP steels have high tensile strength in the range of 500 ~ 1200 MPa and total elongation in the range of 12 ~ 34%, which depend on fractions of ferrite, martensite and bainite [1, 4]. Traditional microstructures of DP steels consist of polygonal ferrite and martensite. To satisfy custom requirements, ferrite-bainite-martensite and ferrite-bainite steels were produced in order to modify mechanical properties: bainite instead of martensite were shown to improve formability with a little decrease of strength [5-7]. The effect of martensite fraction, distribution and martensite region size, and the effect of ferrite fraction and grain size on mechanical behaviour of DP steels have been intensively studied. With increasing the martensite fraction, the yield strength and ultimate tensile strength increase while uniform and total elongations decrease [8, 9]. The distribution of martensite also affects the mechanical behaviour [10-12]. Martensite regions existing as isolated areas within ferrite matrix result in a better combination of strength and ductility than martensite regions forming a chain-like network structure surrounding ferrite [10]. Refinement of ferrite or/and martensite regions simultaneously enhances strength and ductility [13-16]. Ultrafine-grained DP steels with the average ferrite grain size of ~1.2 μm exhibit a high ultimate tensile strength up to 1000 MPa [13].

In industry, the DP steels are successfully produced using hot rolling and cold rolling & annealing [1]. As alternative, the strip casting could be suggested as a more economic and environmentally friendly way for DP steels production. This technology is already used for carbon steels, silicon steels and stainless steels in industry [17, 18]. It allows obtaining several millimetres thick strips directly from molten metals [17, 18]. Due to this and elimination of many subsequent hot rolling

stages required by conventional continuous casting and thin slab casting, the strip casting process has many advantages, such as energy saving and emission reduction, lower capital and operating costs, a smaller and more flexible operating regime, a higher tolerance to a high residual scrap and easy adjustment for different steel grades [17-20].

In this study, the feasibility of producing DP steel using strip casting was investigated in the laboratory. Heat treatment schedules were designed to obtain microstructures with 40% – 90% ferrite. Mechanical properties were tested and compared to hot rolled DP steels. The correlation between microstructure and mechanical properties was analysed.

2.2 Materials and experimental techniques

The chemical composition of studied DP steel is shown in Table 2.1. Cylindrical specimens of 20 mm diameter and 6 mm length were traditionally cast and square specimens of 36 × 36 mm^2 and 1.2 mm thickness were produced via dip tester at Deakin University in order to simulate rapid cooling during solidification in strip casting process [21]. The dip tester is used to immerse a copper substrate into molten steel for a short and controlled period of time to simulate a rapid solidification. As-cast microstructure consisted predominantly of martensite and some bainite as shown in Fig. 2.1.

Table 2.1 Chemical composition of the DP steel (wt. %).

C	Si	Mn	Al	Cu	Cr	P	S	B
0.0768	0.805	1.47	0.0346	0.0126	0.233	0.0055	<0.00050	0.00091

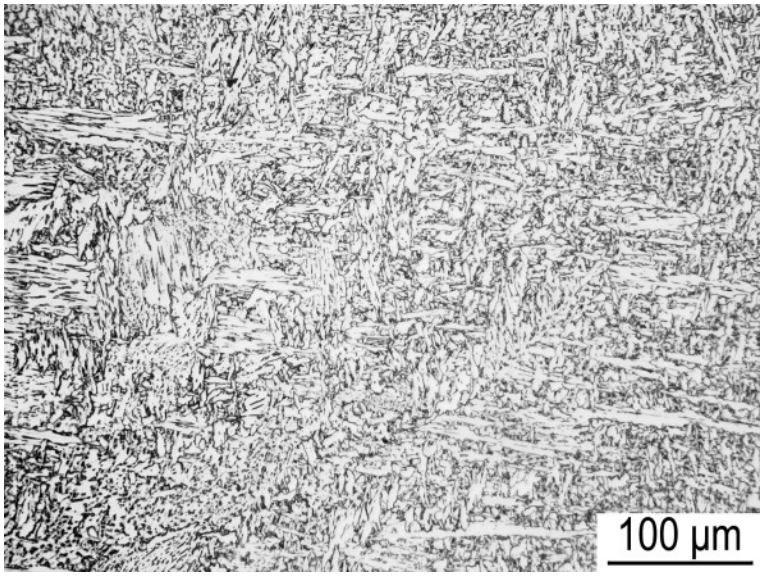

Figure 2.1 The microstructure of DP steel after dip casting.

Heat treatments were carried out using a Theta Dilatronic III Quenching and Deformation dilatometer. It was operated under a vacuum of ~ 6.7 x 10^{-2} Pa which prevented oxidation and decarburization of the samples. The temperature was measured using an S-type (Pt/Pt-10%Rh) thermocouple spot-welded to the surface centre of a cylindrical and flat samples (Fig. 2.2).

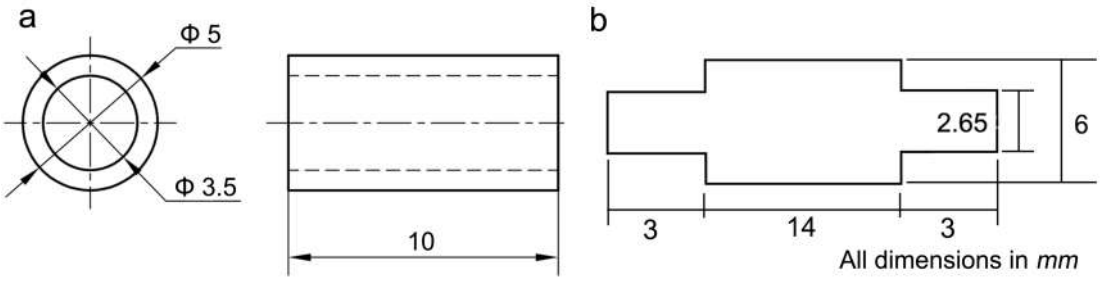

Figure 2.2 (a) Cylindrical samples used for the determination of continuous cooling transformation diagrams, and (b) flat samples used for prior austenite grain size measurement and simulation of strip casting.

To simulate the prior austenite grain size (PAGS) observed in cast samples, the flat samples (Fig. 2.2(b)) were heated at a rate of 30 Ks^{-1} to 1250 or 1300 °C, held for 120 or 180 s, and then helium quenched to room temperature at a rate of around 140 Ks^{-1}.

To obtain the continuous cooling transformation (CCT) diagram, cylindrical samples (Fig. 2.2(a)) were heated at a rate of 30 Ks^{-1} to 1300 °C, held for 180 s to simulate the grain size and distribution of prior austenite in strip casting, and then cooled to room temperate at cooling rates of 0.1, 1, 3, 10, 40 and 90 Ks^{-1}. Noticeably, it is important to maintain the distribution of alloying elements during laboratory simulations as close as possible to the dip-cast samples. Holding at 1300 °C for 180 s would not significantly change the distribution of alloying elements in dip-cast sample as the holding time is short and the migration of alloying elements is very sluggish.

The schedule to simulate strip casting process is illustrated in Fig. 2.3(a). The samples were heated at a rate of 30 Ks^{-1} to the austenitisation temperature T_A=1300 °C, held for time t_A=180 s, cooled to the austenite-to-ferrite transformation region at a rate of 90 Ks^{-1} or cooled to 1000 °C at a rate of 30 Ks^{-1} and then cooled at a rate of 10 Ks^{-1} (hereafter referred as 30-10 Ks^{-1} schedule) to ferrite formation temperature T_F, held for t_F time to achieve the desired ferrite fraction, and then quenched to the room temperature at 140 Ks^{-1} using helium.

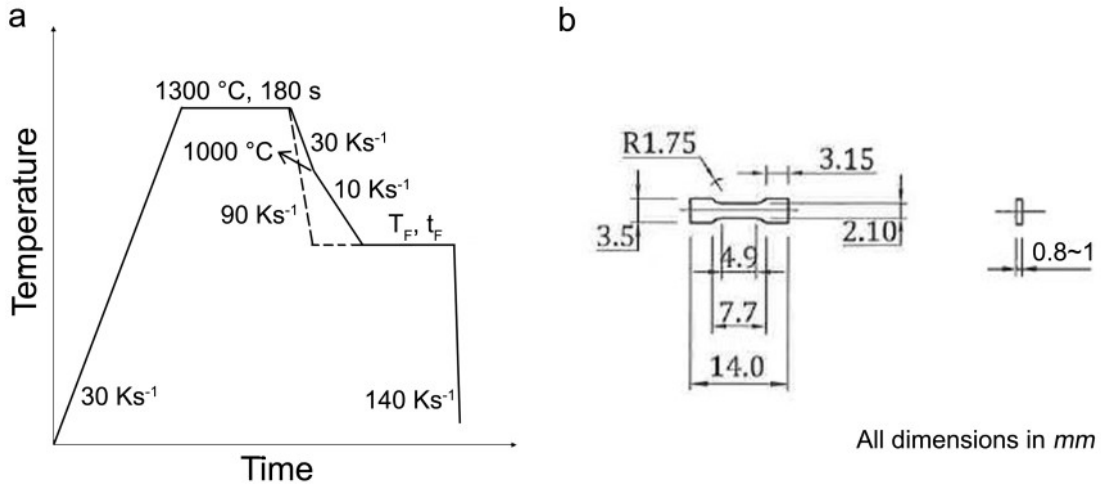

Figure 2.3 Schematic diagrams of (a) heat treatments to simulate strip casting and (b) tensile test sample.

Following the heat treatments, the specimens were cross-cut in the centre perpendicular to the long axis. The centre area of the cross-section was used for observation. To reveal the prior austenite grain boundaries, the specimens were etched for 15~20 s at 65 °C temperature in the solution of saturated picric acid in ethanol plus few drops of benzene sulfonate. Equivalent grain diameter was utilised to describe the distribution of prior austenite grain sizes. Approximately 150 ~ 250 grains were measured for each condition. Etching with 2 vol.% nital was used to reveal ferrite and martensite. Microstructures and fracture surfaces were studied using a Leica DMR research optical microscope (OM), a JEOL JSM-7001F field emission gun – scanning electron microscope (FEG – SEM) operating at 15 kV of accelerating voltage and fitted with an 80 mm^2 X-Max energy dispersive X-ray spectroscopy (EDS) detector, and a JEOL 2011 transmission electron microscope (TEM) operating at 200 kV. Thin foils for TEM were prepared using twin jet electropolishing method with an electrolyte containing 10% of perchloric acid and methanol. The volume fraction of retained austenite was measured using the X-ray diffraction (XRD) technique. XRD was conducted for a scattering angle 2θ = 38-150° on the surface of flat samples (Fig. 2.2(b)) after electropolishing. Fractions of phases were calculated based on pixel quantities of different grey scales using Image Pro-Plus and Photoshop software. The equivalent circle diameter was calculated using at least 260 ferrite grains or martensite regions.

Tensile samples (Fig. 2.3(b)) were cut along the length of dilatometer sample (Fig. 2.2(b)). Tensile testing was carried out using an in-house modified "Kammrath and Weiss GmbH" tensile stage with 5 kN load cell. The thickness of tensile test samples was between 0.8 and 1.0 mm. Tensile tests were carried out on a minimum of two dog-bone samples per condition at an initial strain rate of 4 $\times 10^{-4}$ s^{-1}. The strain hardening rate (θ) and strain hardening exponent (n) were calculated as follows,

$$\theta = d\sigma / d\varepsilon \tag{2.1}$$

$$n = d(\ln \sigma) / d(\ln \varepsilon) \tag{2.2}$$

where σ is true stress and ε is true strain [22].

2.3 Results

2.3.1 Prior austenite microstructure simulation

Fig. 2.4 shows typical prior austenite grain structures in as-cast and heat treated samples. The contrast in as-cast sample is lower than that of heat treated sample due to less carbon segregation to the prior austenite grain boundaries in the former one. PAGS distributions after different austenitisation schedules are shown in Fig. 2.5. PAGS increased with an increase in holding time or holding temperature: after holding at 1250 °C for 120 and 180 s, the average grain size was 48±19 and 83±37 μm respectively; while after holding at 1300 °C for 120 and 180 s, the average grain size was 72±30 and 117±44 μm respectively. The average grain size after holding at 1300 °C for 180 s (117±44 μm) was very close to that of as-cast sample (118±57 μm). In addition, the sample held at 1300 °C for 180 s had comparable prior austenite grain size distribution to that of as-cast sample (c.f. Figs. 2.5(a) and (e)). Therefore, this condition was selected for all future experiments.

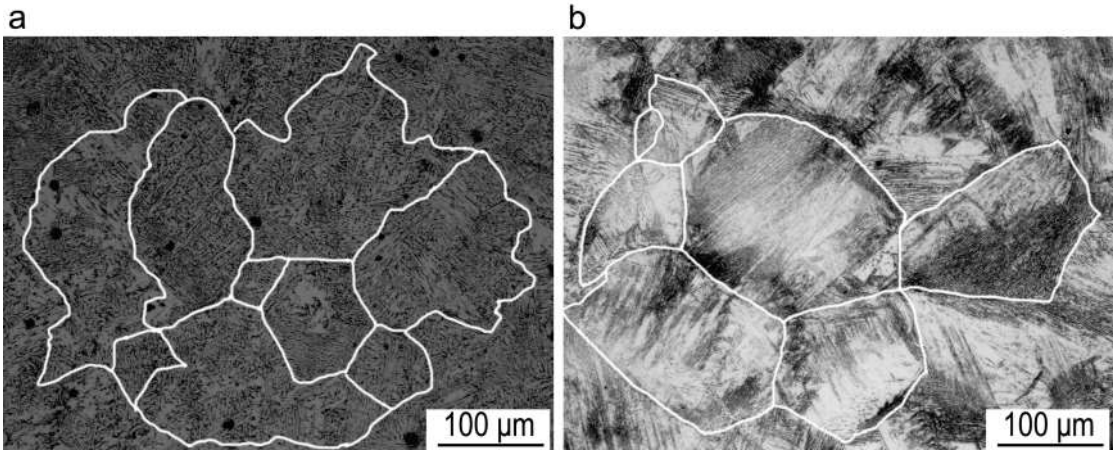

Figure 2.4 Comparison of prior austenite microstructures (a) in as-cast condition and (b) as-quenched after holding at 1300 °C for 180 s.

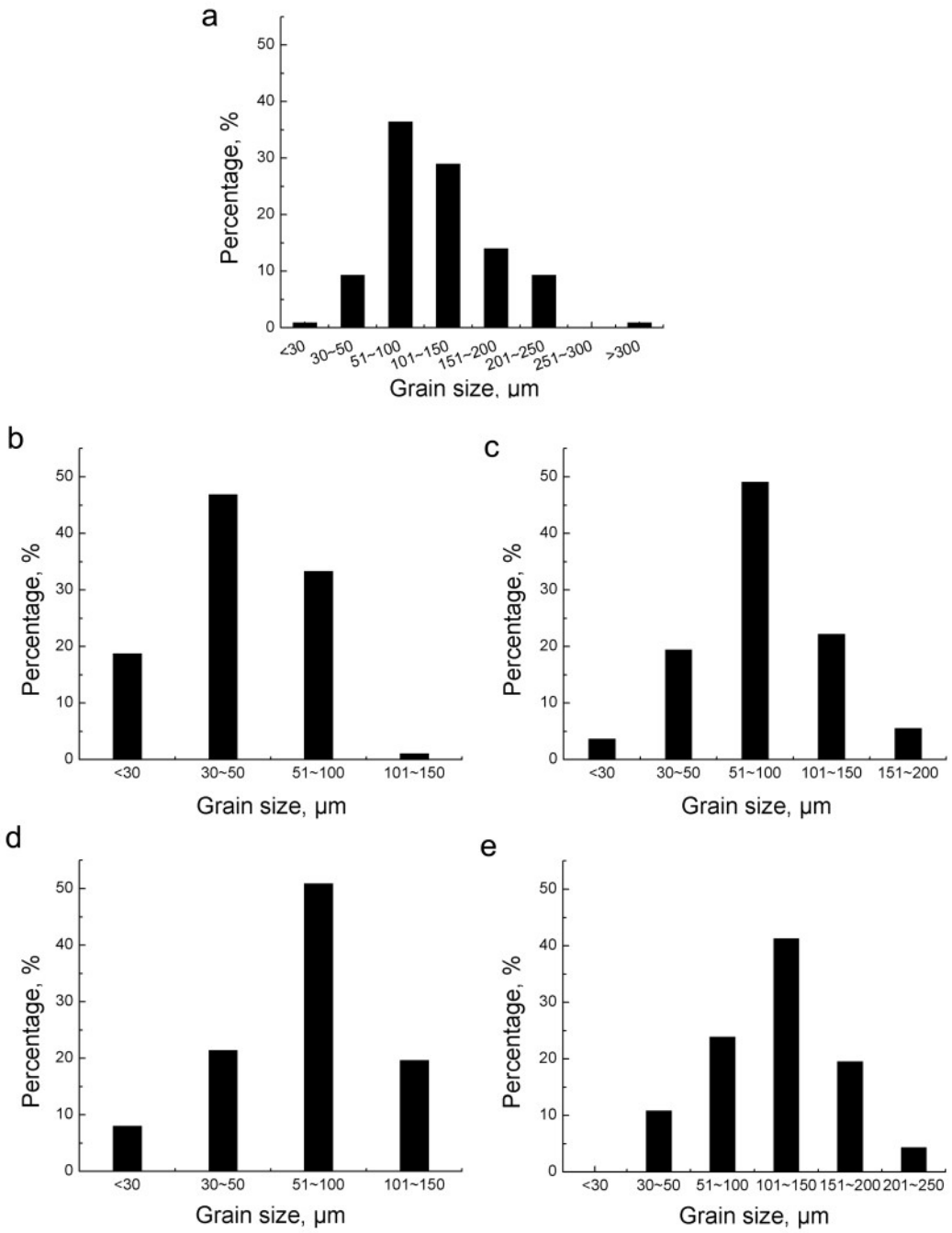

Figure 2.5 Prior austenite grain size distributions in (a) as-cast and (b-e) quenched conditions after holding at (b) 1250 °C for 120 s, (c) 1250 °C for 180 s, (d) 1300 °C for 120 s and (e) 1300 °C for 180 s.

2.3.2 Continuous cooling transformation diagram

The CCT diagram is plotted in Fig. 2.6 while the corresponding microstructures are shown in Fig. 2.7. Ferrite and pearlite formed at the cooling rate of 0.3 Ks^{-1}. When the cooling rate was increased to 1 Ks^{-1}, bainite started to form. A small amount of pearlite was still observed at 3 Ks^{-1}. With cooling rate increasing to 10 and 40 Ks^{-1}, more bainite formed and a very little fraction of allotriomorphic ferrite was found at prior austenite grain boundaries. When cooling rate reached 90 Ks^{-1}, the microstructure was fully bainite and martensite. At 90 Ks^{-1} the bainite transformation start temperature (Bs) was determined to be 644 °C, whereas martensite started to form at Ms = 426 °C. As expected [23], austenite to ferrite transformation start (A_{r1}) and finish (A_{r3}) temperatures tended to decrease with increasing cooling rate. However, the bainite start transformation temperature at first decreased with an increase in cooling rate up to 3 Ks^{-1} from 468 to 398 °C, and then increased with further increasing cooling rate up to 90 Ks^{-1}, which corresponds to observations by other researchers [24, 25].

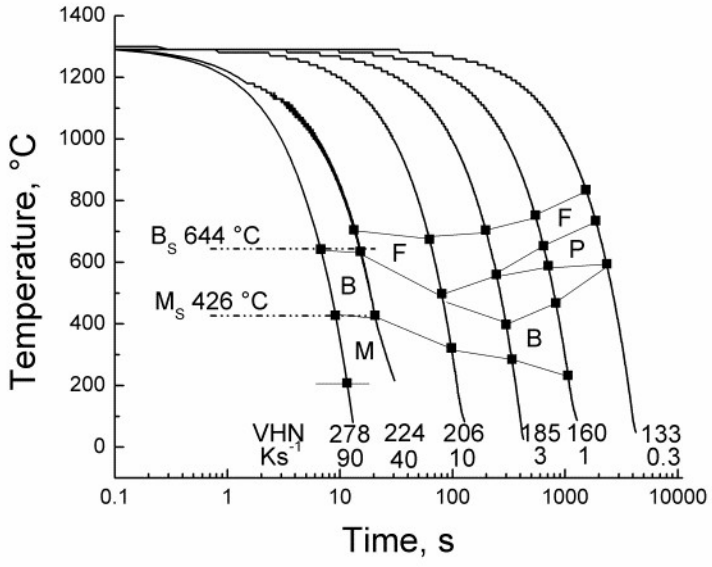

Figure 2.6 Continuous cooling transformation (CCT) diagram of as-cast DP steel cooled from 1300 °C after holding for 180 s. *F* is ferrite, *P* is pearlite, *B* is bainite and *M* is martensite.

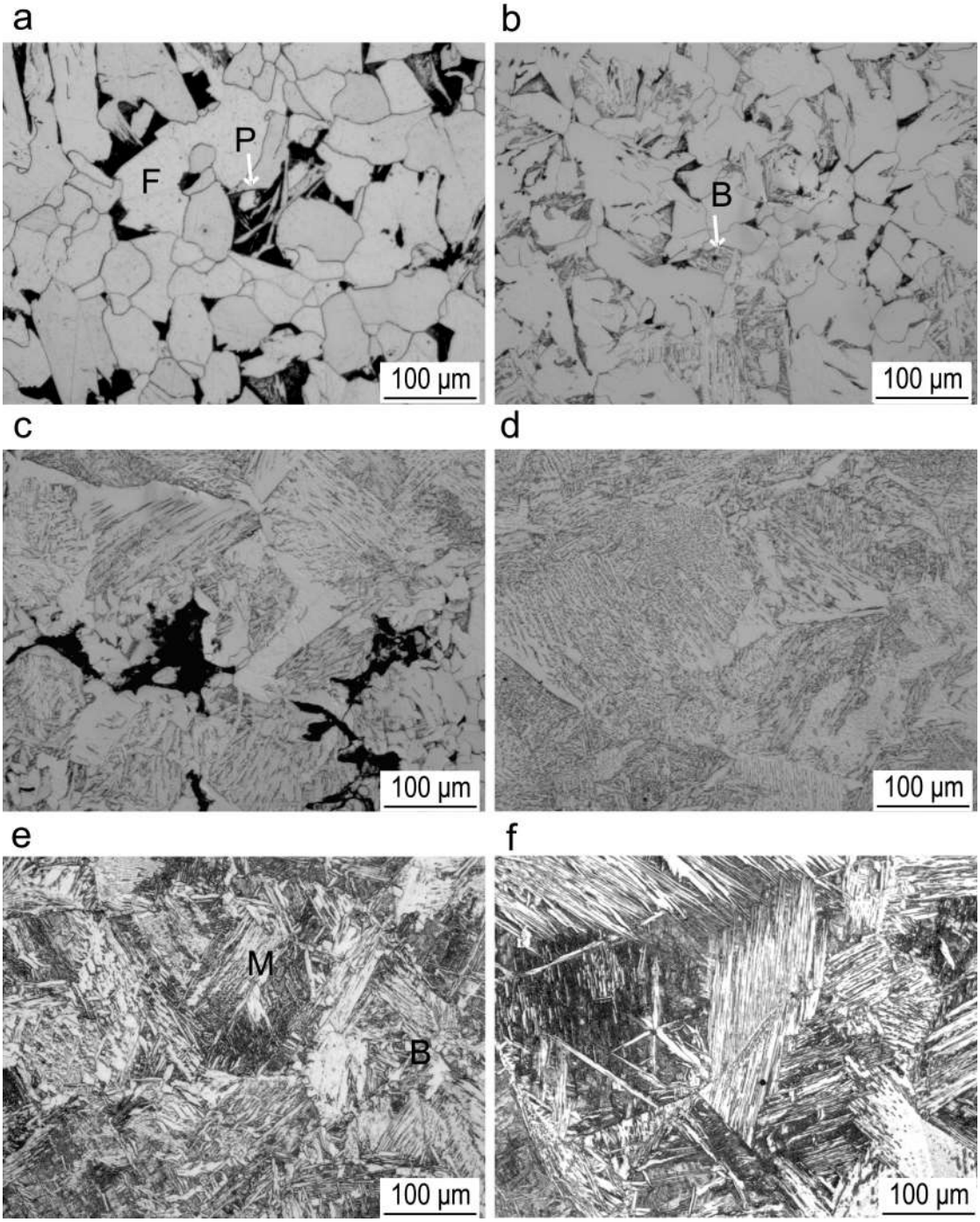

Figure 2.7 Microstructures after austenitising for 180 s at 1300 °C and cooling to room temperature at cooling rates of (a) 0.3, (b) 1, (c) 3, (d) 10, (e) 40 and (f) 90 Ks^{-1}. *F* is ferrite, *P* is pearlite, *B* is bainite and *M* is martensite.

2.3.3 Effect of holding temperature, holding time and cooling rate on austenite to ferrite transformation

Based on the CCT diagram, four holding temperatures of 600, 650, 670 and 700 °C were chosen to investigate ferrite formation and the holding time was 180 s. For the cooling rate of 90 Ks^{-1} from austenitisation temperature to ferrite formation temperature, the Time-Temperature-Transformation (TTT) diagram is schematically plotted in Fig. 2.8(a) based on the observed ferrite fraction. As seen from this diagram, holding at 650 °C required a minimum time to start ferrite formation. Therefore, the temperature of 650 °C was selected for investigation of the effect of time on ferrite formation.

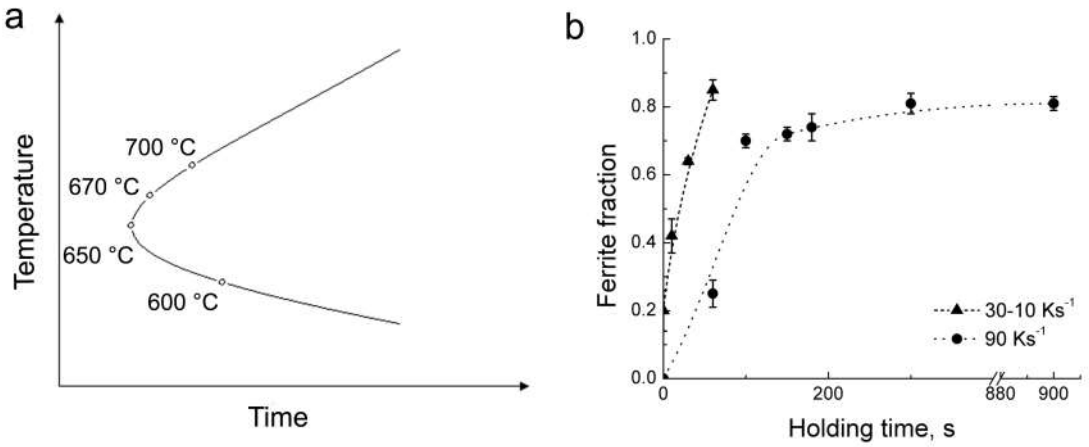

Figure 2.8 (a) Time-Temperature-Transformation (TTT) diagram and (b) ferrite fraction versus holding time when holding at 650 °C.

A dependence of ferrite fraction on holding time for two cooling rates is plotted in Fig. 2.8(b). For the cooling rate of 90 Ks^{-1}, the ferrite formation was fast within the first 100 s of holding. Then, the formation of ferrite continued at a slower rate until reaching 81±2%, the value corresponding to that defined by the lever rule. For the cooling schedule of 30-10 Ks^{-1}, ferrite formed during cooling from 1300 to 650 °C, as evident by the presence of 20 ± 6% ferrite in the sample immediately quenched on reaching 650 °C. Cooling with 30-10 Ks^{-1} schedule resulted in a higher ferrite fraction

for the same holding time (Fig. 2.8(b)), compared to the cooling at 90 Ks^{-1}. In addition, cooling with 30-10 Ks^{-1} schedule better depicts the industrial ones [20, 21]. Thus, the microstructures and mechanical properties were characterised only for the samples with the cooling rate of 30-10 Ks^{-1} in the following sections.

2.3.4 Microstructure characterisation

Microstructures of samples cooled at 30-10 Ks^{-1} and held at 650 °C for different times are shown in Figs. 2.9, 2.10 and 2.11. The ferrite fractions of 0.42±0.06, 0.64±0.05, 0.78±0.01 and 0.85±0.03 were obtained after holding for 30, 40, 50 and 60 s, respectively (Fig. 2.9). Hereafter, these samples were denoted as DP 30, DP 40, DP 50 and DP 60, respectively. The microstructures for all holding times consisted of polygonal ferrite, martensite, and very little amounts of bainite and Widmänstatten ferrite (Figs. 2.10 and 2.11). The XRD measurements showed the absence of face-centred cubic phases (Fig. 2.12). This suggests the absence of retained austenite or its amount below the detection level by XRD. In addition, martensite regions (indicated by arrows in Figs. 2.10(c) and (d)) exhibited concave and convex shape. As an example, the details of microstructure for DP 40 condition are shown in Fig. 2.11. Optical microstructure (Fig. 2.11 (a)) shows a general view of microstructure, containing 64±5% polygonal ferrite and Widmänstatten ferrite with martensite regions. A small amount of bainite was found in martensite regions using SEM (Fig. 2.11(b)). A general view of martensite packets in regions surrounded by polygonal ferrite is seen in bright field TEM image in Fig. 2.11(c). Equaixed polygonal ferrite grains with a low dislocation density are visible in Fig. 2.11(d). Lath martensite with high dislocation density, which formed packets, is shown in Fig. 2.11(e). Unfortunately, Widmänstatten ferrite and bainite were not found using TEM because of their low density.

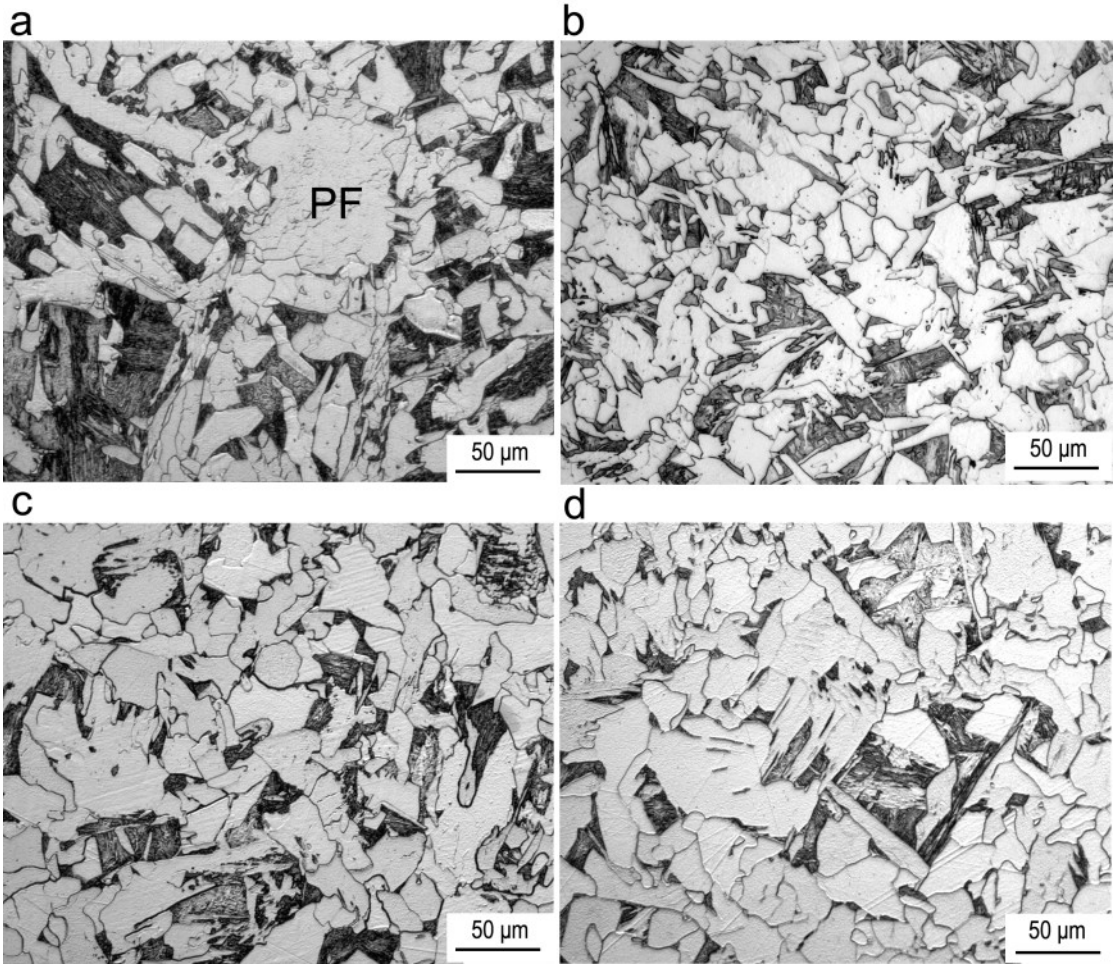

Figure 2.9 Optical microstructures after holding at 650 °C for (a) 30 s, (b) 40 s, (c) 50 s and (d) 60 s. PF is polygonal ferrite.

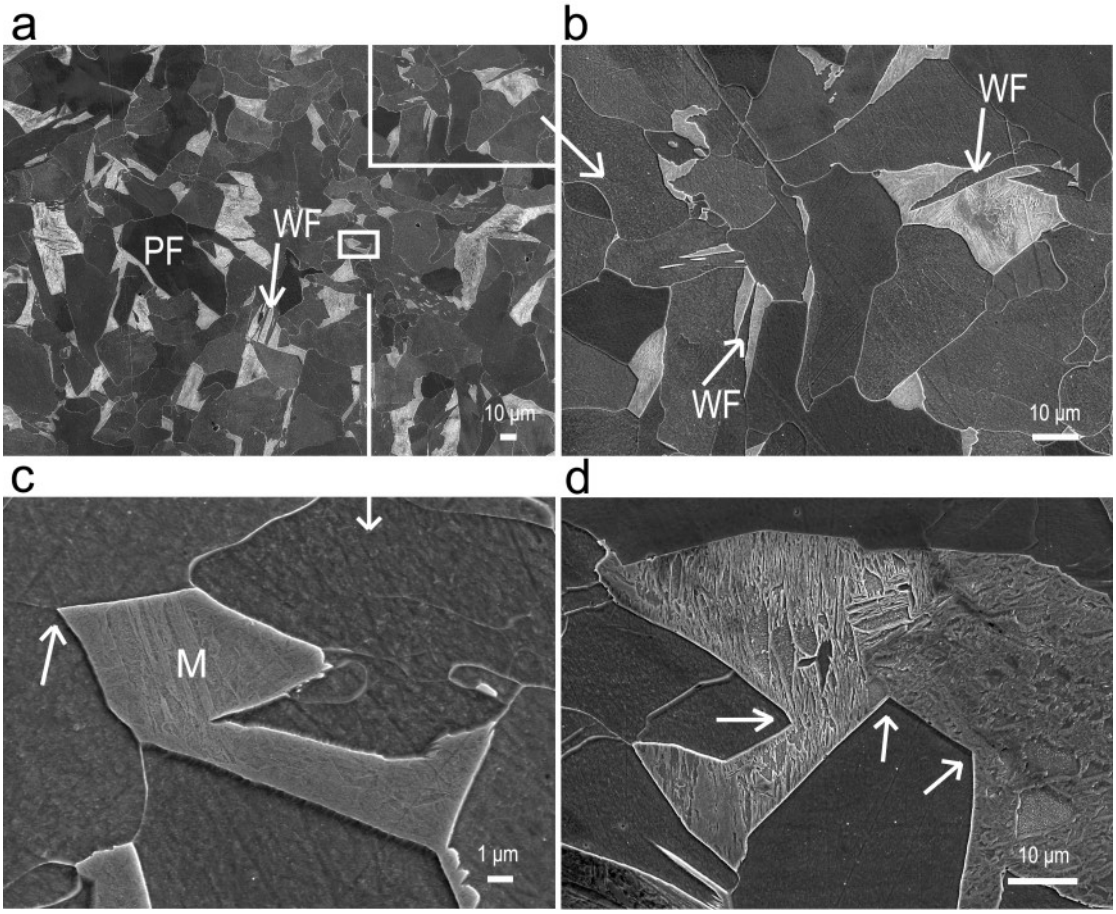

Figure 2.10 Microstructures of DP 60 characterised using scanning electron microscopy. *PF* is polygonal ferrite, *WF* is Widmänstatten ferrite and *M* is martensite. Arrows in (c, d) point the concave and convex shapes of martensite regions.

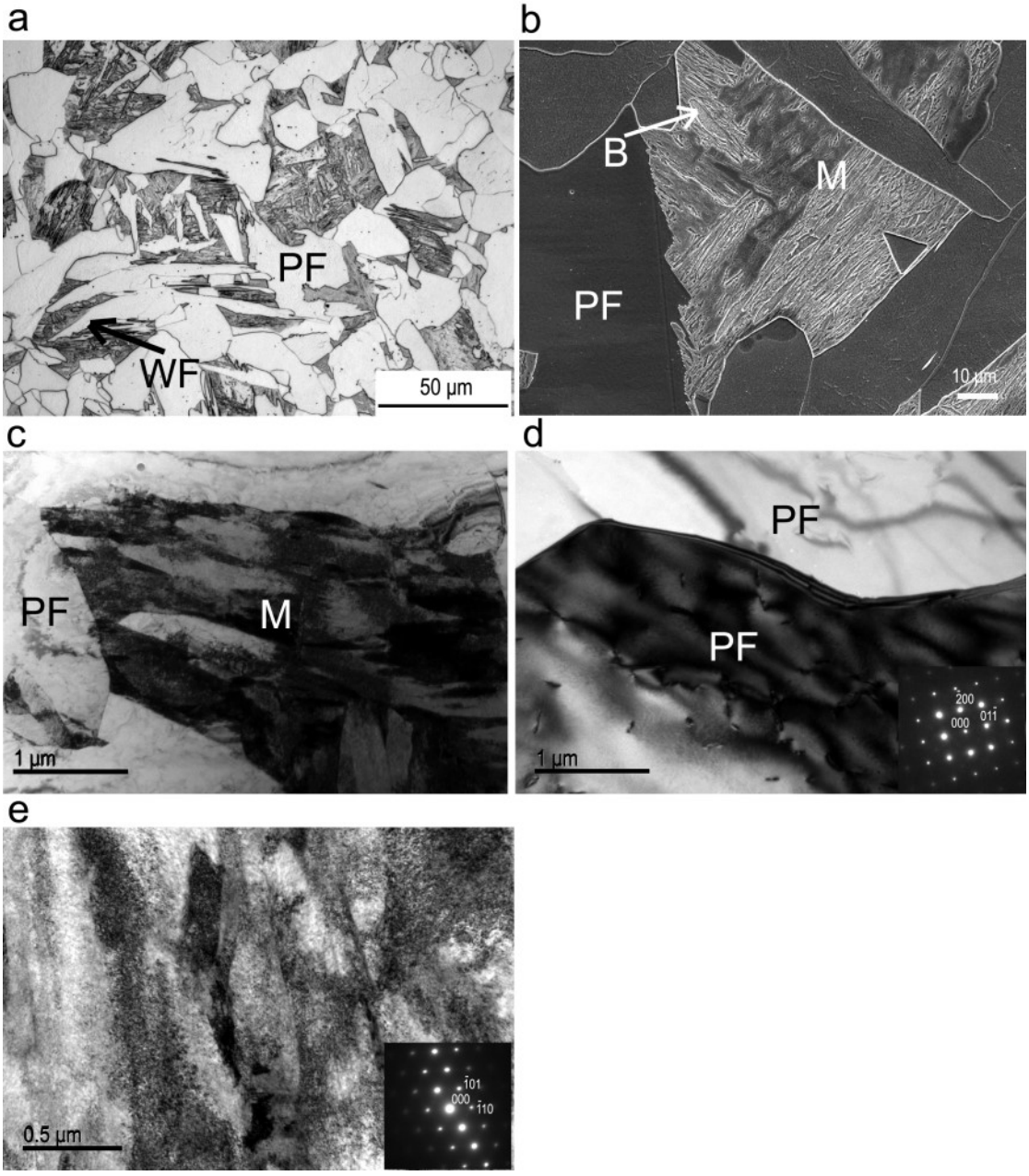

Figure 2.11 Representative microstructures of DP 40: (a) optical, (b) SEM and (c) TEM images. Higher magnification details of polygonal ferrite and lath martensite are shown in (d) and (e) respectively. *PF* is polygonal ferrite, *WF* is Widmänstatten ferrite, *B* is bainite and *M* is martensite. The zone axis of inset in (d) is $[001]_{\alpha}$ and of inset in (c, e) is $[111]_{\alpha}$.

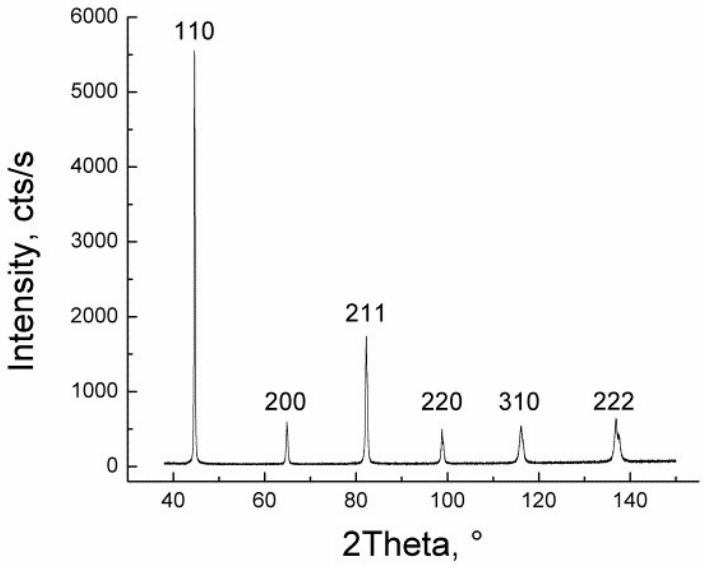

Figure 2.12 X–ray diffraction pattern of DP 40 sample.

Grain sizes of ferrite and sizes of martensite regions are given in Table 2.2 while their representative distributions are plotted in Fig. 2.13. The average grain size of ferrite was around 20 μm while the average size of martensite regions was around 15 μm. The microstructure was inhomogeneous, i.e. a large size difference of one to two orders of magnitude between the largest and smallest grains was observed. DP 40, DP 50 and DP 60 had a log-normal grain size distribution of ferrite (Fig. 2.13(c) shows a representative distribution) while DP 30 exhibited an exponential grain size distribution of ferrite (Fig. 2.13(a)). All of the samples had an exponential size distribution of martensite regions (representative distributions are shown in Figs. 2.13(b) and (d)). Polygonal ferrite nucleated at prior austenite grain boundaries. As holding time increased, polygonal ferrite grains grew, resulting in larger grain size (c.f. Figs. 2.13(a) and (c)). Meanwhile, prior austenite was consumed, leading to smaller size of martensite regions after quenching (c.f. Figs. 2.13(b) and (d)).

Table 2.2 A summary of microstructure statistics.

Specimen	Ferrite fraction	Average size, μm		Largest size, μm		Smallest size, μm	
		Ferrite	Martensite	Ferrite	Martensite	Ferrite	Martensite
DP 30	0.42±0.06	20±15	17±30	77	243	2	3
DP 40	0.64±0.05	17±10	10±9	60	59	4	3
DP 50	0.78±0.01	18±10	12±13	59	99	4	3
DP 60	0.85±0.03	25±14	16±17	69	91	5	3

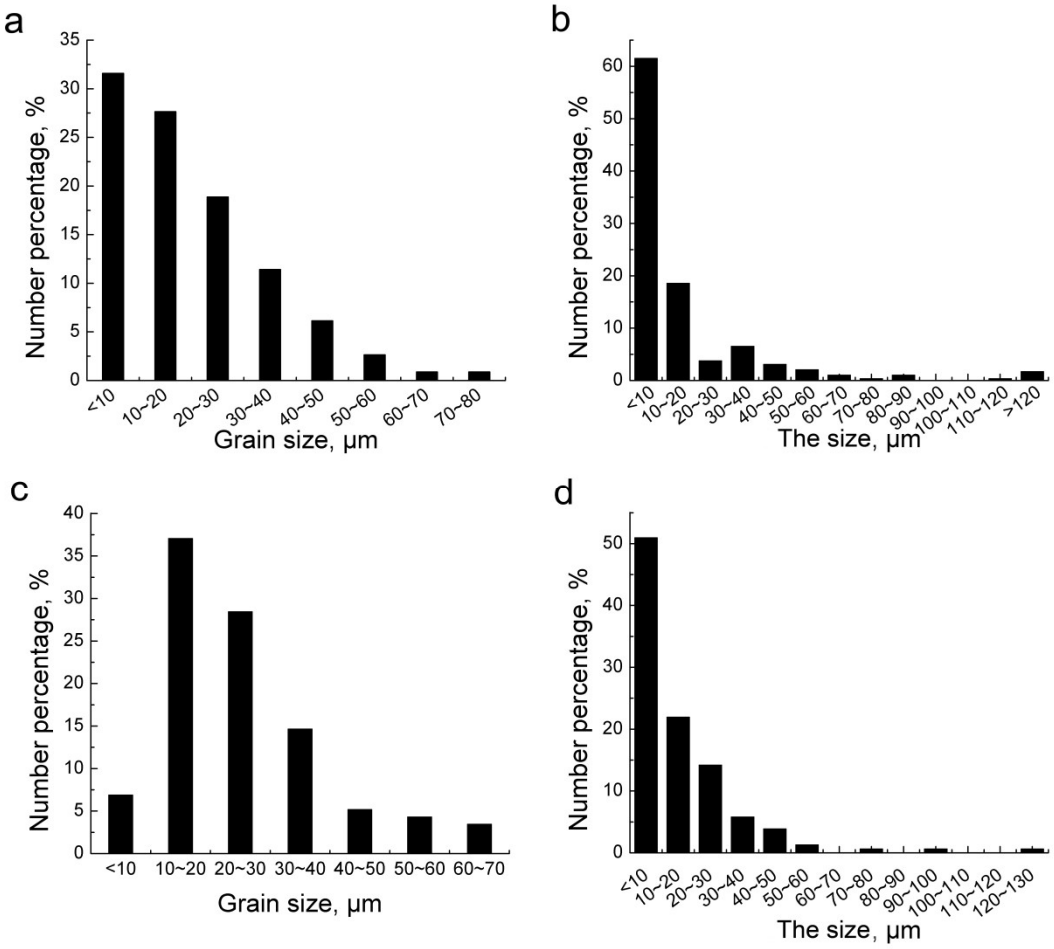

Figure 2.13 The size distributions of (a, c) ferrite grains and (b, d) martensite regions for (a, b) DP 30 and (c, d) DP 60.

2.3.5 Mechanical properties

Typical round-house engineering stress-strain curves inherent in DP steels [10, 26] were also observed in our steel for all four heat treatment conditions (Fig. 2.14(a). With a decrease in ferrite fraction from 0.85 to 0.42 the yield strength (YS) and

ultimate tensile strength (UTS) increased from 290 to 381 MPa and from 461 to 623 MPa, respectively (Table 2.3), while the corresponding uniform elongation and total elongation decreased from 0.17 to 0.063 and from 0.31 to 0.10, respectively. These types of behaviour correspond to those in hot rolled DP steels [9, 27]. The product of UTS and total elongation, which can be used to characterise toughness, increased with increasing ferrite fraction (Table 2.3).

Table 2.3 Mechanical properties of DP steels.

Specimen	Yield strength, MPa	Ultimate tensile strength, MPa	Uniform elongation	Total elongation	Product of ultimate tensile strength and total elongation, MPa%
DP 30	381±28	623±26	0.063±0.007	0.10±0.011	6230
DP 40	324±17	582±11	0.13±0.001	0.20±0.018	11640
DP 50	295±21	489±4	0.17±0.001	0.29±0.008	14181
DP 60	290±16	461±8	0.17±0.005	0.31±0.001	14291

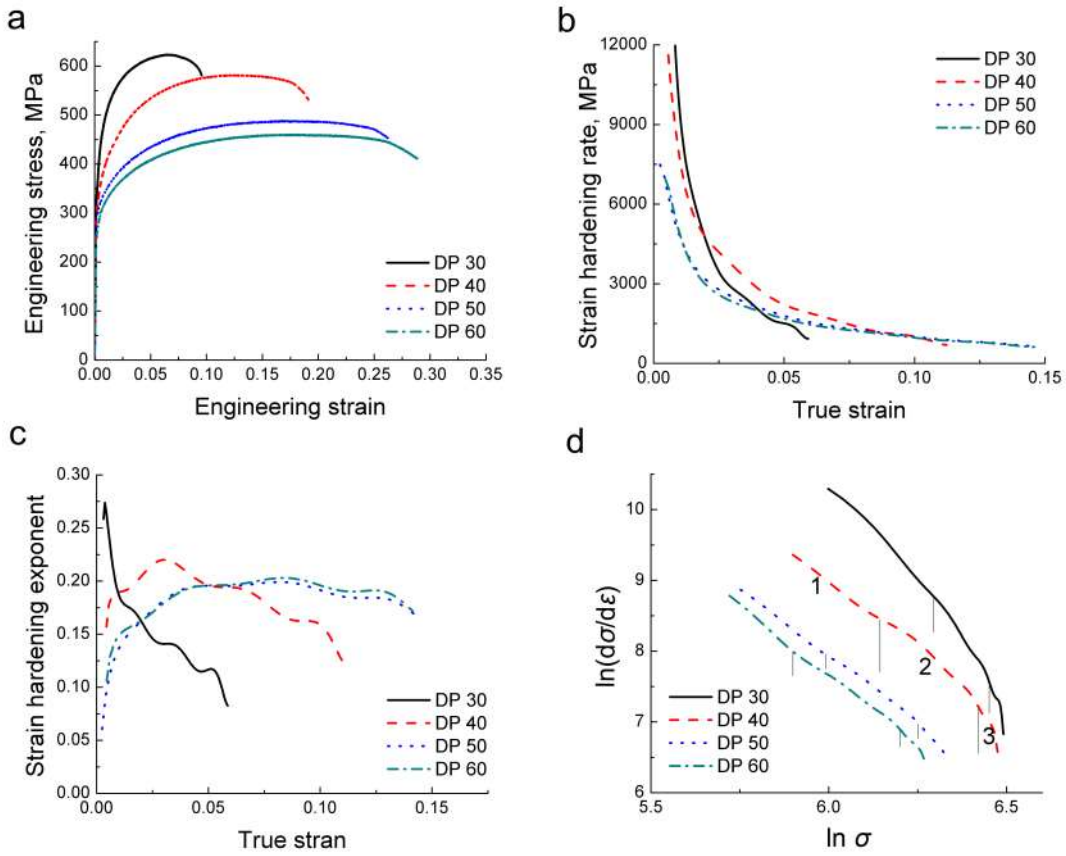

Figure 2.14 (a) Engineering stress-strain curves for all studied conditions, (b) strain hardening rate and (c) instantaneous strain hardening exponent n as a function of true strain, and (d) strain hardening behaviours based on the modified Crussard-Jaoul model analysis, where three distinct stages of strain hardening were denoted by the vertical lines and numbers.

The strain hardening rate decreased with strain following an exponential function (Fig. 2.14(b)). With decreasing ferrite fraction, the strain hardening rate increased. The strain hardening exponent for all heat treatment conditions increased steeply at low strains and then saturated (Fig. 2.14(c)). However, the behaviour of strain hardening exponent varied with ferrite fraction. A sample having a lower amount of ferrite (larger amount of martensite) showed the maximum of the exponent at lower strains. With further straining, the exponent decreased more quickly for a sample with a lower ferrite fraction. For example, it quickly increased to a maximum value of 0.22 at a true strain of 0.03 and then quickly decreased to 0.12 for DP 40. DP 60 showed a

more gradual increase to a maximum value of 0.20 at a true strain of 0.08 and then a gradual, slightly fluctuated decrease to 0.17 at a true strain of 0.14.

2.3.6 Fractography

Although the necking behaviour was observed for all four processing conditions, it varied with ferrite fraction. With an increase in ferrite fraction, the fracture surface at low magnification changed from flat to uneven and to conical shape (Figs. 2.15(a1 - d1)), and the fracture surface at high magnification showed larger and dipper voids at high magnification, the density of which increased with an increase in ferrite fraction (c.f. Figs. 2.15(a2) and (d2)). The sample with 85% ferrite exhibited a ductile fracture surface characterised by many voids (Fig. 2.15(d2)). However, when ferrite fraction increased to 0.42, the fracture surface consisted of many smaller voids and some larger cleavage facets (Fig. 2.15(a2)), indicating the predominant ductile with some brittle fracture. These support the transition to a more ductile behaviour with an increase in ferrite fraction. Besides, in some voids the MnS inclusions were observed for all heat treatment conditions (Fig. 2.16), which could be a site for void formation [6, 28].

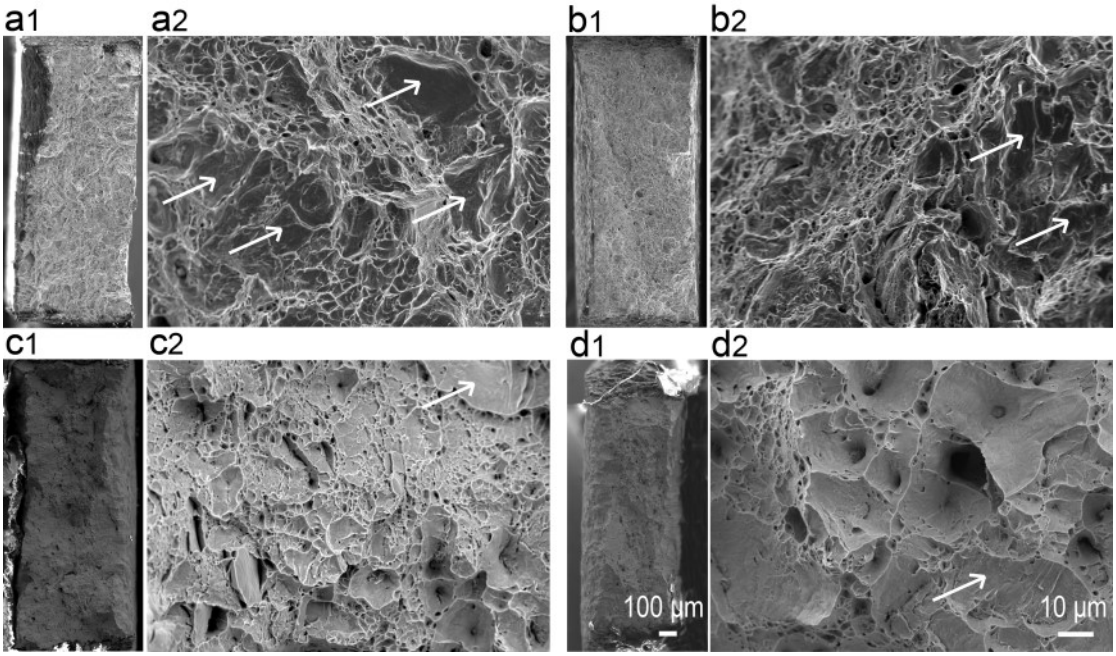

Figure 2.15 The macroscopic (a1 – d1) and microscopic (a2 – d2) fractography of (a) DP 30, (b) DP 40, (c) DP 50 and (d) DP 60. Arrows indicate cleavage facets.

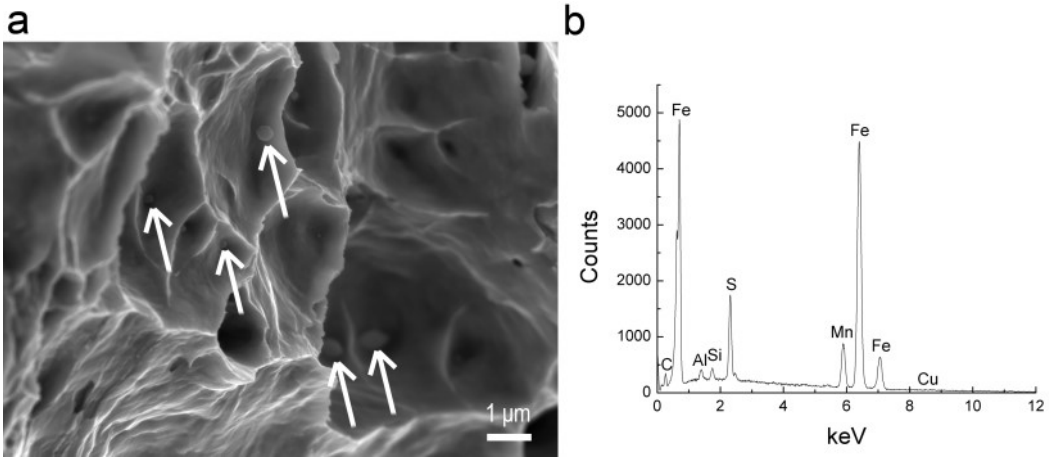

Figure 2.16 (a) Selected SEM image showing MnS inclusions in voids and (b) the representative EDS spectrum of MnS in DP 60. Arrows show some inclusions.

2.4 Discussion

2.4.1 The effect of ferrite fraction on mechanical behaviour

In the studied steel YS increased with a decrease in ferrite fraction (an increase in martensite fraction) due to dislocation density in ferrite increasing with volume

change accommodation of martensite formation [29]. There is non-uniform distribution of dislocations within ferrite grains: low density within the grains (Fig. 2.17(a)); medium density in the regions adjacent to ferrite-ferrite boundaries (Fig. 2.17(b)); high density in the regions adjacent to martensite due to accommodation of volume change during austenite to martensite transformation (Fig. 2.17 (c)) [29]. As ferrite fraction increases, there are fewer regions adjacent to martensite. Thus, the overall density of dislocations in ferrite is lower. It results in lower yield strength because when the density of dislocations is low, it is easy for existing dislocations to move unobstructed due to less interaction between the dislocations [16]. The generation of new dislocations in the material with a low density of dislocations is also easier, as the material has capacity for energy storage [14]. During the tensile test, more dislocations piled up near ferrite-martensite interfaces. With increasing ferrite fraction, ferrite-martensite interfaces decreased, leading to a lower YS. This also was observed in Ref [9]. Furthermore, with decrease in the fraction of martensite regions the overall strength of the material is reduced according to the low of mixtures [28].

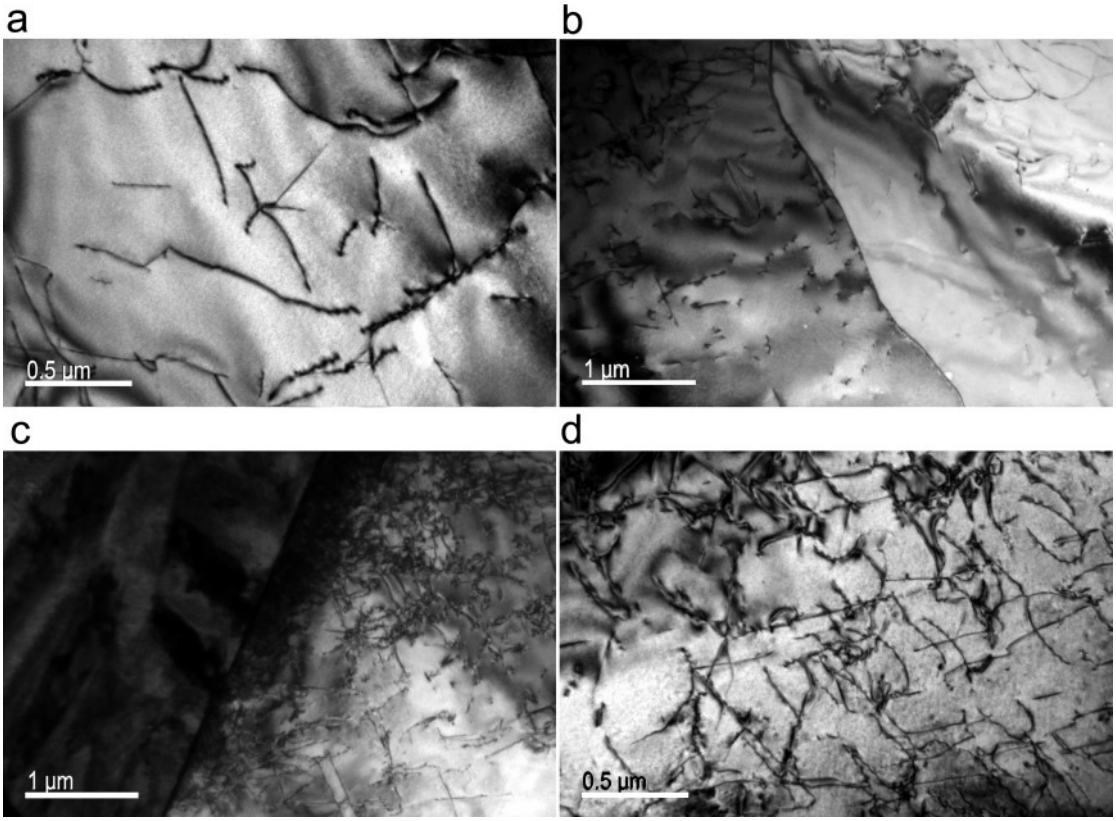

Figure 2.17 Selected TEM micrographs of dislocation structure for DP 60: (a) in polygonal ferrite far from grain boundaries, (b) in the region near ferrite – ferrite grain boundary, and (c) in ferrite adjacent to martensite and (d) a higher magnification of ferrite shown in (c).

The initial strain hardening rate and initial strain hardening exponent increased with a decrease in ferrite fraction (Figs. 2.14(b) and (c)) due to an increased initial density of dislocations leading to an earlier dislocation immobilisation and pile-up [9, 16, 26]. The samples with a larger ferrite fraction had a more gradual increase and then a slower decrease in strain hardening exponent. The samples with a lower ferrite fraction exhibited a sharp increase in the strain hardening exponent during early stages of straining, which could be explained by the more rapid increase in the number of dislocations in ferrite. Higher dislocation density in ferrite would result in a reduced mean free path for dislocation movement and a higher dislocation generation rate leading to an earlier increase in the strain hardening exponent. Finally, this led to a decreased elongation to failure in samples with lower ferrite fraction. Due to a

higher amount of soft phase, the samples with a higher ferrite fraction exhibited more ductile fracture behaviour.

To analyse the multistage strain hardening behaviour in the studied steel the modified Crussard – Jaoul (C–J) model was used [30]:

$$\varepsilon = \varepsilon_0 + c\sigma^m \tag{2.3}$$

where ε_0 is the initial true strain corresponding to the YS, c is a constant and m is the strain hardening index. m can be calculated using the following equation:

$$\ln(d\sigma / d\varepsilon) = (1-m)\ln\sigma - \ln(cm) \tag{2.4}$$

The plots of $\ln(d\sigma/d\varepsilon)$ versus $\ln\sigma$ are shown in Fig. 2.14(d). The strain hardening behaviour showed three stages, which is a typical phenomenon for DP steels [5, 16, 26]. As the modified C–J analysis was unable to fit the flow curve over the entire uniform strain range region, values of strain hardening index m for each strain hardening stage are listed in Table 2.4. A smaller strain hardening index m means higher strain hardening ability. The rate of dislocation accumulation is strongly linked to the ferrite grain size. In this regard, the finer ferrite grain size the smaller is m_1. As could be seen from Table 2.4, DP 40 and DP 50 samples with the lowest average grain sizes (Table 2.2) display the lowest m_1 values. During Stage 1 coarse ferrite grains deformed preferentially because smaller ferrite grains withstood the lower strain [31]. A small fraction of coarse ferrite grains did exist as shown in Figs. 2.9, 2.13(a) and 2.13(c). During Stage 2, ferrite grains were further strain hardened and restrained by martensite with dislocations piling up in the regions adjacent to martensite, resulting in a lower value of m_2 than m_1 for the DP 50 and DP 60 samples, which have high ferrite fractions. On the other hand, the $m_2 > m_1$ value for DP 30 and DP 40 conditions, as higher m-values are associated with the larger martensite fraction [5, 16]. In addition, Widmänstatten ferrite may contribute to deformation in this stage. During Stage 3 the simultaneous deformation of strain hardened ferrite and martensite

took place, leading to a continuous decrease in strain hardening rate and higher m_3-values compared to m_1 and m_2. For all conditions, m_1 is around 5.0 when ferrite fraction is in the range of 0.64 to 0.85. As ferrite fraction decreased to 0.42, m_1 increased to 6.4. It is probably because higher martensite fraction affected almost all ferrite grains and induced much more dislocations in ferrite induced by martensite formation [26, 29, 32], resulting in a decrease in strain hardening ability. m_2 increased with a decrease in ferrite fraction, due to a higher restraint from deformation of ferrite grains by martensite regions, which led to a decrease in strain hardening ability. m_3 increased with an increase in martensite fraction because martensite has less ability to strain harden due to a very high initial dislocation density and the ferrite is already more strain hardened when the amount of martensite is higher. The value of m calculated using the experimental data for entire strain hardening region increased with decreasing ferrite fraction, which qualitatively corresponds to the discussed above increase in m_2 and m_3 and also to an increase in strain hardening exponent (Fig. 2.14(c)).

Table 2.4 Comparison of the modified Crussard – Jaoul (C–J) analysis with the experimental results.

Specimen	Modified C-J model			Experimental m[b]
	m_1[a]	m_2	m_3	
DP 30	6.4	8.7	16.4	16.4
DP 40	4.9	6.0	11.0	8.2
DP 50	5.0	4.9	7.0	6.1
DP 60	5.5	4.8	6.9	6.2

[a] $1 - m_{1\text{-}3}$ = slopes at Stage 1 to 3

[b] $m = 1/(\varepsilon_u - \varepsilon_y)$, where ε_u is maximum uniform true strain and ε_y is true strain at 0.2% offset proof stress

2.4.2 Comparison with mechanical properties of hot rolled DP steels

Fig. 2.18 compares the mechanical properties of the present samples with DP steels that have been conventionally processed. It can be seen that the UTS and YS of the studied DP steel are lower than those of hot rolled ones, while the total elongation is

relatively higher [2, 10, 13, 27, 33-39]. The product of UTS × total elongation is relatively lower than that of hot rolled ones, which suggests a lower toughness in the studied steel compared to the reference steels. According to the microstructure observation (Figs. 2.9, 2.10, 2.11 and 2.17) and metallographic analysis (Figs. 2.13 and Table 2.2), ferrite grain size and its distribution, size and shape of martensite regions, and presence of Widmänstatten ferrite could be responsible for the lower combination of mechanical properties.

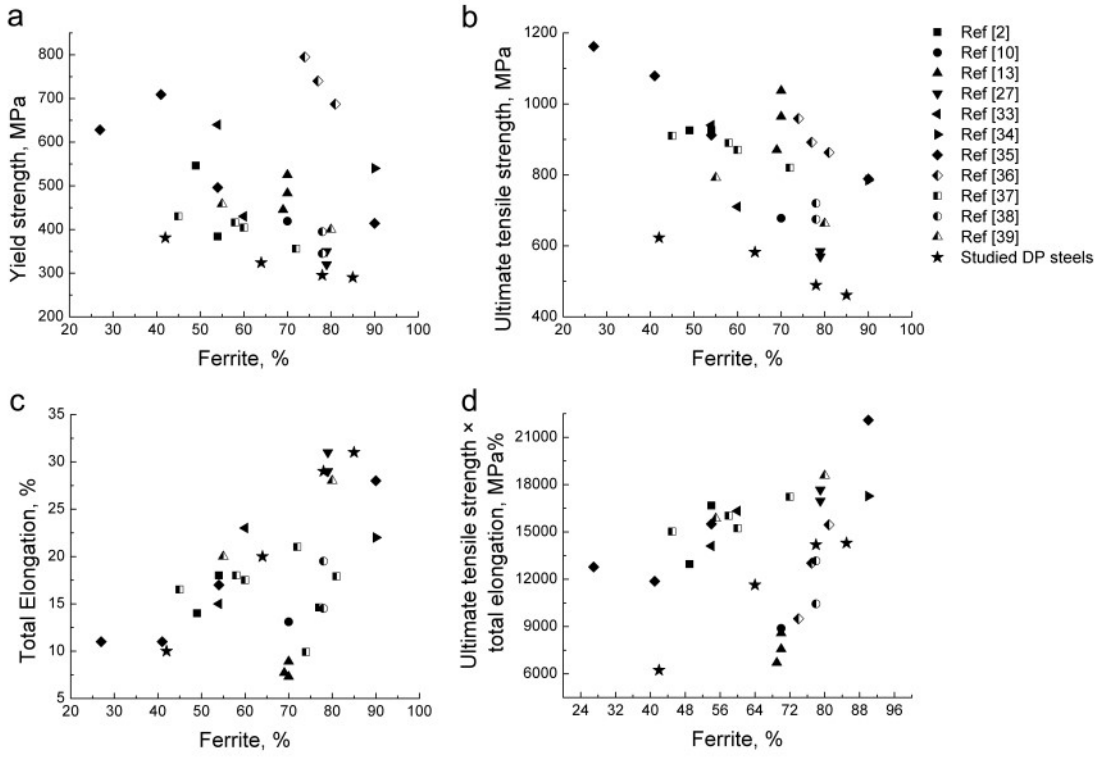

Figure 2.18 Comparison of the mechanical properties of studied steels with the properties of hot rolled DP steels [2, 10, 13, 27, 33-39]: (a) yield strength, (b) ultimate tensile strength, (c) total elongation and (d) ultimate tensile strength × total elongation.

A very coarse prior austenite grain size of 117±44 μm resulted in a large grain size of ferrite due to a small number of ferrite nucleation sites. It is detrimental to YS, UTS and toughness. Based on the Hall – Petch equation ($\sigma = \sigma_0 + kd^{-1/2}$, where σ_0 is lattice friction stress, k is constant, d is average grain size and σ is YS), YS and UTS

decrease with increasing grain size [14]. For example, with an increase in ferrite grain size from 1.2 to 12.4 μm when the ferrite fraction was 0.7, YS and UTS decreased by 80 and 167 MPa, respectively [13]. The studied here DP steel had the ferrite grain size of around 20 μm (Table 2.2), which reflected in significantly reduced strength. The size of martensite regions also affects the strength [16]. Large size of martensite regions is harmful to mechanical properties, due to a decrease in geometrically necessary dislocations and effective barriers to dislocation motion in ferrite [16, 40-42]. In addition, the size distribution of martensite regions was not homogeneous, as shown in Figs. 2.9, 2.13(b) and (d). Some martensite regions exceeding 50 μm (Table 2.2 and Fig. 2.13) could reduce ductility, because a coarser martensite may crack at lower strains following stress accumulation [31, 40].

In studied steel the ferrite grains were mostly of a polygonal shape while martensite regions exhibited less regular shape and had some concave and convex profiles as indicated by the arrows in Figs. 2.10(c) and (d). Such shapes of martensite regions can be explained by a variation in the rates of growing polygonal ferrite from prior austenite boundaries. As demonstrated using *in situ* tensile test in Ref [43], concave and convex parts of martensite regions easily induce stress concentration and plastic deformation localisations, which lead to earlier void formation along the tensile direction and reduce fracture strain.

Widmänstatten ferrite was observed in all four samples as shown in Figs. 2.10(a) and (b), although it is not common in DP steels. Widmänstatten ferrite can form following polygonal ferrite formation [44]. In our DP steel, a very coarse prior austenite grain size (117±44 μm) led to the large remaining austenite areas after the polygonal ferrite formation during holding. This large remaining austenite grains facilitated the formation of Widmänstatten ferrite [45, 46]. Moreover fast cooling following holding at 650 °C also facilitated the formation of Widmänstatten ferrite [46, 47]. According

to Ref [46], Widmänstatten ferrite may increase YS and UTS. However, in the studied DP steel, it also could contribute to the decrease in elongation to failure due to the stress concentration around the tips of Widmänstatten ferrite.

Compared to hot rolling, the studied processing route here did not carry out deformation. In hot rolling deformation in austenite temperature region or in the two-phase region results in an increase in dislocation density and deformation bands in ferrite, and elongated structure [48], leading to the increase in YS and UTS [49, 50]. In the studied DP steel, the dislocation density in ferrite was low (Fig. 2.17 (a) and (b)). On the other hand, deformation facilitates the nucleation and growth of polygonal ferrite, leading to a decrease in the amount of Widmänstatten ferrite [51], a decrease in ferrite grain size and the size of martensite regions [37, 52, 53]. All the aspects of microstructure development discussed here will be taken into account in further technology optimisation.

2.5 Conclusion

The characterisation of microstructure and mechanical properties of DP steel produced by the laboratory simulated strip casting leads to the following conclusions:

(1) The developed processing route for simulation of the strip casting in laboratory, resulted in DP steel microstructures containing 40~90 % polygonal ferrite, martensite and small amounts of bainite and Widmänstatten ferrite.

(2) For DP steel with nominal composition of 0.08C-0.81Si-1.47Mn-0.03Al, wt. %, experimental CCT and TTT diagrams were obtained. The nose temperature of ferrite formation field was determined being around 650 °C. Decreasing the cooling rate from austenitisation temperature to 650 °C resulted in larger fraction of ferrite formed.

(3) The variation of ferrite fraction in DP steel resulted in an ultimate tensile strength in the range of 461 ~ 623 MPa and a corresponding total elongation in the range of 0.31 ~ 0.10. The better strain hardening behaviour was displayed by the samples having higher ferrite fraction (such as 0.42 and 0.64). The strain hardening behaviour of studied steels was similar to that of hot rolled DP steels and was characterised by three stages according to modified Crussard – Jaoul model.

(5) The predominant fracture mode was ductile, with the presence of some isolated cleavage facets, the amount of which increased with an increase in martensite fraction.

(4) Comparison of mechanical properties of the studied steel with those of hot rolled DP steels showed the lower yield stress and ultimate tensile strength, although the comparable elongation in the former one, due to the large ferrite grain size, coarse martensite regions and the presence of Widmänstatten ferrite. The observed differences are associated with the absence of deformation in the utilised processing schedule.

Acknowledgements

This project was supported by the Australian Research Council (DP130101887). The JEOL JSM-7001F FEG-SEM was funded by the Australian Research Council (LE0882613). The authors thank Dr. A.A. Gazder, UOW for modification of tensile stage.

References

[1] R. Kuziak, R. Kawalla, S. Waengler, Arch. Civ. Mech. Eng. 8 (2008) 103-117.

[2] E. Ahmad, T. Manzoor, N. Hussain, N.K. Qazi, Mater. Design 29 (2008) 450-457.

[3] E. Fereiduni, S.S.G. Banadkouki, J. Alloy Compd. 577 (2013) 351-359.

[4] M. Dziedzic, S. Turczyn, Arch. Civ. Mech. Eng. 10 (2010) 21-30.

[5] A. Kumar, S.B. Singh, K.K. Ray, Mater. Sci. Eng. A 474 (2008) 270-282.

[6] N. Saeidi, A. Ekrami, Mater. Sci. Eng. A 523 (2009) 125-129.

[7] A. Ramazani, P.T. Pinard, S. Richter, A. Schwedt, U. Prahl, Comp. Mater .Sci. 80 (2013) 134-141.

[8] M.R. Akbarpour, A. Ekrami, Mater. Sci. Eng. A 477 (2008) 306-310.

[9] M. Asadi, B.C. De Cooman, H. Palkowski, Mater. Sci. Eng. A 538 (2012) 42-52.

[10] K. Park, M. Nishiyama, N. Nakada, T. Tsuchiyama, S. Takaki, Mater. Sci. Eng. A 604 (2014) 135-141.

[11] G. Avramovic-Cingara, Y. Ososkov, M.K. Jain, D.S. Wilkinson, Mater. Sci. Eng. A 516 (2009) 7-16.

[12] M. Mazinani, W.J. Poole, Metall. and Mater. Trans. A 38 (2007) 328-339.

[13] M. Calcagnotto, Y. Adachi, D. Ponge, D. Raabe, Acta Mater. 59 (2011) 658-670.

[14] P.H. Chang, A.G. Preban, Acta Metall. Mater. 33 (1985) 897-903.

[15] M. Calcagnotto, D. Ponge, D. Raabe, Mater. Sci. Eng. A 527 (2010) 7832-7840.

[16] Z. Jiang, Z. Guan, J. Lian, Mater. Sci. Eng. A 190 (1995) 55-64.

[17] S. Ge, M. Isac, R.I.L. Guthrie, ISIJ Int. 52 (2012) 2109-2122.

[18] N. Zapuskalov, ISIJ Int. 43 (2003) 1115-1127.

[19] R. Wechsler, Scand. J. Metall. 32 (2003) 58-63.

[20] S. Ge, M. Isac, R.I.L. Guthrie, ISIJ Int. 53 (2013) 729-742.

[21] L. Strezov, J. Herbertson, G.R. Belton, Metall. Mater. Trans. A 31B (2000) 1023-1030.

[22] I.B. Timokhina, P.D. Hodgson, E.V. Pereloma, Metall. Mater. Trans. A 38 (2007) 2442-2454.

[23] M. Olasolo, P. Uranga, J.M. Rodriguez-Ibabe, B. Lopez, Mater. Sci. Eng. A 528 (2011) 2559-2569.

[24] V. Colla, M. Desanctis, A. Dimatteo, G. Lovicu, R. Valentini, Metall. Mater. Trans. A 42A (2011) 2781-2793.

[25] N. Fonstein, O. Yakubovsky, D. Bhattacharya, F. Siciliano, Mater. Sci. Forum 500-501 (2005) 453-460.

[26] Z.Z. Zhao, T.T. Tong, J.H. Liang, H.X. Yin, A.M. Zhao, D. Tang, Mater. Sci. Eng. A 618 (2014) 182-188.

[27] W. Tan, B. Han, S.Z. Wang, Y. Yang, C. Zhang, Y.K. Zhang, J. Iron Steel Res. Int. 19 (2012) 37-41.

[28] Y. Mazaheri, A. Kermanpur, A. Najafizadeh, Mater Sci. Eng. A 619 (2014) 1-11.

[29] M. Calcagnotto, D. Ponge, E. Demir, D. Raabe, Mater. Sci. Eng. A 527 (2010) 2738-2746.

[30] Y. Tomita, K. Okabayashi, Metall. Trans. A, 16 (1985) 865-872.

[31] F. Al-Abbasi, J. Nemes, Int. J. Solids Struct. 40 (2003) 3379-3391.

[32] A. Karmakar, S. Sivaprasad, S. Kundu, D. Chakrabarti, Metall. Mater. Trans. A 45A (2014) 1659-1664.

[33] P. Deb, M.C. Chaturvedi, Mater. Sci. Eng. 78 (1986) L7-L13.

[34] J. Hu, L.X. Du, J.J. Wang, C.R. Gao, T.Z. Yang, A.Y. Wang, R.D.K. Misra, Metall. Mater. Trans. A 44A (2013) 4937-4947.

[35] N.G. Kolbasnikov, Y.A. Bezobrazov, A.A. Naumov, Steel Transl. 43 (2013) 455-459.

[36] J. Lis, A.K. Lis, C. Kolan, J. Mater. Process Tech. 162 (2005) 350-354.

[37] A.K. Panda, P.K. Ray, R.I. Ganguly, Mater. Sci. Tech. 16 (2000) 648-656.

[38] X.J. Xu, J.Q. Kong, J.P. Lin, R.R. Zheng, Rev. Adv. Mater. Sci. 33 (2013) 348-353.

[39] R. González, J. García, L. Verdeja, M. Quintana, J. Verdeja, Can. Metall. Quart. 53 (2014) 100-106.

[40] M. Erdogan, S. Tekeli, Mater. Design 23 (2002) 597-604.

[41] M. Erdogan, S. Tekeli, Mater. Charact. 49 (2002) 445-454.

[42] K. Kocatepe, M. Cerah, M. Erdogan, J. Mater. Process. Tech. 178 (2006) 44-51.

[43] M. Azuma, S. Goutianos, N. Hansen, G. Winther, X. Huang, Mater. Sci. Tech. 28 (2012) 1092-1100.

[44] S.F. Di Martino, G. Thewlis, Metall. Mater. Trans. A 45 (2014) 579-594.

[45] R.L. Bodnar, S.S. Hansen, Metall. Mater. Trans. A 25 (1994) 665-675.

[46] R.L. Bodnar, S.S. Hansen, Metall. Mater. Trans. A 25 (1994) 763-773.

[47] S.I. Kim, Y. Lee, Met. Mater. Int. 18 (2012) 735-744.

[48] N.M. Xiao, M.M. Tong, Y.J. Lan, D.Z. Li, Y.Y. Li, Acta Mater. 54 (2006) 1265-1278.

[49] K. Nakashima, M. Suzuki, Y. Futamura, T. Tsuchiyama, S. Takaki, Mater. Sci. Forum 503-504 (2006) 627-632..

[50] M.D. Taylor, K.S. Choi, X. Sun, D.K. Matlock, C.E. Packard, L. Xu, E. Barlat, Mater. Sci. Eng. A 597 (2014) 431-439.

[51] R.H. Larn, J.R. Yang, Mater Sci. Eng. A 264 (1999) 139-150.

[52] A.R. Salehi, S. Serajzadeh, A.K. Taheri, J. Mater. Sci. 41 (2006) 1917-1925.

[53] S.C. Hong, K.S. Lee, Mater. Sci. Eng. A 323 (2002) 148-159.

CHAPTER 3 EFFECT OF DEFORMATION ON MICROSTRUCTURE AND MECHANICAL PROPERTIES OF DUAL PHASE STEEL PRODUCED VIA STRIP CASTING SIMULATION

Z.P. Xiong[1*], A.G. Kostryzhev[1], N.E. Stanford[2], E.V. Pereloma[1, 3]

[1]*School of Mechanical, Materials and Mechatronic Engineering, University of Wollongong, Wollongong, NSW 2522, Australia*

[2]*Institute of Frontier Materials, Deakin University, Geelong, Victoria 3216, Australia*

[3]*Electron Microscopy Centre, University of Wollongong, Wollongong, NSW 2519, Australia*

Abstract: The strip casting is a recently appeared technology with a potential to significantly reduce energy consumption in steel production, compared to hot rolling and cold rolling. However, the quantitative dependences of the steel microstructure and mechanical properties on strip casting parameters are unknown and require investigation. In the present work we studied the effects of reduction and interrupted cooling temperature on microstructure and mechanical properties in conventional dual phase steel (0.08C-0.81Si-1.47Mn-0.03Al wt. %). The strip casting process was simulated using a Gleeble 3500 thermo-mechanical simulator. The steel microstructures were studied using optical, scanning and transmission electron microscopy. Mechanical properties were measured using microhardness and tensile testing. Microstructures consisting of 40-80% polygonal ferrite with remaining martensite, bainite and very small amount of Widmanstätten ferrite were produced. Deformation to 0.17-0.46 reduction at 1050 °C refined the prior austenite grain size via static recrystallisation, which led to the acceleration of ferrite formation and the ferrite grain refinement. The yield stress and ultimate tensile strength increased with a decrease in ferrite fraction, while the total elongation decreased. The improvement of mechanical properties via deformation was ascribed to dislocation strengthening and grain boundary strengthening.

Keywords: Dual phase steel; Strip casting; Thermo-mechanical processing; Microstructure characterisation; Mechanical properties; Strengthening mechanisms.

3.1 Introduction

Dual phase (DP) steels are widely used in automotive industry due to their continuous yielding behaviour, low yield stress-to-tensile strength ratio, high work hardening rate and high elongation [1, 2]. From the development of ferrite-martensite DP steels in the mid-1960s [3] until now, the DP steels have been produced by hot rolling and cold rolling followed by annealing [4]. Alternatively, the strip casting is another potential way to manufacture DP steels. The strip casting technology allows a direct production of strip steels from liquid condition, which leads to a shorter processing route [5, 6]. As a result, strip casting is environmentally friendly and economic. At present, this technology is already used for production of carbon steels, silicon steels and stainless steels [5, 7]. However, a coarse prior austenite grain size (PAGS) up to 450 μm presents a challenge for engineers to control the austenite transformation to low temperature phases [8].

It is well known that PAGS affects the final microstructures: coarser prior austenite grains lead to larger ferrite grains, whereas finer ferrite grains are formed from smaller prior austenite grains [9, 10]. Cota *et. al.* reported that the average ferrite gain size increased from 8 to ~ 40 μm when the PAGS increased from 9.5 to 100 μm [11]. Conditioning of prior austenite microstructure before austenite transformation using thermo-mechanical processing is a widely employed and efficient method. The thermo-mechanical processing includes the refinement of prior austenite grains through recrystallisation following deformation at a higher temperature and by heavy deformation carried out in the non-recrystallisation region at a lower temperature [12]. Consequently, the amount of deformation and temperatures, at which deformation is carried out, are critical parameters. Large deformation at high temperature (above the non-recrystallisation temperature) accelerates dynamic and static recrystallisation [9, 13, 14]. In non-recrystallisation region, a higher deformation at lower temperature increases the amount of ferrite nucleation sites, through an increase in prior austenite grain boundary area and defect substructures (microbands, twins, shear bands, etc.), resulting in ferrite grain refinement [15-17]. For example, with a decrease in deformation temperature from 1100 to 845 °C, the ferrite grain size of low carbon Nb–Ti microalloyed steel decreased from 11 to 3 μm [18]. In addition, a decrease in deformation temperature and an increase in strain

increase the dislocation density in ferrite matrix, leading to improved strength [19, 20]. In addition to ferrite grain refinement following austenite grain refinement as result of recrystallisation, rapid heating [21], large strain warm deformation followed by annealing and deformation induced ferrite transformation are also used to refine ferrite grains [2, 22, 23].

To study the feasibility of strip casting technology to manufacture DP steel, the authors produced DP steels in laboratory for the first time via simulated strip casting without deformation [24]. In this study, the effects of deformation and interrupted cooling temperature on microstructure and mechanical properties of DP steel were investigated for the first time. At present, only one rolling stand is installed in the strip casting line in industry [5, 8]. Thus, the effect of deformation only in the recrystallisation temperature region was studied in this work. The microstructures after deformation were characterised in detail. Mechanical behaviour was correlated with the microstructure evolution as a function of reduction.

3.2 Experimental details

As-cast specimens of 36 × 36 mm^2 and 1.2 mm thickness were produced at Deakin University using dip tester, which can simulate rapid cooling rate (~ 1700 Ks^{-1} in strip casting technology [6, 25]) experienced by the liquid steel during solidification [26]. The dip tester was used to immerse a copper substrate into molten steel for a short and controlled period of time and then immediately it was lifted out to simulate the rapid solidification [26]. The chemical composition mainly consisted of 0.0768 C, 0.805 Si, 1.47 Mn, 0.0346 Al, 0.0126 Cu, 0.233 Cr and balance Fe (all wt. %). As-received microstructure contained martensite with some bainite [24].

A Gleeble 3500 thermo-mechanical simulator in hydrawedge mode was employed to carry out the schedule (Fig. 3.1(a)) simulating the strip casting process. The samples were heated at 40 Ks^{-1} to 1000 °C, then at 20 Ks^{-1} to 1300 °C in order to avoid overshooting and held for 180 s. This was followed by cooling at 30 Ks^{-1} to 1050 °C where deformation to 0.17 or 0.46 reduction at a strain rate of 0.5 s^{-1} was applied. After this, the samples were cooled at 10 Ks^{-1} to the interrupted cooling temperatures (T_{IC} = 650, 670, 690, 720 or 830 °C) and then water quenched. Holding at 1300 °C

for 180 s was determined to simulate the prior austenite condition (average grain size of 117±44 μm) in strip casting, as described in the previous study [24]. Hereafter, the following identification of samples is used: DL650, DL 670 and DL 690 denote samples deformed at a reduction of 0.46 and then quenched from 650, 670 and 690 °C, respectively. DS 650 refers to the sample deformed at a reduction of 0.17 and then quenched from 650 °C. For comparison, the samples having 42%, 64%, 78% and 85% ferrite with martensite, small amount of bainite and Widmanstätten ferrite (referred to DP 30, DP 40, DP 50 and DP 60, respectively) were produced using a Theta dilatometer and the same austenitising and cooling schedule (Fig. 3.1(a)), which instead of deformation contained holding at 650 °C for 30, 40, 50 or 60 s before helium quenching. The detailed description of microstructure and mechanical properties for these non-deformed conditions were given in ref [24].

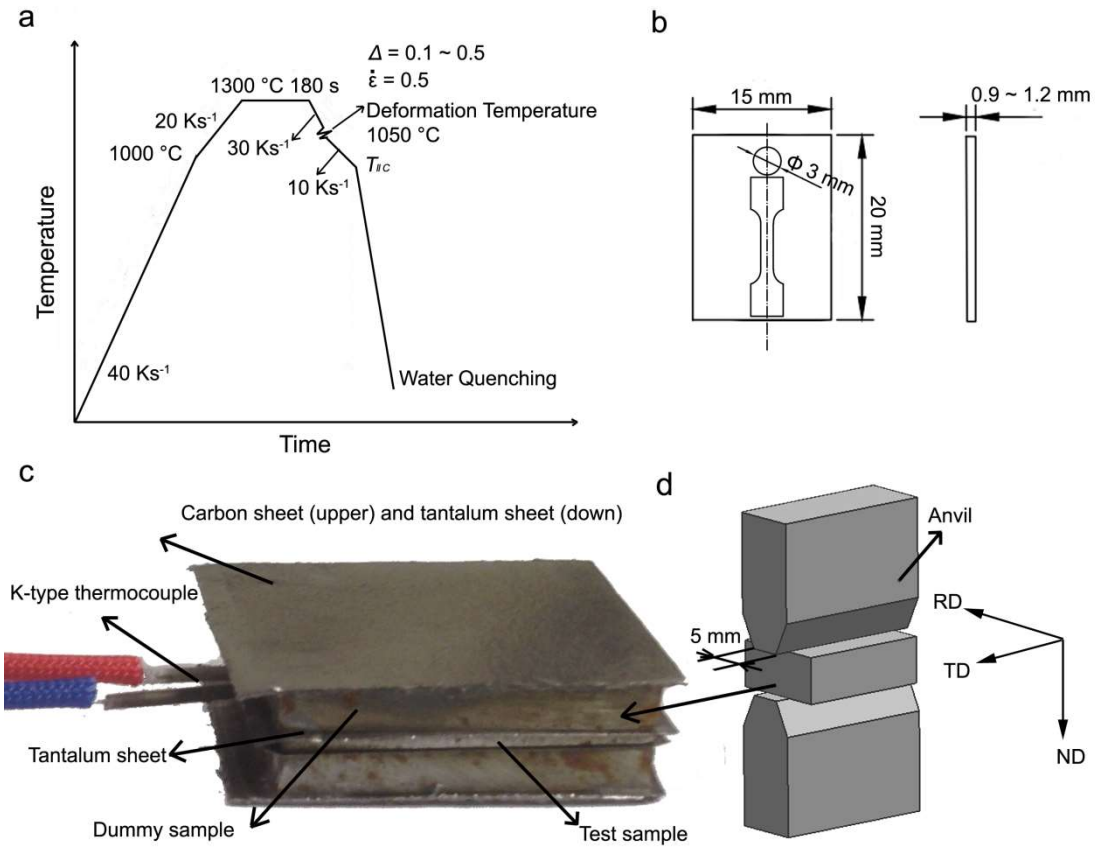

Figure 3.1 Schematic diagrams of (a) the thermo-mechanical processing schedule simulating strip casting process, (b) studied samples' dimensions, (c) a sandwich sample used for processing, and (d) the sandwich sample clamped by two anvils. *RD* is simulated rolling direction, *TD* is transverse direction and *ND* is normal direction.

The samples of 20 x 15 x (0.9 – 1.2) mm^3 size (Fig. 3.1(b)) were cut from as-cast specimens. Unfortunately, the thickness of the samples was beyond the capability of movement control system of the Gleeble 3500 thermo-mechanical simulator. To solve this problem, a sandwich sample was designed (Fig. 3.1(c)). Two dummy samples (2.5 mm thick; made of structural microalloyed steel) were used to clamp the studied sample. Tantalum sheets blocking the elements movement were inserted between them, while carbon sheets were added on the top and bottom. A K-type thermocouple for temperature monitoring was welded to the centre of cross-section of the studied sample. The sandwich sample was clamped by two Gleeble anvils (Fig. 3.1(d)). The width of the anvil was 5 mm. The reduction of the studied sample after deformation was measured using optical microscopy.

For microstructure observations, the Gleeble samples were cut parallel to the RD – ND plane (Fig. 3.1(d)). These samples were mounted, mechanically polished and then etched using 2 % nital. A Leica DMR research optical microscope (OM) and a JEOL JSM-7001F field emission gun – scanning electron microscope (FE - SEM), operating at 15 kV of accelerating voltage and fitted with an 80 mm^2 X-Max energy dispersive x-ray spectroscopy (EDS) detector, were used for general microstructure characterisation. All micrographs were taken from the centre of samples' cross-section. The fractions of phases were calculated based on different grey scales using Photoshop software. At least 260 ferrite grains or second phase regions were used to calculate the equivalent circle diameter.

Detailed microstructure characterisation was undertaken using a JEOL 2011 transmission electron microscope (TEM) operating at 200 kV. The 3 mm discs were electrically wire cut from RD – TD plane (Fig. 3.1(d)). The discs were mechanically polished to 50 – 80 μm thickness and then twin – jet electropolished with an electrolyte containing 10% of perchloric acid in methanol at 40 V. The dislocation density was calculated using linear intercept method [27]. For the dislocation density determination 10 – 15 representative areas were imaged in two-beam condition near [001] and [011] zone axes. The dislocation density in the regions near the ferrite-ferrite and ferrite-martensite boundaries was calculated within 1μm distance from the boundaries. The average dislocation density employed weighted average.

Mechanical properties were evaluated using the Vickers hardness test and tensile test at ambient temperature. Struers Emco-Test DuraScan-70 Vickers hardness tester was employed to measure hardness. The average hardness of polygonal ferrite and second phase region was measured using a load of 25 g and a loading time of 10 s, and calculated using the values for 5 areas by removing the maximum and minimum value among 7 areas. The tensile test samples having a gauge length of 4.9 mm and a width of 2.1 mm (Fig. 3.1(b)) were cut through RD – TD plane. Tensile tests were carried out using an in-house modified 5 kN Kammrath and Weiss GmbH tensile stage at a constant cross head speed of 2 μm s^{-1}, corresponding to an initial strain rate of 4 $\times 10^{-4}$ s^{-1}. At least two samples were tested for each condition.

3.3 Results

3.3.1 Effect of interrupted cooling temperature and deformation on ferrite formation

Figs. 3.2 and 3.3 show the microstructures formed after processing with different deformations and interrupted cooling temperatures (T_{IC}). The microstructures consisted of ferrite and embedded second phase regions. With decreasing T_{IC}, the ferrite fraction increased: from 0.41 to 0.74 for 0.46 reduction and from 0.28 to 0.51 for 0.17 reduction (Fig. 3.4(a)). Ferrite fraction increased from 0.20 to 0.74 with an increase in reduction from 0 to 0.46 for 650 °C cooling conditions (Fig. 3.4(b)). The microstructures for all conditions were inhomogeneous in cross-section, with a much higher amount of second phase in the middle compared to the sub-surface (Fig. 3.2). A layer of ferrite existed along the sub-surface, the width of which increased with an increase in T_{IC} and deformation.

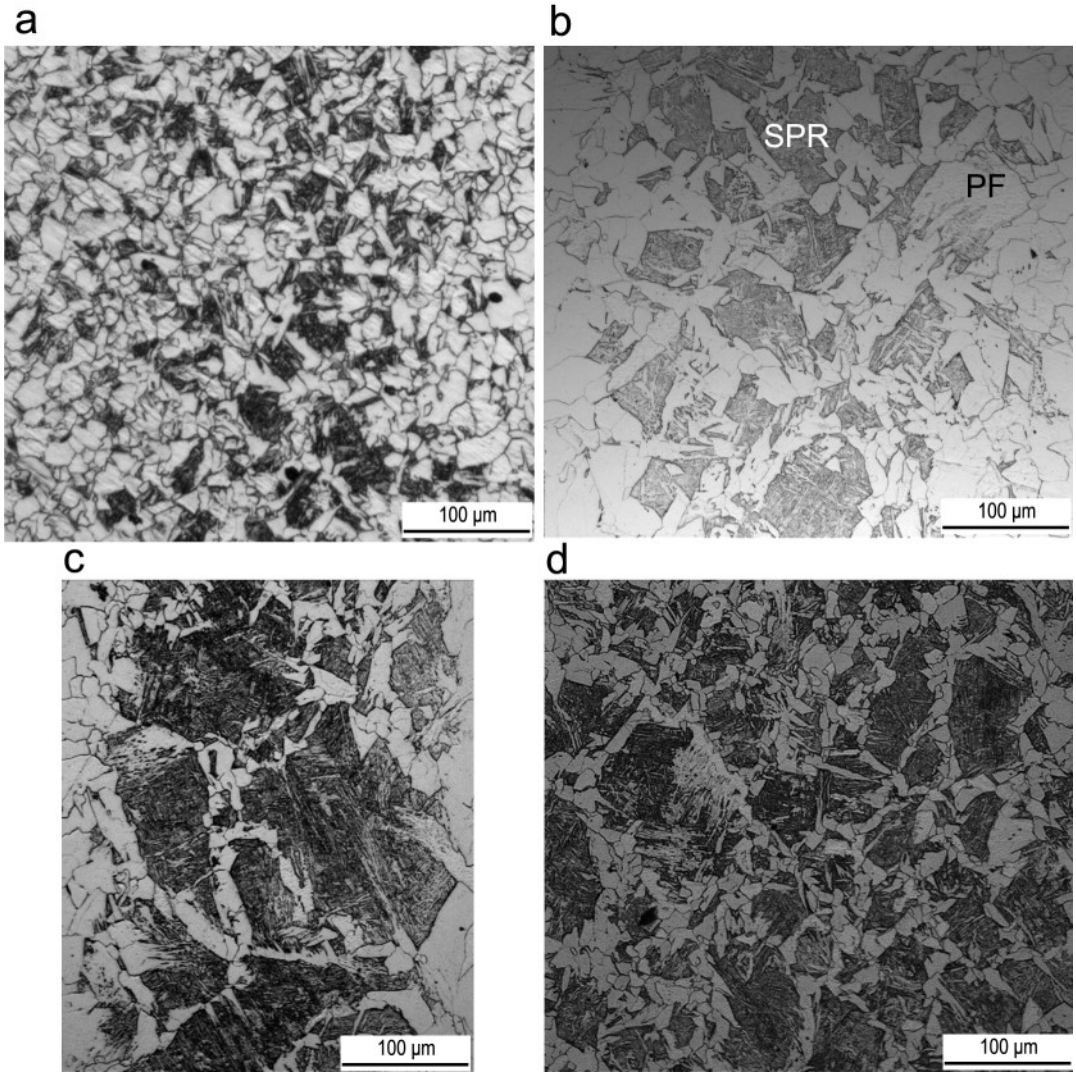

Figure 3.2 Optical microstructures of (a) DL 650, (b) DL 670, (c) DL 690 and (d) DS 650. *PF* is polygonal ferrite, *SPR* is second phase region.

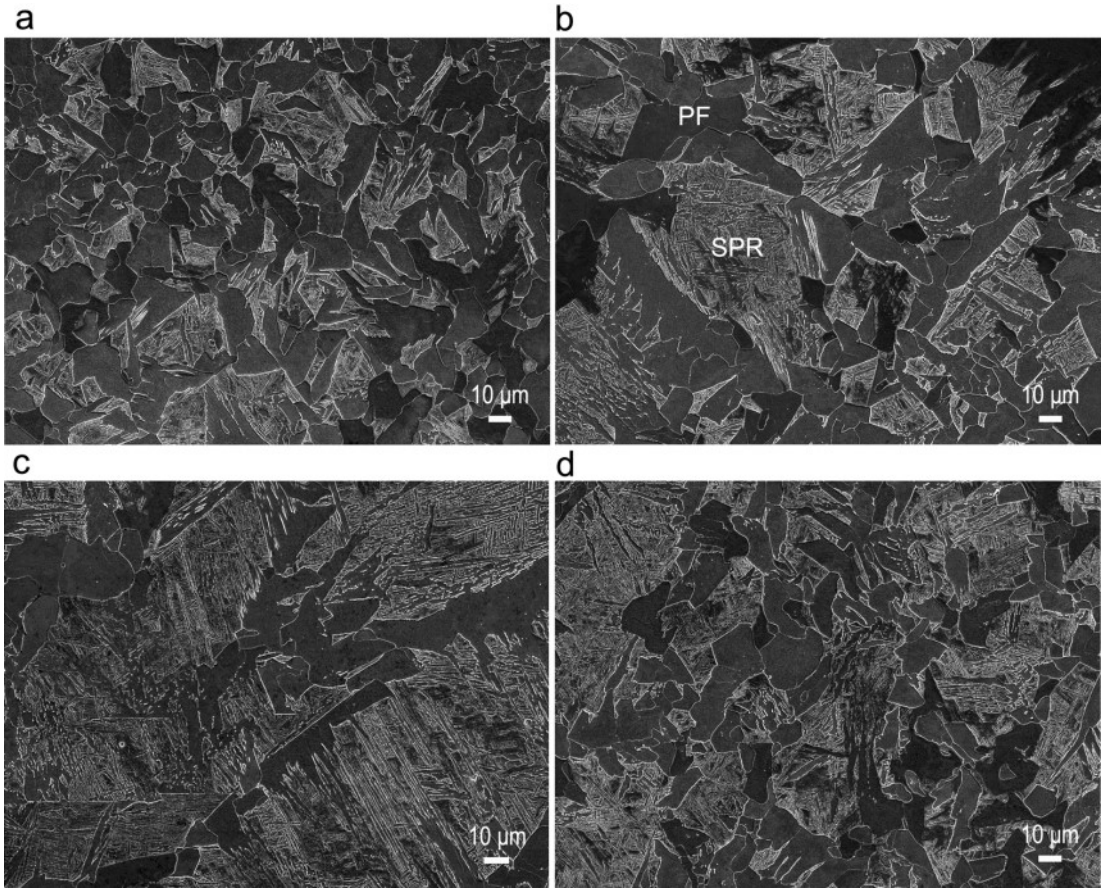

Figure 3.3 General view SEM micrographs of (a) DL 650, (b) DL 670, (c) DL 690 and (d) DS 650 in the centre of cross-section. *PF* is polygonal ferrite and *SPR* is second phase region.

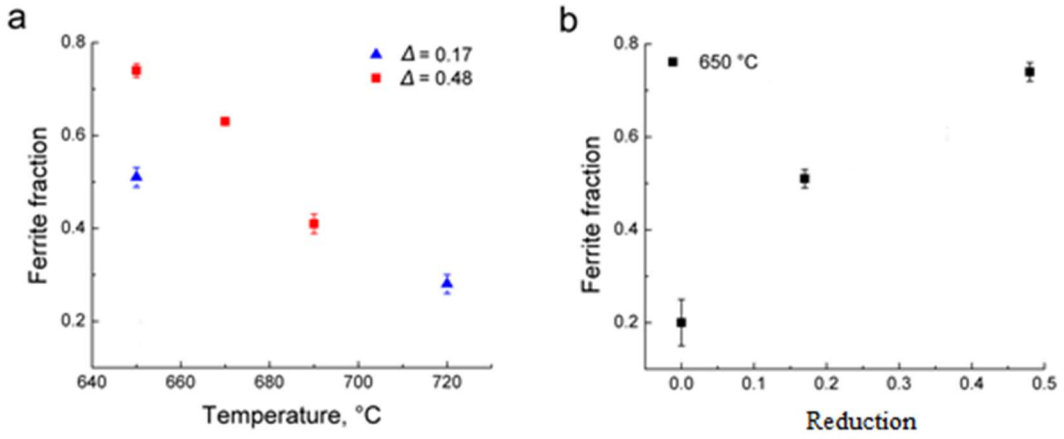

Figure 3.4 The influence of (a) interrupted cooling temperature and (b) deformation on ferrite formation.

Fig. 3.5 illustrates the microstructure constituents in detail, while Table 3.1 shows the microstructure statistics. The second phase regions consisted of a mixture of martensite and bainite, although some Widmänstatten ferrite was also observed in all conditions as indicated by arrows in Fig. 3.5(a), as an example. With a decrease in ferrite fraction, the amount of bainite increased, and the average size of second phase region increased from 9 to 24 μm due to less consumption of prior austenite by ferrite formation (Fig. 3.5(a), (c) and (e), and Table 3.1). The largest observed second phase regions in the range of 63 to 171 μm were simultaneously present with the smallest regions of around 3 μm size, which suggests a very large inhomogeneity. For samples deformed to 0.46 reduction, the ferrite grain size increased from 10 to 17 μm with a decrease in ferrite fraction (Fig. 3.6). However, this trend was not observed for the non-deformed samples. For the same ferrite fraction, the ferrite grain size significantly decreased with the deformation increasing from 0 to 0.46 (Fig. 3.6). Ferrite grain size and the second phase region size distributions are shown in Fig. 3.7. The ferrite grain size showed normal distributions for all the studied conditions (Fig. 3.7(a) and (c)). Only the sample containing 74% ferrite showed a normal size distribution of the second phase region (Fig. 3.7(b)). The other samples with ferrite fraction in the range of 0.41 to 0.63 displayed an exponential size distribution of the second phase region (Fig. 3.7(d)).

Table 3.1 A summary of microstructure statistics.

	Ferrite fraction	Average size, μm		Maximum, μm		Minimum, μm	
		Ferrite	Second phase region	Ferrite	Second phase region	Ferrite	Second phase region
DL 650	0.74±0.01	10±7.3	9±8.1	60	63	3	3
DL 670	0.63±0.01	10±9.8	20±18.0	66	74	3	4
DL 690	0.41±0.02	17±11.6	36±42.4	67	171	3	3
DS 650	0.51±0.02	15±8.8	24±27.6	55	134	3	3

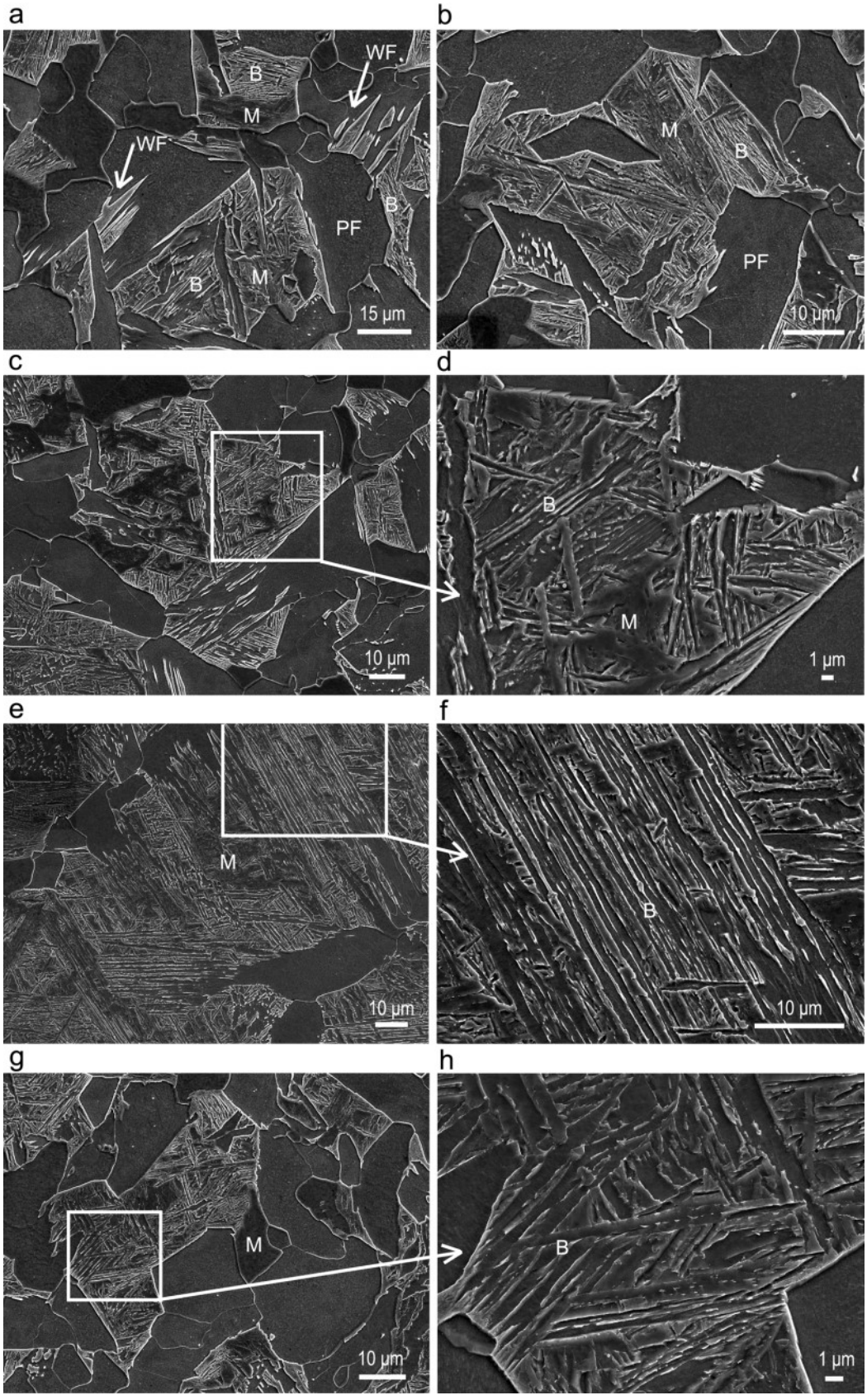

Figure 3.5 Selected SEM images of (a, b) DL 650, (c, d) DL 670, (e, f) DL 690 and (g, h) DS 650. *PF* is polygonal ferrite, *WF* is Widmänstatten ferrite, *B* is bainite and *M* is martensite.

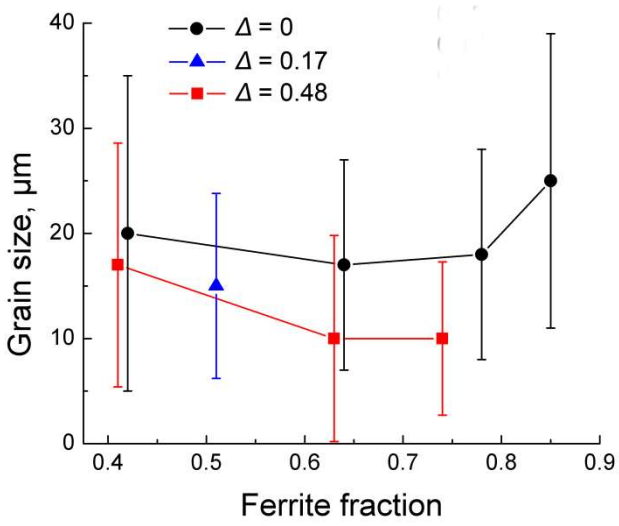

Figure 3.6 Effect of deformation on ferrite grain size.

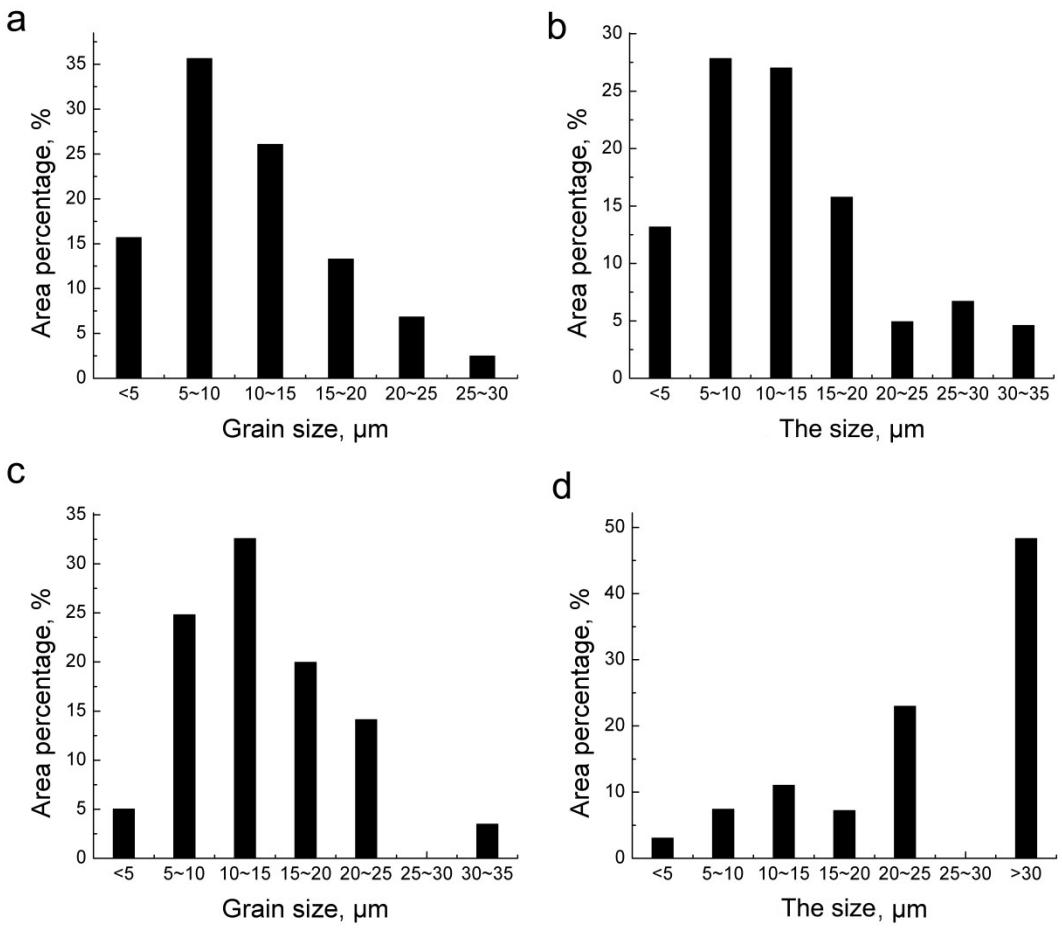

Figure 3.7 (a, c) Ferrite grain size distribution and (b, d) the size distribution of second phase region for (a, b) DL 650 and (c, d) DL 670.

TEM images in Fig. 3.8 show one Widmänstatten ferrite needle between the second phase regions. The Widmänstatten ferrite needle grew from the existing polygonal ferrite via the edge-to-face sympathetic nucleation and stopped at another polygonal ferrite boundary, forming a shape of needle [28]. Many dislocations were observed inside Widmänstatten ferrite. With a decrease in Widmänstatten ferrite width, the density of dislocations in it increased as a larger fraction of the Widmänstatten ferrite needle was affected by the second phase region. The second phase region consisted of martensite and bainite as demonstrated in Fig. 3.9. Lath structure of martensite was observed forming packets with a higher dislocation density. Light area with a lower dislocation density was bainite, which also exhibited a coarser lath structure compared to martensite. These observations support the SEM ones shown in Fig. 3.5(d).

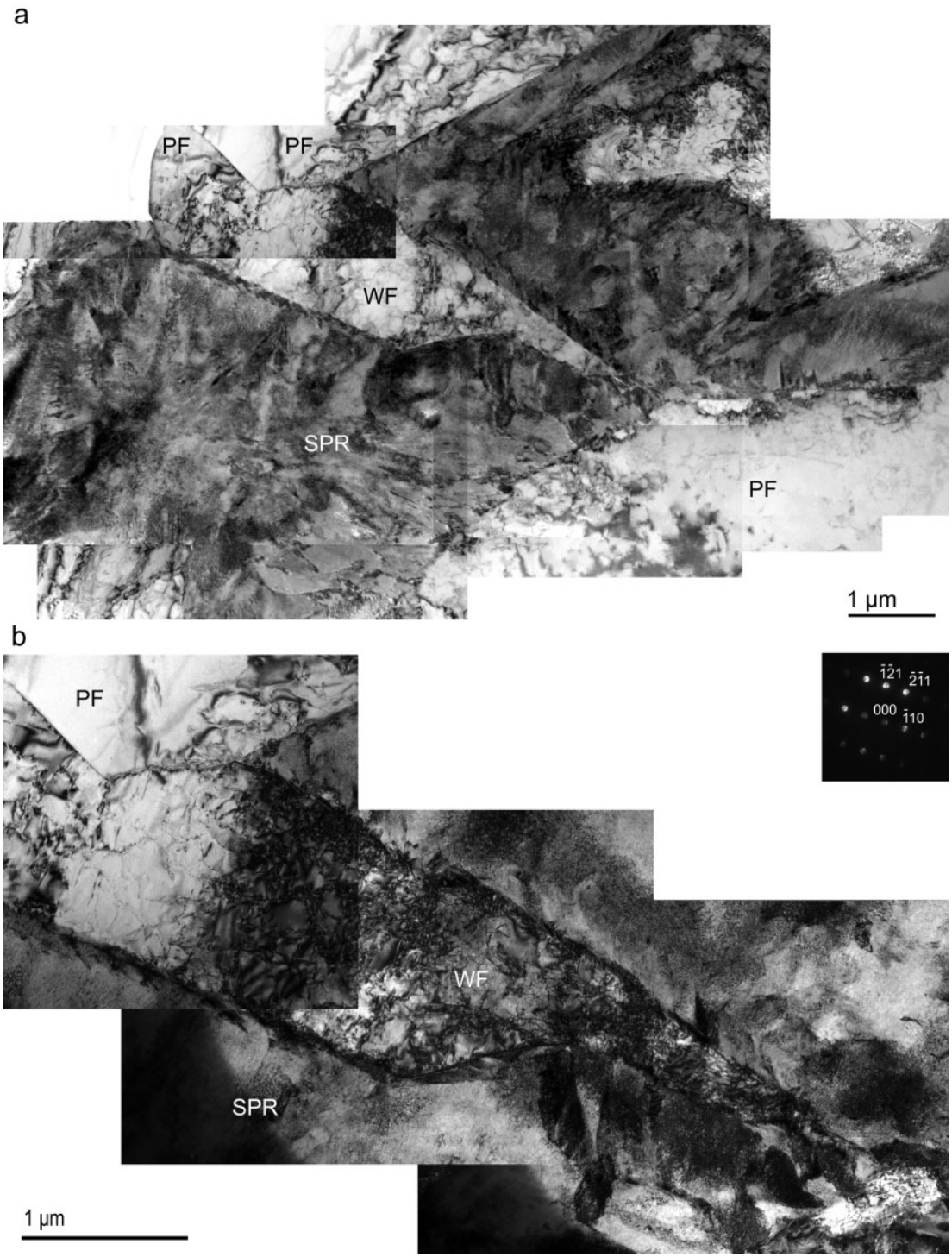

Figure 3.8 (a) A general view of Widmanstätten ferrite needle between the second phase regions and (b) high magnification of Widmanstätten ferrite in (a). The zone axis of inset from Widmänstatten ferrite in (b) is $[113]_{\alpha}$. *PF* is polygonal ferrite, *WF* is Widmänstatten ferrite and *SPR* is second phase region.

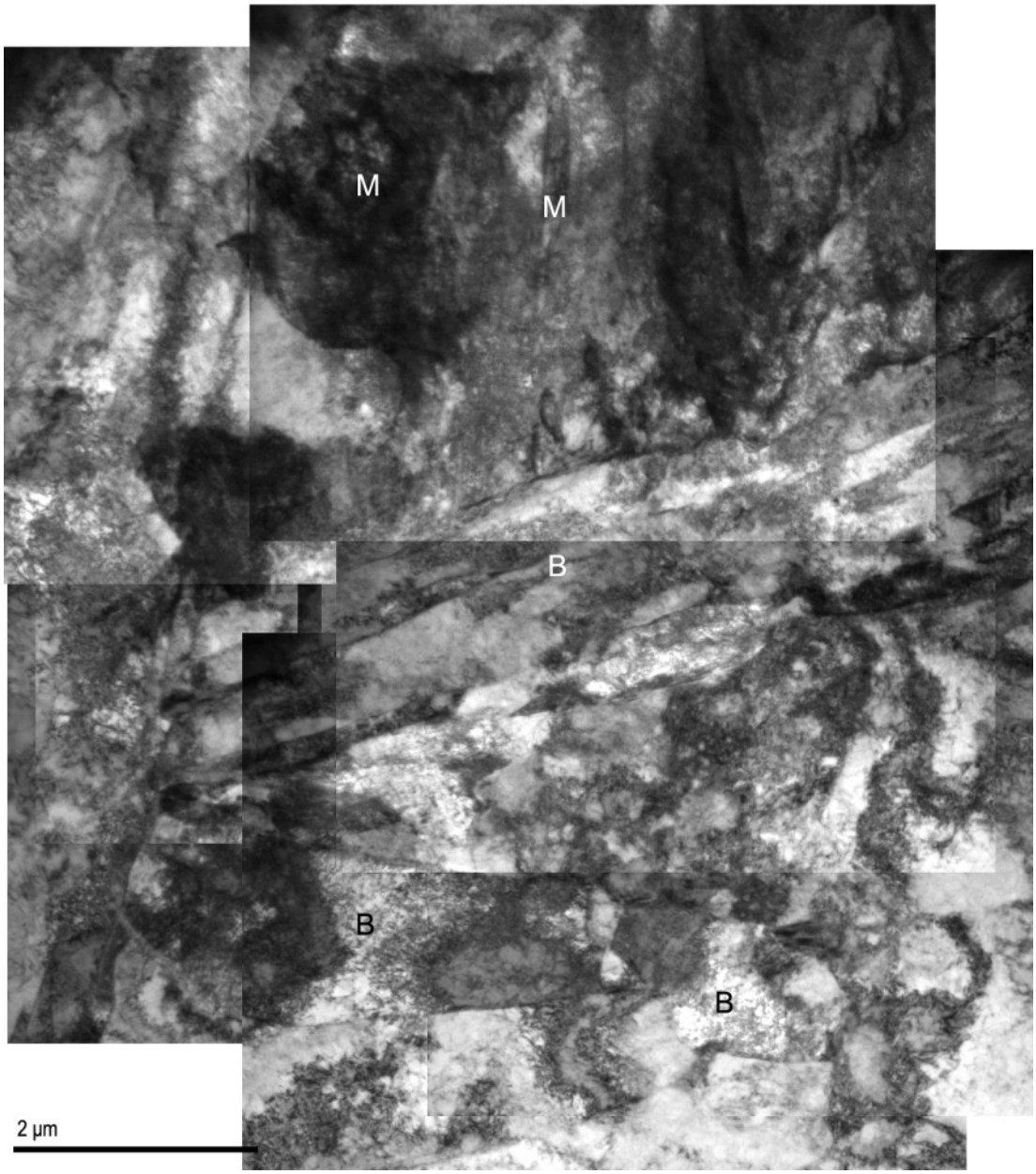

Figure 3.9 Second phase region consisting of martensite(M) and bainite (B) in DL 670.

The dislocation substructure was characterised in detail using images presented in Fig. 3.10, while the corresponding dislocation densities were listed in Table 3.2. Figs. 3.10(a), (d), (g) and (b), (e), (h) showed dislocations in DP 50 and DL 650 respectively, which have similar ferrite fraction of around 0.75. With an increase in deformation from 0 to 0.46 the dislocation density increased significantly in all locations of polygonal ferrite: in the centre increased from 1.2×10^{13} to 5×10^{13} m^{-2}, in the region near ferrite-ferrite boundaries from 1.2×10^{13} to 7.5×10^{13} m^{-2} and in ferrite adjacent to a second phase region from 17.4×10^{13} to 30.2×10^{13} m^{-2} (c.f. Fig.

3.10(a), (d), (g) and (b), (e), (h)). After the same deformation of 0.46 reduction, with a decrease in ferrite fraction from 0.74 to 0.63 the dislocation density in polygonal ferrite also increased from 7.7 $\times 10^{13}$ to 11.0 $\times$ 10^{13} m^{-2} (c. f. Figures 3.10(b), (e), (h) and (c), (f), (i)).

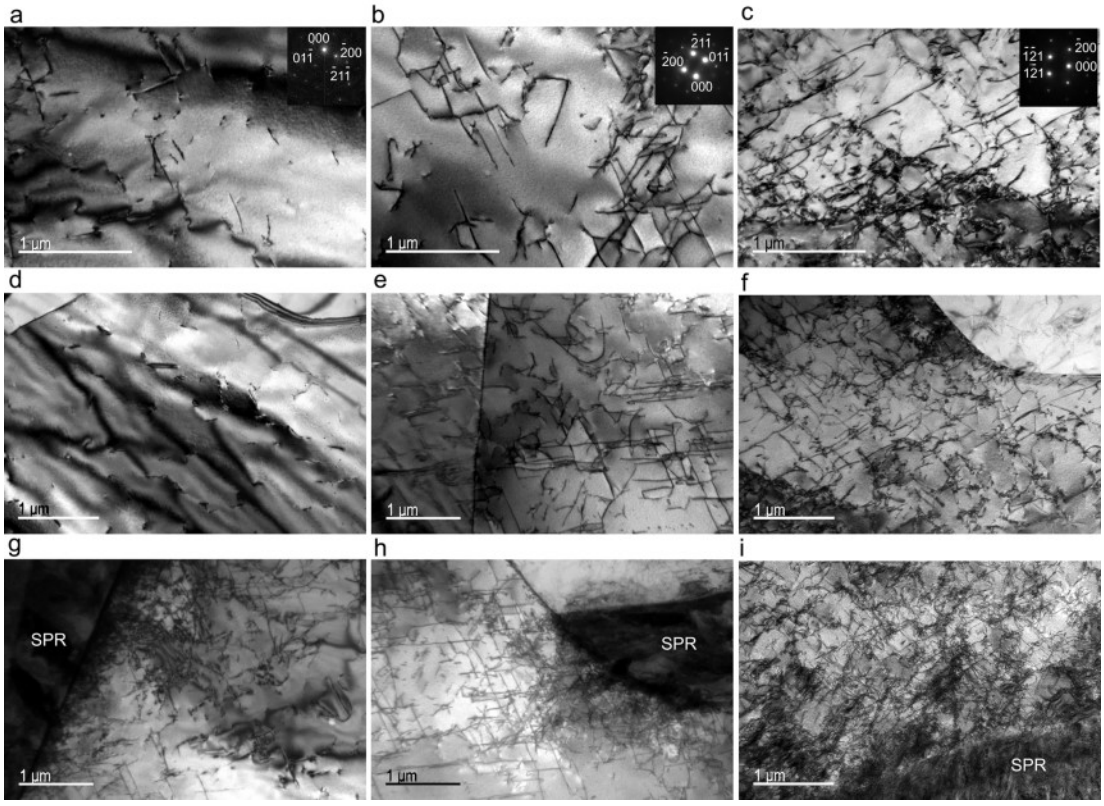

Figure 3.10 Dislocation structures in (a, d, g) DP 50, (b, e, h) DL 650 and (c, f, i) DL 670 samples in (a, b, c) polygonal ferrite far away from grain boundaries, (d, e, f) the region near ferrite-ferrite boundaries and (g, h, i) ferrite adjacent to the second phase region. *SPR* is second phase region. The zone axis of insets in (a, b) and (c) are $[011]_{\alpha}$ and $[012]_{\alpha}$, respectively.

Table 3.2 The statistics for dislocation densities in polygonal ferrite.

	Dislocation densities in different regions, $\times 10^{13}$ m^{-2}			
	In the centre	Near ferrite-ferrite boundaries	Adjacent to second phases	Weighted average
DP 50	1.2±0.14	1.2±0.28	17.4±5.95	2.1
DL 650	5.0±0.81	7.5±0.75	30.2±7.65	7.7
DL 670	7.4±1.70	14.5±2.95	36.3±14.1	11.0

3.3.2 Mechanical properties

Engineering stress – engineering strain curves are shown in Fig. 3.11. The repeatability of tensile curves was good as demonstrated by the reasonable standard deviations in Table 3.3. Typical round-house curves inherent in DP steels [29, 30] were observed here, indicating continuous yielding behaviour for all conditions. Therefore, the yield stress (YS) was determined using 0.2% offset. YS, ultimate tensile strength (UTS), uniform elongation (UE) and total elongation (TE) listed in Table 3.3 were determined from the data shown in Fig. 3.11, and plotted in Fig. 3.12. The data for undeformed samples (DP 30, DP 40, DP 50 and DP 60 [24]) is also included for comparison in Fig. 3.12. In the sample subjected to 0.46 reduction, with an increase in ferrite fraction from 0.41 to 0.74, YS and UTS decreased from 545 and 692 MPa to 433 and 621MPa, respectively, while UE and TE increased from 0.03 and 0.08 to 0.10 and 0.21, respectively (Figs. 3.11(a) and 3.12, and Table 3.3). With an increase in deformation, YS and UTS significantly increased, while UE and TE rapidly decreased as shown in Figs. 3.11(b) and 3.12. In particular for samples having 75% ferrite (DP 50 and DL 650) with an increase in reduction from 0 to 0.46, both the YS and UTS increased by approximately 130 MPa, from 295 and 489 MPa to 433 and 621MPa, respectively.

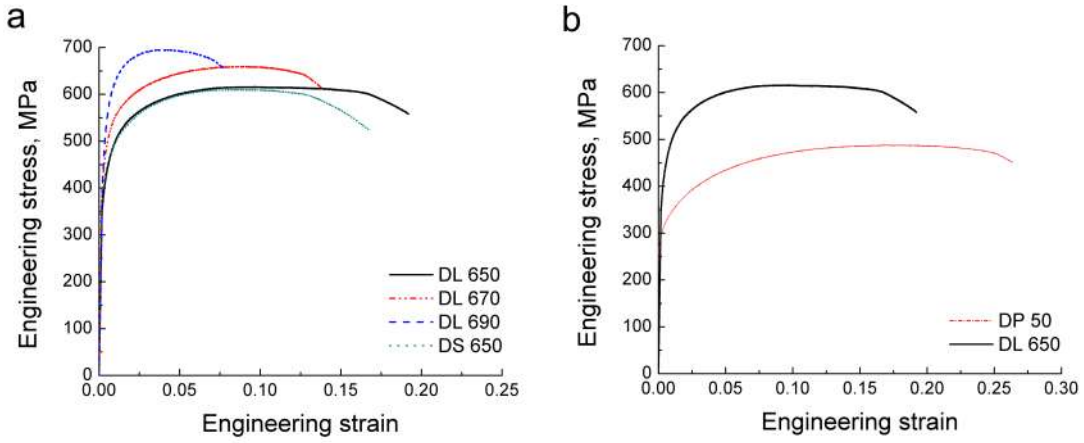

Figure 3.11 (a) Engineering stress – engineering strain curves for different ferrite fractions and reductions applied during processing and (b) comparison of stress – strain curves between undeformed (78% ferrite in DP 50) and deformed samples (74% ferrite in DL650).

Table 3.3 A summary of mechanical properties after different processing schedules.

	Deformation	Interrupted cooling temperature, ° C	Yield strength, MPa	Ultimate tensile strength, MPa	Uniform elongation	Total elongation
DL 650		650	433±12	621±5	0.10±0.003	0.21±0.001
DL 670	0.46±0.033	670	477±11	654±8	0.08±0.002	0.16±0.001
DL 690		690	545±21	692±4	0.03±0.003	0.08±0.008
DS 650	0.17±0.021	650	413±22	637±13	0.07±0.006	0.13±0.010

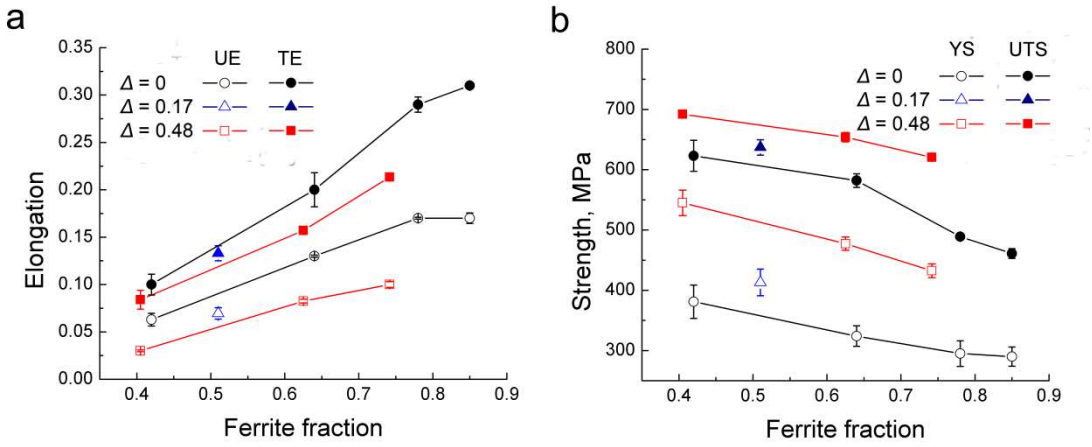

Figure 3.12 The dependence of (a) uniform elongation (UE) and total elongation (TE), and (b) yield stress (YS) and ultimate tensile strength (UTS) on ferrite fraction and amount of deformation.

Vickers hardness values of ferrite and second phase region are shown in Fig. 3.13. The data for undeformed samples (DP 30, DP 40, DP 50 and DP 60 [24]) is also included for comparison. With an increase in ferrite fraction or a decrease in the amount of deformation, the Vickers hardness value of ferrite decreased. In the sample subjected to 0.46 reduction, the Vickers hardness of second phases increased with an increase in ferrite fraction. Whereas, an abrupt decrease in the Vickers hardness value of second phase regions in the sample without deformation was observed. This could be a result of ferrite grain interference with a stress field under the hardness indent during measurement of a small second phase region [31]. The hardness values of second phase regions after deformation were lower than those of samples without deformation, which can be related to a significant amount of bainite forming after deformation instead of martensite (Fig. 3.5). The standard deviation of hardness measurements of second phase regions is large due to the coexistence of martensite and bainite and a significant variation in the second phase grain size.

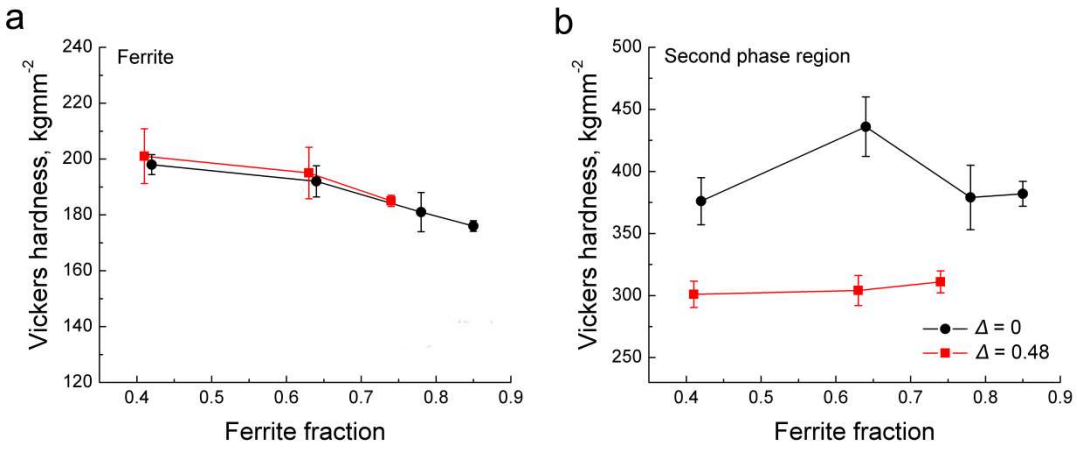

Figure 3.13 Vickers hardness values of (a) ferrite and (b) second phaseregion after different deformation.

3.3.3 Fractography

Necking behaviour was observed for all conditions. The extent of necking increased from 0.14 to 0.17 (the ratio of width variation near fracture surface to original width) with an increase in ferrite fraction (c.f. Fig. 3.14(a) and (b)), which was corresponding to an increase in UE and TE. Accordingly, the appearance of fracture surfaces at low magnification changed from flat to uneven and to conical shape when ferrite fraction increased (c.f. Fig. 3.14(c1-f1)). In addition, as could be seen from the microscopic images (Fig. 3.14(c2-f2), the size of dimples became larger while the amount of cleavage facets decreased with an increase in ferrite fraction. All of the above indicate a transition to a more ductile fracture mode with an increase in ferrite fraction. Larger size of dimples related to polygonal ferrite with larger grain size which deformed easier and earlier, while small size of dimples corresponded to polygonal ferrite with smaller grain size which deformed later. Besides, many inclusions were observed within the dimples, which were determined to be MnS as shown in Fig. 3.14(h). Such inclusions were also observed in the undeformed samples [24]. They could be sites for void formation, facilitating ductile fracture [32, 33].

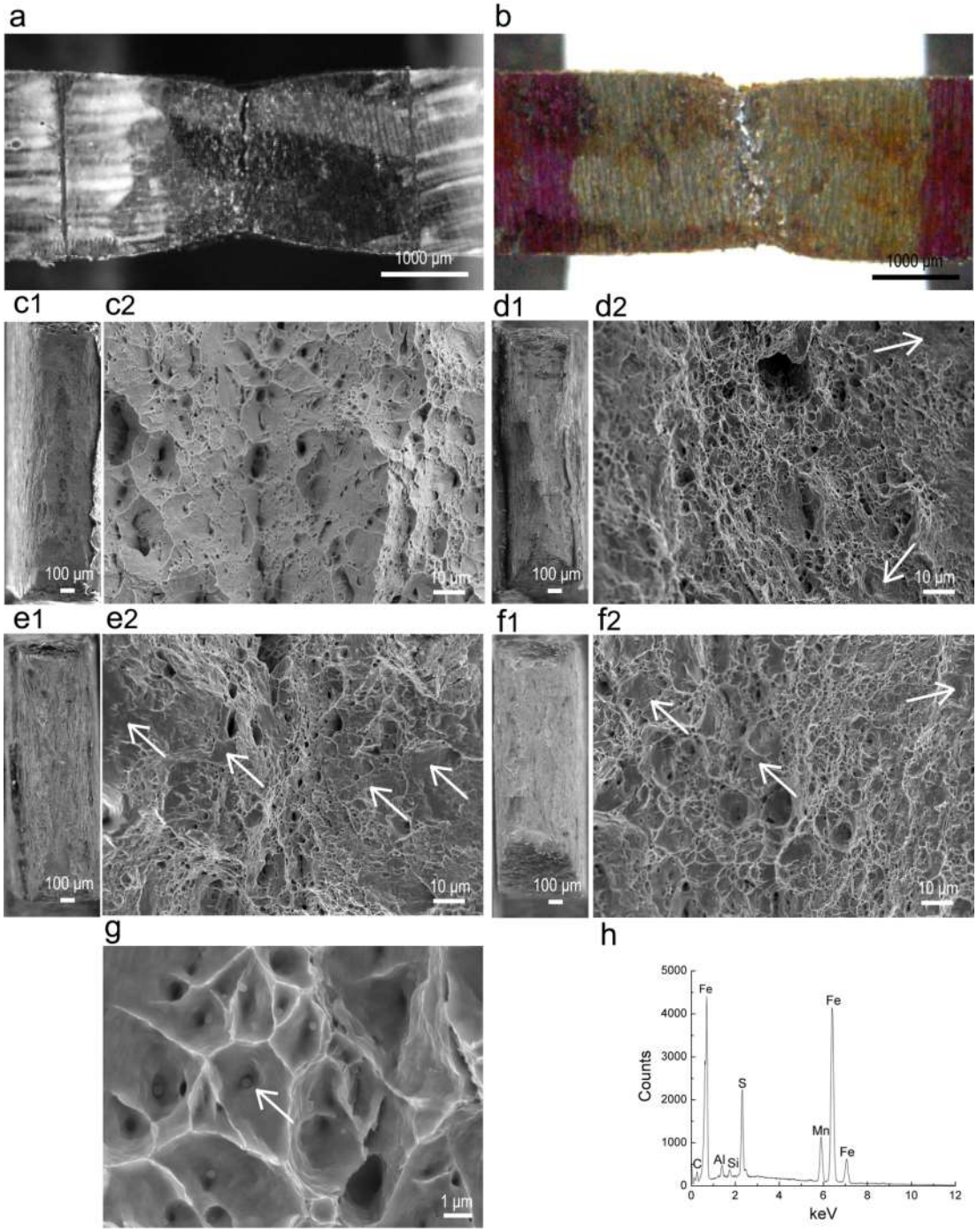

Figure 3.14 (a, b) Optical images of tensile samples (a) DL 650 and (b) DL 690; representative macroscopic (c1 – f1) and microscopic (c2 – f2) SEM images of fracture surfaces of (c) DL 650, (d) DL 670, (e) DL 690 and (f) DS 650; (g) selected SEM image showing MnS inclusions in voids and (h) the representative EDS spectrum of MnS in DL 670. Arrows in (d2 – f2) show cleavage facets and the arrow in (g) shows the inclusion.

3.4 Discussion

3.4.1 Microstructure evolution

In order to simulate the strip casting process, the PAGS of 117±44 μm was achieved in the samples heated to 1300 °C and held for 180 s, which was similar to 118±57 μm of the as-cast samples [24]. Then the samples were cooled at a rate of 30 Ks^{-1} to the deformation temperature of 1050 °C. A reduction of 0.17 or 0.46 was exerted using a strain rate of 0.5 s^{-1}. According to Refs [10, 34-36], the non-recrystallisation temperature of steels having similar chemical compositions to the studied steel was approximately 950 °C. In addition, no elongated grain structure was observed and the prior austenite grains delineated by allotriomorphic ferrite in Fig. 3.15 were of equiaxed shape. These supported the assumption that the deformation temperature of 1050 °C was above the non-recystallisation temperature. Therefore, dynamic recrystallisation during deformation and static recrystallisation during cooling to the interrupted cooling temperature could take place. After deformation to 0.46 reduction, the average grain size of ferrite was 10 and 17 μm for the samples having 63% and 41% ferrite, respectively. Using a linear fit, the sample with 52% ferrite should have a ferrite average grain size of 14 μm, which was similar to that of 15 μm in the sample with 51% ferrite after 0.17 reduction (Fig. 3.6). It means that the difference in reduction between 0.17 and 0.46 had a very little effect on dynamic recrystallisation, probably because both these reductions were lower than the critical strain required for dynamic recrystallisation. This correlates with a strain of 0.79 required for the dynamic recrystallisation completion when the PAGS was 120 μm and the sample (0.05% C, 0.28 Si, 0.54 Mn, 0.01% P, 0.005 S and balance Fe, all in wt. %) was deformed at 1000 °C at a strain rate of 0.1 s^{-1} [25]. Although there was no evidence of dynamic recrystallisation, static recrystallisation definitely took place during the cooling to T_{IC}. In order to measure PAGS, one sample was deformed to a reduction of 0.46 and quenched from 830 °C, the microstructure of which is shown in Fig. 3.15. Based on the presence of allotriomorphic ferrite nucleated at prior austenite boundaries, the average PAGS was determined to be 77±23 μm, which was finer than the PAGS of 117±44 μm after holding at 1300 °C for 180 s. The decrease in PAGS during cooling supports presence of static recrystallisation. The austenite grain size d_{ave} before ferrite formation could be calculated according to the static recrystallisation mode for plain C-Mn steels [35, 37]:

$$d_{ave} = x_{rex} d_{rex} + (1 + x_{rex}) d_0 \tag{3.1}$$

$$x_{rex} = 1 - \exp[-0.693(t / t_{0.5})^{1.5}] \tag{3.2}$$

$$d_{rex} = 343 d_0^{0.38} \varepsilon^{-0.5} \exp(-4500 / RT) \tag{3.3}$$

$$t_{0.5} = 3.6 \times 10^{-12} d_0 \varepsilon^{-2.5} \exp(230000 / RT) \tag{3.4}$$

where x_{rex} is the fraction of recrystallised austenite in time t, d_0 and d_{rex} are the grain sizes of initial and recrystallised austenite respectively, $t_{0.5}$ is the time for 50% recrystallisation, R is gas constant and T is deformation temperature in Kelvin.

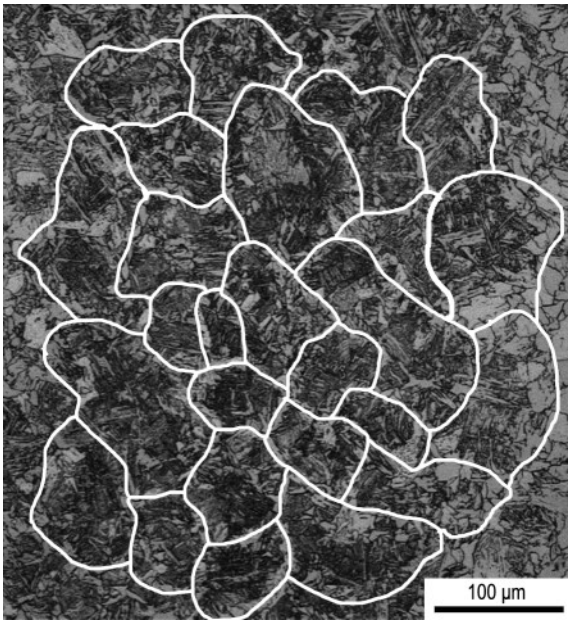

Figure 3.15 Depicted prior austenite grain boundaries based on allotriomorphic ferrite in the sample deformed to 0.46 reduction and water quenched from 830 °C.

In this study after deformation at 1050 °C the sample was cooled to the assumed non-recrystallisation temperature 950 °C at 10 Ks^{-1}; therefore, the time t available for static recrystallisation during cooling can be set as the maximum 10 s. For the time t equal to 10 or 5 s, the d_{ave} was calculated to be 52 or 67µm respectively, both of which were smaller than the measured grain size of 77±23 µm. A smaller average grain size predicted using Eqs. 1-4, compared to the measured one, was also reported in Ref [10]. This discrepancy could be explained by the retardation of static

recrystallisation due to a large austenite grain size leading to a decrease in the number of nucleation sites, such as grain boundary area [9, 37, 38].

As shown in Fig. 3.4, the ferrite fraction increased with increasing deformation. Besides, the ferrite grain size was refined after deformation (Fig. 3.6). For instance, with an increase in stain from 0 to 0.46, the ferrite grain size decreased from 18 to 10 μm (for the same ferrite fraction of about 0.75). This is a result of an increased number of ferrite nuclei, which impinge each other during growth, leading to grain refinement [17]. In addition, the spread of ferrite grain sizes slightly decreased with an increase in reduction (Fig. 3.6). All these behaviours could be explained by the following. The refinement of PAGS leads to an increase in the prior austenite grain boundary area, which can act as ferrite nucleation sites. The dislocation bands induced by deformation are also favourable sites for ferrite formation [2, 17, 39]. However, the dislocation bands were not observed using TEM, due to recrystallisation after deformation, and thus did not play an important role in increasing the number of ferrite nucleation sites. Therefore, the deformation-accelerated ferrite formation was a result of prior austenite grain refinement. With a decrease in T_{IC}, the ferrite fraction increased due to an increased time during cooling available for ferrite nucleation and growth (Fig. 3.4).

Although polygonal ferrite is normally formed in DP steels, a very small amount of Widmänstatten ferrite (Fig. 3.5(a)) was observed in the studied steel. It is probably because the recrystallisation of prior austenite was not completed and Widmänstatten ferrite formation was promoted in remaining coarse austenite grains. Unexpectedly, a significant amount of bainite was observed in association with martensite. In addition, with a decrease in ferrite fraction, the second phase regions became larger. Martensite formation was expected on water quenching, however, the sandwich sample configuration somewhat restricted the water access to the tested sample (Fig. 3.1(c)). Thus, a slower cooling rate in the centre of studied sample could be a reason for bainite transformation. Another course can be associated with the carbon diffusion during austenite transformation. When polygonal ferrite forms, carbon is rejected into austenite. If the transformation time is short, small ferrite fraction forms and the carbon content is lower in remaining austenite, compared to the case when

the transformation time is long and a large fraction of ferrite forms. A decreased carbon content in austenite leads to a decrease in hardenability [40] and formation of more bainite, instead of martensite, in the larger second phase region (Fig. 3.5).

On the other hand, much more ferrite formed near the surfaces of the strip than that in the centre (Fig. 3.2), which was also observed by Killmore *et al.* [8]. As Killmore *et al.* pointed out, the as-cast austenite grain size increased from 120 μm at the surface to 180 μm in the centre of the strip; with an increase in deformation, the recrystallisation process extended from the surface to the centre, resulting in accelerated ferrite formation at the surface [8].

3.4.2 Correlation of mechanical properties with microstructure

YS and UTS increased, while UE and TE decreased, with an increase in deformation and a decrease in ferrite fraction (Fig. 3.12), which also corresponds to an increase in polygonal ferrite hardness with a decrease in ferrite fraction and an increase in deformation (Fig. 3.13(a)). It is normally observed in DP steels [41, 42] and ascribed to an increase in dislocation density in polygonal ferrite [43, 44]. As shown in Fig. 3.10 and Table 3.2, for samples containing ~ 75% ferrite, the dislocation density in polygonal ferrite increased from 4.1 × 1013 to 7.7 × 1013 m-2, with an increase in deformation from 0 to 0.46 reduction. An increase in the amount of deformation creates more defects, resulting in more dislocations [45]. For samples deformed to 0.46 reduction, the dislocation density in polygonal ferrite increased from 7.7× 1013 to 11.0 × 1013 m-2 with a decrease in ferrite fraction from 0.74 to 0.63. This is due to a larger area of polygonal ferrite being affected by martensitic transformation with a decrease in ferrite fraction, resulting in a higher dislocation generation to accommodate the volume change [46]. Fig. 3.16 shows one small polygonal ferrite grain in DL 670, which was significantly influenced by martensitic transformation leading to the generation of higher dislocation density in it (32.7±4.9 × 1013 m-2) compared to that (11.0 × 1013 m-2) in larger ferrite grains shown in Fig. 3.10(c), (f), (i). An increase in dislocation density of polygonal ferrite with the deformation increasing and ferrite fraction decreasing was observed by other researchers [39, 45, 46].

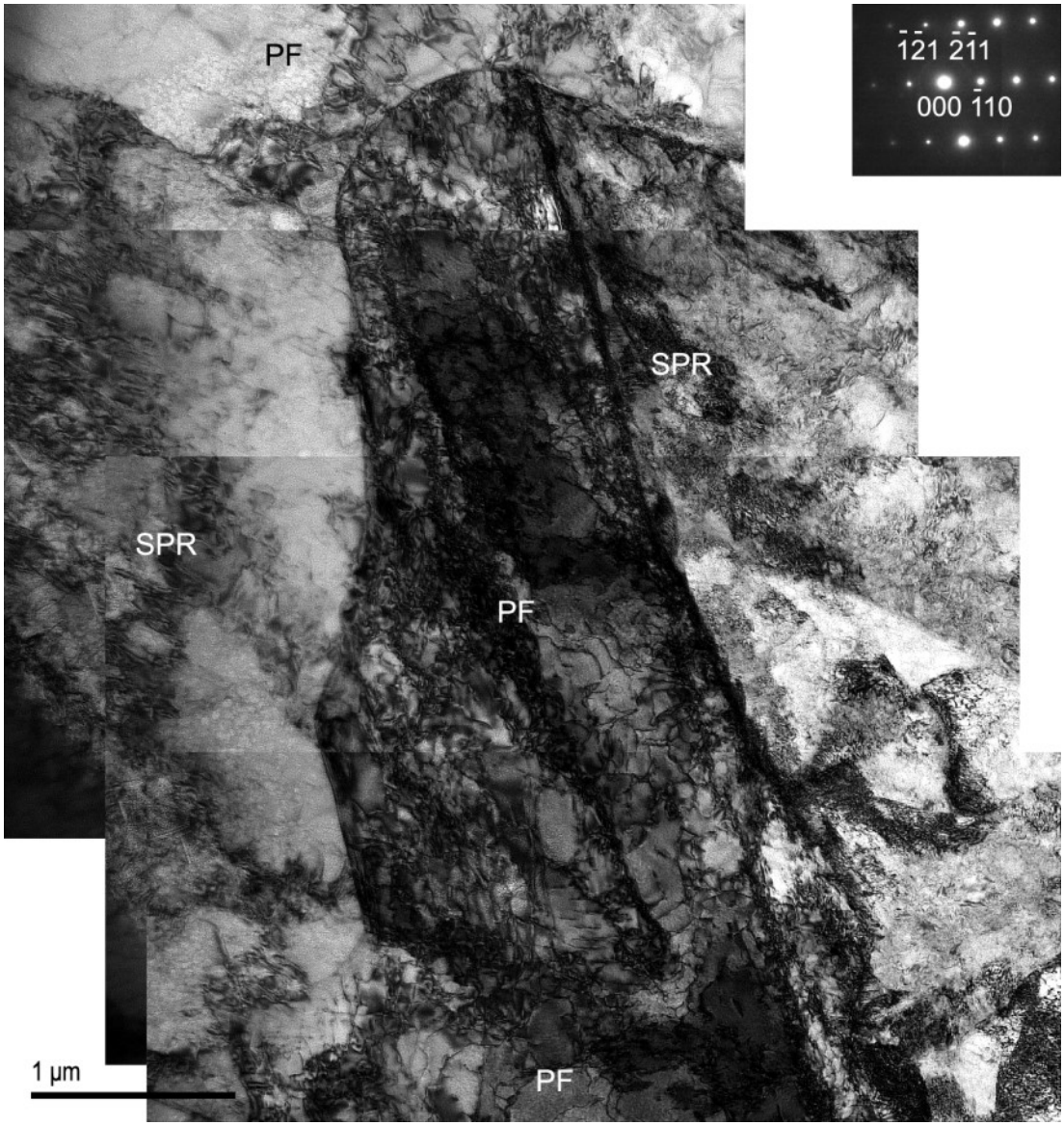

Figure 3.16 A small polygonal ferrite grain in DL 670 sample with relatively high dislocation density sandwiched between two second phase regions. *PF* is polygonal ferrite and *SPR* is second phase region. The zone axis of inset is $[113]_{\alpha}$.

A higher initial dislocation density in polygonal ferrite leads to a higher YS, as the movement of existing dislocations and generation of new dislocations are more difficult and require a higher applied force [47]. During the tensile test, more dislocations piled up near the ferrite-martensite interfaces, which served as strong barriers to their movement. With increasing ferrite fraction, the length of ferrite-martensitic interfaces decreased, leading to a lower UTS. In addition, the refinement of ferrite grain size after deformation also contributed to an increase in YS and UTS [44]. Besides, some bainite, which was observed in the second phase regions instead

of martensite (Figs. 3.5 and 3.9), could reduce the strength and enhance the ductility [33, 41, 48].

Fig. 3.17 illustrates the exponentially decreasing strain hardening rates of samples with different ferrite fractions after different amounts of deformation. For samples with similar ferrite fraction (Fig. 3.17(a) and (b)), heavier deformed sample exhibited a higher initial strain hardening rate. With an increase in true strain, the strain hardening rate decreased more quickly for the heavier deformed sample. For samples deformed to the same reduction (Fig. 3.17(c)), the sample having a higher ferrite fraction (0.74) exhibited a lower initial strain hardening rate, although the strain hardening rate decreased slower. It could be explained by the higher initial dislocation density in the sample subjected to a higher deformation or having a lower ferrite fraction. The initial strain hardening rate was higher for samples with increased initial dislocation density due to an earlier dislocation immobilisation and pile-up [30, 47, 49]. As strain hardening continued, the strain hardening rate decreased more quickly in samples with a higher initial dislocation density, compared to that with a lower dislocation density (c.f. DP 50 and DL 650 in Fig. 3.17(a); c.f. DP 30 and DL 690 in Fig. 3.17(b); c.f. DL 650, DL 670 and DL 690 in Fig. 3.17(c)). It could be explained by a decrease in mean free path for dislocation movement with an increase in dislocation density. As a result, an earlier necking and lower elongation were observed in the samples with initial higher dislocation densities. In addition, the Widmänstatten ferrite probably contributed to an increase in strength and a decrease in elongation, because of a higher dislocation density in it compared to that in polygonal ferrite (Fig. 3.8).

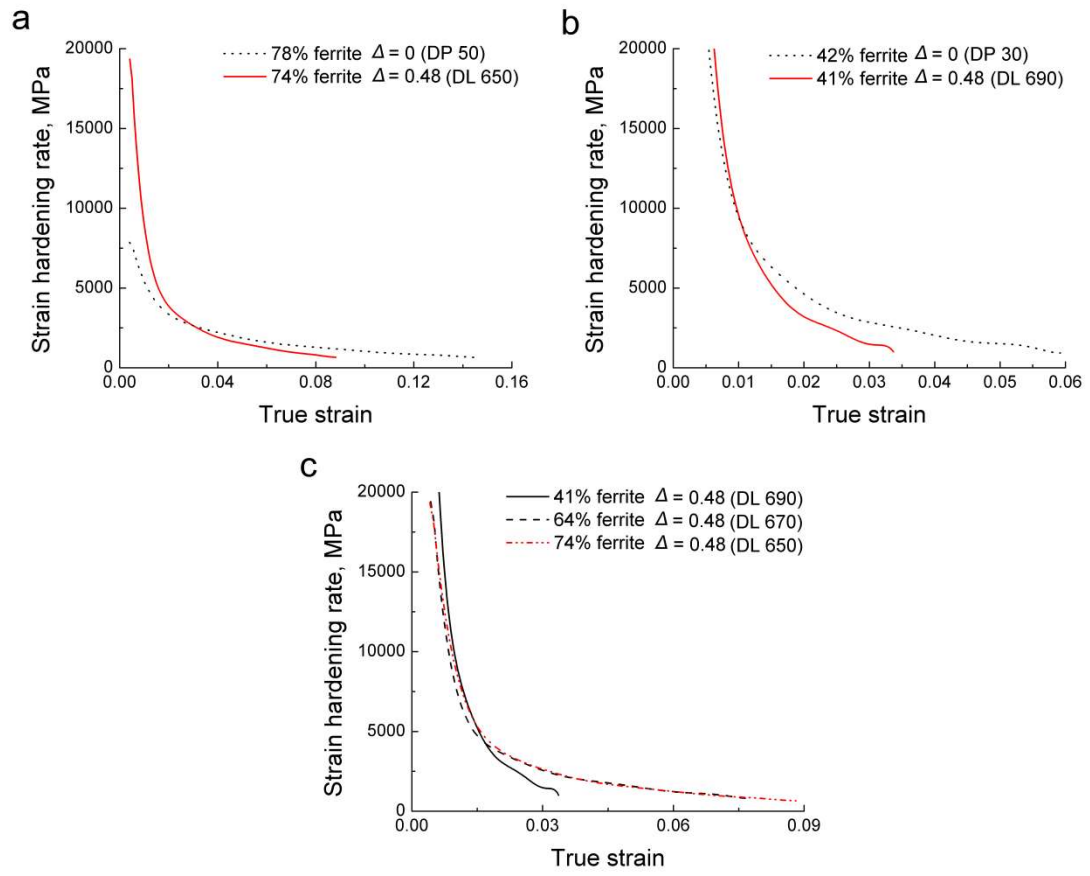

Figure 3.17 Strain hardening rate vs true strain for various samples showing: effect of deformation for (a) DL 650 and DP 50 samples with a similar ferrite fraction of around 0.75 and for (b) DL 690 and DP 30 samples with a similar ferrite fraction of around 0.41; effect of ferrite fraction for (c) DL 650, DL 670 and DL 690 samples subjected to the same reduction of 0.46.

Fig. 3.18 shows the comparison of mechanical properties between the studied samples and DP steels from ArcelorMittal Company's brochure [50]. The DL 650 sample (74% ferrite) had comparable mechanical properties with cold rolled and annealed or hot rolled DP steels. But with a decrease in ferrite fraction, DL 670 and DL 690 samples exhibited much worse mechanical properties (lower strength and elongation). It can be a result of the microstructure inhomogeneity (Figs. 3.2 and 3.3) and a coarser ferrite grain size (Table 3.1 and Fig. 3.6). With a decrease in deformation from 0.46 to 0.17, the properties degraded further in DS 650 due to a lower density of dislocations and a coarser grain size.

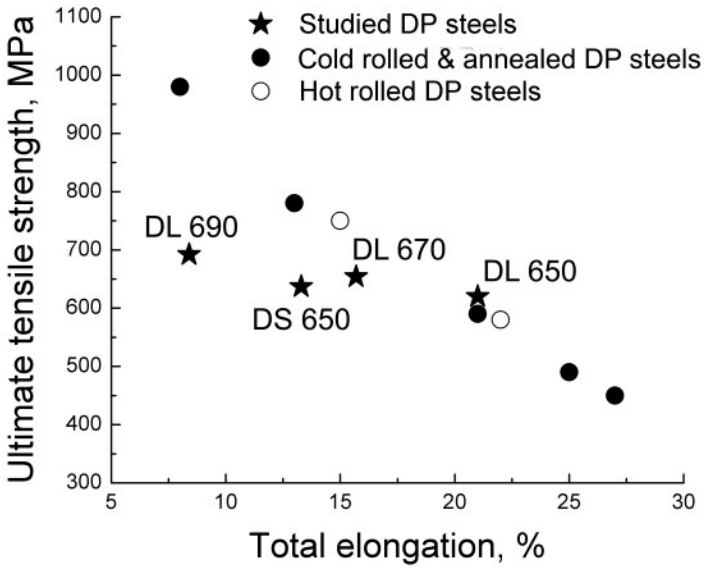

Figure 3.18 Comparison of mechanical properties between the studied steels and DP steels from Arcelormittal Company's brochure [45].

The controlled hot rolling in industry includes high temperature deformation in the recrystallisation region followed by a heavy deformation in non-recrystallisation region [12]. At present, there is only one rolling stand in strip casting process [5, 8]. Thus, only one deformation in recrystallisation temperature region was carried out in this work. If in the future, the further development of strip casting process results in availability of two-stand rolling, then the production of a wider range of DP steel grades may become possible.

3.4.3 The contribution to strengthening due to deformation

Strengthening in high strength low alloyed (HSLA) steels is usually ascribed to lattice friction, solid solution, precipitation, grain boundaries and dislocation [51, 52]. As the YS for dual phase steel is determined by polygonal ferrite [42], and the studied DP steels all had second phase regions embedded in polygonal ferrite (Figs. 3.2 and 3.3), the effect of second phases on YS is ignored in this discussion. Precipitation strengthening is not considered due to the absence of precipitates proven by the TEM observations. The solid solution strengthening was assumed to be the same between deformed and non-deformed samples, as the chemical composition was the same. Based on the experimental evidence presented, the main

microstructural changes observed in ferrite of differently processed samples were dislocation density and grain size. Thus, the difference in YS values between conditions arises due to dislocation strengthening and grain boundary strengthening (grain size refinement). To correlate the microstructure and YS, the structure-based strength calculation models were used. Bailey – Hirsch relationship was used to characterise the dislocation strengthening as follows [51, 53]:

$$\sigma_{dis} = M\alpha Gb\rho^{1/2} \tag{3.5}$$

where M is the Taylor factor (M = 0.275 for random textured bcc metals), α is a constant (α = 0.38 in bcc iron), G is shear modulus (G = 81.6 GPa), b is the Burgers vector (b = 0.248) and ρ is the average dislocation density in polygonal ferrite. The grain boundary strengthening was calculated as follows [51]:

$$\sigma_{gb} = 210 d_{\theta>2^\circ}^{-1/2} \tag{3.6}$$

$d_{\theta>2^\circ}$ in μm is the average spacing between >2° boundaries above.

The weighted average of dislocation density (Table 3.2) was used in Eq. 3.5, while the average grain size of polygonal ferrite was used as $d_{\theta>2^\circ}$ in Eq. 3.6. Table 3.4 lists contributions of the dislocation and grain boundary strengthening to the YS. As can be seen, the difference between the measured YS for DL 670 and DL 650 samples was 44 MPa, which is higher than 36 MPa of the calculated difference in grain boundary and dislocation strengthening contributions. Similarly, the difference between the measured YS values for DL 650 and DP 50 sample was 138 MPa, which is higher than 108 MPa of the calculated difference in grain boundary and dislocation strengthening contributions. There may be two major reasons for that: (1) in Eq.3.7 instead of $d_{\theta>2^\circ}$ the average ferrite grain size was used; as the ferrite grain size is larger than the distance between the >2° angle boundaries, the grain boundary strengthening contribution could be underestimated; and (ii) the second phase contributions vary with processing conditions. For deformed samples DL 650 and DL 670, other strengthening contributions were similar. However, these contributions were higher in DL 650 compared to DP 50 sample, although the ferrite fraction was the same. This was probably due to the variation in the second phase type. In addition, YS is not simply the sum of values contributed from different strengthening mechanisms [51, 52, 54], interactions between various microstructural

features should be taken into account. As a conclusion, the dislocation strengthening and grain boundary strengthening can be considered as the main strengthening mechanisms contributing to the YS increase after deformation.

Table 3.4 The comparison of experimental and calculated strength.

	Yield stress, MPa	Dislocation strengthening σ_{dis}, MPa	Grain boundary strengthening σ_{gb}, MPa	$\sigma_{dis} + \sigma_{gb}$	Other strengthening mechanisms, MPa
DP 50	295±21	97	47	144	151
DL 650	433±12	186	66	252	181
DL 670	477±11	222	66	288	189
The difference, MPa					
DL 650 – DP 50	138	89	19	108	30
DL 670 – DL 650	44	36	0	36	8

3.5 Conclusions

Conventional dual phase (DP) steel (0.08C-0.81Si-1.47Mn-0.03Al wt. %) was processed using a Gleeble 3500 thermo-mechanical simulator according to a strip casting schedule. The following conclusions were drawn from observations of microstructure and mechanical behaviour.

(1) DP steel microstructures with 40 - 80 % ferrite were obtained using the proposed processing schedules. The second phases consisted of martensite, bainite and very small amount of Widmanstätten ferrite.

(2) Ferrite fraction increased with a decrease in interrupted cooling temperature and an increase in the amount of deformation. Refinement of both ferrite grain size and the size of second phase regions occurred following the deformation, as a result of static recrystallisation and an increased prior austenite grain boundary area leading to an increase in number of ferrite nucleation sites.

(3) The ultimate tensile strength increased from 621 to 692 MPa, while the total elongation decreased from 0.21 to 0.08, with a decrease in ferrite fraction from 0.74 to 0.41.The extent of ductile fracture decreased with a decrease in ferrite fraction. These can be explained by an increase in dislocation density of ferrite, ferrite grain size, and the amount of hard phases with a decrease in ferrite fraction.

(4) For the samples having ~ 75% ferrite, the dislocation density increased from 2.1 to 7.7 $\times 10^{13}$ m^{-2} when the deformation increased from 0 to 0.46 reduction. For the samples deformed to 0.46 reduction, the dislocation density increased from 7.7 to 11.0 $\times 10^{13}$ m^{-2} with an increase in ferrite fraction from 0.63 to 0.74. For the sample having lower ferrite fraction or deformed to a higher reduction, the initial strain hardening rate was larger and decreased more rapidly, as a result of a higher initial dislocation density.

(5) The microstructure was more homogeneous for higher ferrite fraction conditions. Only the mechanical properties of studied steel with the largest ferrite fraction were comparable to those of the industrial products.

Acknowledgements

This project was supported by the Australian Research Council (DP130101887). The JEOL JSM-7001F FEG-SEM was funded by the Australian Research Council (LE0882613). The authors thank Dr. A.A. Gazder for modification of tensile stage and Dr. Liang Chen for the operation of the Gleeble 3500 thermo-mechanical simulator.

References

[1] D.S. Liu, F. Fazeli, M. Militzer, ISIJ Int. 47 (2007) 1789-1798.

[2] S.C. Hong, K.S. Lee, Mater. Sci. Eng. A 323 (2002) 148-159.

[3] M.S. Rashid, Annu. Rev. Mater. Sci. 11 (1981) 245-266.

[4] W. Bleck, D. Hömberg, U. Prahl, P. Suwanpinij, N. Togobytska, Steel Res. Int. 85 (2014) 1328-1333.

[5] N. Zapuskalov, ISIJ Int. 43 (2003) 1115-1127.

[6] D.J. Sosinsky, P. Campbell, R. Mahapatra, W. Blejde, F. Fisher, Metallurgist 52 (2008) 691-699.

[7] S. Ge, M. Isac, R.I.L. Guthrie, ISIJ Int. 52 (2012) 2109-2122.

[8] C. Killmore, H. Creely, A. Phillips, H. Kaul, P. Campbel, M. Schueren, J.G. Williams, W. Blejde, Mater. Forum 32 (2008) 13-24.

[9] A.I. Fernandez, P. Uranga, B. Lopez, J.M. Rodriguez-Ibabe, Mater. Sci. Eng. A 361 (2003) 367-376.

[10] M. Arribas, B. Lopez, J.M. Rodriguez-Ibabe, Mater. Sci. Eng. A 485 (2008) 383-394.

[11] A.B. Cota, C.A.M. Lacerda, F.L.G. Oliveira, F.A. Machado, D. Silva Araújo, Scripta Mater. 51 (2004) 721-725.

[12] M. Olasolo, P. Uranga, J.M. Rodriguez-Ibabe, B. Lopez, Mater. Sci. Eng. A 528 (2011) 2559-2569.

[13] L.X. Du, Z.P. Zhang, G.F. She, X.H. Liu, G.D. Wang, J. Iron Steel Res. Int. 13 (2006) 31-35.

[14] A. Yoshie, H. Morikawa, Y. Onoe, K. Itoh, T. Iron Steel I. Jpn. 27 (1987) 425-431.

[15] T. Kvackaj, I. Mamuzic, ISIJ Int. 38 (1998) 1270-1276.

[16] P. Cizek, B.P. Wynne, C.H.J. Davies, B.C. Muddle, P.D. Hodgson, Metall. Mater. Trans. A 33 (2002) 1331-1349.

[17] N.M. Xiao, M.M. Tong, Y.J. Lan, D.Z. Li, Y.Y. Li, Acta Mater. 54 (2006) 1265-1278.

[18] B. Eghbali, A. Abdollah-Zadeh, J. Mater. Proc. Tech. 180 (2006) 44-48.

[19] H. Niakan, A. Najafizadeh, Mater. Sci. Eng. A 527 (2010) 5410-5414.

[20] W. Tan, B. Han, S.Z. Wang, Y. Yang, C. Zhang, Y.K. Zhang, J. Iron Steel Res. Int. 19 (2012) 37-41.

[21] H. Azizi-Alizamini, M. Militzer, W.J. Poole, ISIJ Int. 51 (2011) 958-964.

[22] M. Calcagnotto, D. Ponge, D. Raabe, ISIJ Int. 48 (2008) 1096-1101.

[23] K. Mukherjee, S.S. Hazra, M. Militzer, Metall. Mater. Trans. A 40 (2009) 2145-2159.

[24] Z.P. Xiong, A.G. Kostryzhev, N.E. Stanford, E.V. Pereloma, Mater. Design 88 (2015) 537-549.

[25] H.Y. Gao, Z.X. Xie, Y. Yu, Y. Fang, J. Wang, B.D. Sun, ISIJ Int. 49 (2009) 546-552.

[26] K. Mukunthan, P.D. Hodgson, P. Sellamuthu, L. Strezov, Y. Durandet, N. Stanford, ISIJ Int. 53 (2013) 1803-1811.

[27] I.B. Timokhina, P.D. Hodgson, E.V. Pereloma, Metall. Mater. Trans. A 38A (2007) 2442-2454.

[28] L. Cheng, K.M. Wu, X.L. Wan, R. Wei, Mater. Charact. 87 (2014) 86-94.

[29] K. Park, M. Nishiyama, N. Nakada, T. Tsuchiyama, S. Takaki, Mater. Sci. Eng. A 604 (2014) 135-141.

[30] Z.Z. Zhao, T.T. Tong, J.H. Liang, H.X. Yin, A.M. Zhao, D. Tang, Mater. Sci. Eng. A 618 (2014) 182-188.

[31] E. Fereiduni, S.S.G. Banadkouki, J. Alloy Compd. 577 (2013) 351-359.

[32] Y. Mazaheri, A. Kermanpur, A. Najafizadeh, Mater. Sci. Eng. A 619 (2014) 1-11.

[33] N. Saeidi, A. Ekrami, Mater. Sci. Eng. A 523 (2009) 125-129.

[34] S. Vervynckt, K. Verbeken, B. Lopez, J.J. Jonas, Int. Mater. Rev. 57 (2012) 187-207.

[35] S.M.K. Hosseini, A. Zarei-Hanzaki, E. Essadiqi, S. Yue, Mater. Sci. Tech. 24 (2008) 1354-1361.

[36] J. Gautam, A. Miroux, J. Moerman, C. Barbatti, P. van Liempt, L.A.I. Kestens, Mater. Sci. Forum 706-709 (2012) 2722-2727.

[37] Z.X. Xie, H.Y. Gao, J. Wang, Y. Yu, Y.A. Fang, B.D. Sun, J. Iron Steel Res. Int. 18 (2011) 45-51.

[38] Y.W. Xu, D. Tang, Y. Song, X.G. Pan, Mater. Design 36 (2012) 275-278.

[39] V.M. Khlestov, E.V. Konopleva, H.J. McQueen, Can. Metall. Quart. 37 (1998) 75-89.

[40] M. Zhang, Y.H. Wang, C.L. Zheng, F.C. Zhang, T.S. Wang, Mater. Sci. Eng. A 596 (2014) 9-14.
[41] A. Kumar, S.B. Singh, K.K. Ray, Mater. Sci. Eng. A 474 (2008) 270-282.
[42] M.D. Taylor, K.S. Choi, X. Sun, D.K. Matlock, C.E. Packard, L. Xu, E. Barlat, Mater. Sci. Eng. A 597 (2014) 431-439.
[43] A. Rizk, D.L. Bourell, Scripta Metall. Mater. 16 (1982) 1321-1324.
[44] Z.G. Jiang, J.K. Liu, J.H. Lian, Acta Metall. Mater. 40 (1992) 1587-1597.
[45] Z.D. Li, Z.G. Yang, C. Zhang, Z.Q. Liu, Mater. Sci. Eng. A 527 (2010) 4406-4411.
[46] M. Calcagnotto, D. Ponge, E. Demir, D. Raabe, Mater. Sci. Eng. A 527 (2010) 2738-2746.
[47] Z.H. Jiang, Z.Z. Guan, J.S. Lian, Mater. Sci. Eng. A 190 (1995) 55-64.
[48] A. Ramazani, P.T. Pinard, S. Richter, A. Schwedt, U. Prahl, Comp. Mater. Sci. 80 (2013) 134-141.
[49] M. Asadi, B.C. De Cooman, H. Palkowski, Mater. Sci. Eng. A 538 (2012) 42-52.
[50] http://automotive.arcelormittal.com/europe/products/AHSS/EN.
[51] N. Kamikawa, K. Sato, G. Miyamoto, M. Murayama, N. Sekido, K. Tsuzaki, T. Furuhara, Acta Mater. 83 (2015) 383-396.
[52] Y. Mazaheri, A. Kermanpur, A. Najafizadeh, ISIJ Int. 55 (2015) 218-226.
[53] J.E. Bailey, P.B. Hirsch, Philos. Mag. 5 (1960) 485-497.
[54] E. Hornbogen, E.A. Starke Jr, Acta Metall. Mater. 41 (1993) 1-16.

CHAPTER 4 STRAIN-INDUCED FERRITE FORAMTION AND ITS EFFECT ON MECHANICAL PROPERTIES OF A STRIP CAST DUAL PHASE STEEL

Z.P. Xiong[1*], A.A. Saleh[1], A.G. Kostryzhev[1], E.V. Pereloma[1, 2]

[1]*School of Mechanical, Materials and Mechatronic Engineering, University of Wollongong, Wollongong, NSW 2522, Australia*

[2]*Electron Microscopy Centre, University of Wollongong, Wollongong, NSW 2519, Australia*

Abstract: Thermo-mechanical processing of a strip cast dual phase (DP) steel was carried out using a Gleeble thermo-mechanical simulator. The effect of deformation temperatures in the range from 1050 to 700 °C on the microstructure evolution was investigated using optical, scanning and transmission electron microscopy along with electron backscattering diffraction (EBSD). Strain-induced ferrite (SIF) formation was observed following austenite deformation (~ 0.41 reduction) in the 800 – 700 °C temperature range, leading to a ferrite grain refinement down to 3.1±2.3 μm. A novel segmentation procedure was applied to separate selected EBSD maps into polygonal ferrite, SIF and second phase regions (bainite/martensite). Following this, the microtexture, misorientation angle distribution and the deviation from the Kurdjumov–Sachs and Nishiyama–Wasserman orientation relationships of each microstructure constituent were analysed. Based on iso-work modelling analysis of tensile stress-strain curves, the SIF was found to enhance strength with a slight decrease in ductility compared to polygonal ferrite. The tensile mechanical properties after deformation at 750 °C reached the level of DP 600 produced in industry, highlighting the potential to manufacture DP steels via the strip casting technique.

Keywords: Dual phase steel; Deformation temperature; Strain-induced ferrite; Diffusional transformation; EBSD.

4.1 Introduction

Dual phase (DP) steels are widely studied because of their simultaneously high strength and ductility, which satisfy the requirement of car weight reduction and fuel saving in the automotive industry [1-3]. DP steels are typically produced commercially via hot rolling and cold rolling followed by annealing [1, 2]. Another potentially competitive technology for commercial production of DP steels is the strip casting process, wherein strips are directly obtained from molten metal, followed by a subsequent rolling [4-6]. In this regard, the strip casting process has been successfully used for *industrial* production of carbon steels, stainless steels and silicon steels [6, 7] as well as *laboratory* production of twinning-induced plasticity steel [8]. In addition, the present authors have undertaken laboratory scale trials to produce transformation-induced plasticity steel [9, 10] and DP steel [11, 12], and their microstructures and mechanical properties were analysed in detail. According to the results published so far, the coarse prior austenite grain size (PAGS) remains a primary challenge on the way of obtaining optimal mechanical properties via the strip casting technology [6].

Thermo-mechanical controlled processing (TMCP) is widely used in steel industry to tune and refine microstructures with deformation temperature being one of the key parameters in this process. Deformation above non-recrystallisation temperature (T_{nr}) leads to austenite recrystallisation and in turn an increase in the number of polygonal ferrite nucleation sites, resulting in microstructure refinement [13, 14]. When the deformation temperature is below T_{nr}, the microstructure is further refined due to the increased number of polygonal ferrite nucleation sites in the interior of the pancaked austenite grains [15, 16]. However, most commonly applied TMCP schedules can only achieve a minimum grain size of ~ 5 μm for carbon and alloyed steels [17, 18].

Alternatively, advanced TMCP, such as strain-induced ferrite (SIF) formation, provides the possibility to reduce the grain size down to ~ 1 μm [19, 20]. Therefore, it is attractive for future applications as it can be utilised for mass production on currently available industrial facilities or after minor modifications. When the deformation temperature is in the range from austenite-to-ferrite transformation start temperature (Ar_3) to (Ar_3 + 100) °C, SIF transformation reduces the average ferrite

grain size (considering both polygonal ferrite and SIF) to 1 μm [20-22]. Hurley *et al.* [18, 23, 24] and Beladi *et al.* [17] produced low carbon steels (0.0022 – 0.17 wt. % C) with fine-grained SIF, resulting in an average ferrite grain size of 1 – 3 μm. Karmakar *et al.* [22] and Mukherjee *et al.* [25] also successfully produced DP steels with an average ferrite grain size of ~ 1.5 μm by the application of SIF transformation.

The effects of deformation temperature, strain, strain rate and PAGS on SIF formation was systematically studied for DP steels [22, 25, 26]. SIF was found to preferentially nucleate along prior austenite grain boundaries, with in-grain nucleation promoted by a decrease in deformation temperature and an increase in strain, leading to more nucleation sites for SIF. Increasing the strain rate also increases the SIF nucleation sites, but reduces the time for its growth. Here increasing the SIF nucleation sites leads to a finer average ferrite grain size.

Despite all the above studies, the SIF transformation mechanism is not fully clarified yet due to the complexities associated with its rapid formation during deformation and its subsequent evolution during cooling to room temperature [18, 27, 28]. For deformation temperatures between Ar_3 and the equilibrium austenite-to-ferrite transformation start temperature (Ae_3), SIF formation was successfully simulated as *diffusional* transformation process in a 0.13 C-0.19Si-0.49Mn steel (wt. %), using the classical theory of ferrite nucleation and grain growth controlled by carbon diffusion [28, 29]. Alternatively, for deformation temperatures above the Ae_3, SIF formation was suggested to occur via a *diffusionless* transformation accompanied with carbon diffusion during or after its growth in 0.06 – 0.79 C microalloyed steels (wt. %) [27]. A *massive* transformation was also suggested for SIF formation in steels having a very low carbon content (0.0008 wt. %) [30].

To this end, the present work investigates the effect of deformation temperature on ferrite formation during TMCP of strip cast DP steel using optical (OM), scanning (SEM) and transmission (TEM) electron microscopy, along with electron backscattering diffraction (EBSD). For the first time, ferrite grain refinement (~ 3 μm) was achieved via SIF formation in strip cast DP steel. Mechanical properties

measured using tensile testing were comparable to commercially produced DP 600 steel. A novel segmentation procedure was developed to separate the EBSD maps into polygonal ferrite, SIF and second phase regions (bainite/martensite). The analysis of misorientation angle distributions, deviations from the Kurdjumov–Sachs (K–S) and Nishiyama–Wasserman (N–W) orientation relationships (ORs), and dislocation substructures of different microstructure constituents indicates a higher probability of SIF formation via a *diffusional* transformation mechanism rather than *diffusionless* transformation.

4.2 Experimental details

Chemical composition of the studied steel was similar to conventional DP steels [1, 2] and contained 0.077 C, 0.81 Si, 1.47 Mn, 0.03 Al, 0.01 Cu, 0.23 Cr (wt. %) and balance Fe. As-cast specimens of 36 × 36 mm^2 in plane and 1.2 mm thick were produced at Deakin University using dip tester [31]. A copper substrate was immersed into molten steel for a short and controlled period of time, and then immediately lifted out to simulate the rapid solidification when liquid steel contacts the twin rolls [5].

The processing schedules shown in Fig. 4.1 were carried out using a Gleeble 3500 thermo-mechanical simulator. Samples with 20 × 15 mm^2 in plane and ~ 1 mm thick were cut from as-cast specimens. As the sample thickness was below the movement control capability of the Gleeble simulator, the investigated samples were sandwiched between two blocks of dummy samples (20 × 15 × 2.5 mm^3; made of structural microalloyed steel) as shown in Fig. 1.12. The samples were heated at 40 Ks^{-1} to 1000 °C to prevent any precipitation, then continuously heated at 20 Ks^{-1} to 1300 °C in order to avoid temperature overshooting. Holding at 1300 °C for 180 s was employed to simulate the PAGS (117±44 μm) resulting from dip casting [12]. After austenitisation, the samples were cooled at 30 Ks^{-1} to the deformation temperatures, T_D ranging from 1050 to 700 °C, where deformation to ~ 0.41 reduction was applied at a strain rate of 0.5 s^{-1}. This was followed by cooling at 10 Ks^{-1} to 670 °C and water quenching to room temperature. At a cooling rate of 30 Ks^{-1} without prior deformation the Ar_3 was 695 °C [12]. Based on our previous study [11], cooling to 670 °C is expected to result in 0.5 – 0.9 ferrite fraction depending on the deformation temperature. Hereafter, the samples deformed at 700, 750, 800, 850, 950

and 1050 °C are referred to as DT 700, DT 750, DT 800, DT 850, DT 950 and DT 1050, respectively.

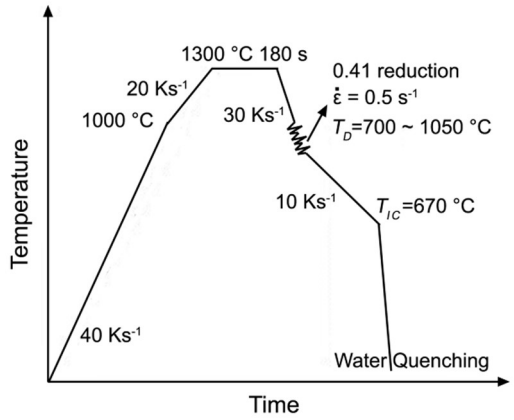

Figure 4.1 Schematic diagrams of thermo-mechanical schedules.

Since our thermo-mechanical processing simulates plain strain compression during hot rolling, the rolling convention (Fig. 1.12) is used throughout the text such that the compression direction is parallel to the normal direction (ND) and the samples extended along the rolling direction (RD) and were constrained along the transverse direction (TD). For microstructure characterisation, the deformed samples were cut parallel to the RD–ND plane. After hot mounting and standard mechanical polishing, the samples were etched using 2 vol. % nital. The centre of the cross-section was investigated using a Leica DMR research optical microscope and a JEOL JSM-7001F field emission gun (FEG) – SEM. Fractions of phases were calculated based on pixel counts of different grey scales using Image Pro-Plus and Photoshop software. The equivalent circle diameter (ECD) was calculated using at least 260 ferrite grains or second phase regions in optical micrographs.

EBSD and TEM were conducted on selected samples, namely the DT 750, DT 800 and DT 850 samples. After polishing to the colloidal silica stage, EBSD was undertaken on the same JEOL JSM-7001F FEG – SEM, operating at 15 kV accelerating voltage, 5.1 nA probe current and a working distance of 12 mm. A step size of 0.1 μm was used to map an area of 180 × 240 μm^2. The maps returned an overall indexing rate of ~ 98% and were further processed using the Oxford Instruments Channel-5 software package. Any potential wild orientation spikes were first eliminated then cyclic extrapolation from 8 to 6 neighbours filled in zero

solutions. In all maps, subgrain/grain structures were reconstructed using 2° as the minimum misorientation angle and a minimum spatial resolution of 3 pixels was also maintained constant. Misorientation angles (θ) within the range $2° \leq \theta < 15°$ are defined as low angle grain boundaries (LAGBs), whereas $\theta \geq 15°$ denotes high angle grain boundaries (HAGBs). Σ3 boundaries are defined using the ⟨111⟩ 60° axis-angle relationship via the Palumbo–Aust criterion (i.e., $\Delta\theta \leq 15° \Sigma^{-5/6}$ with a tolerance limit $\Delta\theta = 6°$) [32]. Average grain size and subgrain size were determined via the equivalent circle diameter method using boundary identification angles of 15° and 2°, respectively, and a fixed critical boundary completion angle of 2°.

Since the microstructures of the DT 750, DT 800 and DT 850 samples generally comprised polygonal ferrite, SIF and second phase regions (bainite and martensite), all of which display the body-centred cubic (bcc) crystal lattice, the following procedure was developed to segment the EBSD maps. Firstly, a mean angular deviation (MAD) criterion was applied to separate the second phase regions from the total ferrite fraction (comprising polygonal ferrite and SIF). MAD is the average angular misfit (in degrees) between detected and simulated Kikuchi bands and is a measure of the goodness of fit. Here the second phase regions exhibit higher MAD values due to the elastically distorted lattices and higher density of crystalline defects in bainite or martensite compared to ferrite. Consequently, a MAD threshold value of 0.15° was used such that higher values correspond to the second phase regions. Secondly, a subgrain/grain size criterion was applied to separate the total ferrite fraction into polygonal ferrite and SIF. Here, and only for the purpose of segmenting the total ferrite fraction, the boundary identification angle was kept at 2°, while the critical subgrain boundary completion angle was reduced from 2° to 0.5°. Reducing the boundary completion angle ensures full delineation of the individual subgrains of SIF. Then a subgrain size threshold of 4 μm was used such that smaller values correspond to the SIF fraction.

Following phase segmentation, a Matlab code based on the MTex toolbox [33] was written to calculate the angular deviation from the ideal K–S and N–W ORs for each microstructure constituent in the DT 750 map. Firstly, the misorientation angles/axes were calculated between each two neighbouring grains (for polygonal ferrite and SIF)

or martensitic/bainitic laths (in the second phase regions). Subsequently, the calculated misorientation angles/axes were compared with the inter-variant misorientation angles/axes of the 24 possible variants of the K–S OR [34] and the 12 possible variants of the N–W OR [35]. The minimum angular deviation value out of the resultant set of solutions was assigned to the grain/lath under consideration. A more detailed description of this approach was given in Ref. [36].

In order to obtain more statistically representative texture information, an additional set of larger maps (547 × 602 μm^2) were acquired on the DT 750, DT 800 and DT 850 samples using a step size of 0.5 μm. The orientation distribution functions (ODFs) (ϕ_2 = 0° and 45° sections) of the small and large maps are depicted using Bunge's notation after exporting EBSD data to the JTex software [37].

For TEM analysis, 3 mm diameter discs were cut through ND direction (Fig. 1.12) and then mechanically polished to 80 μm thickness. After this, thin foils were prepared using twin-jet electropolishing with an electrolyte containing 10 vol.% perchloric acid in methanol. Bright-field imaging and selected area electron diffraction were undertaken on a JEOL 2011 TEM operating at 200 kV.

Dog-bone tensile samples were cut from the RD–TD plane (Fig. 1.12) with 4.9 mm gauge length (parallel to TD) and 2.1 mm width (parallel to RD). An in-house modified Kammrath and Weiss GmbH tensile stage was used to carry out the tensile tests at a constant speed of 2 $\mu m s^{-1}$, which corresponds to an initial strain rate of 4 $\times 10^{-4}$ s^{-1}. At least, two samples were tested for each condition.

4.3 Results

4.3.1 The effect of deformation temperature on microstructure evolution

Optical and scanning electron micrographs after deformation at different temperatures are shown in Figs. 4.2 and 4.3, respectively. After deformation at 1050 °C (DT 1050 sample), both ferrite and the second phase regions generally exhibited a polygonal shape. The second phase regions consisted of martensite and bainite (Fig. 4.3(a)), with some interspersed ferrite (Fig. 4.3(b)). For deformation

temperatures below 1050 °C, the second phase regions became elongated. A higher ferrite fraction was observed in the near-surface regions compared to the centre of the samples (Fig. 4.2) probably due to the through-thickness strain gradient [6]. Deformation at 800, 750 and 700 °C resulted in some patches indicated by arrows in Figs. 4.2(d, e, f), which were identified to be SIF grains. This is more clearly demonstrated in Figs. 4.3(d, e, f, g). After deformation at 800 °C (DT 800 sample), only a small fraction of SIF (0.04±0.01, as estimated from optical micrographs) was observed (Fig. 4.3(d)). With a decrease in the deformation temperature to 750 °C (DT 750 sample), the fraction of SIF increased significantly to 0.18±0.03. With further decrease in the deformation temperature to 700 °C (DT 700 sample), the fraction of SIF decreased to 0.03±0.01. Some Widmänstatten ferrite was also observed at 700 °C as indicated by the arrow in Fig. 4.3(h).

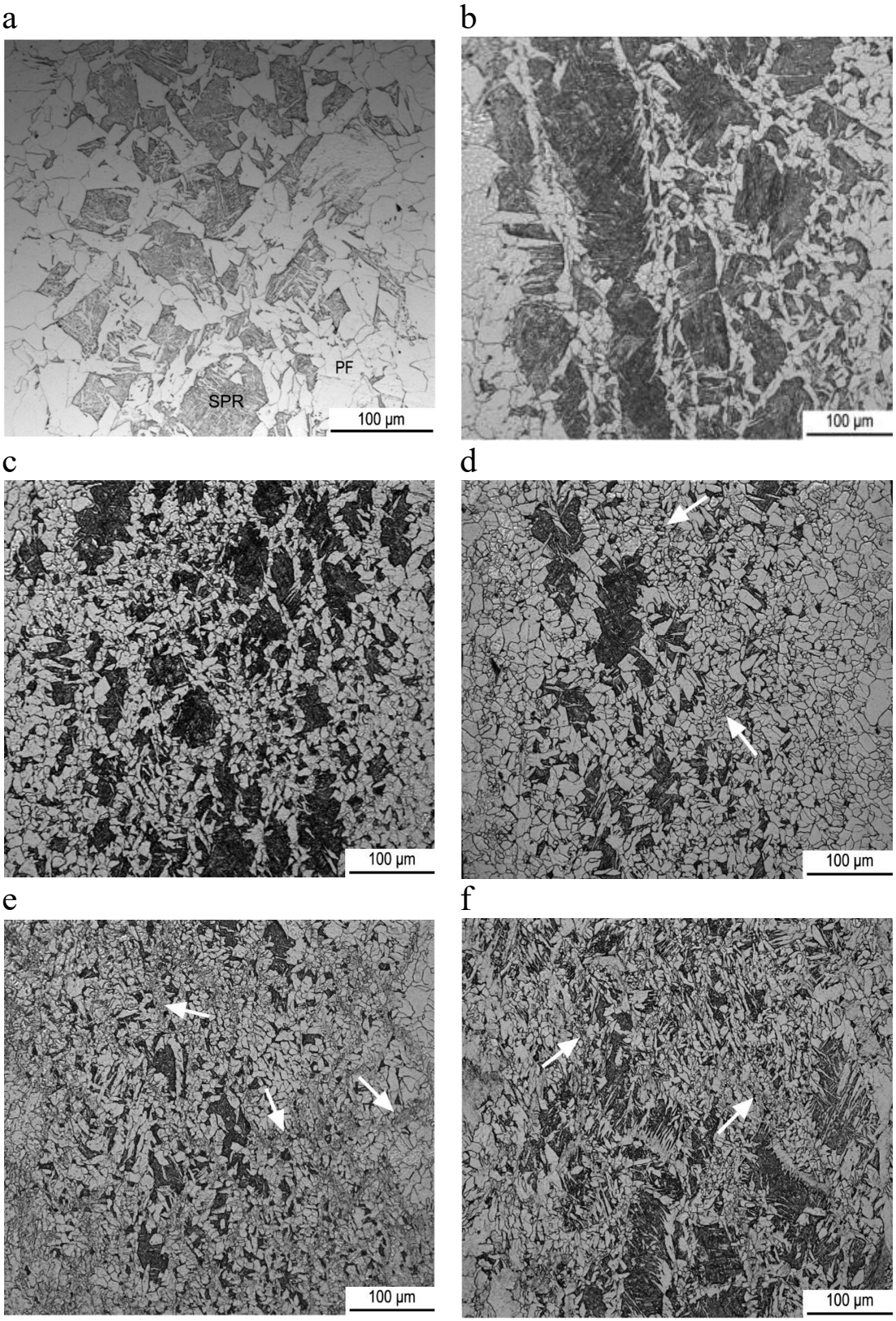

Figure 4.2 Optical images of (a) DT 1050, (b) DT 950, (c) DT 850, (d) DT 800, (e) DT 750 and (f) DT 700 samples. The ND and RD directions are respectively horizontal and vertical. *PF* is polygonal ferrite, *SPR* is second phase region.

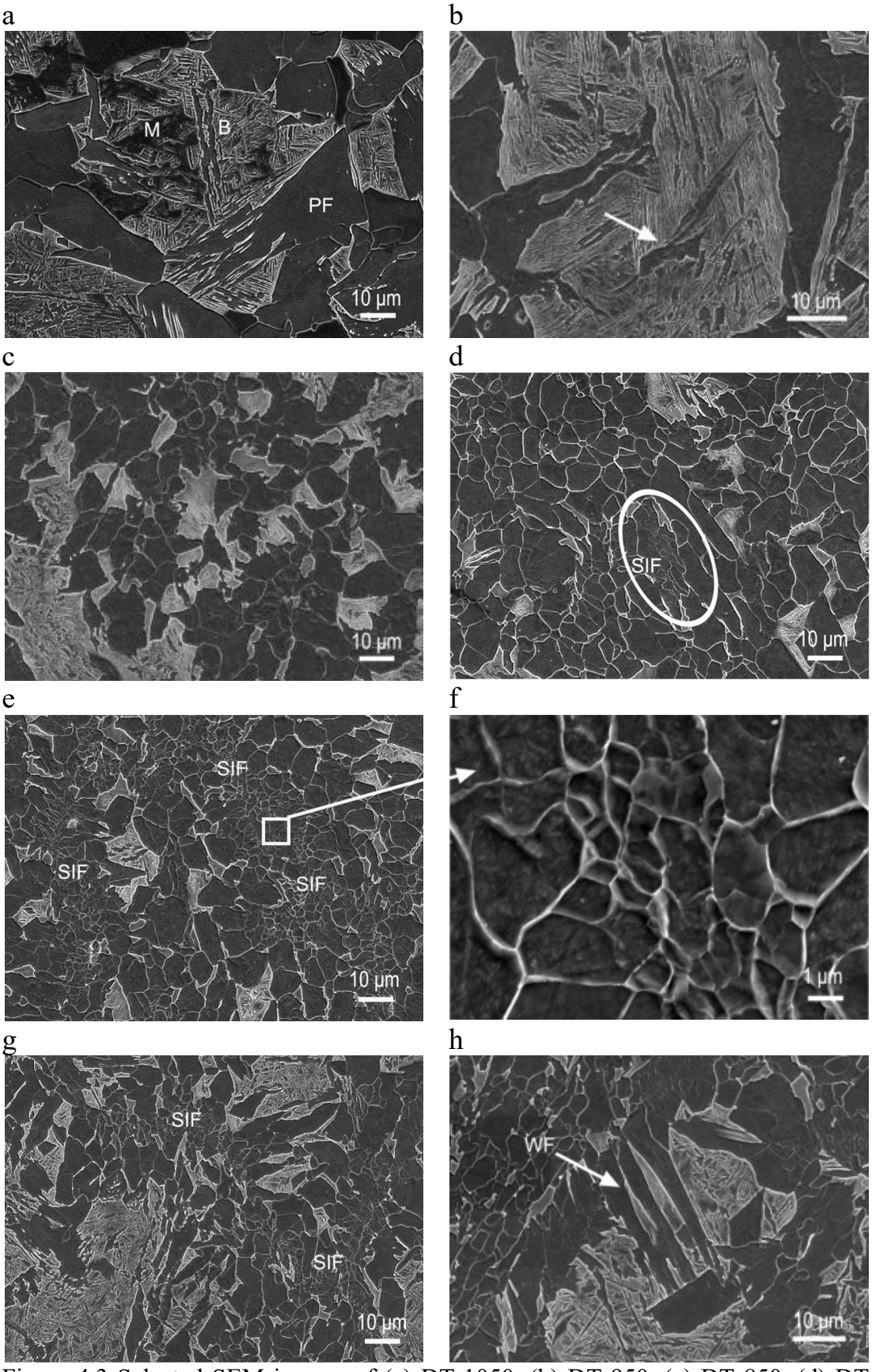

Figure 4.3 Selected SEM images of (a) DT 1050, (b) DT 950, (c) DT 850, (d) DT 800, (e, f) DT 750, and (g, h) DT 700 samples. *PF* is polygonal ferrite, *B* is bainite, *M* is martensite, *SIF* is strain-induced ferrite and *WF* is Widmänstatten ferrite.

As seen from Table 4.1 and Fig. 4.4(a), when deformation temperature decreased from 1050 to 950 °C, the ferrite fraction decreased from 0.63 to 0.53. With a further decrease in the deformation temperature to 750 °C, the ferrite fraction increased to a maximum of 0.81, which subsequently decreased to 0.7 after deformation at 700 °C. The average ferrite grain size showed a maximum of 11.9±7.7 μm at 950 °C and a minimum of 3.1±2.3 μm at 750 °C (Fig. 4.4(b)). The average grain size of SIF exhibited a similar trend to polygonal ferrite with a minimum of 2.1±0.9 μm after deformation at 750 °C (Table 4.1). The average size of second phase region decreased from 20.0±18.0 to 5.5±4.3 μm when the deformation temperature decreased from 1050 to 750 °C (Fig. 4.4(b) and Table 4.1). Then the average second phase region size increased to 6.6±8.2 μm with a decrease in deformation temperature to 700 °C. In addition, the largest size of the ferrite and second phase region tended to decline from 66 to 26 μm and 179 to 44 μm, respectively, with a decrease in deformation temperature from 1050 to 750 °C. This indicates that the microstructure tends to become more uniform with decreasing deformation temperature. However, a further decrease in the deformation temperature to 700 °C led to a significant increase in the maximum sizes of ferrite and second phase regions due to a decrease in polygonal ferrite fraction.

Table 4.1 Summary of microstructure statistics.

	Ferrite fraction	Average size, μm		Maximum size, μm		Average size, μm	
		Ferrite	Second phase region	Ferrite	Second phase region	Polygonal ferrite	Strain-induced ferrite
DT 1050	0.63±0.01	10.2±9.8	20.0±18.0	66	74	--	--
DT 950	0.53±0.02	11.9±7.7	13.0±18.8	58	179	--	--
DT 850	0.66±0.01	9.3±5.2	12.0±13.3	37	109	--	--
DT 800	0.78±0.01	7.4±4.4	7.8±8.0	37	87	8.9±4.1	2.9±0.7
DT 750	0.81±0.02	3.1±2.3	5.5±4.3	26	44	6.5±2.7	2.1±0.9
DT 700	0.70±0.02	6.4±4.9	6.6±8.2	50	88	8.5±5.0	2.8±0.7

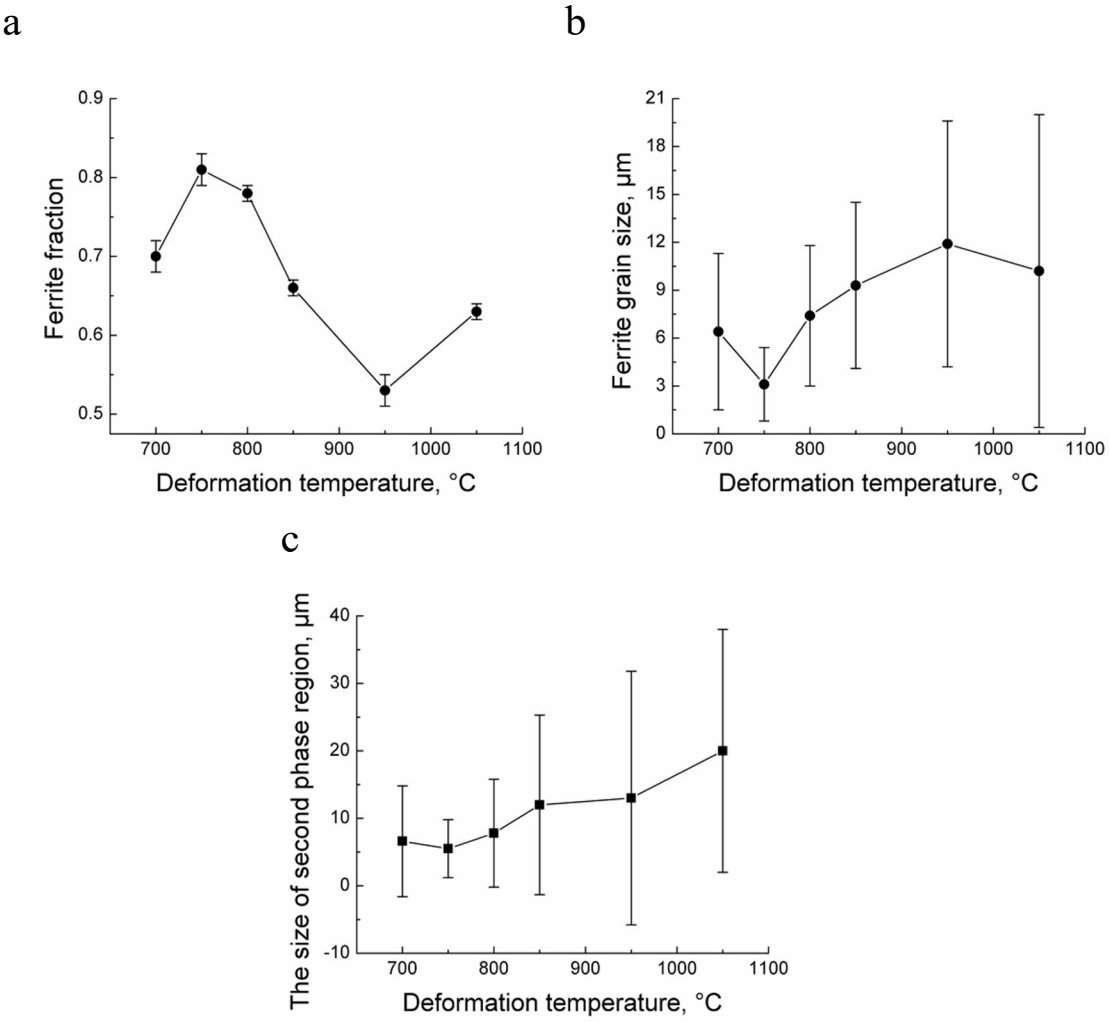

Figure 4.4 The dependences of (a) ferrite fraction, (b) ferrite grain size and (c) the size of second phase region on deformation temperature.

4.3.2 Microstructure characterisation using transmission electron microscopy

As seen in the above optical and scanning electron microscopy results, SIF formation occurred following deformation in the temperature range 800 – 700 °C (DT 800, DT 750 and DT 700 samples). Therefore, further microstructure characterisation was undertaken on the DT 800 and DT 750 samples using TEM and EBSD. The DT 850 sample was also investigated for comparison. Due to the detrimental effect of Widmänstatten ferrite (observed after deformation at 700 °C in Fig. 4.3(h)) on the final mechanical properties, the DT 700 sample was not considered for further analysis.

Typical polygonal ferrite grains in DT 850 and DT 750 samples are shown in Figs. 4.5(a, b) and Figs. 4.6(a, b), respectively. The dislocation substructures in polygonal ferrite comprised isolated dislocations (Fig. 4.5(a)), dislocation tangles (Figs. 4.5(b) and 4.6(a)) and areas of increased dislocation density adjacent to the interfaces between polygonal ferrite and second phase regions (Fig. 4.6(b)), resulting from the increased local strains due to the volume change associated with the accommodation of martensitic and/or bainitic transformations. The dislocation structures in SIF did not show significant variation from that in the polygonal ferrite. However, a slightly higher average dislocation density could be noticed in the SIF ($5.1\pm0.5 \times 10^{-13}$ m^{-2}) compared to polygonal ferrite ($4.6\pm0.4 \times 10^{-13}$ m^{-2}) in the DT 750 sample due to the preferential nucleation of SIF along prior austenite grain boundaries where more deformation defects existed. Well-arranged dislocation walls in the polygonal ferrite (Figs. 4.5(b) and 4.6(d)) and SIF (Fig. 4.6(c)) suggest that recovery could be taking place during cooling to 670 °C (prior to quenching).

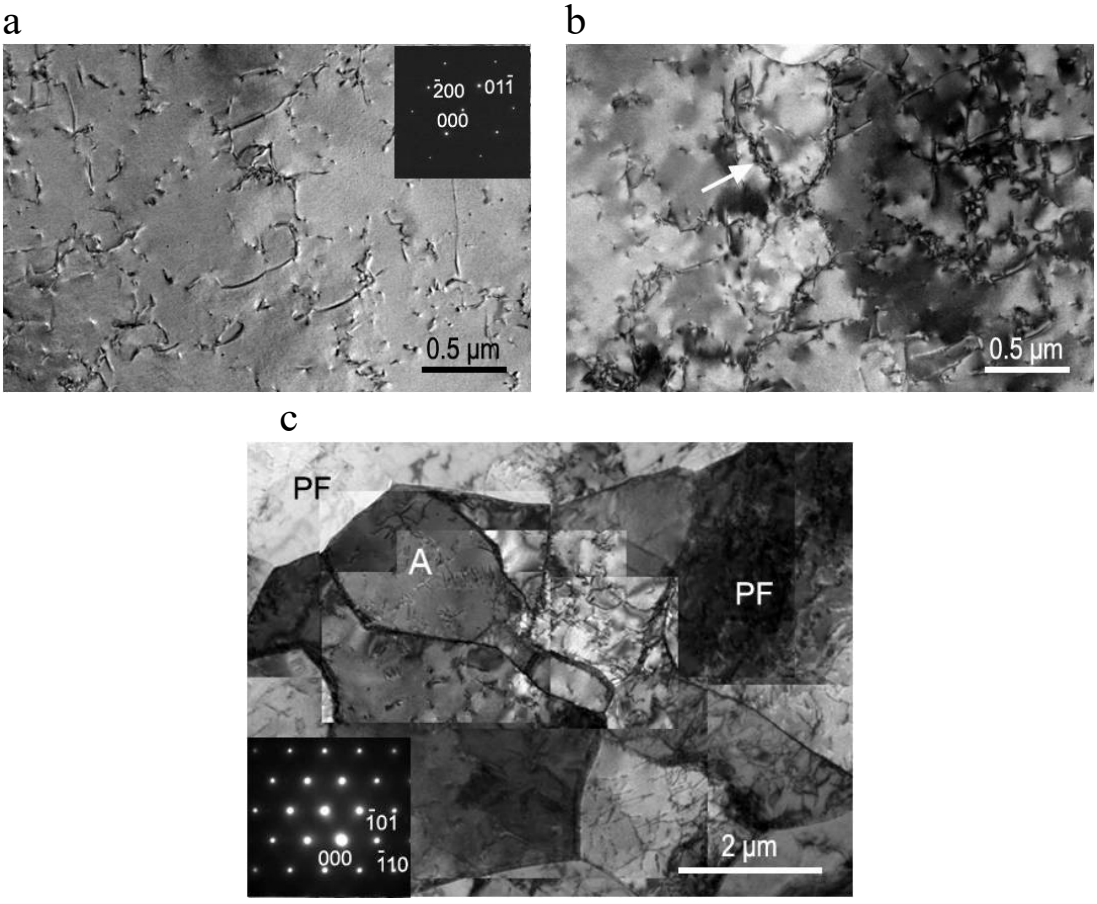

Figure 4.5 TEM images of (a, b) polygonal ferrite in DT 850 sample (the zone axis of inset is $[011]_{\alpha}$) and (c) strain-induced ferrite in DT 800 sample (the zone axis of diffraction pattern from A shown in inset is $[111]_{\alpha}$). *PF* is polygonal ferrite. The arrow in (b) shows dislocation walls in polygonal ferrite.

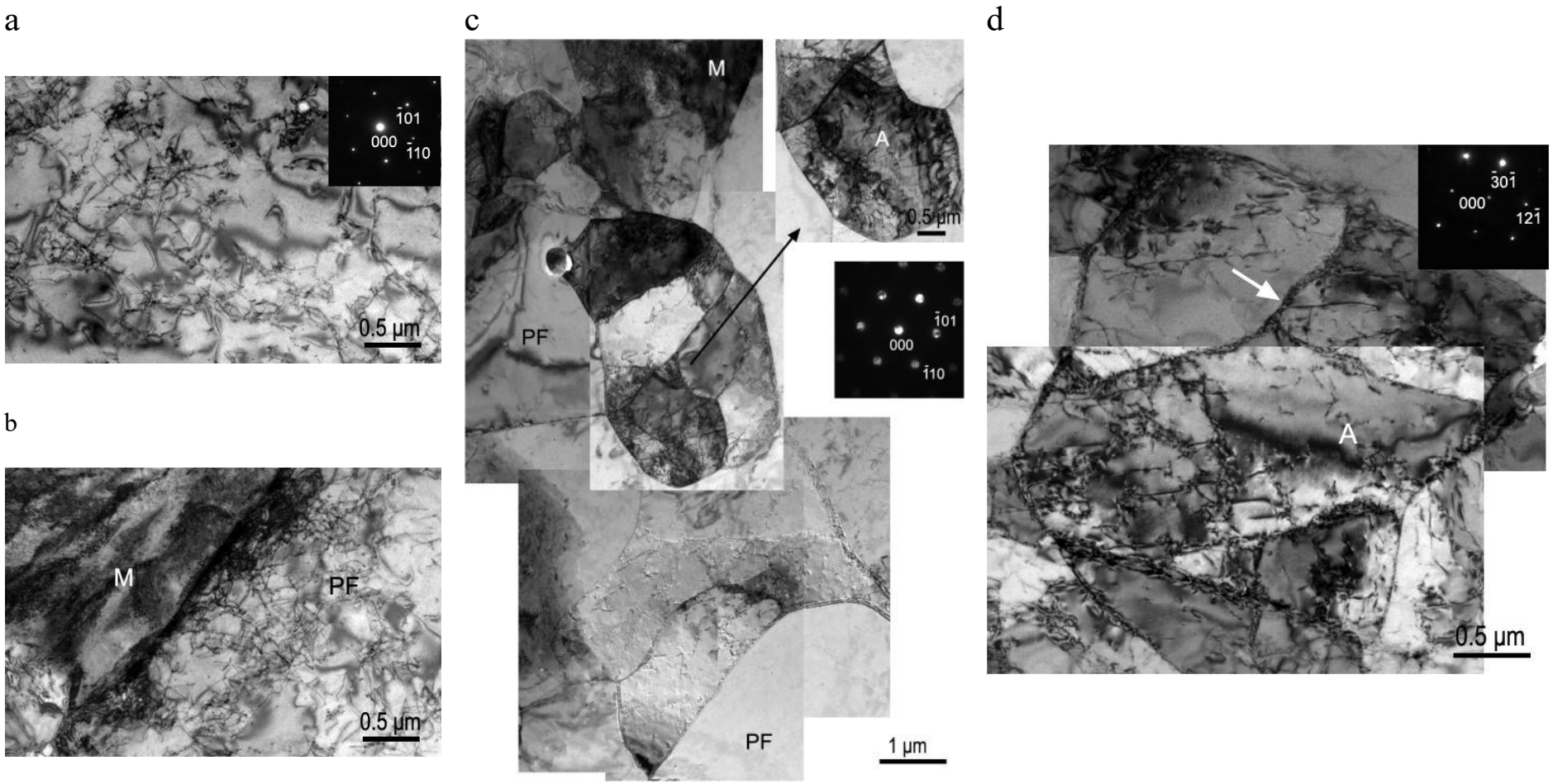

Figure 4.6 TEM images of DT 750 sample: (a, b) typical polygonal ferrite microstructure after deformation (the zone axis of inset in (a) is $[111]_{\alpha}$); (c) strain-induced ferrite (the zone axis of diffraction pattern from A shown in inset is $[111]_{\alpha}$); (d) dislocation walls indicated by the white arrow in polygonal ferrite (the zone axis of diffraction pattern from A shown in inset is $[\bar{1}23]_{\alpha}$). *PF* is polygonal ferrite and *M* is martensite.

4.3.3 Electron backscattering diffraction characterisation of microstructure constituents

The band contrast maps in Figs. 4.7(a, c, e) show the variation in grayscale contrast between ferrite (polygonal ferrite and SIF) and the second phase regions. The lath-like structures of the second phase regions contained a relatively high fraction of Σ3 (60° ⟨111⟩) boundaries, typically arising from the self-accommodation of transformation strain during austenite-to- bainite/martensite transformation with the operation of the K–S [34] or N–W [35] ORs. The results of microstructure segmentation are superimposed on band contrast maps in Figs. 4.7(b, d, f), with polygonal ferrite, SIF and second phase regions shown in blue, green and red, respectively. With a decrease in deformation temperature from 850 to 750 °C, the SIF fraction increased from 0 to 0.18 and the second phase fraction decreased from 0.32 to 0.14, which corresponds to the data obtained using optical microscopy (Table 4.1). The SIF average grain size and subgrain size determined using EBSD were respectively 2.6±1.0 and 1.8±0.8 μm (DT 750 sample), and 2.5±0.5 and 2.1±0.5 μm (DT 800 sample). These values are again similar to the SIF average grain sizes (2 – 3 μm) measured using optical images (Table 4.1).

Fig. 4.8 shows the misorientation angle distributions in different microstructure constituents, and the corresponding fractions of LAGBs are listed in Table 4.2. As can be seen, the misorientation angle distributions for the full maps of the three investigated temperatures generally exhibit similar trends, with LAGB fractions within the range of 0.37 – 0.45. Here one may argue that the high LAGB fraction in the total ferrite subset (comprising polygonal ferrite and SIF, Fig. 4.8(c)) could simply be forming due to deformation and subsequent recovery of polygonal ferrite. However, since the deformation temperature of 750 °C is much higher than the Ar_3 temperature (695 °C), it is SIF that is expected to form during deformation, whereas polygonal ferrite forms later on during cooling. In other words, there are no deformation substructures in polygonal ferrite to be recovered during cooling. It follows that the observed high fraction of LAGBs is mainly associated with SIF formation (Fig. 4.8(c))) as further discussed in *section 4.4.1*. The observed increase in the LAGBs fraction in both polygonal ferrite and SIF with decreasing deformation

temperature is likely due to a decrease in the recovery rate (see for example Figs. 4.6(c, d)) during cooling to 670 °C.

The misorientation distributions of the second phase regions in all three conditions are typical of diffusionless transformation from austenite to bainite/martensite following the K–S or N–W ORs, with misorientation angles between crystallographic variants being predominant in the ranges from 10.5 to 14.9° and from 49.5 to 60.0° [34, 35]. The observation of high fraction of low misorientation angles (< 10°) in the second phase regions is also typical of fast diffusionless transformation [38]. Expectedly, the above misorientation peaks (associated with crystallographic variants) were not observed in the polygonal ferrite fraction which forms via diffusional transformation. Interestingly, these peaks were also absent from the misorientation distributions of SIF and it alludes to the diffusional mechanism of its formation.

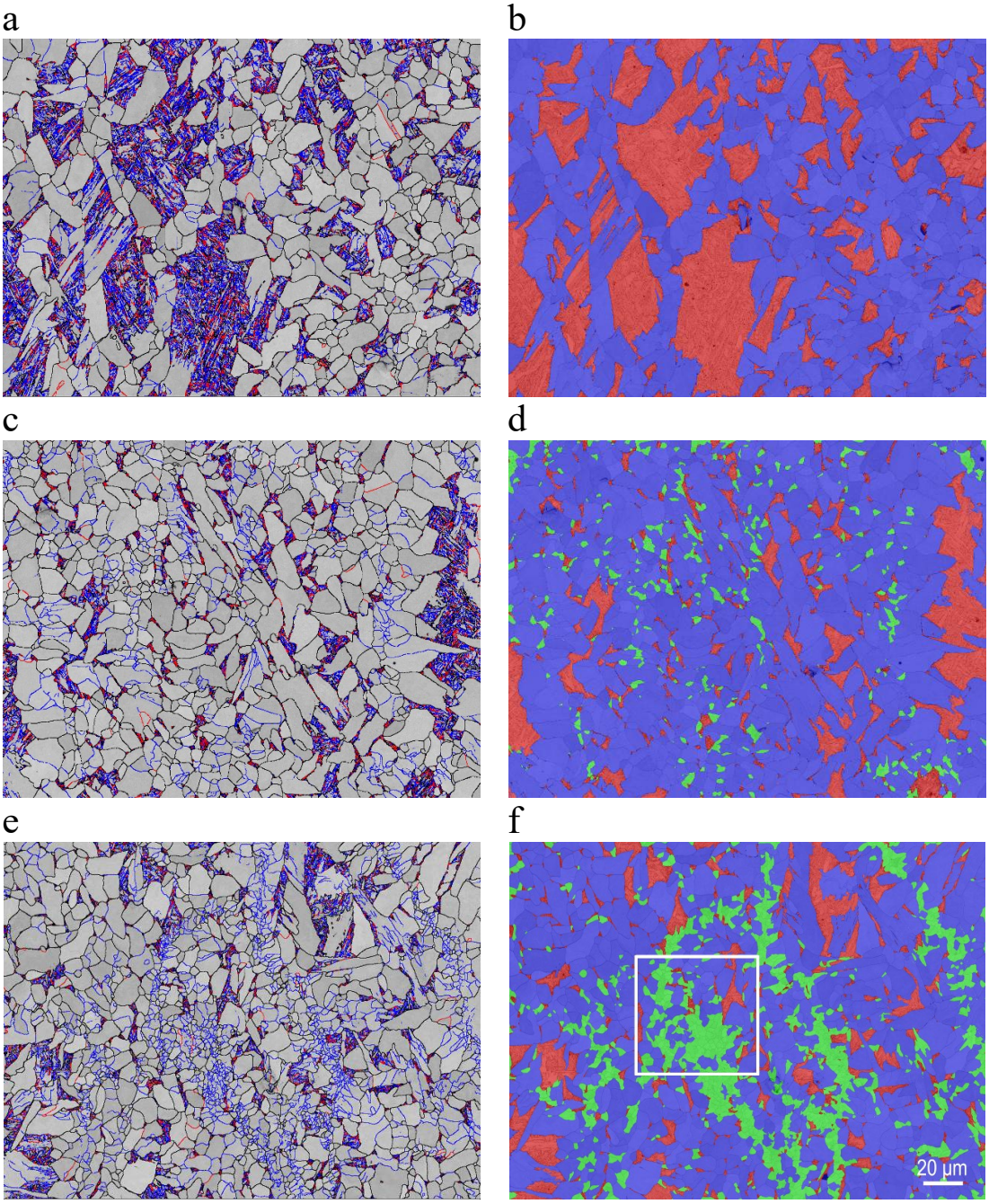

Figure 4.7 (a, c, e) EBSD maps of band contrast with grain boundaries (LAGBs = 2 – 15° = blue, HAGBs ≥ 15° = black and ⟨111⟩ 60° Σ3 = red) and (b, d, f) phase separation maps for (a, b) DT 850, (c, d) DT 800 and (e, f) DT 750 samples, respectively. The ND and RD directions are respectively horizontal and vertical. Second phase regions are red, polygonal ferrite is blue and strain-induced ferrite is green.

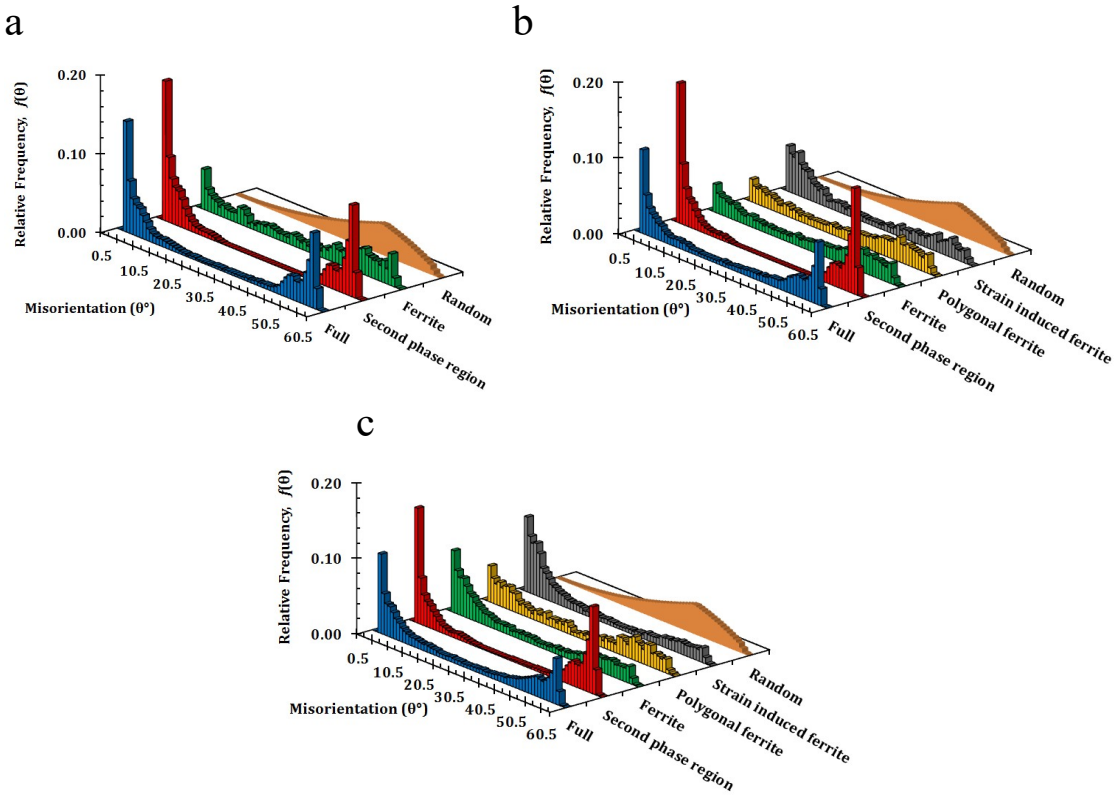

Figure 4.8 Misorientation angle distributions in (a) DT 850, (b) DT 800 and (c) DT 750 samples. Random denotes the McKenzie distribution for untextured cubic materials.

Table 4.2 Fractions of low angle grain boundaries (2 – 15°) after deformation at different temperatures.

	Full map	Second phase region	Ferrite	Polygonal ferrite	Strain-induced ferrite
DT 750	0.42	0.42	0.46	0.34	0.57
DT 800	0.37	0.48	0.25	0.24	0.47
DT 850	0.45	0.53	0.24	0.24	N/A

4.3.4 Texture evolution

Fig. 4.9(a) is a schematic $\phi_2 = 0°$ and $\phi_2 = 45°$ ODF sections for rolled bcc steels, which identify the α-fibre (⟨110⟩||RD) and γ-fibre (⟨111⟩||ND), along with the $(001)[\bar{1}\,\bar{1}0]$ rotated cube component. The orientations belonging to the bcc α-fibre extend from $(001)[1\,\bar{1}0]$ through $(112)[1\,\bar{1}0]$ to $(111)[1\,\bar{1}0]$ in the range from $\Phi = 0 – 55°$ at $\phi_1 = 0°$ and $\phi_2 = 45°$. Orientations belonging to the γ-fibre includes two pairs of equivalent orientations $(111)[1\,\bar{1}0]$, $(111)[0\,\bar{1}1]$ and $(111)[1\bar{2}1]$, $(111)[\bar{1}\,\bar{1}2]$; located between $\phi_1 = 60 – 90°$ at $\Phi = 54.5°$ and $\phi_2 = 45°$.

When hot deformation of steel is undertaken in the austenite region, the crystallographic orientations of the parent face-centred cubic (fcc) austenite phase will affect the ones of the bcc transformation products (such as ferrite, bainite and/or martensite). Since the three investigated temperatures (850, 800 and 750 °C) are below T_{nr}, austenite is expected to develop the β-fibre (extending from the Copper (Cu, {112}⟨111⟩) to the Brass (Br, {110}⟨112⟩) through the S ({123}⟨634⟩)), along with a weaker Goss (G, {110}⟨001⟩) component [15, 39, 40]. The transformation of the former parent fcc orientations to their bcc product orientations, following the K–S OR, is indicated in Fig. 4.9(a) [39]. The ODFs calculated from the large area (547× 602 μm^2) maps are shown in Figs. 4.9(b, c, d). The texture observed after deformation at 850 °C (DT 850 sample, Fig. 4.9(b)) exhibit a slightly curved γ-fibre skeleton line, typical of hot rolling textures in steel [40, 41]. The orientations along this γ-fibre predominantly originate from the Br and G orientations in austenite. Similar texture was observed after deformation at 800 °C (DT 800 sample, Fig. 4.9(c)), with a slight decrease in intensity due to the smaller fraction of second phase regions [41]. After deformation at 750 °C (DT 750 sample, Fig. 4.9(d)), the γ-fibre became less uniform, with orientations clustering near $(111)[1\bar{2}1]$ and $(332)[\bar{1}\,\bar{1}3]$, along with intensification of the rotated cube ($(001)[\bar{1}\,\bar{1}0]$) orientation. This intense rotated cube orientation indicates the formation of a strong Br component in the pancaked austenite with decreasing deformation temperature [15, 41].

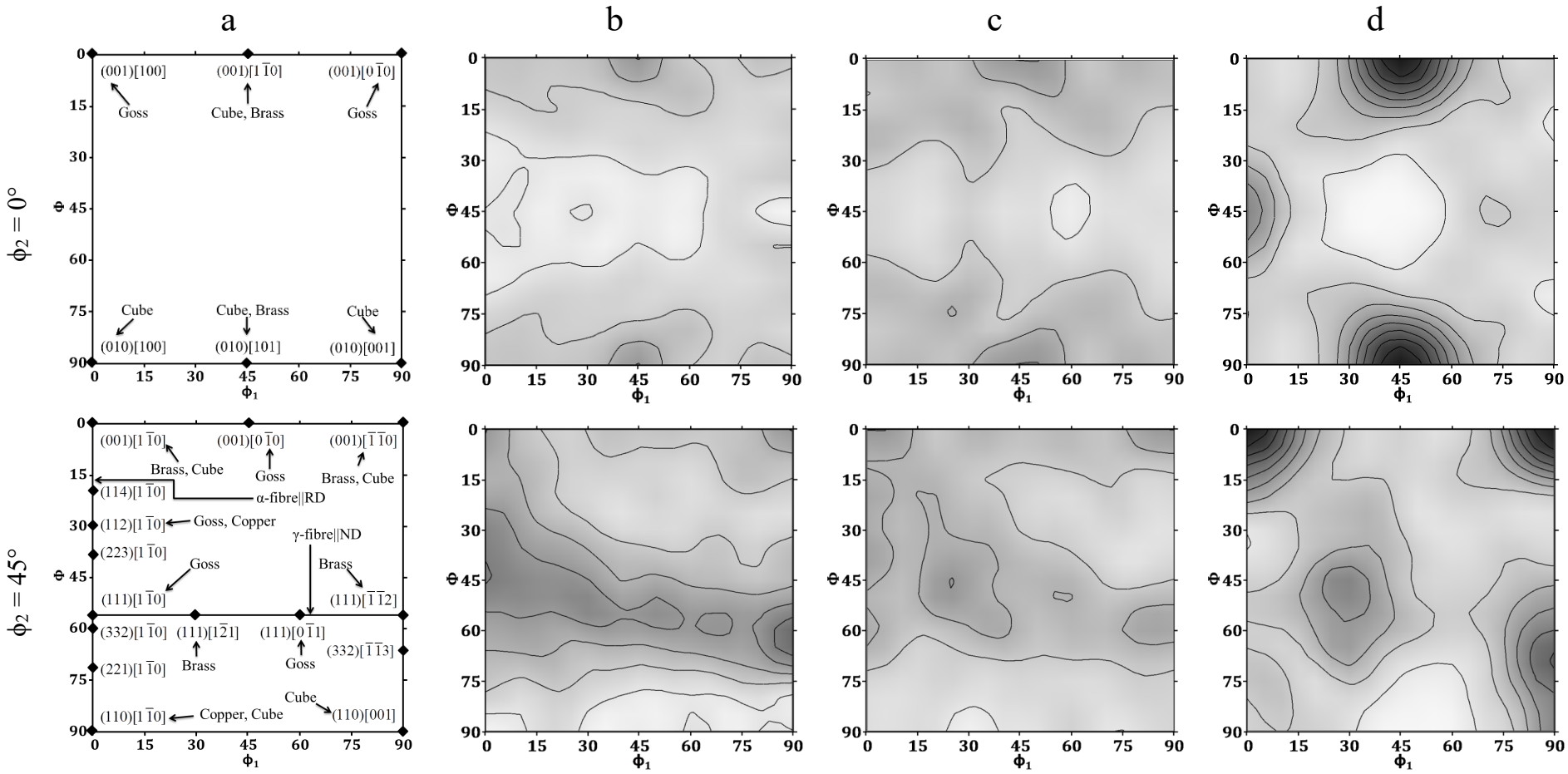

Figure 4.9 $\phi_2 = 0°$ and $45°$ ODF sections of the (a) ideal body-centred cubic product orientations with their major parent orientations named, (b) DT 850, (c) DT 800 and (d) DT 750 samples from a scanning area of 547 × 602 μm^2.

Fig. 4.10 depicts the ODFs (full map and the individual microstructure constituents) calculated from the DT 750 sample map shown in Fig. 4.7(f). It is noted that the ODF calculated from the full map (Fig. 4.10(a)) is generally in good agreement with the ODF calculated from the large area map shown before in Fig. 4.9(d). The lower intensity around the $(001)[\bar{1}\,\bar{1}0]$ rotated cube component in Fig. 4.10(a) is associated with the smaller investigated area.

The texture of polygonal ferrite (Fig. 4.10(b)) mirrors that of the full map (Fig. 4.10(a)). While the polygonal ferrite and SIF textures are generally similar (c.f. Figs. 4.10(b, c)), higher intensity and less spread were observed for the latter. This is probably due to the preferential nucleation of SIF grains along the prior austenite grain boundaries following the K–S OR with at least one neighbouring parent austenite [36], as well as the limited growth of SIF [41, 42].

As pointed out in Refs. [41, 43], there is no strong evidence for variant selection during diffusional transformation, whereas variant selection typically occurs during diffusionless transformation. Consequently, while variant selection analysis is beyond the scope of the present study, it is expected to contribute to the observed differences between the ODFs of the diffusional and diffusionless transformation products as discussed below.

The higher texture intensities observed for the second phase regions (Fig. 4.10(d)) is likely due to the diffusionless transformation of austenite to bainite/martensite, which results in more intense textures than diffusional transformation [40, 41, 44]. Compared also to polygonal ferrite and SIF, the maximum intensity near the γ-fibre at $\phi_1 = 90°$ shifts from $(332)[\bar{1}\,\bar{1}3]$ towards $(111)[\bar{1}\,\bar{1}2]$ in the second phase regions (Fig. 4.10(d)). Here both the $(332)[\bar{1}\,\bar{1}3]$ and $(111)[\bar{1}\,\bar{1}2]$ orientations originate from the Br component in austenite [41]. As reported in Ref. [15], during transformation from the Br Component, the $(332)[\bar{1}\,\bar{1}3]$ orientation is favoured over the $(111)[\bar{1}\,\bar{1}2]$ orientation, when assuming equal probability of all the 24 possible variants of the K–S OR. It follows that, variant selection is likely responsible for the higher intensity of the $(111)[\bar{1}\,\bar{1}2]$ orientation compared to the $(332)[\bar{1}\,\bar{1}3]$ orientation (Fig. 4.10(d))

[41]. Additional point of difference between polygonal ferrite and SIF (Figs. 4.10(b, c)) on one hand and the second phase regions (Fig. 4.10(d)) on the other hand is the spread of the orientations clustered around $(111)[1\bar{2}1]$ (at [30° 55° 45°]) towards [21° 60° 45°] and [40° 54° 45°]. This shift in intensity can be ascribed to the transformation of stronger S and G components in the austenite fraction that undergoes diffusionless transformation to bainite/martensite, following the K–S OR [41, 43].

Lastly, the observation of weak orientations near (012)[100] (at ~ [0° 30° 0°]) and (021)[100] (at ~ [0° 60° 0°]) only in polygonal ferrite and SIF (Figs. 4.10(b, c)) is likely associated with the presence of $\{103\}\langle 001\rangle$ orientations in the respective parent austenite grains.

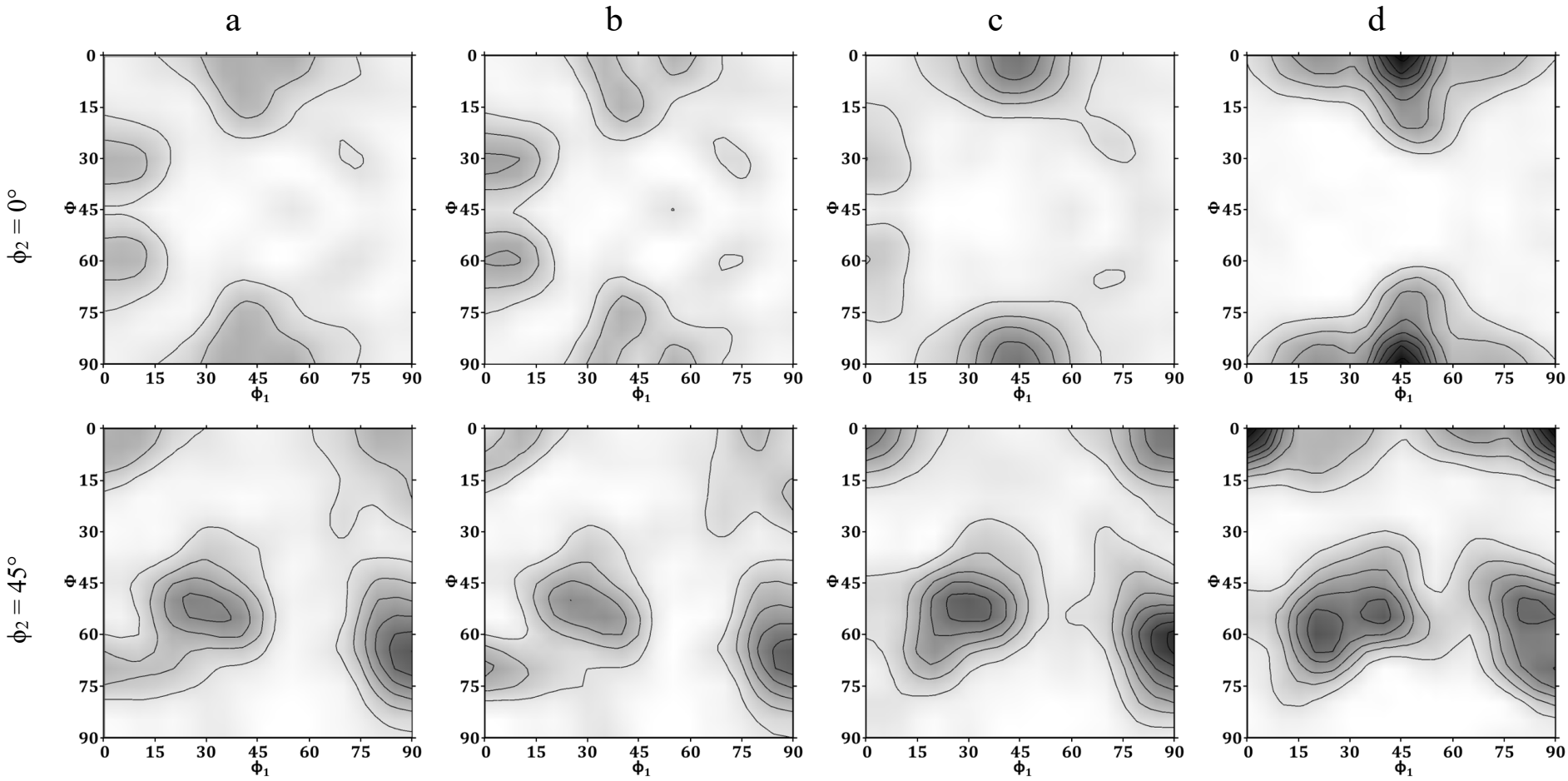

Figure 4.10 ϕ_2 = 0° and 45° ODF sections of (a) full map, (b) polygonal ferrite, (c) SIF and (d) second phase region in DT 750 sample from a scanning area of 180 × 240 μm^2 (Figure 7(f)).

4.3.5 Mechanical properties

Tensile curves after deformation at different temperatures are shown in Fig. 4.11, while the mechanical properties retrieved from these curves are listed in Table 4.3. Compared to the DT 800 and DT 750 samples, the DT 1050 and DT 700 samples showed higher 0.2% offset yield stress (YS) and ultimate tensile strength (UTS) with lower uniform elongation (UE) and total elongation (TE). This could be ascribed to the higher second phase regions fraction in the DT 1050 and DT 700 samples (Table 4.1). The optimal combination of strength and ductility was observed after deformation at 750 °C (UTS × TE = 18067 MPa%).

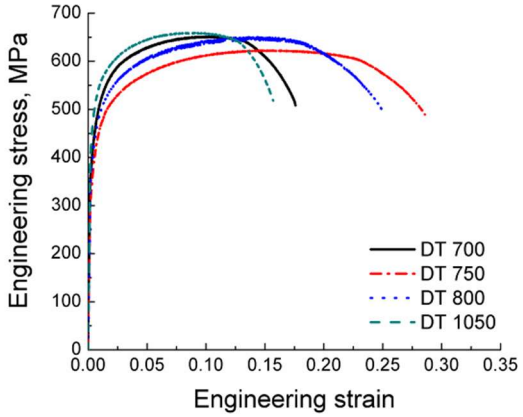

Figure 4.11 Engineering stress–engineering strain curves after deformation at different temperatures.

Table 4.3 Tensile properties after deformation at different temperatures.

	Yield strength, MPa	Ultimate tensile strength, MPa	Uniform elongation	Total elongation	Ultimate tensile strength × total elongation, MPa%
DT 700	416±12	658±10	0.10±0.001	0.17±0.005	11186
DT 750	386±11	623±7	0.14±0.002	0.29±0.002	18067
DT 800	401±14	648±4	0.14±0.004	0.25±0.001	16200
DT 1050	477±11	654±8	0.08±0.002	0.16±0.001	10464

4.4 Discussion

4.4.1 Strain-induced ferrite formation

The observation of SIF after deformation between 700 and 800 °C is in accordance with Refs. [21, 22], as this temperature range corresponds to the region from Ar_3 to (Ar_3 + 100) °C where SIF formation is expected. The lowest SIF fraction (0.03±0.01)

obtained in DT 700 sample can be ascribed to the formation of proeutectoid ferrite before deformation, which occupies SIF nucleation sites along the prior austenite grain boundaries and consequently hinders SIF formation. Alternatively, the higher SIF fraction observed in DT 750 sample (0.18±0.03) compared to DT 800 sample (0.04±0.01) is attributed to the increase in driving force for ferrite nucleation with the decrease in deformation temperature [28, 45]. Thus, the following discussion is focused on the DT 750 sample with the largest SIF fraction.

An enlargement of the rectangular region in the DT 750 phase map (Fig. 4.7(f)) is given in Fig. 4.12(a) and it shows two groups of differently oriented SIF subgrains (marked by "A" and "B") separated by a HAGB. Fig. 4.12(b) is a point-to-point misorientation profile along the white line in Fig. 4.12(a), which clearly shows the high misorientation (~ 46°) across the boundary between A and B. Since SIF preferentially nucleate along prior austenite grain boundaries [28, 45, 46], groups A and B can be assumed to transform from two different prior austenite grains such that subgrains within the same group exhibit similar orientations and do not develop high misorientation angles (Fig. 4.12 (a)). This is likely linked to the limited coalescence and growth of SIF grains due to the high carbon concentration at the austenite/SIF and SIF/SIF interfaces, which in turn decreases the driving force for the interface migration [28]. Accordingly, high LAGB fraction is observed in the SIF subset (Table 4.2). Another potential reason for the observed high fraction of LAGBs is the occurrence of recovery (Fig. 4.6(c)) during slow cooling to 670 °C after deformation, leading to rearrangement of dislocation tangles.

The high LAGB fraction observed in the present work after 0.41 reduction (Table 4.2) is in agreement with previous studies on low carbon [18] and DP steels [25], wherein similarly high LAGB fraction (~ 0.50) was reported following a reduction range of 0.2 – 0.5. In contrast, a low LAGB fraction (~ 0.15) was recorded in Refs. [22, 47, 48] for a reduction of ~ 0.8. In the latter case, higher reductions reduce the LAGB fraction as the LAGBs formed during the initial stages of deformation progressively transform to HAGBs via subgrain rotation and dislocation incorporation into LAGBs [47, 49].

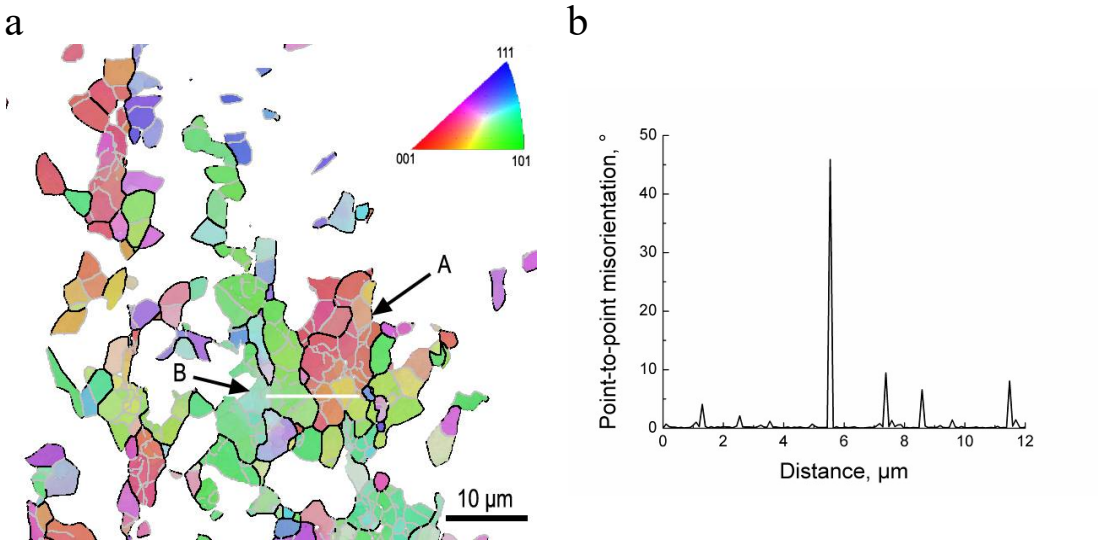

Figure 4.12 (a) Inverse pole figure with grain boundaries of strain-induced ferrite after deformation at 750 °C, which was enlarged from the rectangle region in Figure 7(f); (b) corresponding point-to-point misorientation along the white line in (a) from left to right. LAGBs = 2 – 15° = silver and HAGBs ≥ 15° = black.

Depending on the deformation temperature, SIF formation may generally occur via *diffusionless* (> Ae_3 [27]) or *diffusional* (between Ar_3 and Ae_3 [28, 29]) transformation. Under the present experimental conditions (deformation between Ar_3 and Ae_3) SIF is expected to form via diffusional transformation as supported by the following observations. Firstly, the misorientation angle distribution of SIF (Fig. 4.8) is markedly different from that of the second phase regions (forming via *diffusionless* transformation) and is similar to that of polygonal ferrite (forming via *diffusional* transformation). Secondly, the TEM micrographs in Fig. 4.6, show similar dislocation substructures and recovery phenomenon in both SIF and polygonal ferrite. Lastly, the calculated deviations for each microstructure constituent from the ideal K–S and N–W ORs also suggest SIF formation by *diffusional* transformation. As seen in Fig. 4.13 and Table 4.4, the distributions and fractions of deviation angles for SIF are more similar to polygonal ferrite compared to the second phase regions.

To this end, Fig. 4.13 and Table 4.4 also indicate that phase transformation in the present study followed the K–S OR more closely than the N–W OR as evidenced by the higher fraction of low deviation angles (within 5°) for the former compared to the latter. In addition, SIF exhibited less deviation from the K–S OR compared to polygonal ferrite due to its preferential nucleation along prior austenite grain

boundaries (Fig. 4.7(f)) while following the K–S OR with at least one neighbouring parent austenite [36].

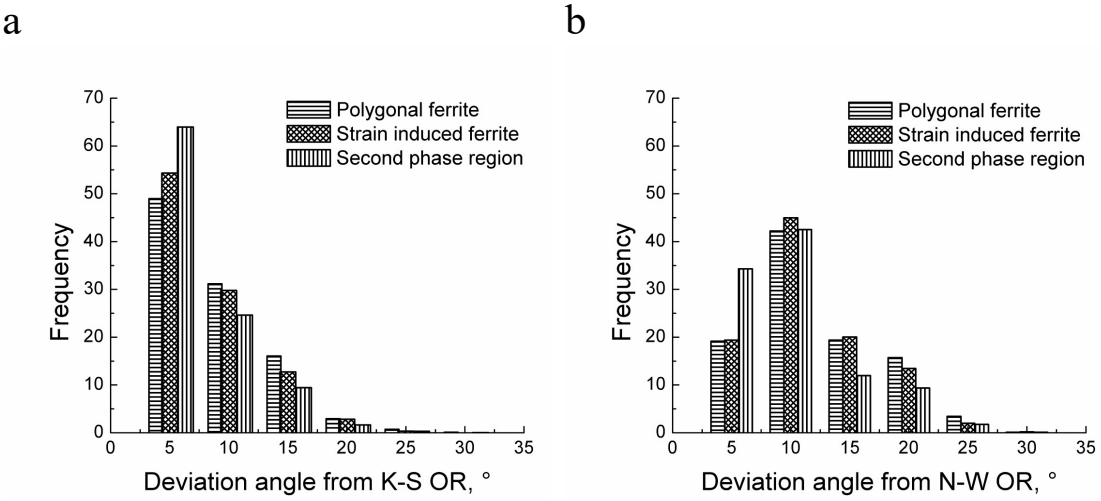

Figure 4.13 The distribution of deviation angles from (a) Kurdjumov–Sachs (K-S) and (b) Nishiyama–Wasserman (N-W) orientation relationships (ORs) for DT 750 sample.

Table 4.4 Fractions of deviation angles from the K–S and N–W ORs for the DT 750 sample. *PF* is polygonal ferrite, *SIF* is strain-induced ferrite and *SPR* is second phase region.

	K–S OR			N–W OR		
	SPR	PF	SIF	SPR	PF	SIF
0 – 5°	64	49	54	34	19	19
5 – 10°	25	31	30	43	42	45

4.4.2 The dependence of ferrite formation on deformation temperatures

Understanding the effect of deformation temperature on ferrite nucleation and growth is of significant practical importance as the processing route in industrial strip casting lines comprises only one rolling mill [4, 6]. The effect of deformation temperature on the nucleation and growth of ferrite [22, 45, 47, 50, 51] is schematically illustrated in Fig. 4.14 for the present DP steel. Deformation at 1050 °C, which is above $T_{nr} \approx 950$ °C [13, 14, 16], resulted in static recrystallisation, decreased PAGS and increased prior austenite grain boundary areas available for polygonal ferrite nucleation. Deformation at 950 °C, which is near T_{nr}, resulted in pancaked austenite and elongated polygonal ferrite and second phase regions as seen

in Fig. 4.2(b). The decrease in polygonal ferrite fraction from 0.63 to 0.53 (Table 4.1) with a decrease in deformation temperature from 1050 to 950 °C can be a consequence of a reduced number of nucleation sites in the pancaked austenite (at 950 °C) with coarser grain size, compared to the recrystallised austenite (at 1050 °C) with smaller grain size. With a decrease in deformation temperature to 850 °C, the number of deformation-induced crystal defects increased, resulting in more nucleation sites not only along the prior austenite grain boundaries but also inside the grains [52], which led to an increase in polygonal ferrite fraction.

After deformation at 800 and 750 °C, the SIF formation took place. The total ferrite fraction increased due to a significant increase in the number of SIF nucleation sites along prior austenite grain boundaries [26] and polygonal ferrite nucleation sites in the interior of prior austenite grains [52]. Both polygonal ferrite and SIF exhibited polygonal shape while the second phase regions were elongated following transformation from the deformed pancaked austenite (Figs. 4.2(d, e)). Decreasing the deformation to 700 °C decreased the total ferrite fraction from 0.81 to 0.70 (Table 4.1) as the time available for growth decreased.

In accordance with the above discussion, the increase in the number of ferrite nucleation sites with decreasing deformation temperature leads to fine average ferrite grain size of ~ 3 μm (Table 4.1), following SIF formation.

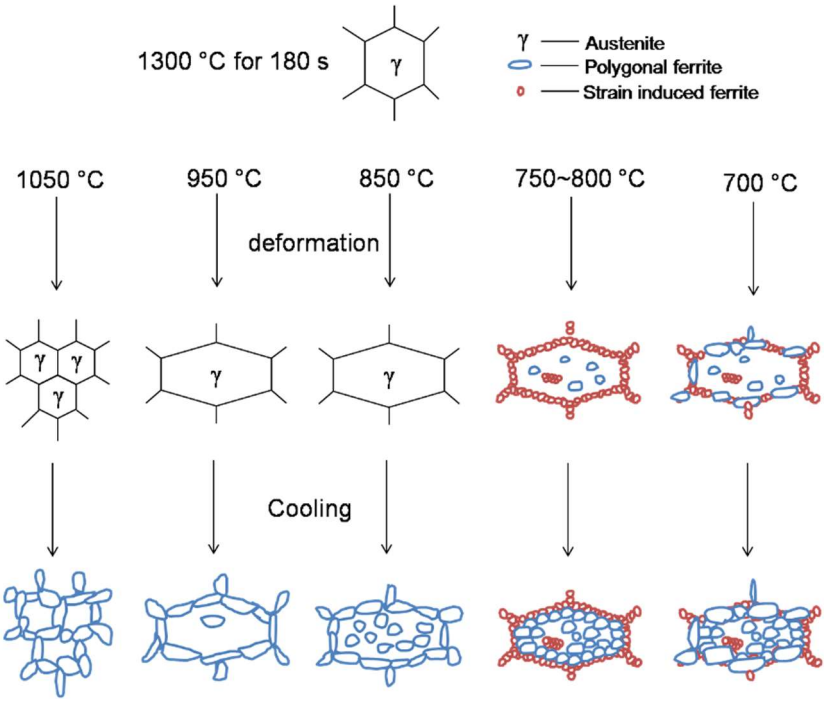

Figure 4.14 A schematic diagram of ferrite formation after different deformation temperatures.

4.4.3 Mechanical properties

The individual contribution of polygonal ferrite, SIF and second phase regions to the strain hardening is analysed by correlating the true stress (σ) and true strain (ε) of each microstructure constituent using the following equation [53, 54]:

$$\sigma = \sigma_0 + \Delta\sigma + \alpha \cdot \mu \cdot M \cdot \sqrt{b} \cdot \sqrt{\frac{1-\exp(-Mk\varepsilon)}{kL}} \tag{4.1}$$

where σ_0 considers the Peierls stress and solid solution strengthening as function of the weight percentages of substitutional alloying elements (taken here to be equal to the nominal chemical composition) [54]:

$$\sigma_0 = 77 + 80[Mn] + 750[P] + 60[Si] + 80[Cu] + 60[Cr] \tag{4.2}$$

$\Delta\sigma$ represents the strengthening by carbon in solution. Considering the similarities between polygonal ferrite and SIF as shown in the above analysis, $\Delta\sigma$ is assumed to be the same for both constituents and calculated as [54]:

$$\Delta\sigma = 5000[C] \tag{4.3}$$

For the second phase regions, $\Delta\sigma$ is expressed as [54]:

$$\Delta\sigma = 3065[C] - 161 \tag{4.4}$$

For the three constituents, α is a material constant (0.33), μ is the shear modulus (80000 MPa), M is the Taylor factor (3), b is the Burger's vector (2.5×10^{-10} m), L is the mean free path of dislocations, and k is the recovery rate [54]. For polygonal ferrite and SIF, L was assumed to be equal to the average subgrain size determined from EBSD and k is equal to $10^{-5}/L$. For the second phase regions, L is an order of magnitude smaller than the lath width determined from EBSD and k is set as 41 [54]. The carbon concentration [C] in polygonal ferrite and SIF was considered to be 0.004 wt. % based on carbon solubility in iron at room temperature [55] (leading to a solution strengthening of 20 MPa), whereas the carbon concentration in the second phase regions (0.39 and 0.36 wt. % for DT 750 and DT 800, leading to a solution strengthening of 1034 and 942 MPa, respectively) was calculated based on the carbon balance in the steel. Solution strengthening by carbon for ferrite (Eq. 4.3) and second phase regions (Eq. 4.4) is different probably due to a much higher carbon content in second phase region, leading to overlapping of interaction fields of C atoms with dislocation and in turn a reduction of per carbon atom contribution to the solution strengthening [56].

The modified iso-work model was used to correlate the true stress and true strain increments ($d\varepsilon$) of each microstructure constituent [57]:

$$\sigma_{PF} d\varepsilon_{PF} = \sigma_{SIF} d\varepsilon_{SIF} = w\sigma_{SPR} d\varepsilon_{SPR} \tag{4.5}$$

where the subscripts *PF*, *SIF* and *SPR* denote polygonal ferrite, SIF and second phase regions, respectively, and w is weighted constant for the second phase regions and is used as a fitting parameter.

The total macroscopic true strain increment ($d\varepsilon_{macro}$) is given by rule of mixtures [58]:

$$d\varepsilon_{macro} = f_{PF} d\varepsilon_{PF} + f_{SIF} d\varepsilon_{SIF} + f_{SPR} d\varepsilon_{SPR} \tag{4.6}$$

where f_{PF}, f_{SIF} and f_{SPR} denote fractions of polygonal ferrite, SIF and second phase regions, respectively. The macroscopic true stress (σ_{macro}) can be expressed as follows:

$$\sigma_{macro} = f_{PF}\sigma_{PF} + f_{SIF}\sigma_{SIF} + f_{SPR}\sigma_{SPR} \tag{4.7}$$

As seen in Figs. 4.15(a, b), the calculated macroscopic true stress-strain curves for the DT 750 and DT 800 samples are in a good agreement with their experimental counterparts. The slight overestimation in the elastic-plastic transition region is because the model does not account for elastic deformation [57].

As shown in Fig. 4.15(c) for the DT 750 sample, the strain hardening of the second phase regions reached a saturation level at a small strain of 0.02, while more sustainable strain hardening was observed in both polygonal ferrite and SIF. The small grain size of SIF enhances the strength such that the calculated flow stress in SIF was ~ 80 MPa higher than that in polygonal ferrite. At a macroscopic true strain of 0.140 (corresponding to the UTS), the true strains in polygonal ferrite, SIF and second phase regions were 0.160, 0.139 and 0.075, respectively, indicating that SIF formation slightly decreased ductility.

Comparison of the true stress-strain curves of polygonal ferrite and SIF for the DT 750 and DT 800 samples (Fig. 4.15(d)) shows that both polygonal ferrite and SIF in DT 750 sample exhibited higher true stresses, which again resulted from smaller grain sizes in the DT 750 sample than those in the DT 800 sample (Table 4.1).

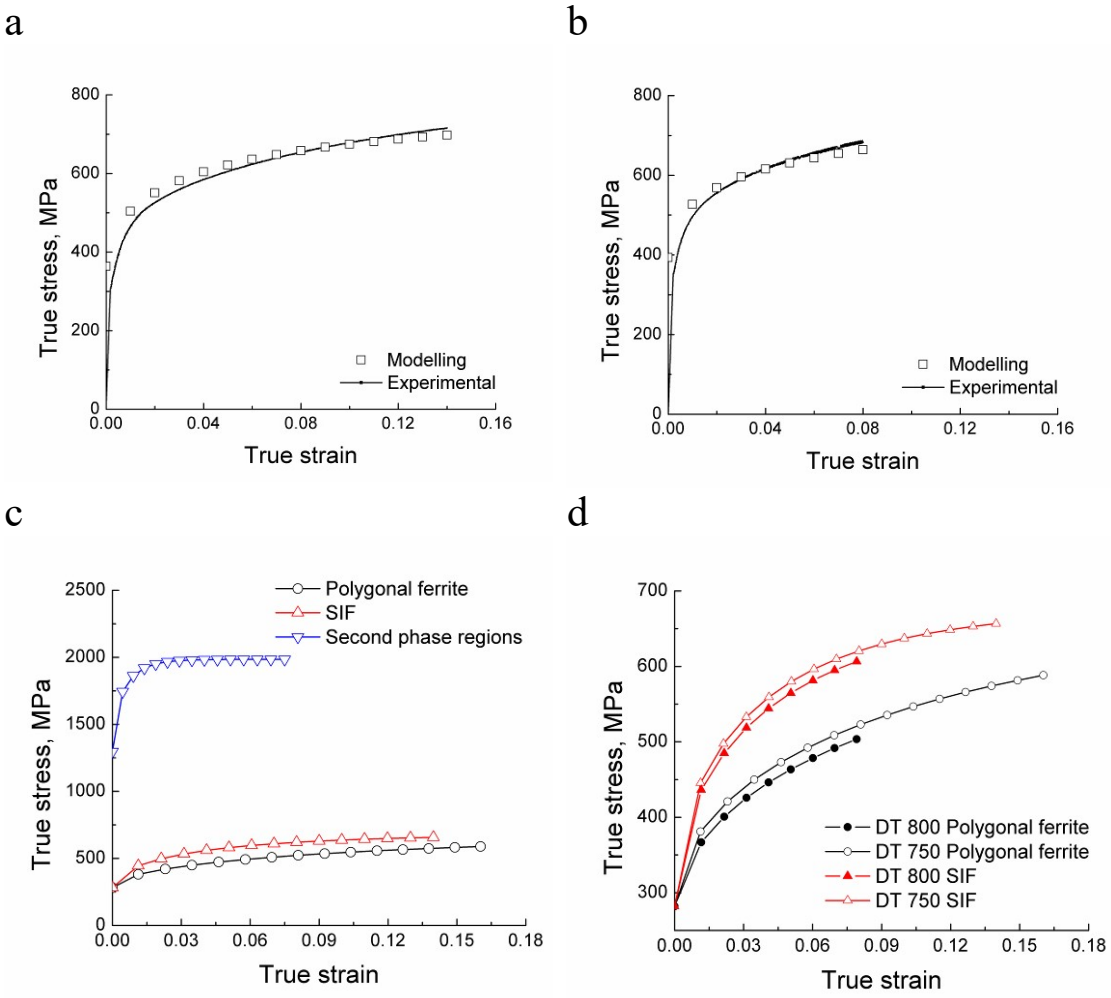

Figure 4.15 (a, b) Experimental true stress-strain curves and iso-work modelling results of (a) DT 750 and (b) DT 800 samples; (c) calculated true stress-strain curves for polygonal ferrite, strain-induced ferrite and second phase regions in DT 750 sample; (d) comparison of polygonal ferrite and strain-induced ferrite true stress-strain curves for the DT 750 and DT 800 samples. *SIF* is strain-induced ferrite.

Lastly, the mechanical properties of the present strip cast DP steel are compared with those of commercially produced hot and cold rolled DP steels. The hollow stars in Fig. 4.16 show the mechanical properties of strip cast DP steel produced using heat treatment without deformation [12], while the half-hollow stars denote the improved mechanical properties as a result of deformation above the T_{nr} temperature [11]. In the current study (solid stars) a further step in the property improvement was made via deformation below T_{nr}, namely in the 700 – 950 °C temperature range, a part of which led to SIF formation and significant grain refinement. The high ferrite fraction and refined microstructures of the DT 750 and DT 800 samples resulted in UTS × TE in the range of 16000 – 18000 MPa% (Fig. 4.16 and Table 4.3). These tensile

properties significantly outperforms the industrially produced DP 600 steel (12760 – 14740 MPa%) and underscores the feasibility to produce DP steels using the strip casting technology.

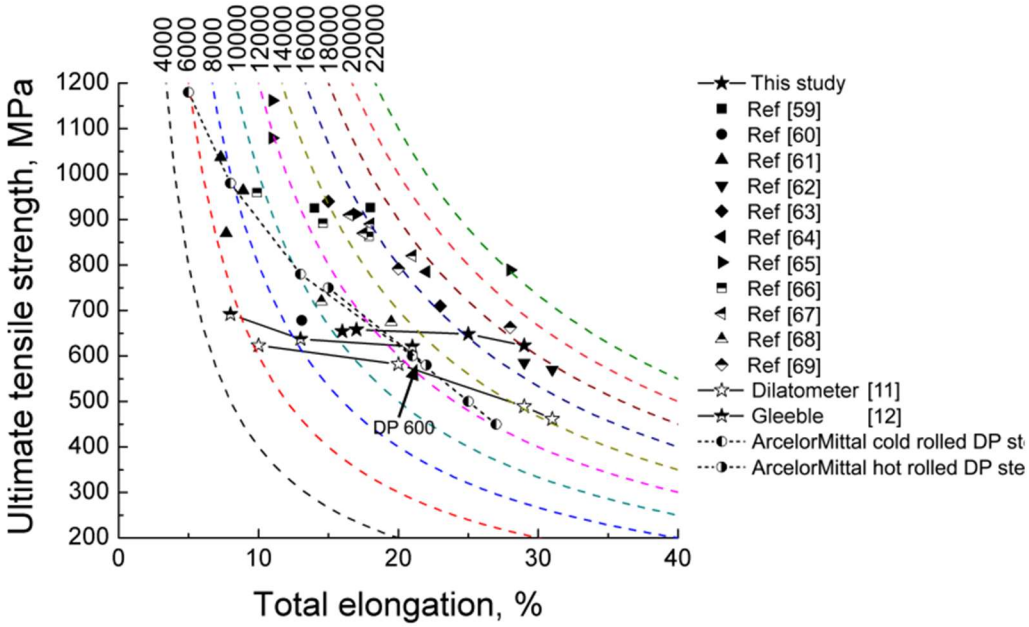

Figure 4.16 Comparison of mechanical properties among the studied steels [11, 12], hot rolled DP steels [59-69] and DP steels from ArcelorMittal Company's brochure [70].

4.5 Conclusions

Investigation of the dependence of ferrite formation and mechanical properties on deformation temperature in strip cast dual phase steel showed that:

(1) With a decrease in deformation temperature from 1050 to 700 °C, the ferrite fraction tended to increase, and the average ferrite grain size and the average size of second phase region tended to decrease. The SIF formation was observed following deformation in the 700 – 800 °C temperature range, with the maximum fraction and minimum grain size obtained at 750 °C.

(2) Similar dislocation substructures, such as isolated dislocations, dislocation tangles and walls, were observed in SIF and polygonal ferrite. The dislocation walls suggested that the recovery phenomenon occurred during cooling after deformation.

(3) The textures observed after deformation in the temperature range 750 – 800 °C are typical steel hot rolling textures, which extends from the $(111)[1\bar{2}1]$ component through the $(111)[0\bar{1}1]$ to $(332)[\bar{1}\bar{1}3]$ along the γ-fibre. The SIF texture was more similar to polygonal ferrite than to the second phase regions.

(4) The similarity between various microstructure features (misorientation angle distributions, deviation from the theoretical K–S and N–W orientation relationships and dislocation structures) of SIF and polygonal ferrite suggests SIF formation via diffusional transformation.

(5) The optimal combination of strength and ductility (UTS × TE) was obtained after deformation in the SIF formation temperature range of 750 – 800 °C. Our present UTS × TE values (16000 – 18000 MPa%) are much higher than those of industrially manufactured hot/cold rolled DP 600 steel (12760 – 14740 MPa%).

(6) The modified iso-work modelling analysis of the flow stress suggests that SIF could enhance strength while slightly decrease ductility.

Acknowledgement:
This project was supported by the Australian Research Council (DP130101887). The JEOL JSM-7001F FEG-SEM was funded by the Australian Research Council (LE0882613). The authors thank Drs. A.A. Gazder and L. Chen, UOW for modification of tensile stage and operation of the Gleeble 3500 thermo-mechanical simulator, respectively. The authors also thank Associate Professor N.E. Stanford, Monash University for the dip tests.

References

[1] R. Kuziak, R. Kawalla, S. Waengler, Arch. Civ**.** Mech. Eng. 8 (2008) 103-117.

[2] C.C. Tasan, M. Diehl, D. Yan, M. Bechtold, F. Roters, L. Schemmann, C. Zheng, N. Peranio, D. Ponge, M. Koyama, K. Tsuzaki, D. Raabe, Annu. Rev. Mater. Res. 45 (2015) 391-431.

[3] A.P. Hardwick, T. Outteridge, Int. J. Life Cycle Assess. 21 (2016) 1616-1623.

[4] D.J. Sosinsky, P. Campbell, R. Mahapatra, W. Blejde, F. Fisher, Metallurgist 52 (2008) 691-699.

[5] H.Y. Gao, Z.X. Xie, Y. Yu, Y. Fang, J. Wang, B.D. Sun, ISIJ Int. 49 (2009) 546-552.

[6] C.R. Killmore, A. Phillips, H. Kaul, J.C. Williams, H. Creely, P. Campbell, M.M. Schueren, W. Blejde, Iron Steel Technol. 4 (2007) 90-105.

[7] S. Ge, M. Isac, R.I.L. Guthrie, ISIJ Int. 52 (2012) 2109-2122.

[8] M. Daamen, C. Haase, J. Dierdorf, D.A. Molodov, G. Hirt, Mater. Sci. Eng. A 627 (2015) 72-81.

[9] Z.P. Xiong, A.G. Kostryzhev, A.A. Saleh, L. Chen, E.V. Pereloma, Mater. Sci. Eng. A 664 (2016) 26-42.

[10] Z.P. Xiong, A.G. Kostryzhev, L. Chen, E.V. Pereloma, Mater. Sci. Eng. A 677 (2016) 356-366.

[11] Z.P. Xiong, A.G. Kostryzhev, N.E. Stanford, E.V. Pereloma, Mater. Sci. Eng. A 651 (2016) 291-305.

[12] Z.P. Xiong, A.G. Kostryzhev, N.E. Stanford, E.V. Pereloma, Mater. Des. 88 (2015) 537-549.

[13] M. Arribas, B. López, J. Rodriguez-Ibabe, Mater. Sci. Eng. A 485 (2008) 383-394.

[14] S. Hosseini, A. Zarei-Hanzaki, E. Essadiqi, S. Yue, Mater. Sci. Technol. 24 (2008) 1354-1361.

[15] M. Butron-Guillen, J. Jonas, R. Ray, Acta Metall. Mater. 42 (1994) 3615-3627.

[16] S. Vervynckt, K. Verbeken, B. Lopez, J. Jonas, Int. Mater. Rev. 57 (2012) 187-207.

[17] H. Beladi, G. Kelly, A. Shokouhi, P. Hodgson, Mater. Sci. Eng. A 367 (2004) 152-161.

[18] P.J. Hurley, P. Hodgson, B. Muddle, Scripta Mater. 40 (1999) 433-438.

[19] L. Storojeva, D. Ponge, R. Kaspar, D. Raabe, Acta Mater. 52 (2004) 2209-2220.
[20] E.**V.** Pereloma, Metallofiz. Nov. Tekh. 31 (2009) 191-207.
[21] L. Du, C. Zhang, H. Ding, X. Liu, G. Wang, ISIJ Int. 42 (2002) 1119-1124.
[22] A. Karmakar, R. Misra, S. Neogy, D. Chakrabarti, Metall. Mater. Trans. A 44 (2013) 4106-4118.
[23] P. Hurley, P. Hodgson, Mater. Sci. Technol. 17 (2001) 1360-1368.
[24] P. Hurley, P. Hodgson, Mater. Sci. Eng. A 302 (2001) 206-214.
[25] K. Mukherjee, S. Hazra, M. Militzer, Metall. Mater. Trans. A 40 (2009) 2145-2159.
[26] S.C. Hong, K.S. Lee, Mater. Sci. Eng. A 323 (2002) 148-159.
[27] C. Ghosh, V.V. Basabe, J.J. Jonas, Y.M. Kim, I.H. Jung, S. Yue, Acta Mater. 61 (2013) 2348-2362.
[28] C. Zheng, N. Xiao, L. Hao, D. Li, Y. Li, Acta Mater. 57 (2009) 2956-2968.
[29] C.W. Zheng, D. Raabe, D.Z. Li, Mater. Sci. Forum 706-709 (2012) 1592-1597.
[30] H. Yada, C.M. Li, H. Yamagata, ISIJ Int. 40 (2000) 200-206.
[31] K. Mukunthan, P.D. Hodgson, P. Sellamuthu, L. Strezov, Y. Durandet, N. Stanford, ISIJ Int. 53 (2013) 1803-1811.
[32] G. Palumbo, K.T. Aust, Acta Metall. Mater. 38 (1990) 2343-2352.
[33] R. Hielscher, H. Schaeben, J. Appl. Crystallogr. 41 (2008) 1024-1037.
[34] N. Takayama, G. Miyamoto, T. Furuhara, Acta Mater. 60 (2012) 2387-2396.
[35] H. Beladi, Y. Adachi, I. Timokhina, P.D. Hodgson, Scripta Mater. 60 (2009) 455-458.
[36] E. Novillo, D. Hernandez, I. Gutierrez, B. Lopez, Mater. Sci. Eng. A 385 (2004) 83-90.
[37] J.J. Fundenberger, B. Beausir, Université de Lorraine - Metz, 2015, JTEX - Software for Texture Analysis, http://jtex-software.eu/.
[38] L. Ryde, Mater. Sci. Technol. 22 (2006) 1297-1306.
[39] A.A. Gazder, A.A. Saleh, M.J.B. Nancarrow, D.R.G. Mitchell, E.V. Pereloma, Steel Res. Int. 86 (2015) 1204-1214.
[40] C. Mesplont, B. De Cooman, Mater. Sci. Technol. 19 (2003) 875-886.
[41] R. Ray, J. Jonas, Int. Mater. Rev. 35 (1990) 1-36.
[42] C. Ghosh, C. Aranas Jr, J.J. Jonas, Prog. Mater. Sci. 82 (2016) 151-233.

[43] T. Waterschoot, L. Kestens, B. De Cooman, Metall. Mater. Trans. A 33 (2002) 1091-1102.
[44] B. Hutchinson, L. Ryde, E. Lindh, K. Tagashira, Mater. Sci. Eng. A 257 (1998) 9-17.
[45] X. Sun, H. Luo, H. Dong, Q. Liu, Y. Weng, ISIJ Int. 48 (2008) 994-1000.
[46] S. Wang, H. Yu, T. Zhou, T. Wang, Mater. Des. 88 (2015) 847-853.
[47] L. Hao, M. Sun, N. Xiao, D. Li, J. Mater. Sci. Technol. 28 (2012) 1095-1101.
[48] B. Eghbali, A. Abdollah-Zadeh, Scripta Mater. 54 (2006) 1205-1209.
[49] G.L. Kelly, H. Beladi, P.D. Hodgson, ISIJ Int. 42 (2002) 1585-1590.
[50] B. Eghbali, A. Abdollah-Zadeh, J. Mater. Process. Technol. 180 (2006) 44-48.
[51] C. Zhang, M. Zhang, T. Guo, J. Yang, Y. Kong, D. Cai, Q. Li, Mater. Charact. 113 (2016) 10-16.
[52] N. Xiao, M. Tong, Y. Lan, D. Li, Y. Li, Acta Mater. 54 (2006) 1265-1278.
[53] Y. Estrin, H. Mecking, Acta Metall. 32 (1984) 57-70.
[54] R.M. Rodriguez, I. Gutiérrez, Mater. Sci. Forum 426-432 (2003) 4525-4530.
[55] A. Ramazani, P.T. Pinard, S. Richter, A. Schwedt, U. Prahl, Comput. Mater. Sci. 80 (2013) 134-141.
[56] P.G. Winchell, M. Cohen, Trans. ASM 55 (1962) 347-61.
[57] S.K. Paul, M. Mukherjee, Comput. Mater. Sci. 84 (2014) 1-12.
[58] E.J. Seo, L. Cho, Y. Estrin, B.C. De Cooman, Acta Mater. 113 (2016) 124-139.
[59] E. Ahmad, T. Manzoor, N. Hussain, N. Qazi, Mater. Des. 29 (2008) 450-457.
[60] K. Park, M. Nishiyama, N. Nakada, T. Tsuchiyama, S. Takaki, Mater. Sci. Eng. A 604 (2014) 135-141.
[61] M. Calcagnotto, Y. Adachi, D. Ponge, D. Raabe, Acta Mater. 59 (2011) 658-670.
[62] T. Wen, H. Bin, S. Wang, Y. Yi, C. Zhang, Y. Zhang, J. Iron Steel Res. Int. 19 (2012) 37-41.
[63] P. Deb, M. Chaturvedi, Mater. Sci. Eng. 78 (1986) L7-L13.
[64] J. Hu, L.X. Du, J.J. Wang, C.R. Gao, T.Z. Yang, A.Y. Wang, R. Misra, Metall. Mater. Trans. A 44 (2013) 4937-4947.
[65] N. Kolbasnikov, Y.A. Bezobrazov, A. Naumov, Steel Transl. 43 (2013) 455-459.
[66] J. Lis, A. Lis, C. Kolan, J. Mater. Process. Technol. 162 (2005) 350-354.
[67] A. Panda, P. Ray, R. Ganguly, Mater. Sci. Technol. 16 (2000) 648-656.
[68] X. Xu, J. Kong, J. Lin, R. Zheng, Rev. Adv. Mater. **Sci** 33 (2013) 348-353.

[69] R. González, J. García, L. Verdeja, M. Quintana, J. Verdeja, Can. Metall. Q. 53 (2014) 100-106.
[70] http://automotive.arcelormittal.com/europe/products/AHSS/EN.

CHAPTER 5 MICROSTRUCTURES AND MECHANICAL PROPERTIES OF TRIP STEEL PRODUCED BY STRIP CASTING SIMULATED IN THE LABORATORY

Z.P. Xiong[1*], A.G. Kostryzhev[1], A.A. Saleh[1], L. Chen[1], E.V. Pereloma[1, 2]

[1]*School of Mechanical, Materials and Mechatronic Engineering, University of Wollongong, Wollongong, NSW 2522, Australia*

[2]*Electron Microscopy Centre, University of Wollongong, Wollongong, NSW 2519, Australia*

Abstract: Conventional transformation-induced plasticity (TRIP) steel (0.17C-1.52Si-1.61Mn-0.03Al, wt. %) was produced via strip casting technology simulated in the laboratory. Effects of holding temperature, holding time and cooling rate on ferrite formation were studied via analysis of the continuous cooling transformation diagram obtained here. A typical microstructure for conventional TRIP steels consisting of ~ 0.55 fraction of polygonal ferrite with bainite, retained austenite and martensite was obtained. However, coarse prior austenite grain size of ~ 80 μm led to large polygonal ferrite grain size of ~ 17 μm, coarse second phase regions of ~ 21 μm size, small amount of retained austenite (0.02 – 0.045) and the presence of Widmanstätten ferrite. Optimisation of the microstructure-property relationship was reached via a variation in the isothermal bainite transformation temperature. The highest retained austenite fraction of 0.045±0.003 with medium carbon content of 1.23±0.01 wt. % was obtained after holding at 400 °C, resulting in the highest ultimate tensile strength of 590±35 MPa and largest total elongation of 0.27±0.05. The presence of TRIP effect in the studied steel was revealed through the analysis of strain hardening exponent and modified Crussard – Jaoul model. Effect of processing parameters on retained austenite retention and stress-strain behaviour was discussed.

Keywords: Strip casting; TRIP steel; Mechanical properties; Retained austenite; Isothermal bainite transformation; Prior austenite grain size.

5.1 Introduction

Transformation-induced plasticity (TRIP) steel is one of the advanced high strength steels, which is used in automotive industry [1]. Compared to dual phase (DP) steel, TRIP steel has a better combination of strength and formability in terms of both elongation and strain hardening exponent, which attracted many researchers to study it in recent decades [1, 2]. In order to produce such multi-phase steel, a strict control of processing window parameters is needed, which somewhat restricts a wide production of TRIP steels. The microstructure of TRIP steel consists of polygonal ferrite, bainite, retained austenite (RA) and martensite [3-11]. RA is a key phase which ensures a good combination of high strength and high ductility through the transformation of RA to martensite during deformation [12-16]. The production of TRIP steel includes a two-stage heat treatment following hot rolling or cold rolling [15, 17]. The first stage of heat treatment results in austenite-to-ferrite transformation. At this stage, a TRIP steel is cooled through or held in the austenite-ferrite two phase temperature region. The ferrite fraction is controlled by the adjustment of cooling rate or holding time and temperature [3, 4]. At the second stage, a TRIP steel is fast cooled to bainite temperature region, in order to avoid pearlite formation, and held at a selected temperature for a certain time period to assure bainite formation and austenite enrichment with carbon. The isothermal bainite holding (IBT) temperature and time are used to adjust the retained austenite fraction and its stability [7, 12, 18]. Following cooling to the ambient temperature from the bainite transformation temperature, the microstructure will contain some retained austenite, amount of which will determine the scale of TRIP effect.

At present, most of researchers are focusing on hot rolling and cold rolling followed by intercritically annealing, which are technologies that demonstrated their feasibilities to produce TRIP steel in industry [1]. However, the strip casting is another potential way to produce TRIP steel. It is defined as production of strip steels through direct casting from molten metal in a single process, which may combine subsequent inline hot-rolling by a micro-mill [19]. At present the strip casting is utilised for industrial manufacture of carbon steels, silicon steels and stainless steels, and also lead, aluminium and brass strips [20, 21]. Besides, a conventional DP steel was produced using strip casting technology in the laboratory [22, 23]. Due to the

strips being directly manufactured from liquid metal, the strip casting technology eliminates many subsequent processing stages inherent for conventional processing routes, such as multi-pass rough rolling of continuously cast thick slab and finishing rolling in continuous rolling mills. Therefore, the strip casting process has many advantages, such as energy saving and emission reduction, lower capital and operating costs, a more flexible operating regime, a shorter production line, smaller amount of residual scrap and easy adjustment of equipment for different steel grades [21, 24].

In this study, a laboratory simulation of strip casting to produce 0.17C-1.52Si-1.61Mn-0.03Al wt. % TRIP steel was carried out for the first time. The average grain size and grain size distribution of prior austenite were simulated being equal to those of cast products. In order to obtain typical microstructures of TRIP steels, a two-stage heat treatment was carried out: first stage – for ferrite formation; the second stage – for bainite formation. The microstructures were studied using optical, scanning and transmission electron microscopy, X-ray diffraction, electron backscattered diffraction, and atom probe tomography. Mechanical properties measured via tensile testing were correlated to the microstructural parameters and process variations.

5.2 Materials and experimental techniques

5.2.1 Processing route

The chemical composition of studied steel is listed in Table 5.1. As-cast specimens of 36 × 36 mm^2 and 1.2 mm thickness were produced using dip tester at Deakin University [25], which can simulate fast cooling during solidification between twin rolls in strip casting process [24, 26]. The dip tester is used to immerse a copper substrate into molten steel for a short and controlled period of time and then immediately lift it out to simulate rapid solidification [27]. Microstructure after casting contained martensite and bainite (Fig. 5.1).

Table 5.1 The chemical composition of the studied steel (wt. %).

C	Si	Mn	Al	Cu	Cr	P	S	B
0.172	1.520	1.610	0.0266	0.0153	0.195	0.0044	<0.00050	0.00057

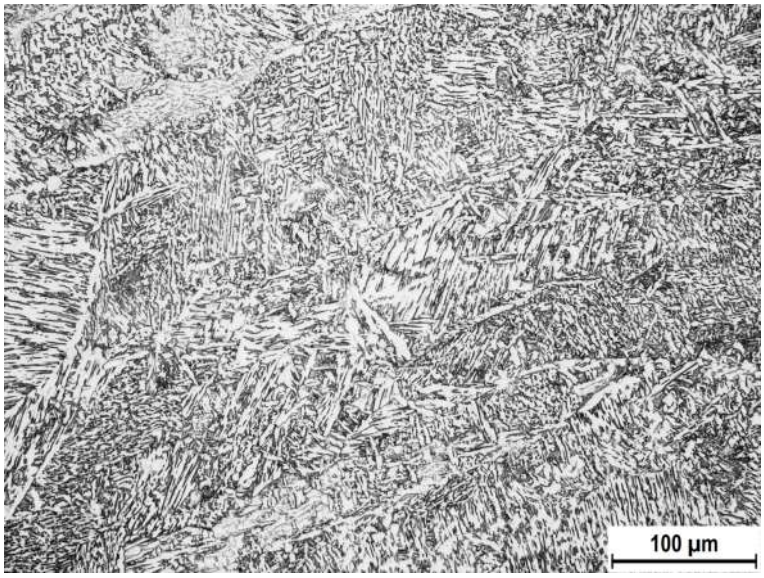

Figure 5.1 As-cast microstructure of studied steel.

A Theta Dilatronic III dilatometer was used to carry out heat treatments. To prevent oxidation or decarburization of the samples, it was operated under vacuum of ~ 6.7 x 10^{-2} Pa. The temperature was monitored using an S-type (Pt/Pt-10%Rh) thermocouple spot-welded to the surface centre of cylindrical and flat samples. The cylindrical samples had an outer diameter of 5 mm and an inner diameter of 3.5 mm with the length of 10 mm, and were used for determination of the continuous cooling transformation (CCT) diagram. The flat samples of 14 × 6 mm^2 and ~ 1 mm thickness with small holders at each port were used for the other experiments.

To simulate the prior austenite grain size (PAGS) observed in as-cast specimen, the flat samples were heated at a rate of 30 Ks^{-1} to 1250 or 1300 °C, held for 180 or 300 s, and then helium quenched to room temperature at a cooling rate of approximately 140 Ks^{-1}. Noticeably, the sample melted when it was heated to 1300 °C, thus 1250 °C austenitising temperature was selected for further experiments.

To obtain the CCT diagram, cylindrical samples were heated to 1250 °C at a rate of 30 Ks^{-1}, held for 300 s, and then cooled to ambient temperature at cooling rates of 1, 10, 40 or 110 Ks^{-1}.

The schedule used to simulate the strip casting process is illustrated in Fig. 5.2. The flat samples were heated at 30 Ks^{-1} to austenitisation temperature T_A=1250 °C, held for time t_A=300 s, cooled at a rate of 90 Ks^{-1} to austenite-to-ferrite transformation temperature or cooled to 1000 °C at a rate of 30 Ks^{-1} followed by cooling at a rate of 10 Ks^{-1} to ferrite formation temperature T_F (630, 650 and 670 °C) (hereafter referred to as 30-10 Ks^{-1} schedule), held for time t_F (0 – 300 s), quickly cooled at a rate of 50 Ks^{-1} to IBT temperatures T_{IBT} of 350, 400, 450 and 500 °C, held for time t_{IBT} = 900 s at these temperatures, and helium quenched to room temperature at a rate of ~ 140 Ks^{-1}.

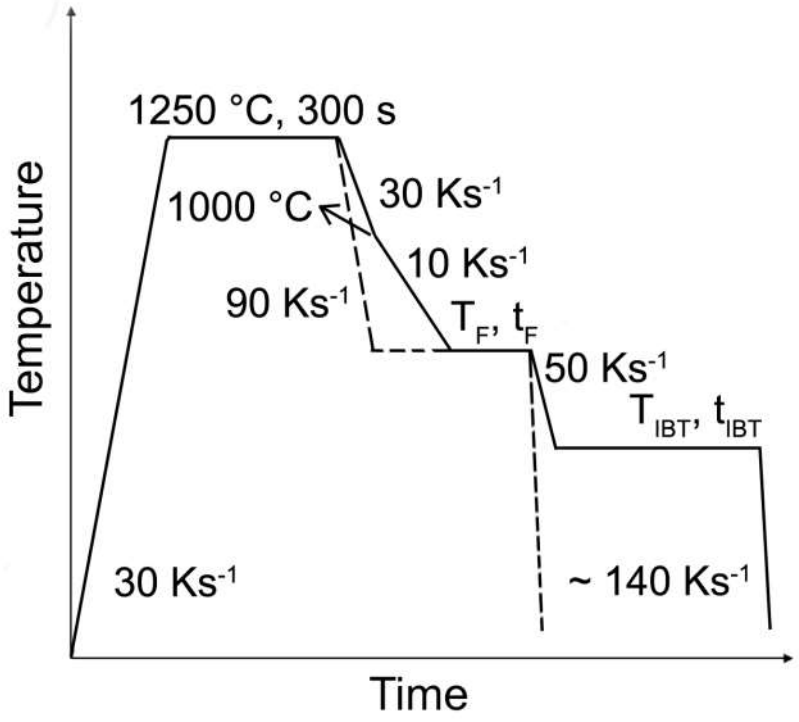

Figure 5.2 A schematic diagram of heat treatments to simulate strip casting.

5.2.2 Microstructure characterisation

5.2.2.1 Optical microscopy

The heat treated samples were cross-cut in the centre perpendicular to the long axis. The central area of the cross-section was used for observations. A Leica DMR research optical microscope (OM) was employed. To reveal the prior austenite grain boundaries, the specimens were etched for 15 – 20 s at a temperature of 65 °C in the

solution of saturated picric acid in ethanol plus few drops of benzene sulfonate. Equivalent circle diameter was utilised to describe the grain size distribution of prior austenite. Approximately 150 – 250 grains were measured for each condition.

To observe the room temperature microstructures, the heat treated samples were mechanically polished and then electropolished using an electrolyte of 330 ml methanol, 330 ml butoxyethanol and 40 ml perchloric acid at 50 V, ~ 1.0 mA and 17 °C for ~ 90 s. Microstructures were revealed using etching in 2 vol.% nital. Fractions of phases were calculated based on pixel quantities of different grey scales using Photoshop and Image Pro-Plus software. The equivalent circle diameter was calculated using at least 260 polygonal ferrite grains or second phase regions.

In addition, colour etching was employed to distinguish polygonal ferrite, bainite, martensite and retained austenite according to Ref. [28]. The samples were firstly dipped for 18 – 20 s in a solution of 4 % picral (4 gm dry picric acid in 100 ml ethanol) mixed with few drops of concentrated hydrochloric acid (1 ml per 100 ml of picral solution) and then etched for 6 – 8 s with freshly prepared 10 % aqueous sodium metabisulfite solution.

5.2.2.2 Scanning electron microscopy

Microstructures were studied further using a JEOL JSM-7001F field emission gun – scanning electron microscope (FEG – SEM) operating at 15 kV accelerating voltage and ~ 5.1 nA probe current and fitted with an 80 mm^2 X-Max energy dispersive X-ray spectroscopy (EDS) detector and a Nordlys-II(S) EBSD detector interfacing with the Oxford Instruments Aztec software suite. Electron backscattering diffraction (EBSD) and EDS information were obtained simultaneously at the centre of the electropolished cross-section using a step size of 0.04 μm and a working distance of 12 mm.

5.2.2.3 Transmission electron microscopy

A JEOL 2011 transmission electron microscope (TEM) operating at 200 kV was used to characterise the microstructure in detail. The 3 mm diameter discs were mechanically polished to ~ 80 μm thickness, and then electropolished using twin-jet

electropolishing method with an electrolyte containing 10 vol. % perchloric acid in methanol.

5.2.2.4 Atom probe tomography

Atom probe tomography (APT) experiment was carried out at Deakin University using a LEAP 4000 HR instrument (CAMECA Instruments Inc.) operating in voltage mode with a 20% pulse fraction, while the needle-like sample was at a temperature of 53 Kelvin and a pressure of 9.6 $\times 10^{-9}$ Pa. The needle-like sample was prepared applying a standard two-stage electropolishing technique [29]. The data was analysed using IVAS 3.6.8 software.

5.2.2.5 X-ray diffraction technique

The RA fraction was measured using a PANalytical X'pert-Pro MRD goniometer equipped with Ni-filtered Cu K_α radiation. It was operated at 40 kV accelerating voltage and 45 mA beam current. The X-ray diffraction (XRD) scans were conducted over range of $2\theta = 38 - 150°$ at a step size of 0.01° and a step time of 750 s on the surface of electropolished samples. The RA fraction was calculated using the integrated intensities of four austenite peaks {(111), (200), (220) and (113)} and four ferrite peaks {(110), (200), (211) and (310)} [13]. The carbon content in RA was determined using the following empirical equation [30]:

$$a = 3.572 + 0.033 \times [C\%] + 0.0012 \times [Mn\%] - 0.00157 \times [Si\%] + 0.0056 \times [Al\%] \quad (5.1)$$

where a is austenite lattice parameter (Å) [31], and [C%], [Mn%], [Si%] and [Al%] represent the concentrations in weight percentage of carbon, manganese, silicon and aluminum, respectively. For convenience, the contents of alloying elements in RA were assumed to be equivalent to the nominal steel's composition for all processing conditions.

5.2.3 Tensile tests

An in-house modified Kammrath and Weiss GmbH tensile stage was used to carry out tensile tests at a constant crosshead speed of 2 μms^{-1}, which assured an initial strain rate of 4 $\times 10^{-4}$ s^{-1}. The dog-bone tensile test samples had 4.9 mm gauge length, 2.1 mm width and ~ 1 mm thickness. At least, two samples were tested for each condition. The strain hardening rate (θ) and strain hardening exponent (n) were calculated as follows,

$$\theta = d\sigma / d\varepsilon \tag{5.2}$$

$$n = d(\ln \sigma) / d(\ln \varepsilon) \tag{5.3}$$

where σ is true stress and ε is true strain. The modified Crussard – Jaoul (C – J) model was used to analyse the multistage hardening behaviour in the studied steel [32]:

$$\varepsilon = \varepsilon_0 + c\sigma^m \tag{5.4}$$

where ε_0 is the initial true strain, c is a constant and m is the strain hardening index. m is calculated using the following equation:

$$\ln(d\sigma / d\varepsilon) = (1 - m)\ln \sigma - \ln(cm) \tag{5.5}$$

5.3 Results

5.3.1 Prior austenite microstructure simulation

Fig. 5.3 shows typical prior austenite microstructures and PAGS distributions in as-cast and heat treated samples. The PAGBs were identified based on the traces of grain boundaries revealed by the picral etching. The different contrast between as-cast and heat treated samples is due to the different etching time and higher carbon content at PAGBs arising from the longer time for carbon diffusion to the PAGBs in the heat treated samples. PAGS increased with an increase in holding time. After holding at 1250 °C for 180 and 300 s, the average grain size was 71±28 and 80±27 μm, respectively. The average grain size of 80±27 μm after holding at 1250 °C for 300 s was similar to as-cast sample's average grain size of 83±31 μm. In addition, the sample held at 1250 °C for 300 s had comparable PAGS distribution to that of the as-cast sample (c.f. Figs. 5.3(c, d)). Thus, this condition was selected for all future experiments (Fig. 5.2).

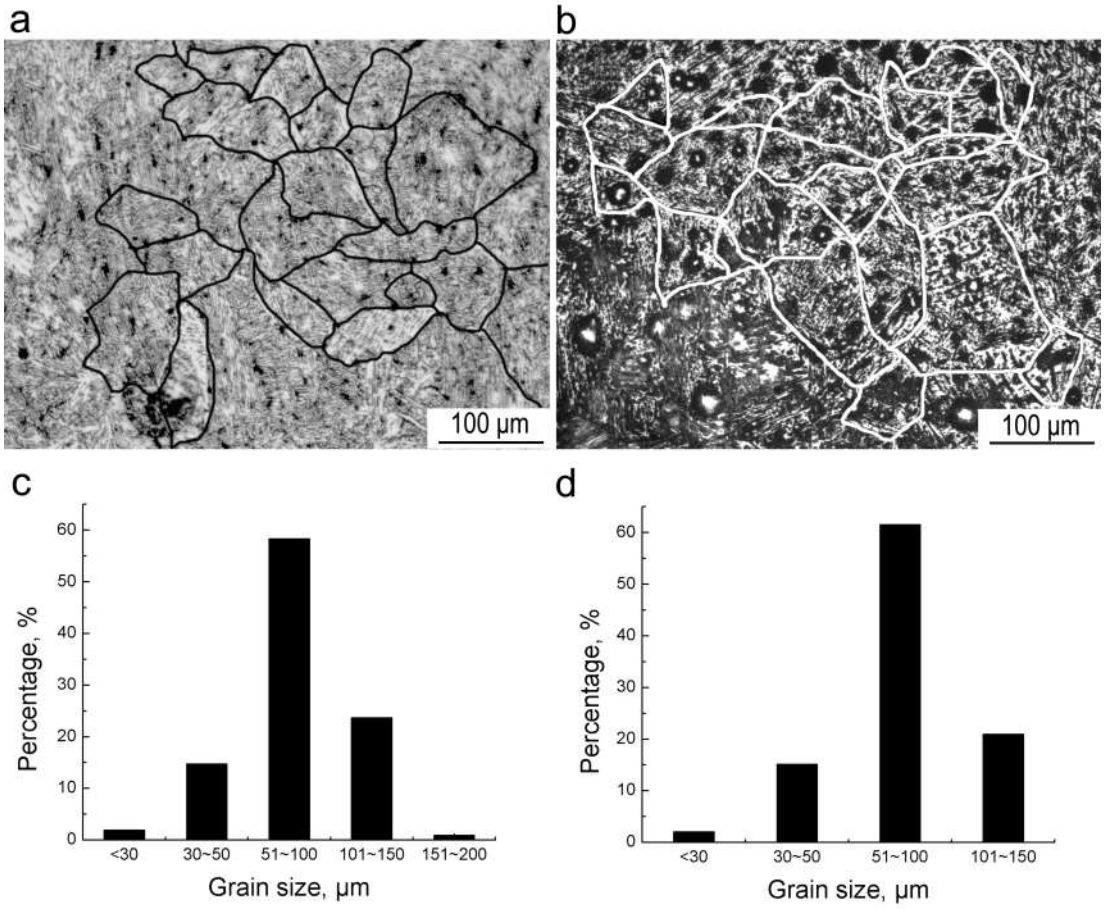

Figure 5.3 Comparison of (a, b) prior austenite microstructures and (c, d) prior austenite grain size distribution (a, c) in as-cast condition and (b, d) as-quenched after holding at 1250 °C for 300 s.

5.3.2 Continuous cooling transformation diagram

To assess the effect of cooling rate on phase balance, the CCT diagram was obtained (Fig. 5.4) using microstructures shown in Fig. 5.5. A small amount of ferrite and pearlite, and a large amount of bainite and martensite were observed at the cooling rate of 1 Ks^{-1}. At cooling rates between 10 and 110 Ks^{-1}, the microstructures consisted of bainite and martensite. Bainite was still observed at the highest cooling rate of 110 Ks^{-1}, due to large prior austenite grains [33, 34]. Ferrite transformation start temperature (A_{r1}) decreased from 662 to 625 °C when the cooling rates increased from 1 to 10 Ks^{-1}. Bainite transformation start temperature (B_s) first increased from 559 to 625 °C, when the cooling rate increased from 1 to 10 Ks^{-1} and then decreased from 625 to 530 °C, with an increase in cooling rate to 40 Ks^{-1}. On further increasing cooling rate to 110 Ks^{-1}, the B_s increased again up to 631 °C. It

corresponds to observations by other researchers [33, 35]. B_s and martensite transformation start temperature (M_s) were calculated as 625 and 415 °C, respectively, based on Steven & Haynes's [36] and Andrews's [37] equations. The calculated B_s and M_s are consistent with the experimental values as shown in Fig. 5.4.

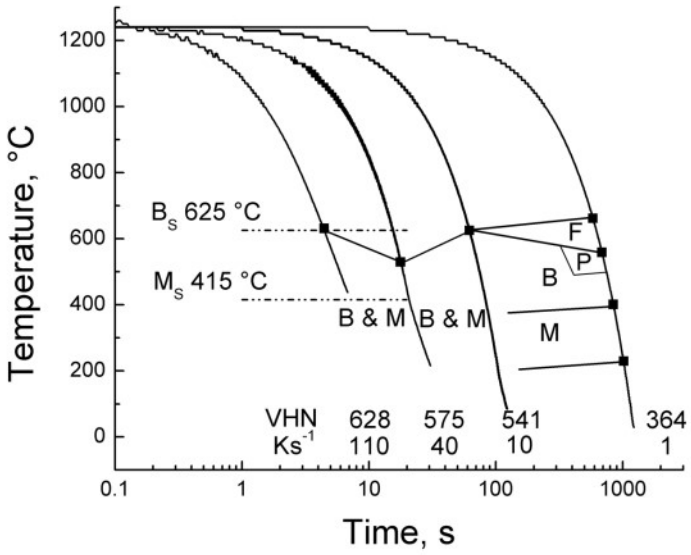

Figure 5.4 Continuous cooling transformation diagram of as-cast TRIP steel cooled from 1250 °C after holding for 300 s. *F* is ferrite, *P* is pearlite, *B* is bainite and *M* is martensite.

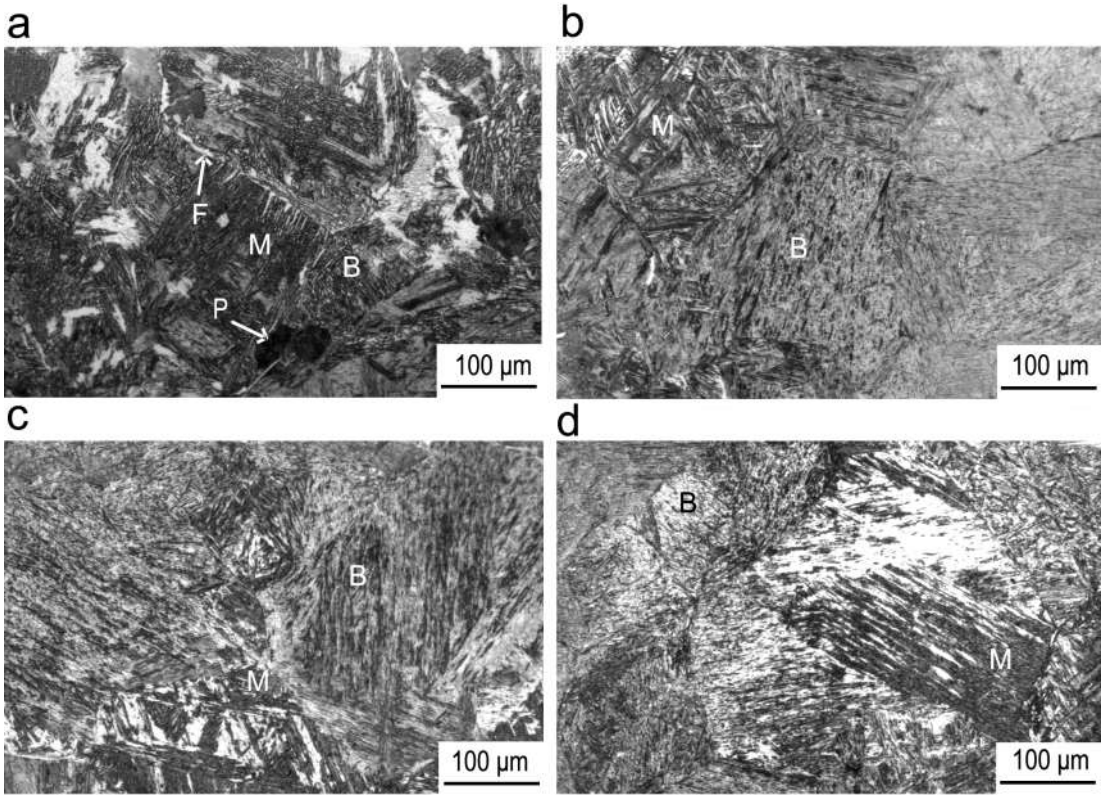

Figure 5.5 Microstructures after austenitising for 300 s at 1250 °C and cooling at (a) 1, (b) 10, (c) 40 and (d) 110 Ks^{-1}. *F* is ferrite, *P* is pearlite, *B* is bainite and *M* is martensite.

5.3.3 Effect of holding temperature, holding time and cooling rate on ferrite and pearlite formation

According to the CCT diagram (Fig. 5.4), three holding temperatures of 630, 650 and 670 °C were selected to investigate ferrite formation. For the cooling rate of 90 Ks^{-1} from austenitisation temperature to ferrite formation temperature, after holding for 300 s at ferrite formation temperature followed by helium quenching to room temperature, the corresponding microstructures are shown in Fig. 5.6. The ferrite fractions were 0.46±0.04, 0.56±0.02 and 0.50±0.03 after holding at 630, 650 and 670 °C, respectively. With an increase in holding temperature, the ferrite fraction increased and then decreased, showing a maximum point after holding at 650 °C. A maximum of ferrite fraction corresponds to the nose temperature of ferrite transformation field (~ 650 °C) of the CCT diagram. However, some pearlite was observed after holding at 630 and 650 °C (Figs. 5.6(a, b, d)), which is adverse to TRIP steel [4, 38]. In addition, the ferrite grain obviously exhibited a more polygonal

shape after holding at 670 °C than that after holding at 630 °C. Therefore, the temperature of 670 °C was set as holding temperature at austenite-to-ferrite transformation region.

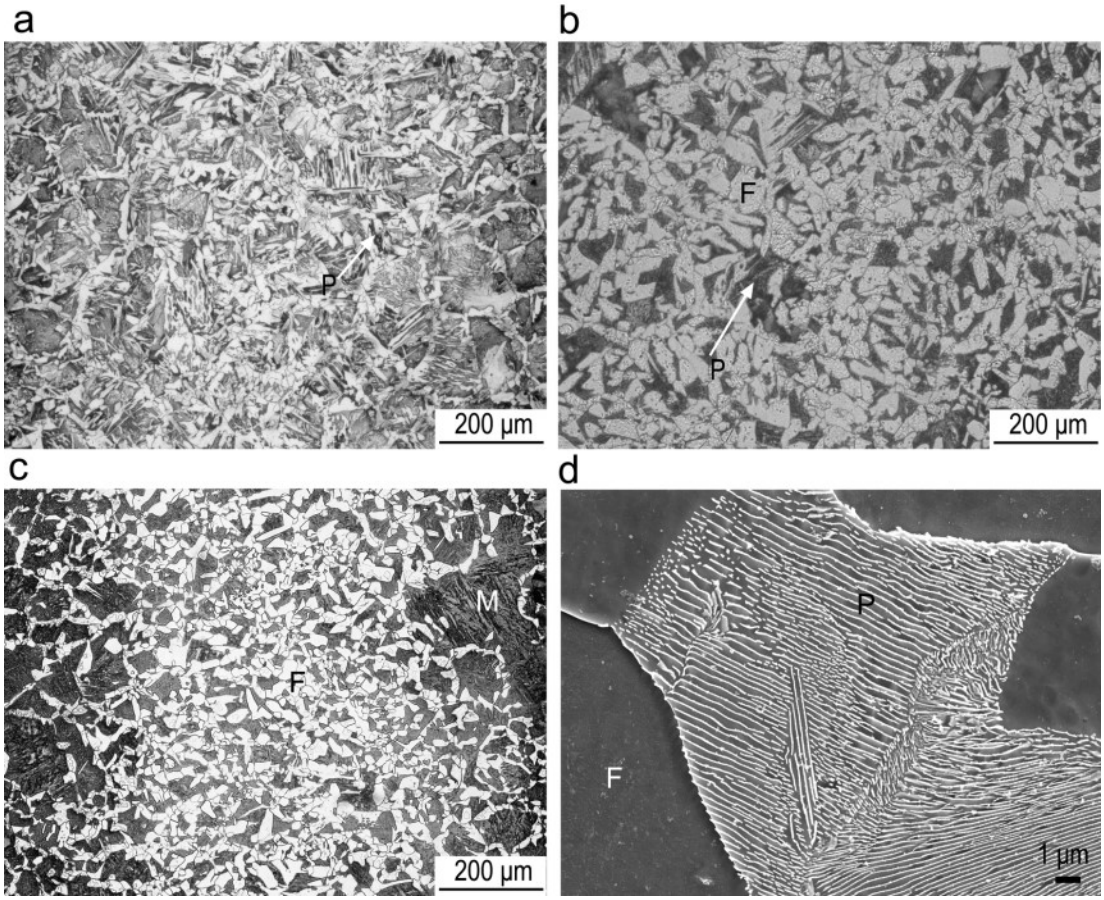

Figure 5.6 Microstructures after austenitising at 1250 °C for 300 s, cooling at 90 Ks^{-1} to ferrite formation region and then holding at (a) 630 °C for 300 s, (b, d) 650 °C for 300 s and (c) 670 °C for 300 s. *F* is ferrite, *P* is pearlite and *M* is martensite.

The influence of holding time for two cooling rates on ferrite fraction is plotted in Fig. 5.7. For the cooling schedule of 30-10 Ks^{-1}, the ferrite formation was fast within the first 100 s of holding. After holding for more than 100 s, the formation of ferrite continued at a slow rate. A similar phenomenon was observed in Ref. [3]. After 0 s holding, 0.22±0.01 ferrite was observed, which supported the ferrite formation during cooling from 1250 to 670 °C**.** Thus, the cooling schedule of 30-10 Ks^{-1} resulted in a higher ferrite fraction for the same holding time, compared to the cooling rate of 90 Ks^{-1}. In addition, cooling with 30-10 Ks^{-1} schedule better depicted the industrial processing [24]. Thus, the cooling rate of 30-10 Ks^{-1} was chosen as the

cooling rate from austenitisation temperature to ferrite formation temperature. Based on published data [4, 18], the presence of ~ 0.5 fraction of ferrite resulted in a better combination of mechanical properties in TRIP steels. Therefore, holding at 670 °C for 90 s, which led to 0.53±0.04 ferrite formation, was chosen for austenite-to-ferrite transformation.

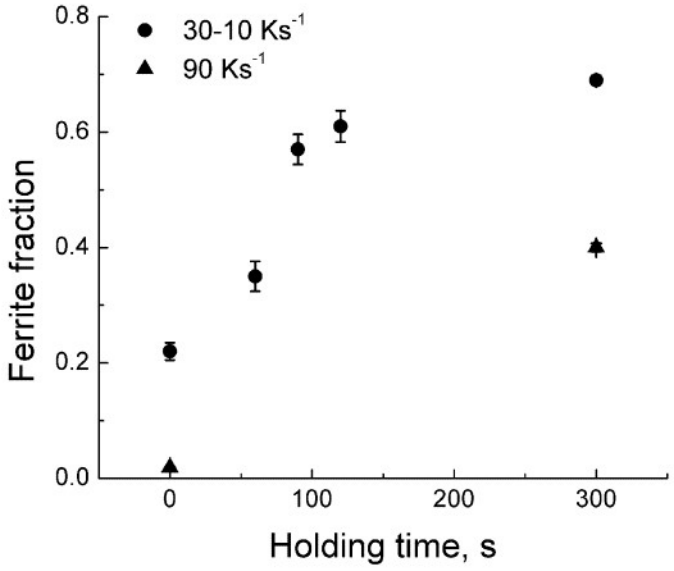

Figure 5.7 The ferrite fraction variation with holding time when holding at 670 °C.

5.3.4 Microstructure characterisation

After holding at 670 °C for 90 s, samples were quickly cooled at a rate of 50 Ks^{-1} to IBT temperature in order to avoid pearlite formation during cooling [38, 39] and then held for 900 s (in order to simulate the coiling process in industry). Four IBT temperatures of 350, 400, 450 and 500 °C were chosen. Hereafter, TQ refers to the sample directly quenched from 670 °C to room temperature, and T 350, T 400, T 450 and T 500 refer to the samples held at 350, 400, 450 and 500 °C, respectively.

5.3.4.1 Optical microstructures

Fig. 5.8 shows the nital- and colour-etched microstructures. Polygonal ferrite, martensite and a small amount of Widmanstätten ferrite were formed in TQ sample (Figs. 5.8(a, b)) after direct quenching to room temperature from ferrite formation temperature. On the other hand, after the subsequent holding at bainite formation

temperature, the samples consisted of polygonal ferrite, bainite, martensite, retained austenite, and Widmanstätten ferrite (Figs. 5.8(c-h)).

After holding at 350 °C, very small austenite islands remained after ferrite formation (referred to as remaining austenite hereafter) transformed to bainite, as demonstrated by dark bluish colour (indicated by the arrows) in Fig. 5.8(d). Very little amount of retained austenite at room temperature (hereafter referred to as retained austenite, RA) located in the vicinity of the interfaces between polygonal ferrite and second phase region. When the IBT temperature increased to 400 °C, the colour etched images showed less of small dark bluish islands and more RA adjacent to the interfaces between polygonal ferrite and second phase region (Fig. 5.8(f)). In addition, some RA was surrounded by polygonal ferrite, and some blocky martensite was revealed adjacent to the interfaces between polygonal ferrite and second phase region. With an increase in IBT temperature to 450 °C, the colour etching image showed more martensite (brown islands in Fig. 5.8(h)). Noticeably, more RA adjacent to the interfaces between polygonal ferrite and second phase region was observed in T 400 sample, whereas more martensite islands in T 450 sample were at these locations (c.f. Figs. 5.8 (f, h)). In addition, the small second phase region in T 450 sample was composed of more martensite and less RA compared to the T 400 sample (c.f. Figs. 5.8 (f, h)).

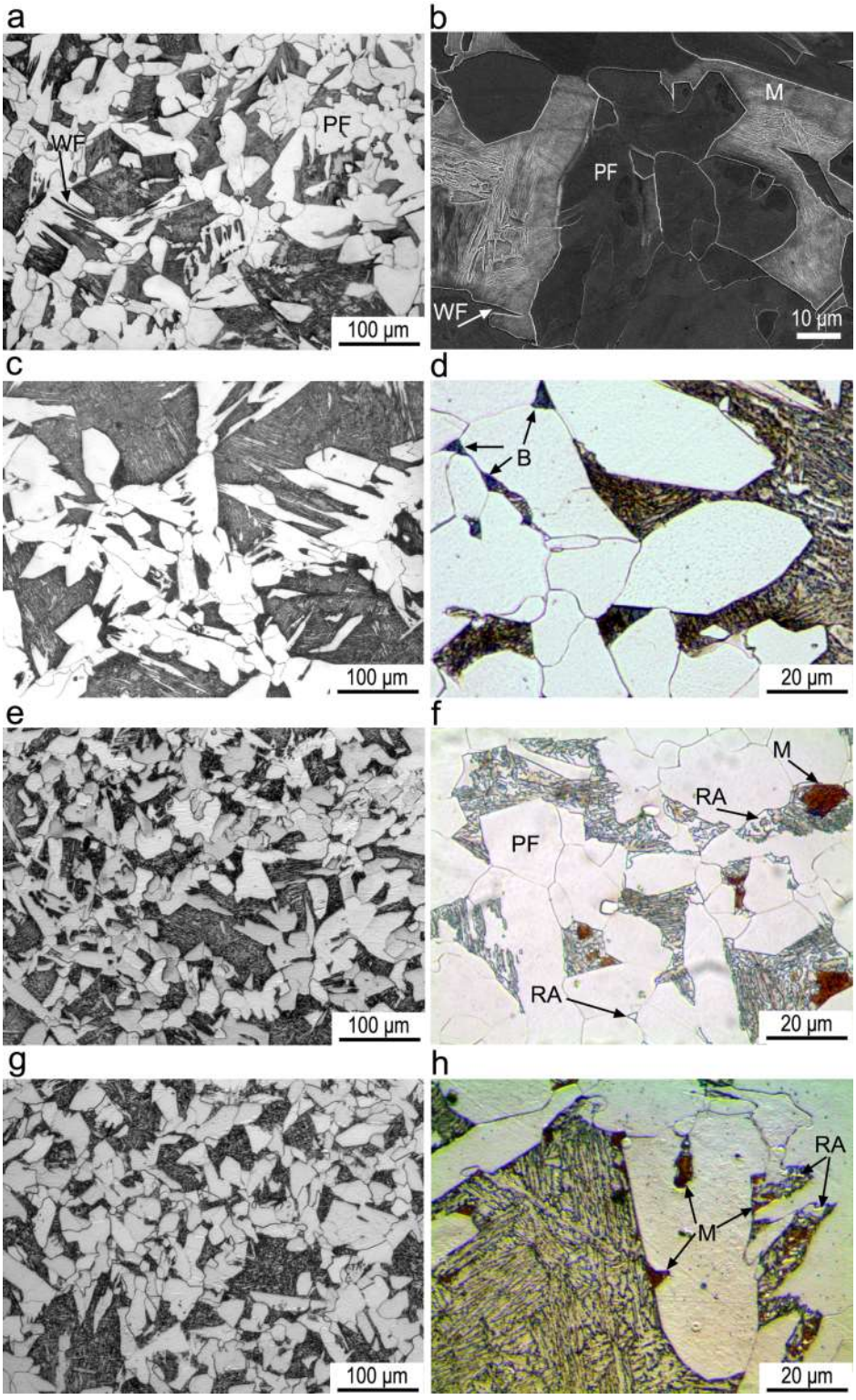

Figure 5.8 Optical and SEM images of microstructures after directly quenching following the holding at 670 °C for 90 s; (c, e, g) nital and (d, f, h) colour etched microstructures after holding at (c, d) 350 °C, (e, f) 400 °C and (g, h) 450 °C for 900 s (15 min). Ferrite is shown with grey/white, bainite with dark grey/bluish, retained austenite with grey/white and martensite with brown colours in (d, f, h). *PF* is polygonal ferrite, *B* is bainite, *M* is martensite, *RA* is retained austenite and *WF* is Widmanstätten ferrite.

In the T 400 sample, the average polygonal ferrite grain size was 17±10 μm while the average size of second phase region was 21±24 μm. The other samples had a very similar polygonal ferrite average grain size and the size of second phase region. The distributions of the sizes in T 400 sample are shown as a representative of all the samples in Fig. 5.9. Polygonal ferrite exhibited a normal distribution and the second phase region showed an exponential distribution. The inhomogeneity of the size distribution of second phase region was related to large area percentage of the second phase islands larger than 100 μm.

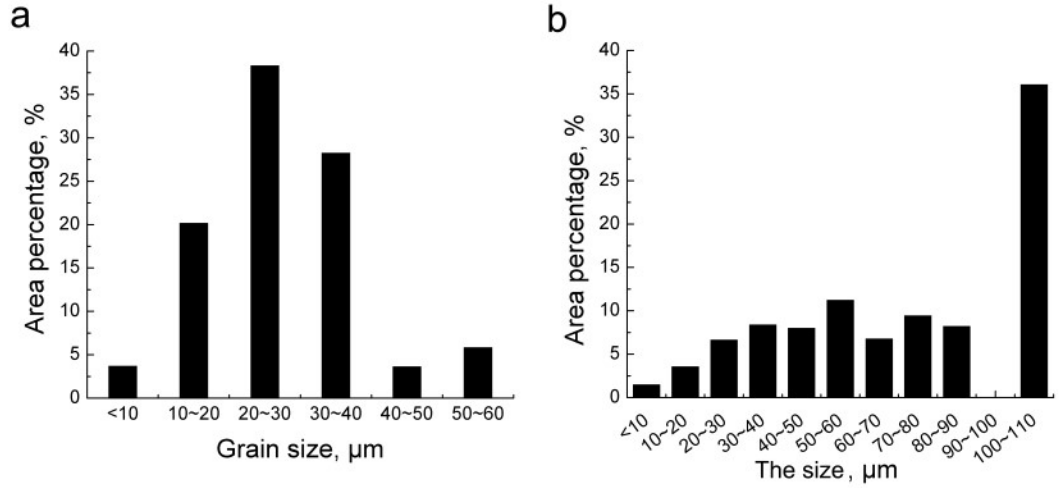

Figure 5.9 (a) Ferrite grain size distribution and (b) the size distribution of second phase region for T 400 sample.

5.3.4.2 X-ray diffraction analysis

Fig. 5.10(a) shows the XRD patterns for different heat treated samples. After IBT holding, the face-centred cubic phase was detected, which revealed the existence of RA. On the other hand, RA was not detected in TQ sample. The RA fraction increased from 0.025±0.002 to 0.045±0.003 and then decreased to 0.023±0.002 when IBT increased from 350 to 400 and 450 °C (Fig. 5.10(b)). The carbon content in RA decreased from 1.36±0.01 to 0.92±0.01 wt.%.

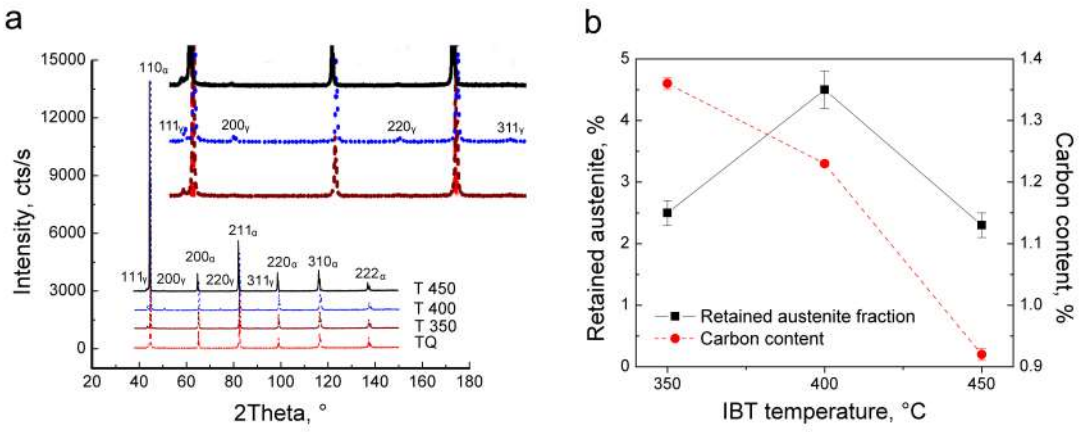

Figure 5.10 (a) X-ray diffraction patterns after different heat treatments; (b) retained austenite fraction and carbon content as a function of bainite holding temperature.

5.3.4.3 Scanning and transmission electron microscopy observations

After holding at 350 °C, second phase regions consisted of predominantly bainitic ferrite, some granular bainite, and martensite and/or retained austenite islands (Fig. 5.11(a)). Bainitic ferrite is defined as ferrite laths separated by film RA and/or martensite; whereas, granular bainite is the arrangement of carbide-free bainite with irregular-shaped ferrite and dispersed blocky RA/martensite constituent [40]. Small second phase regions (3 – 5 μm in equivalent circle diameter) transformed to bainitic ferrite or granular bainite during IBT holding (Fig. 5.11(b)), which support the dark bluish bainite areas observed in Fig. 5.8(d). When the islands were smaller than 1 μm, they were martensite and/or RA islands (Fig. 5.11(b)). Some of the martensite and RA islands were located at the polygonal ferrite/second phase region interfaces.

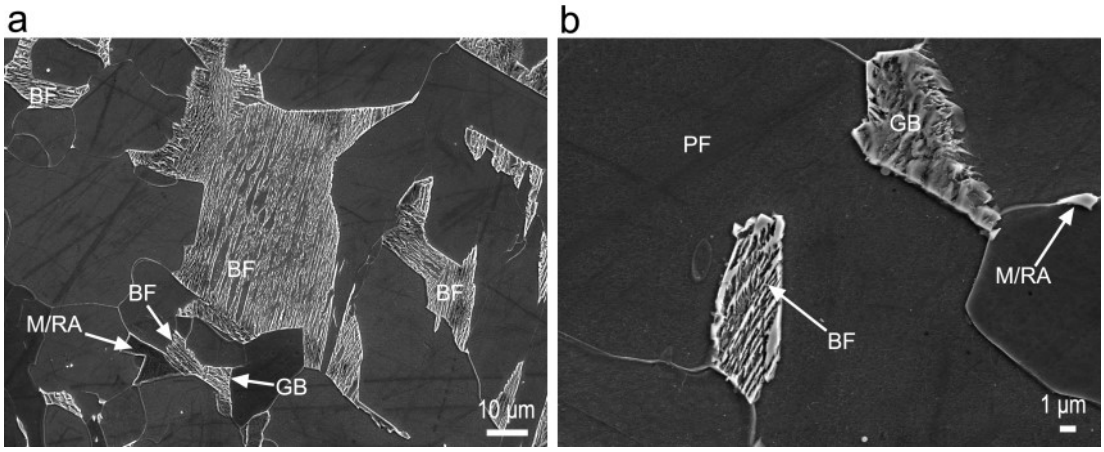

Figure 5.11 Typical SEM images of (a) overview and (b) small second phase regions after holding at 350 °C for 900 s (15 min). *PF* is polygonal ferrite, G*B* is granular bainite, *BF* is bainitic ferrite, and *M/RA* is martensite and/or retained austenite.

When the holding temperature was 400 °C, the microstructure of large second phase regions (> 20 μm) consisted of predominately bainitic ferrite, some martensite and/or RA islands embedded in them (Fig. 5.12(b)). Small second phase regions (< 20 μm) included bainitic ferrite and/or granular bainite (Figs. 5.12(c, d)). Bainitic ferrite laths in large second phase region showed multi-orientations (Fig. 5.12(b)); whereas, in small second phase region bainitic ferrite exhibited only one orientation (Fig. 5.12(d)). Very small martensite and/or RA islands, indicated by an arrow in Fig. 5.12(c), were observed within polygonal ferrite grains. Some martensite or RA islands were located between polygonal ferrite and second phase region, which corresponded to the observation in Fig. 5.8(f). Film martensite or RA could also be seen between bainitic ferrite laths.

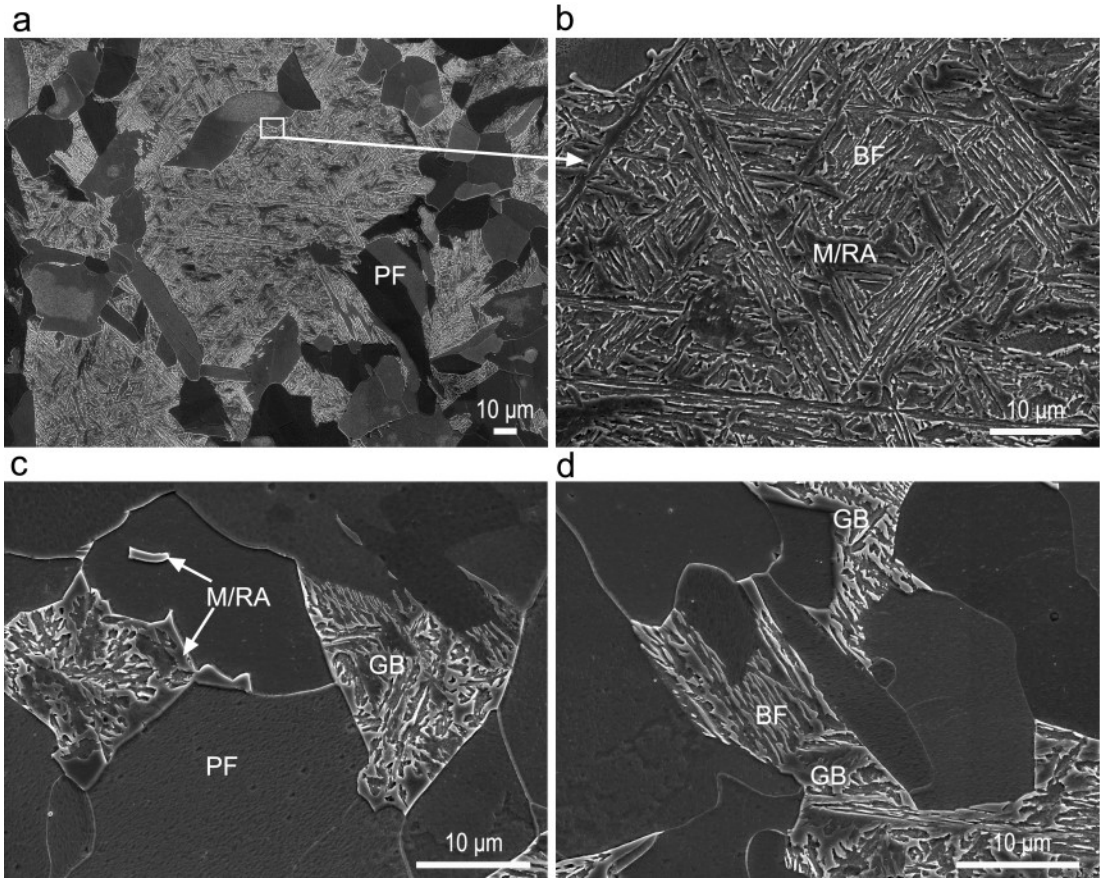

Figure 5.12 Typical SEM images of (a) overview, (b) large second phase region and (c, d) small second phase regions after holding at 400 °C for 900 s (15 min). *PF* is polygonal ferrite, G*B* is granular bainite, *BF* is bainitic ferrite, and *M/RA* is martensite and/or retained austenite.

Film RA of smaller than 200 nm size (Figs. 5.13 (a, b)) was observed between bainitic ferrite laths in the large second phase regions (such as the one in Fig. 5.12(a)). The RA near the polygonal ferrite/second phase region interfaces and the RA in granular bainite were observed in Fig. 5.13(c). Martensite was also observed adjacent to the polygonal ferrite/second phase region interface (Fig. 5.13(d)). The TEM observations (Fig. 5.13) corresponded to those presented in the colour etching images in Fig. 5.8(f) and SEM images in Fig. 5.12. An increased dislocation density near the martensite-ferrite grain boundary (Fig. 5.13(d)) is clearly visible.

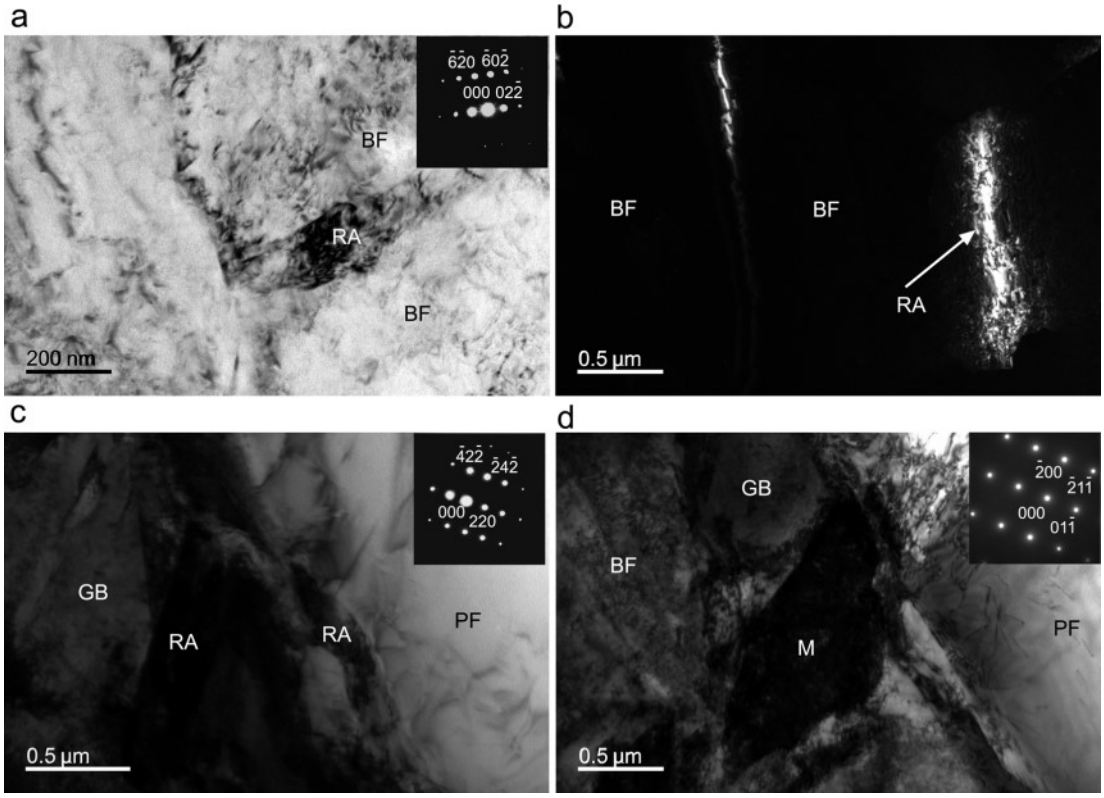

Figure 5.13 TEM images after holding at 400 °C for 900 s (15 min): (a) bright field and (b) dark field images showing retained austenite between bainitic ferrite laths (the zone axis of inset in (a) is $[\bar{1}33]_\gamma$, and dark field image was taken from $(02\bar{2})_\gamma$; (c) retained austenite and (d) martensite adjacent to the interfaces between polygonal ferrite and second phase region (the zone axis of insets in (c, d) are $[\bar{1}13]_\gamma$ and $[011]_\alpha$, respectively). *PF* is polygonal ferrite, G*B* is granular bainite, *BF* is bainitic ferrite, *RA* is retained austenite and *M* is martensite.

For the 450 °C IBT temperature, the microstructure was similar to that of T 400 sample (c.f. Figs. 5.12 and 5.14). The largest difference observed was the presence of serrated interfaces between polygonal ferrite and second phase regions (indicated by a circle in Fig. 5.14(c)). They probably contained martensite. Adjacent to the polygonal ferrite/second phase region interfaces, smaller blocky RA and larger blocky martensite were observed in granular bainite (Fig. 5.15(a)). Fig. 5.15(b) demonstrated a film martensite (instead of RA) present between bainitic ferrite laths, which may indicate transformation of unstable RA to martensite during cooling from IBT to ambient temperature. Twinned martensite was also observed, and a blocky martensite with small RA was present near the twinned martensite (Fig. 5.15(c)), which may be the microstructure similar to the circled area in Fig. 5.14(c). The twinned martensite forms from higher carbon content austenite and at lower

temperature compared to martensite with only dislocation substructure [41]. In addition, a blocky martensite was observed, along with small blocky RA (Fig. 5.15(d)) corresponding to the martensite/RA constituent in Figs. 5.8(h) and 5.14(b).

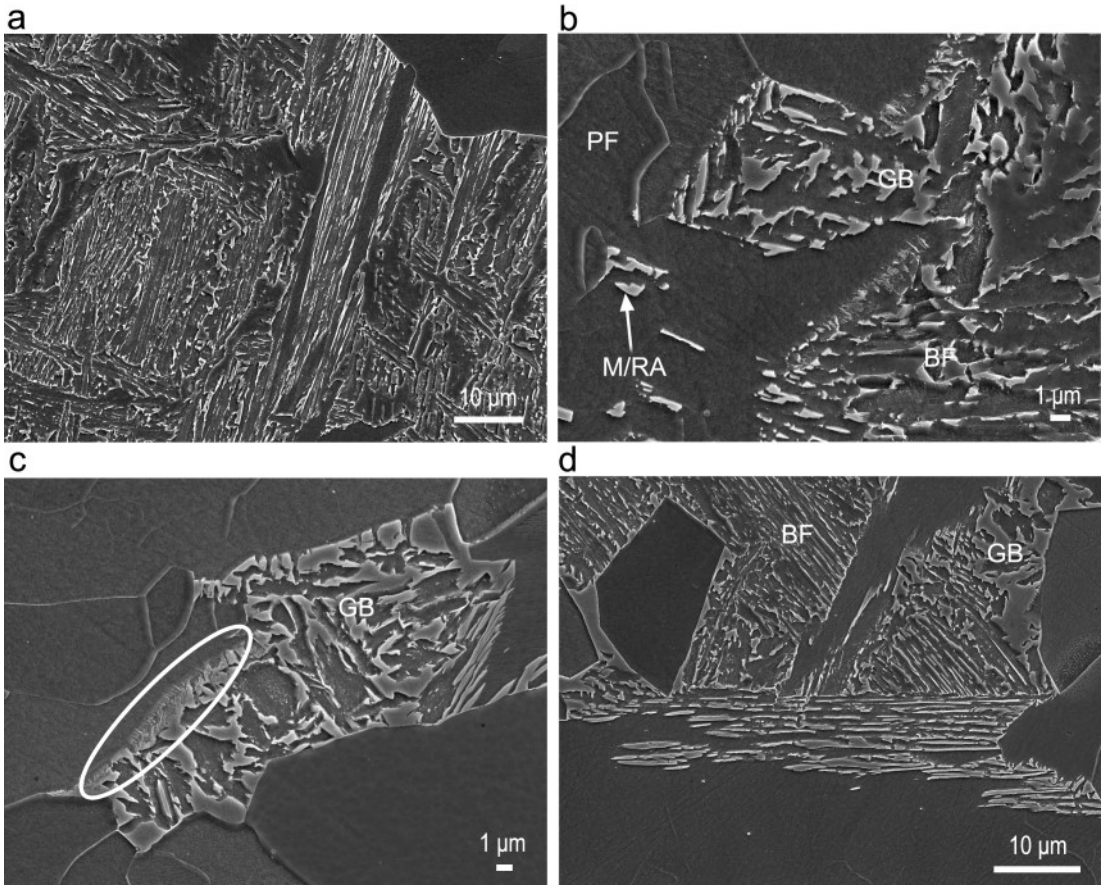

Figure 5.14 Typical SEM images of (a) large second phase region and (b, c, d) small second phase regions after holding at 450 °C for 900 s (15 min). *PF* is polygonal ferrite, G*B* is granular bainite, *BF* is bainitic ferrite and *M/RA* is martensite and/or retained austenite.

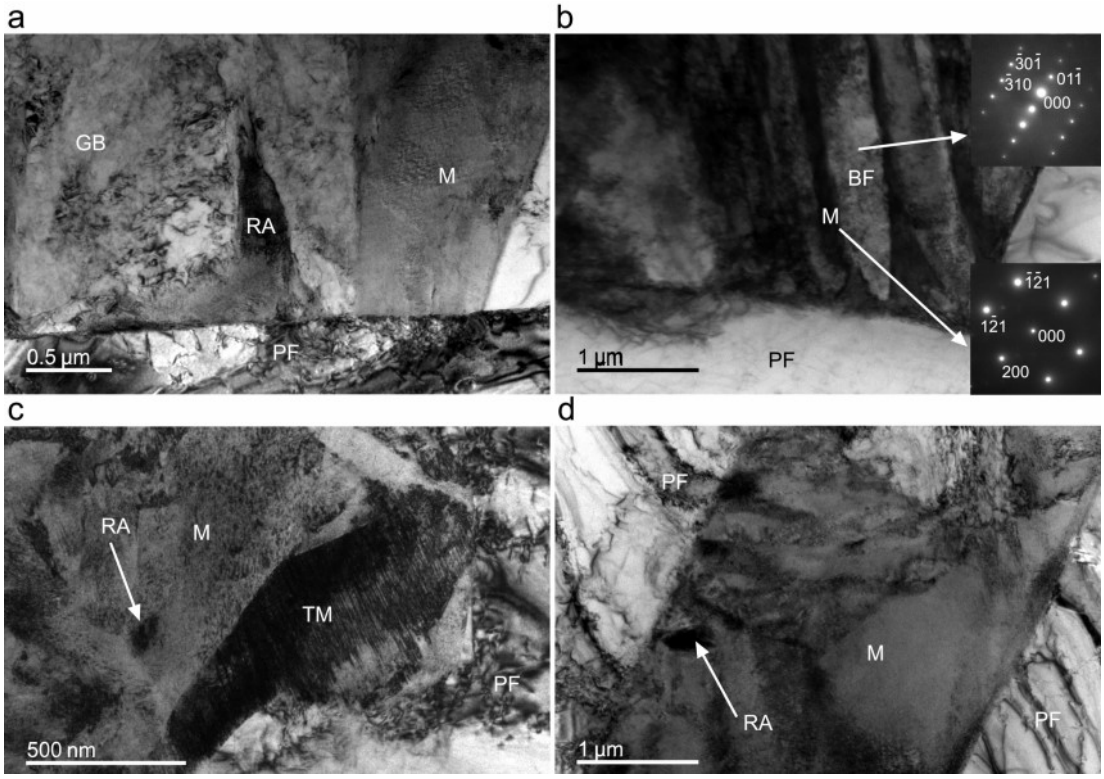

Figure 5.15 TEM images of microstructures after holding at 450 °C for 900 s (15 min): (a) retained austenite and martensite near the interface between polygonal ferrite and second phase region; (b) martensite between bainitic ferrite laths (the zone axis of BF and M is $[\bar{1}33]_{\alpha}$ and $[012]_{\alpha}$, respectively); (c) twinned martensite; (d) martensite island with some retained austenite among polygonal ferrite. *PF* is polygonal ferrite, G*B* is granular bainite, *BF* is bainitic ferrite, *RA* is retained austenite, *M* is martensite and *TM* is twinned martensite.

With increasing IBT temperature up to 500 °C, some pearlite was observed by optical microscopy (Fig. 5.16(a)), which was revealed as a lamellar structure using SEM (Fig. 5.16(b)). Some large martensite islands were also observed (Fig. 5.16(b)).

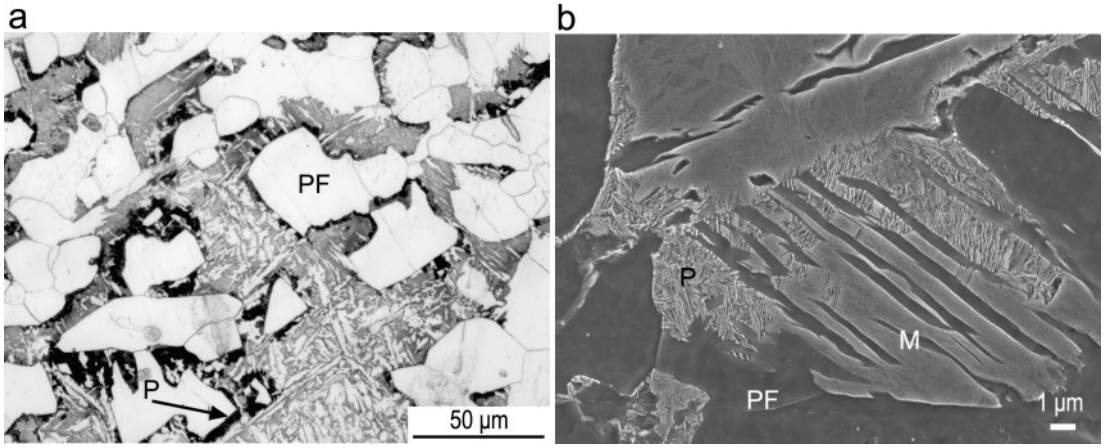

Figure 5.16 (a) Optical and (b) SEM images after holding at 500 °C for 900 s (15 min). *PF* is polygonal ferrite, *P* is pearlite and *M* is martensite.

5.3.4.4 EBSD and APT analysis of the T 400 sample

The microstructure of T 400 sample was further studied using EBSD and APT because this sample contained the largest RA fraction. Fig. 5.17 shows the EBSD maps and partly corresponding EDS maps of carbon and manganese. In the larger second phase region, RA was mainly located near the interfaces between second phase region and polygonal ferrite; although, some very tiny RA between bainitic ferrite laths or between bainitic packets were also observed (Fig. 5.17(b)). In the smaller second phase region, more RA was observed in bainitic ferrite and granular bainite (Fig. 5.17(b)). Based on this, the smaller second phase region contained more RA, however, it should be noted that only RA larger than 120 nm could be detected by EBSD due to the step size of 40 nm used. The sensitivity of EDS/EBSD simultaneous approach to carbon was proved by correlative electron microscopy study on TRIP steel [40]. As could be clearly seen in Fig. 5.17(c), the polygonal ferrite is depleted in carbon compared to bainite regions. The grain boundary between polygonal ferrite and second phase region had a larger carbon content (Fig. 5.17 (c)), which was also observed in Ref. [42]. The RA regions were carbon enriched (Fig. 5.17(c)). Some carbon enriched areas which did not correspond to RA in phase map were martensite (c.f. Figs. 5.17(c, d)). On the other hand, manganese was nearly homogeneously distributed (Fig. 5.17(d)). This can be a result of a low tendency for partitioning of substitutional alloying elements [43] and also of the less variation in Mn content between different phases compared to the order of magnitude

difference for carbon [44]. The rectangle area in Fig. 5.17(c) was contaminated by carbon during the focusing process.

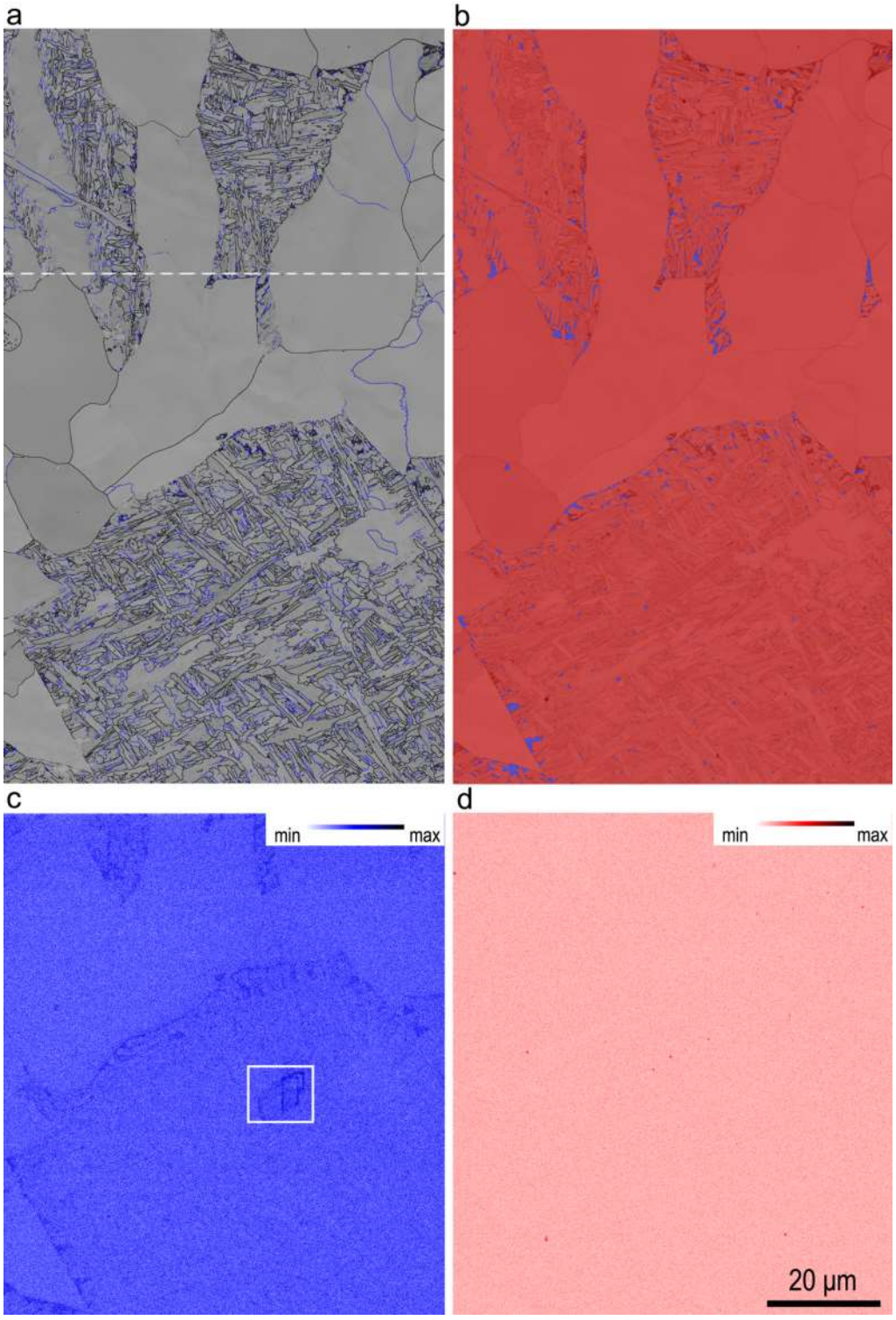

Figure 5.17 T 400 sample's EBSD maps of (a) the band contrast with grain boundaries (black = high angle grain boundaries, blue = low angle grain boundaries) and (b) phase distribution (blue = fcc austenite, red = bcc ferrite), and corresponding EDS maps of (c) carbon and (d) manganese for the area below the dash line in (a). The area marked by a rectangle in (c) was contaminated by carbon during focusing.

Although SEM and TEM data did not show the presence of any carbides, atom probe revealed several carbon segregations (Fig. 5.18(a)). The carbon depleted area having 0.6 at.% carbon was bainitic ferrite lath according to the similar reported values of carbon content in bainitic ferrite laths based on APT studies of comparable steels [39, 45]. The carbon content in this enriched area was approximately 25 at.% (Figs. 5.18(b, c)) and corresponds to that of the cementite [46]. As can be seen in Fig. 5.18(c), the carbon content rapidly increased across the interface between bainitic ferrite lath and cementite while the silicon content obviously decreased due to its rejection from cementite [13, 18]. A slight enrichment of Mn in cementite is also present.

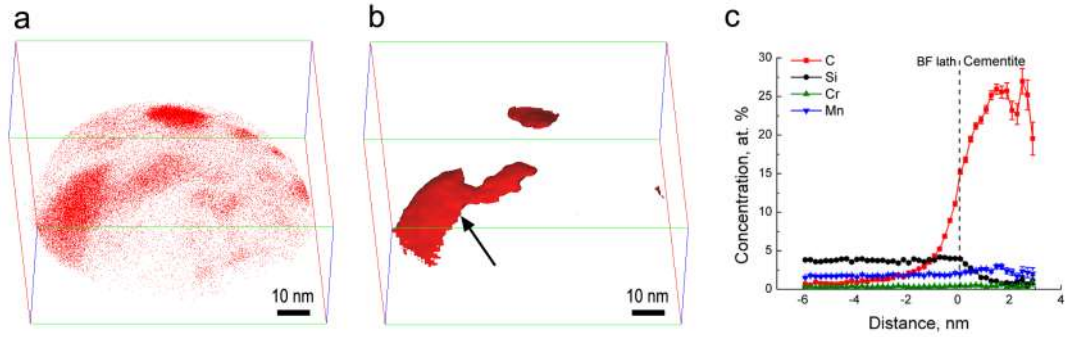

Figure 5.18 Atom probe tomography characteristisation of T 400 sample: (a) carbon atom map, (b) carbon iso concentration surface at 12.0 at. % and (c) a proximity histogram across the bainitic ferrite lath/cementite interface indicated by the arrow in (b). *BF* is bainitic ferrite.

5.3.5 Mechanical properties

Fig. 5.19 shows mechanical behaviours of differently heat treated samples, while corresponding mechanical properties extracted from the engineering strain – engineering stress curves are listed in Table 5.2. Thus, the T 500 sample was not tensile tested due to the harmful effect of pearlite on mechanical properties via a decrease in RA fraction [4, 38]. Continuous yielding was observed for all conditions (Fig. 5.19(a)), which is characteristic of multiphase microstructures [47]. Thus, the yield stress (YS) was determined using 0.2 % offset. The TQ sample exhibited a typical behaviour of ferrite-martensite DP steel [6, 22]: larger YS and ultimate tensile strength (UTS), and lower uniform elongation (UE) and total elongation (TE) compared to the samples held at bainite transformation temperature. Amongst samples held for bainite formation, the T 400 sample showed the largest UTS and TE, leading to the best combination of mechanical properties (Table 5.2). The strain

hardening rate for all conditions showed an exponential decrease with an increase in true strain (Fig. 5.19(b)). With respect to IBT held samples, the strain hardening rate of TQ sample decreased more slowly at lower strains but much faster at higher strains. Amongst IBT held samples, the strain hardening rate of T 400 sample decreased faster at lower strains but more slowly at higher strains than for other conditions.

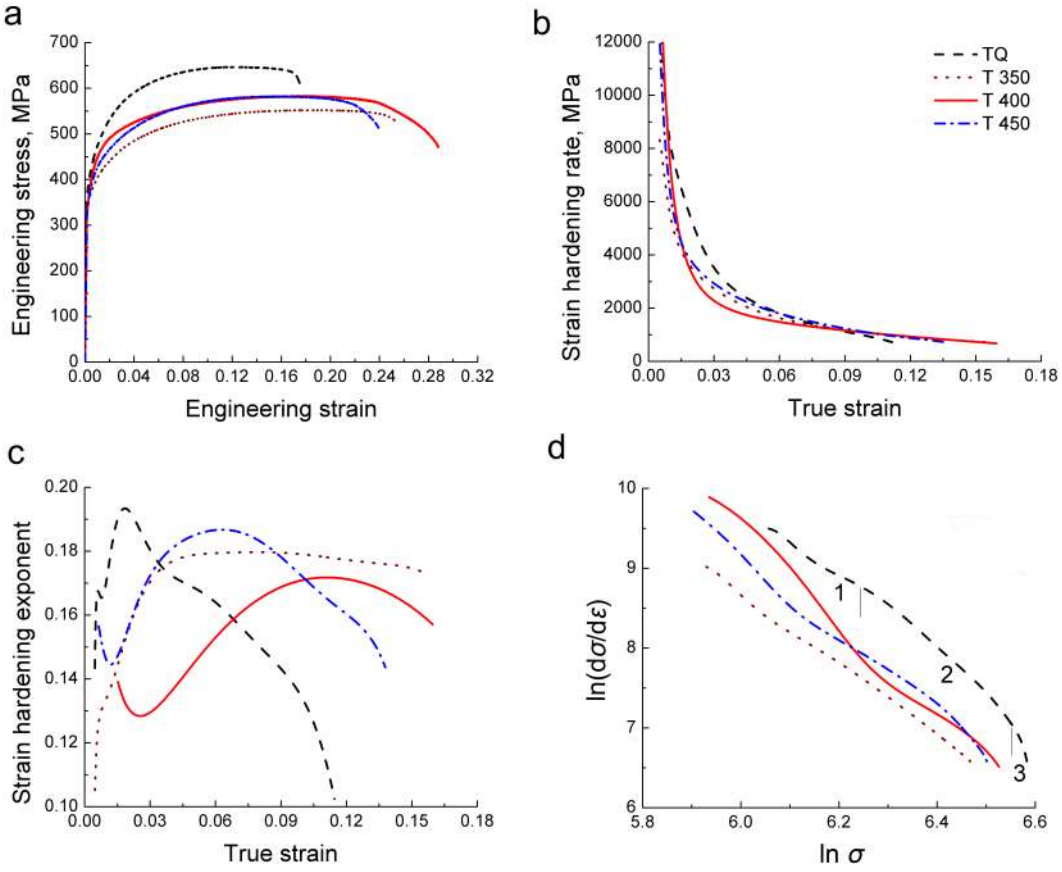

Figure 5.19 (a) Engineering stress – strain curves, (b) strain hardening rate and (c) instantaneous strain hardening exponent *n* as a function of true strain, and (d) strain hardening behaviours based on the modified Crussard – Jaoul model analysis, where three distinct stages of strain hardening were denoted by the vertical lines and numbers.

Table 5.2 Mechanical properties.

Specimen	Ferrite fraction	Yield strength, MPa	Ultimate tensile strength, MPa	Uniform elongation	Total elongation	Product of ultimate tensile strength and total elongation, MPa%
TQ	0.56±0.03	398±22	608±39	0.13±0.008	0.20±0.018	12160
T 350	0.60±0.04	344±20	552±31	0.17±0.007	0.25±0.012	13800
T 400	0.55±0.06	356±12	590±35	0.17±0.029	0.27±0.049	15930
T 450	0.54±0.05	335±23	581±3	0.15±0.004	0.24±0.014	13944

The TQ sample showed a strain hardening exponent behaviour similar to ferrite-martensite DP steel [6, 22], which is a rapid increase to a maximum point of 0.193 and then a fast decrease (Fig. 5.19(c)). The T 350 sample also had a quick increase in strain hardening exponent to a maximum point of 0.190 but then showed a slow decrease. The strain hardening exponents of the T 400 and T 450 samples slowly increased to maximum points of 0.187 and 0.172, respectively. Then they decreased at an intermediate rate. Similar observations were reported in Refs. [31, 48]. The rate of strain hardening exponent variation in the T 400 sample was lower than that in the T 450 sample.

In addition, the strain hardening behaviour was analysed using a modified C – J model. The strain hardening behaviour was divided into three stages (Fig. 5.19(d)). The strain hardening index for every stage was included in Table 5.3. A smaller strain hardening index m means a higher strain hardening ability. m increased from stage 1 to stage 3 for the TQ and T 350 samples, while m decreased first from stage 1 to stage 2 and then increased from stage 2 to stage 3 for the T 400 and T 450 samples. The T 400 sample had the lowest experimental m, while TQ had the largest one.

Table 5.3 Comparison of the modified Crussard – Jaoul (C – J) analysis with the experimental results.

Specimen	Modified C-J model			Experimental m[b]
	m_1[a]	m_2	m_3	
TQ	4.9	7.5	25.6	9.1
T 350	5.4	5.6	11.4	6.6
T 400	7.3	5.0	34.6	6.4
T 450	6.4	5.6	32.9	7.4

[a] $1 - m_{1\text{-}3}$ = slopes at stage 1 to 3

[b] $m = 1/(\varepsilon_u - \varepsilon_y)$, where ε_u is maximum uniform true strain and ε_y is true strain at 0.2% offset proof stress. The derivation process is specifically described in Ref. [32] based on the plastic instability criterion at the maximum uniform strain.

5.4 Discussion

5.4.1 The dependence of microstructure on isothermal bainite transformation temperature

After holding at 350, 400 and 450 °C, the samples consisted of polygonal ferrite, bainitic ferrite, granular bainite, martensite, retained austenite and very little amount of Widmanstätten ferrite, characterised using XRD (Fig. 5.10), OM (Fig. 5.8), SEM (Figs. 5.11, 5.12 and 5.14), EBSD (Fig. 5.17), TEM (Figs. 5.13 and 5.15) and APT

(Fig. 5.18). Except for the Widmanstätten ferrite, the microstructure was similar to a typical microstructure of hot rolled TRIP steels [3-5, 13, 14].

The fraction of RA in T 400 sample was the largest among all conditions, which was 0.045±0.003 with the average carbon content of 1.23±0.01 wt.% (Fig. 5.10(b)), although, nano-scale cementite was also observed in T 400 sample using APT (Fig. 5.18). It was reported that the nano-scale carbides precipitation could take place despite a high silicon concentration (1.5 wt. %) in TRIP steel [39, 49]. When the IBT temperature increased to 450 °C, the amount of RA decreased to 0.025±0.002. This could be explained by the increase in IBT temperature reducing the driving force for bainite formation, leading to a lower bainite fraction [13, 17, 50]. Therefore, the remaining austenite was insufficiently stabilised and transformed to martensite during quenching to room temperature. As can be seen from Fig. 5.10(b), the carbon content in RA decreased from 1.23±0.01 to 0.92±0.01 wt. % when the IBT temperature increased from 400 to 450 °C. This corresponds to a larger martensite fraction observed using colour etching in the T 450 sample, compared to that in the T 400 sample (c.f. Figs. 5.8(f, h)). On further increasing in IBT temperature to 500 °C, pearlite formation took place (Fig. 5.16), which was detrimental for RA formation as this consumed carbon [38]. The consumption of carbon by carbide and pearlite reduced the carbon content in remaining austenite, which affected the chemical stability of RA leading to its transformation to martensite during quenching [7, 39]. On the other hand, when the IBT temperature was decreased from 400 to 350 °C, the RA fraction also decreased. As shown in Figs. 5.8 and 5.11, a small amount of bainitic ferrite or granular bainite (3 – 5 μm diameter regions) was formed in the T 350 sample, while in contrast such regions in the T 400 sample consisted of RA and/or martensite (Fig. 5.12(c)). Such observations in the phase variation could be explained by an increase in the driving force for bainite transformation with a decrease in IBT temperature [7, 13, 50], leading to a larger fraction of remaining austenite transforming to bainitic ferrite and granular bainite (Fig. 5.11). This resulted in a decrease in RA fraction with decreasing the IBT temperature from 400 to 350 °C. An increase in the amount of polygonal ferrite and bainite led to more carbon being rejected into RA. In addition, RA fraction in T 350 was smaller than

that in T 400 sample. These two reasons resulted in increased carbon content in RA measured for the T 350 sample compared to that for the T 400 sample (Fig. 5.10).

In summary, the IBT temperature of 400 °C was the best choice for obtaining the largest RA fraction with medium carbon content. It consents with many researches [4, 6, 17, 51]. A higher IBT temperature would increase the tendency for carbide precipitation or pearlite formation. This would reduce the carbon content in the remaining austenite, leading to its transformation to martensite during subsequent cooling. A lower IBT temperature may result in more bainite formation from remaining austenite during holding leading to a reduced fraction of RA. Higher carbon content in the RA after lower temperature holding would increase the RA stability at room temperature. However, the TRIP effect may be less pronounced due to a reduced RA fraction and the overstabilisation of RA [8, 10, 15, 16].

5.4.2 The influence of coarse prior austenite structure on microstructure evolution and retained austenite retention

The challenge to produce TRIP steel using strip casting is the coarse prior austenite microstructure. The average PAGS of 80±27 μm in this study before ferrite transformation was very large. As the deformation was not exerted during heat treatment such defects induced by deformation as deformation bands, dislocation tangles and sub-grain boundaries were not present [38, 52]; therefore, ferrite nucleated preferentially at prior austenite grain boundaries. Due to few nucleation sites, the polygonal ferrite grain size was large (17±10 μm) as the impingement between them was postponed [42]. Such a size was very coarse compared to the typical polygonal ferrite grain size of ~ 10 μm obtained via conventional thermo-mechanical processing [14]. The consumption of prior austenite by polygonal ferrite growth from the boundary to the centre of prior austenite grains determined the size of second phase region. The PAGS ranged from 23 to 146 μm (Fig. 5.3(d)). When the prior austenite grain was large, the corresponding second phase region was also coarse. For example, the largest second phase region observed was 137 μm. Conversely, the size of second phase region was small when the prior austenite grain was small. In the T 400 sample, the average size of second phase region was 21±24 μm (Fig. 5.9(b)), which held a large standard deviation due to the inhomogeneous

prior austenite structure (Fig. 5.3(d)). Besides, a small amount of Widmanstätten ferrite observed (Fig. 5.8) in all conditions was also probably due to the coarse PAGS.

Carbon and manganese are the most important elements for the stability of austenite [17, 53]. Fig. 5.17(c) showed that carbon concentration near the polygonal ferrite/second phase region interface was higher than in the centre in the second phase region (namely remaining austenite at higher temperature), which lead to higher retained austenite presence. It can be explained by the carbon diffusing from polygonal ferrite to remaining austenite during ferrite growth [52]. A lager second phase region had a longer distance for carbon diffusion to the centre, leading to a larger difference in carbon content between the interface and the centre. A smaller second phase region had a larger area of polygonal ferrite/second phase region interfaces per volume than a larger second phase region, resulting in an increase in the rate of carbon and Mn diffusion during ferrite growth [4, 54]. As a result, the smaller second phase region was more chemically homogeneous with higher carbon content. Besides, very small areas inside the second phase region also showed high carbon content due to the carbon rejection into remaining austenite from bainite (Fig. 5.17(c)). Fig. 5.17(d) showed a nearly homogeneous manganese distribution with some dark red dots, which were MnS inclusions according to EDS analysis. However, the manganese content should be higher in RA and bainite than that in polygonal ferrite, due to manganese being one of austenite forming elements [53]. This phenomenon was not observed here probably because of EDS accuracy and small difference in Mn content between phases.

Most of carbon enriched area corresponded to the RA, whereas, some carbon enriched areas were martensite (c.f. Figs. 5.17(b, c)). Besides, when the remaining austenite in polygonal ferrite was small, it also did not transform during quenching (Figs. 5.8(f) and 5.12(c)) despite having only benefit of carbon enrichment from polygonal ferrite, as other factors such as grain size, stress state and morphology also affect the stability of austenite [6]. In interior of large second phase regions, which may have a lower carbon content, the bainitic ferrite lath tended to coalesce with neighbours [47], leading to enlargement of bainitic ferrite lath (Fig. 5.17(a)). This

would reduce the amount of RA between bainitic ferrite lath, as demonstrated by very tiny RA films observed using TEM (Fig. 5.13(b)) and EBSD (Fig. 5.17(b)). The same phenomenon was also observed in Ref. [55].

5.4.3 Correlation of mechanical properties with microstructure

As expected, the highest UTS and lowest TE were obtained after directly quenching from austenite-to-ferrite region (TQ sample, Table 5.2). Martensite formation resulted in a higher dislocation density in the TQ sample [17], compared to the IBT held samples containing predominantly bainite as the second phase. Therefore, in the TQ sample, the strain hardening exponent increased and then decreased faster, compared to the strain hardening behaviour of the IBT samples. As a result, the TE was low in the TQ sample.

For IBT held samples, RA played an important role in mechanical behaviours. Besides, other factors such as polygonal ferrite grain size and its fraction, and the interaction between polygonal ferrite and second phases also affected the mechanical behaviour [6, 9, 12, 16]. In this discussion, because of similar microstructures, only the effect of RA on mechanical behaviours is addressed. The strain hardening exponent of the T 350 sample increased very quickly at first and then decreased at a very slow rate (Fig. 5.19c); probably some of RA transformed to martensite during deformation leading to a larger TE than that of the TQ sample. As the carbon content in RA in the T 350 sample was very high (1.36±0.01 wt. %) and most of RA were of film shape leading to high stability of RA, the austenite-to-martensite transformation during tensile test was very slow and some RA may not have transformed. The strain hardening exponent of the T 400 sample increased at a moderate rate and then slowly decreased with an increase in true strain. Probably, the RA continuously transformed to martensite during straining. The blocky RA could transform to martensite at lower strains, while the film RA between bainitic ferrite would transform at larger strains due to high stability [7, 18]. The RA transformation resulted in the dislocation generation around the martensite, due to the accommodation of volume change (Fig. 5.13(d)) [17, 56]. This process contributed to a continuous increase in the strain hardening exponent by inhibiting the glide of dislocations and then a slow decrease after the maximum point [6], leading to the highest observed TE of 0.27 (Table 5.2).

The highest TE in T 400 sample resulted in the largest product of UTS and TE (Table 5.2) among all the samples. The T 450 sample showed the highest initial strain hardening exponent among all IBT held samples, which could be explained by the following. The carbon content in RA decreased from 1.23±0.01 to 0.92±0.01 wt.% with the IBT temperature increasing from 400 to 450 °C. This could lead to a decrease in RA stability, earlier transformation of RA and a higher initial strain hardening exponent [57, 58]. Because of an earlier RA transformation, the TRIP effect became less pronounced at higher strains, leading to a quicker decrease in the strain hardening exponent. As a result, a lower TE was obtained in the T 450 sample than that in the T 400 sample.

Based on the modified C – J model, the strain hardening behaviour could be divided into three stages (Fig. 5.19(d)). The TQ sample showed a typical strain hardening behaviour of ferrite-martensite DP steel [59]: stage 1 was related to work hardening of polygonal ferrite during deformation; stage 2 corresponded to co-deformation of polygonal ferrite and martensite, when the ferrite was work hardened enough; during stage 3 the deformation was restricted by the dislocation pile-up leading to dislocation immobilisation [22, 59]. Thus, the strain hardening index m increased from stage 1 to stage 3. The product of UTS and TE in TQ sample was lower than those in the T 350, T 400 and T 450 samples, indicating the mechanical properties enhancement via the IBT holding stage [56]. The strain hardening behaviour of the T 350, T 400 and T 450 samples also had three stages (Fig. 5.19(d)). At stage 1 the deformation of polygonal ferrite dominated, as the RA with about 1 wt. % carbon had a higher yield stress than the ferrite matrix [14]. At stage 2 the co-deformation of different phases took place. The T 350 sample showed the m increased from stage 1 to 3. However, in the T 400 or T 450 samples, the m_2 were smaller than m_1, meaning a higher work hardening ability in stage 2. This could be explained by an earlier transformation of RA to martensite in the T 400 and T 450 samples than that in the T 350 sample. Deformation during stage 3 was restricted by the hardened phases. In addition, the experimental m in the T 400 and T 350 samples was lower than that in the T 450 sample. A higher RA fraction and higher stability due to a larger carbon content in the T 400 sample resulted in a lower experimental m compared to the T 450 sample. On the other hand, a higher stability of RA in the T 350 sample was

responsible for a lower experimental *m* compared to the T 450 sample, although they had similar RA fraction. The experimental *m* in the T 400 sample was lower than that in the T 350 sample because the T 400 sample had more RA.

5.4.4 The approaches to improve mechanical properties

The average PAGS of 80±27 μm observed in this work resulted in the polygonal ferrite grain size of 17±10 μm, which was larger than 10 μm in hot rolled steels [14]. The coarser polygonal ferrite had a lower strength based on the Hall-Petch relationship [60]. In addition, the large second phase region here (21±24 μm) was detrimental for tensile properties [57, 61].

The other more important factors are the RA fraction and its stability; as was shown previously, to maximise the TRIP effect and enhance mechanical properties an increased RA fraction with medium stability would be required [13, 16, 18, 31]. The amount of RA observed here ranged from 0.023 to 0.045, which was much lower than the ~ 0.05 – 0.2 fraction usually present in this kind of conventional low alloyed TRIP steels [12, 13, 15]. The maximum achieved RA fraction of 0.045 here was ascribed to the coarse prior austenite structure as discussed above. For comparison, a TRIP steel with similar composition to the one studied here, which had around 0.1 RA, exhibited a higher UTS of ~ 720 MPa with a corresponding higher TE of ~ 0.26 [57].

In addition, a small amount of Widmanstätten ferrite observed here was also harmful to the mechanical properties. The formation of Widmanstätten ferrite was probably due to large PAGS.

Thus, the first step to improve mechanical properties in strip cast TRIP steel is to refine the microstructures. Addition of alloying elements, such as V, Ti and Nb, could refine PAGS and the final microstructure by grain growth retardation [17, 62, 63]. Deformation above the non-recrystallisation temperature can help to reduce the austenite grain size by dynamic/static recrystallisation; and deformation below the non-recrystallisation temperature may increase the amount of crystal defects (dislocations, deformation bands) acting as nucleation sites for ferrite formation,

which would refine the low temperature microstructure [38, 64]. These effects of deformation will be studied in the future taking into account the limitations for strip casting technology with respect to the amount of deformation imparted.

5.5 Conclusions

In this study a possibility to obtain conventional TRIP steel via strip casting technology was investigated via the process simulation in the laboratory. The analysis of effect of isothermal bainite transformation temperature on microstructure evolution and mechanical properties resulted in the following conclusions:

(1) A processing route based on strip casting was developed to produce conventional TRIP steel with the microstructure consisting of ~ 0.55 polygonal ferrite, bainite, 0.02 – 0.045 retained austenite, and small amounts of martensite and Widmanstätten ferrite.

(2) For TRIP steel with nominal composition of 0.17C-1.52Si-1.61Mn-0.03Al (wt. %), an experimental CCT diagram was obtained. The nose temperature of ferrite formation field was determined being around 650 °C. As expected, decreasing the cooling rate from austenitisation temperature to 670 °C resulted in an increase in ferrite fraction.

(3) With an increase in isothermal bainite transformation temperature from 350 to 400 and to 450 °C, the retained austenite fraction increased from 0.025 to 0.045 and then decreased to 0.023. Meantime, the carbon content decreased from 1.36 to 0.92 wt. %. A large amount of retained austenite was located along the polygonal ferrite/second phase region interfaces. The retained austenite fraction decreased towards the centre of second phase region due to the carbon inhomogeneity arising from its rejection from the neighbouring polygonal ferrite.

(4) The best combination of ultimate tensile strength (590 MPa) and total elongation (0.27) was achieved after holding at 400 °C. At the same time, the maximum retained austenite fraction of 0.045 was obtained with an intermediate carbon content of 1.23 wt. %.

(5) The strain hardening behaviour was divided into three stages based on Crussard – Jaoul model. The TRIP effect predominately affected the second stage, resulting in a decrease in strain hardening index. The stronger TRIP effect led to a larger decrease in the strain hardening index.

Acknowledgements

This project was supported by the Australian Research Council (DP130101887). The JEOL JSM-7001F FEG-SEM was funded by the Australian Research Council (LE0882613). The authors thank Dr. A.A. Gazder, UOW for modification of tensile stage. The authors thank Associate Professor N.E. Stanford and Dr. R. Marceau in Deakin University for strip casting simulation and atom probe data acquisition, respectively.

References

[1] R. Kuziak, R. Kawalla, S. Waengler, Arch. Civ. Mech. Eng. 8 (2008) 103-117.

[2] M. Bhargava, A. Tewari, S.K. Mishra, Mater. and Design 85 (2015) 149-155.

[3] M. El Mehtedi, S. Spinarelli, J. Zrnik, Metall. Ital. (2010) 5-10.

[4] A. Zarei-Hanzaki, S. Yue, ISIJ Int. 37 (1997) 583-589.

[5] A. Zarei-Hanzaki, P.D. Hodgson, S. Yue, Metall. Mater. Trans. A 28 (1997) 2405-2414.

[6] A. Mertens, E.M. Bellhouse, J.R. McDermid, Mater. Sci. Eng. A 608 (2014) 249-257.

[7] S. Zaefferer, J. Ohlert, W. Bleck, Acta Mater. 52 (2004) 2765-2778.

[8] E. Pereloma, H. Beladi, L. Zhang, I. Timokhina, Metall. Mater. Trans. A 43 (2012) 3958-3971.

[9] I. Timokhina, P. Hodgson, E. Pereloma, Metall. Mater. Trans. A 35 (2004) 2331-2341.

[10] E. Pereloma, I. Timokhina, P. Hodgson, Mater. Sci. Eng. A 273 (1999) 448-452.

[11] E. Pereloma, A. Gazder, I. Timokhina, in: R. Colas, G.E. Totten (Eds.), Retained austenite: Transformation-Induced Plasticity, in Encyclopedia of Iron, Steel and their Alloys, Taylor and Francis, Inc. New York, 2016, pp. 3088-3103.

[12] P.J. Jacques, J. Ladriere, F. Delannay, Metall. Mater. Trans. A 32 (2001) 2759-2768.

[13] R. Ranjan, H. Beladi, S.B. Singh, P.D. Hodgson, Metall. Mater. Trans. A 46A (2015) 3232-3247.

[14] Y. Tomota, H. Tokuda, Y. Adachi, M. Wakita, N. Minakawa, A. Moriai, Y. Morii, Acta Mater. 52 (2004) 5737-5745.

[15] K. Sugimoto, N. Usui, M. Kobayashi, S. Hashimoto, ISIJ Int. 32 (1992) 1311-1318.

[16] E.V. Pereloma, A.A. Gazder, I.B. Timokhina, Mater. Sci. Forum 738(2013) 212-216.

[17] A. Pichler, S. Traint, T. Hebesberger, P. Stiaszny, E.A. Werner, Steel Res. Int. 78 (2007) 216-223.

[18] S.J. Kim, C.G. Lee, I. Choi, S. Lee, Metall. Mater. Trans. A 32 (2001) 505-514.

[19] R. Nooning Jr, C. Killmore, H. Kaul, A. Phillips, D. Edelman, P. Campbell, J. Williams, in: International Conference on Microalloyed Steels, 2007, pp. 16-19.

[20] S. Ge, M. Isac, R.I.L. Guthrie, ISIJ Int. 52 (2012) 2109-2122.

[21] N. Zapuskalov, ISIJ int. 43 (2003) 1115-1127.

[22] Z.P. Xiong, A.G. Kostryzhev, N.E. Stanford, E.V. Pereloma, Mater. Design 88 (2015) 537-549.

[23] Z.P. Xiong, A.G. Kostryzhev, N.E. Stanford, E.V. Pereloma, Mater. Sci. Eng. A 651 (2016) 291-305.

[24] S. Ge, M. Isac, R.I.L. Guthrie, ISIJ Int. 53 (2013) 729-742.

[25] K. Mukunthan, P.D. Hodgson, L. Strezov, N. Stanford, ISIJ Int. 53 (2013) 2152-2159.

[26] H.Y. Gao, Z.X. Xie, Y. Yu, Y. Fang, J. Wang, B.D. Sun, ISIJ Int. 49 (2009) 546-552.

[27] L. Strezov, J. Herbertson, ISIJ Int. 38 (1998) 959-966.

[28] A.K. De, J.G.. Speer, D.K. Matlock, Adv. Mater. Process 161 (2003) 27-30.

[29] M.K. Miller. Atom probe tomography, New York: Kluwer, Academic/Plenum Press, 2000.

[30] T. Nakagaito, Tetsu-to-Hagane, 101 (2015) 426-434.

[31] H.X. Yin, A.M. Zhao, Z.Z. Zhao, X. Li, S.J. Li, H.J. Hu, W.G. Xia, Int. J. Min. Metall. Mater. 22 (2015) 262-271.

[32] Y. Tomita, K. Okabayashi, Metall. Trans. A 16 (1985) 865-872.

[33] Z.M. Zhang, Q.W. Cai, W. Yu, X.L. Li, L.D. Wang, J. Iron Steel Res. Int. 19 (2012) 73-78.

[34] L.Y. Lan, X.W. Kong, C.L. Qiu, Mater. Charact.105 (2015) 95-103.

[35] J. Kobayashi, D. Ina, N. Yoshikawa, K. Sugimoto, ISIJ Int. 52 (2012) 1894-1901.

[36] Z.B. Zhao, C. Liu, Y.X. Liu, D.O. Northwood, J. Mater. Sci. 36 (2001) 5045-5056.

[37] D. Barbier, Adv. Eng. Mater. 16 (2014) 122-127.

[38] S.M.K. Hosseini, A. Zaeri-Hanzaki, S. Yue, Mater. Sci. Eng. A 618 (2014) 63-70.

[39] J.B. Seol, D. Raabe, P.P. Choi, Y.R. Im, C.G. Park, Acta Mater. 60 (2012) 6183-6199.

[40] A.A. Gazder, F. Al-Harbi, H.T. Spanke, D.R. Mitchell, E.V. Pereloma, Ultramicroscopy 147 (2014) 114-132.

[41] F. Fazeli, X. Wang, ISIJ Int. 47 (2007) 1341-1350.
[42] N.M. Xiao, M.M. Tong, Y.J. Lan, D.Z. Li, Y.Y. Li, Acta Mater. 54 (2006) 1265-1278.
[43] S. Yoon, S.J. Lee, ISIJ Int. 54 (2014) 1453-1455.
[44] Z.D. Li, Z.G. Yang, C. Zhang, Z.Q. Liu, Mater. Sci. Eng. A 527 (2010) 4406-4411.
[45] E. Pereloma, I.B. Timokhina, M.K. Miller, P.D. Hodgson, Acta Mater. 55 (2007) 2587-2598.
[46] F.G.. Caballero, M.K. Miller, C. Garcia-Mateo, Mater. Sci. Tech. Lond. 30 (2014) 1034-1039.
[47] H.K.D.H. Bhadeshia, Mater. Sci. Tech. Lond. 31 (2015) 758-763.
[48] I.B. Timokhina, E.V. Pereloma, P.D. Hodgson, Mater. Sci. Forum 539-543 (2007) 4315-4320.
[49] F.G.. Caballero, M.K. Miller, C. Garcia-Mateo, C. Capdevila, S.S. Babu, Acta Mater. 56 (2008) 188-199.
[50] W. Gong, Y. Tomota, Y. Adachi, A.M. Paradowska, J.F. Kelleher, S.Y. Zhang, Acta Mater. 61 (2013) 4142-4154.
[51] M. Gomez, C.I. Garcia, A.J. Deardo, ISIJ Int. 50 (2010) 139-146.
[52] S. van der Zwaag, Mater. Sci. Forum 284-286 (1998) 27-38.
[53] C. Zhao, C. Zhang, W.Q. Cao, Z.G.. Yang, H. Dong, Y.Q. Weng, ISIJ. Int. 54 (2014) 2875-2880.
[54] K. Tsuzaki, T. Maki, J. Phys. IV 5 (1995) 61-70.
[55] S.M.K. Hosseini, A. Zarei-Hanzaki, E. Essadiqi, S. Yue, Mater. Sci. Tech. Lond. 24 (2008) 1354-1361.
[56] E. Girault, A. Mertens, P. Jacques, Y. Houbaert, B. Verlinden, J. Van Humbeeck, Scripta Mater. 44 (2001) 885-892.
[57] P.J. Evans, L.K. Crawford, A. Jones, Ironmak. Steelmak. 24 (1997) 361-367.
[58] B. Fu, W.Y. Yang, L.F. Li, Z.Q. Sun, Mater. Sci. Eng. A 603 (2014) 134-140.
[59] A. Kumar, S.B. Singh, K.K. Ray, Mater. Sci. Eng. A 474 (2008) 270-282.
[60] S. Nag, P. Sardar, A. Jain, A. Himanshu, D.K. Mondal, Mater. Sci. Eng. A 597 (2014) 253-263.
[61] M. Erdogan, S. Tekeli, Mater. Design 23 (2002) 597-604.

[62] S. Yan, X. Liu, W.J. Liu, H. Lan, H. Wu, Mater. Sci. Eng. A 640 (2015) 137-146.
[63] G.W. Yang, X.J. Sun, Q.L. Yong, Z.D. Li, X.X. Li, J. Iron Steel Res. Int. 21 (2014) 757-764.
[64] M. Shaban, B. Eghbali, J. Mater. Sci.Tech. 27 (2011) 359-363.

CHAPTER 6 MICROSTRUCTURE AND MECHANICAL PROPERTIES OF STRIP CAST TRIP STEEL SUBJECTED TO THERMO-MECHANICAL SIMULATION

Z.P. Xiong[1*], A.G. Kostryzhev[1], L. Chen[1], E.V. Pereloma[1, 2]

[1]*School of Mechanical, Materials and Mechatronic Engineering, University of Wollongong, Wollongong, NSW 2522, Australia*

[2]*Electron Microscopy Centre, University of Wollongong, Wollongong, NSW 2519, Australia*

Abstract: Instead of hot rolling and cold rolling followed by annealing, strip casting is a more economic and environmentally friendly way to produce transformation-induced plasticity (TRIP) steels. According to industrial practice of strip casting, rapid cooling in this work was achieved using a dip tester, and a Gleeble 3500 thermo-mechanical simulator was used to carry out the processing route. A typical microstructure of TRIP steels, which included ~ 0.55 fraction of polygonal ferrite with bainite, retained austenite and martensite, was obtained. The effects of deformation (0.41 reduction) above non-recrystallisation temperature, isothermal bainite transformation temperature and the size of second phase region on microstructure and mechanical properties were studied. The steel isothermally transformed at 400 °C had the best combination of ultimate tensile strength (UTS) and total elongation (TE), whether deformation was applied or not. The deformation resulted in the improvement of mechanical properties after holding at 400 °C: the UTS increased from 590 to 696 MPa and TE decreased from 0.27 only to 0.26. It was predominantly ascribed to grain size refinement and dislocation strengthening. The studied TRIP steel had comparable mechanical properties with TRIP 690 produced commercially.

Keywords: TRIP steel; Strip casting; Thermo-mechanical processing; Mechanical properties; Carbon diffusion; Isothermal bainite transformation.

6.1 Introduction

The development of advanced high strength steels (AHSSs) for the automotive industry is driven by the request for weight reduction in order to improve the fuel economy [1, 2]. Low-alloyed transformation-induced plasticity (TRIP) assisted steels are good AHSS candidates due to their excellent ductility combined with high strength. TRIP steels have a multi-phase microstructure, including polygonal ferrite, bainite, martensite and retained austenite (RA) [3-9]. In fact, the key characteristic of these steels is the presence of stabilised austenite at room temperature [4, 6, 10, 11]. This stabilised austenite can transform to martensite during deformation, which contributes to an increase in ductility. The stability of RA is mainly controlled through its carbon content and morphology, which offers a chance to tune the microstructure through thermo-mechanical processing [4, 10]. The processing schedules contain two important stages [12, 13]. The first stage is to form polygonal ferrite via cooling through or holding for a certain time in the austenite-ferrite temperature region. The polygonal ferrite provides ductility in this steel and leads to the carbon enrichment of austenite; the austenite enriched with carbon is stable against martensitic transformation during rapid cooling to isothermal bainite transformation (IBT) temperature [1, 12-14]. The second stage is to form carbide-free bainite during holding at bainite formation temperature following rapid cooling from the austenite-ferrite temperature region. At this stage, the austenite is further enriched with carbon, which results in the RA preserved at room temperature [1, 12-14].

The strip casting aims to directly produce strip steels from liquid metals [15]. Compared to hot and cold rolling, the strip casting eliminates many procedures, such as rough rolling and reheating, resulting in a decrease in gas emission, energy consumption and operation cost [15]. However, the large prior austenite grain size (PAGS) (approximately 100 – 200 μm) complicates tuning of the microstructure via the adjustment of heat treatment parameters [15, 16]. It is well known that the PAGS dictates the final microstructure of the transformation products at room temperature such that refining the former leads to a fine grain size of the latter [17-19]. For example, Cota *et. al.* reported that the average ferrite gain size increased from 8 to ~ 40 μm when the PAGS increased from 9.5 to 100 μm [18]. In addition, PAGS also

affects the bainite transformation in such a way that a coarser PAGS leads to larger bainite packet size and a decrease in bainite transformation rate [20-22].

At present, carbon steels, silicon steels and stainless steels are manufactured in industry by the strip casting technology [23, 24]. Daamen *et. al.* reported a trial to obtain twinning-induced plasticity (TWIP) steels using this technology in the laboratory [25]. The dual phase steels were obtained by the present authors via the simulation of strip casting [26, 27]. For TRIP steels, researchers focus on further development of hot rolling and cold rolling followed by annealing. Except our previous paper, which presented the microstructure and mechanical properties of TRIP steels obtained via the simulation of strip casting without deformation [28], there is no other published study on the production of TRIP steels using strip casting technology. This paper presents a further step in our investigation, namely the effect of austenite deformation on the microstructure and mechanical properties. With an increase in the amount of deformation the microstructure was refined and the mechanical properties were enhanced. The strengthening mechanisms responsible for the properties improvement were analysed; in particular, the effect of second phase region size on RA retention was discussed based on the carbon distribution.

6.2 Experimental Details

The chemical composition of studied steel mainly consisted of 0.172 C, 1.520 Si, 1.610 Mn, 0.0266 Al, 0.0153 Cu, 0.195 Cr and balance Fe (all in wt. %). It was similar to the chemical composition of conventional TRIP steels [1, 2]. As-cast specimens of 36 × 36 mm^2 and 1.2 mm thickness were produced at Deakin University using a dip tester [29]. The dip tester was designed to simulate the initial contact conditions of a twin roll caster used in strip casting technology [25, 30]. The copper substrates spot welded with R-type thermocouple were used as contact surfaces between liquid metals and twin rollers, which was immersed into the molten metal for a certain time in order to achieve different high cooling rates of up to ~ 1700 Ks^{-1} [25, 31] characteristic for the strip casting process. Then the copper substrates were removed from the furnace and the solidified samples were then used in this study.

The thermo-mechanical schedule illustrated in Fig. 6.1 was carried out on a Gleeble 3500 thermo-mechanical simulator in hydrawedge mode. Samples of 20 x 15 x (0.9 – 1.2) mm^3 were cut from the as-cast samples. Because of the small thickness beyond the movement control capability of the Gleeble 3500 simulator, a sandwiched sample was designed [26]. The studied sample spot welded with a K-type thermocouple was clamped by two dummy samples (2.5 mm thick; made of structural microalloyed steel). The sandwiched samples were heated at 40 Ks^{-1} to 1000 °C, then at 20 Ks^{-1} to 1250 °C in order to avoid overshooting and held for 300 s. This was followed by the cooling at 30 Ks^{-1} to 1050 °C, where the reduction (Δ = 0.41±0.02) was applied at a strain rate of 0.5 s^{-1} and then by cooling at 10 Ks^{-1} to the interrupted cooling temperature (T_{IC} = 670, 690 and 710 °C). After this, the samples were cooled at 50 Ks^{-1} to the IBT temperature (T_{IBT} = 350, 400, 450 and 500 °C) and held for 900 s in order to provide time for bainite transformation. Finally, the samples were water quenched to room temperature. Some samples were directly water quenched from different T_{IC} to room temperature in order to study the effect of T_{IC} on ferrite formation. Holding at 1250 °C for 300 s was determined in order to simulate the prior austenite grain structure (the average grain size of 83±31 μm) inherent for strip casting, as described in the previous study [28].

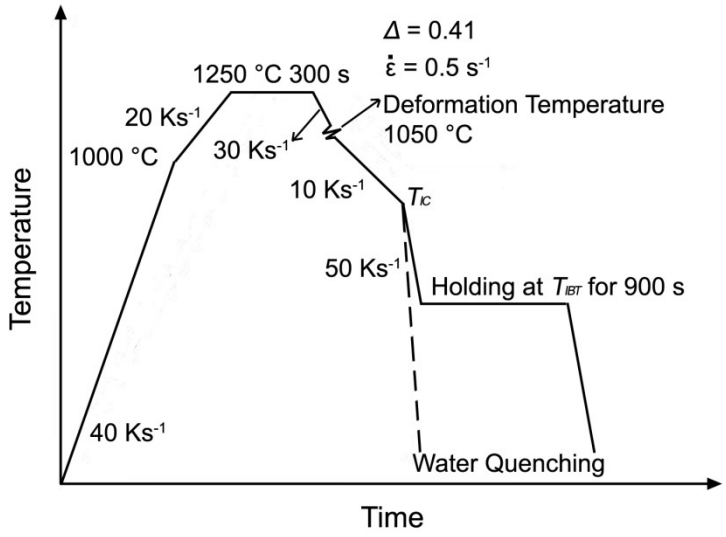

Figure 6.1 The thermo-mechanical schedule to produce the microstructure of TRIP steels.

Plain strain compression during hot rolling was simulated in the thermo-mechanical experiments. Thus, the coordinate of normal direction (ND), rolling direction (RD) and transverse direction (TD) is used in this study. The deformed samples were cut parallel to the RD-ND plane, and then were hot mounted, mechanically polished and etched using 2 vol. % nital for optical microscopy and scanning electron imaging. The microstructures were characterised using a Leica optical microscope (OM) and a JEOL JSM-7001F field emission gun – scanning electron microscope (FEG – SEM) operating at 15 kV. All micrographs were taken from the centre of samples' cross-section. The fractions of ferrite and second phase region were calculated based on the variation in grey scales in the optical micrographs using Photoshop and Image Pro-Plus software. At least 260 ferrite grains or second phase regions were used to calculate the equivalent circle diameter. It is noted that the RA fraction could not be measured in the present study using X-ray diffraction due to small sample width (~ 2.5 mm) after deformation.

Simultaneous electron backscattering diffraction (EBSD) and energy dispersive X-ray spectroscopy (EDS) mapping was undertaken on the same JEOL JSM-7001F FEG – SEM operating at 15 kV accelerating voltage, 5 nA probe current and fitted with a Nordlys-II(S) EBSD and an 80 mm^2 X-Max EDS detectors interfacing with the Oxford Instruments Aztec software suite. The sample preparation included mechanical polishing up to 1 μm followed by electropolishing using an electrolyte of 330 ml methanol, 330 ml butoxyethanol and 40 ml perchloric acid at 50 V, ~ 1.0 mA and 17 °C for ~ 90 s. EBSD-EDS mapping was conducted at the centre of the sample cross-section using a step size of 0.04 μm. The discs for transmission electron microscopy (TEM) were cut parallel to the RD-TD plane using electrical discharge machine, polished to 80 μm thickness using silicon papers, and twin-jet electropolished with an electrolyte containing 10 vol. % perchloric acid in methanol. The JEOL 2011 TEM and JEOL JEM-ARM200F operating at 200 kV were used to characterise the microstructures.

The dog-bone shaped samples for tensile testing were cut through RD-TD plane; their gauge length, width and thickness were 4.9, 2.1 and ~ 0.6 mm, respectively. The tensile tests were carried out using an in-house modified 5 kN Kammrath and

Weiss GmbH tensile stage at a constant crosshead speed of 2 μm s^{-1}, corresponding to an initial strain rate of 4 × 10^{-4} s^{-1}. At least two samples were tested for each condition.

6.3 Results

6.3.1 Effect of interrupted cooling temperatures on ferrite formation

As shown in Fig. 6.2, the ferrite fraction increased from 0.52±0.03 to 0.71±0.02 with a decrease in T_{IC} from 710 to 670 °C because the time for ferrite formation was extended. As expected, it was consistent with many published results [32, 33]. The T_{IC} = 710 °C was chosen in the following experiments as this temperature assured formation of ~ 0.5 fraction of ferrite. TRIP steels with 0.5 ferrite fraction were demonstrated to have a good combination of mechanical properties [34, 35].

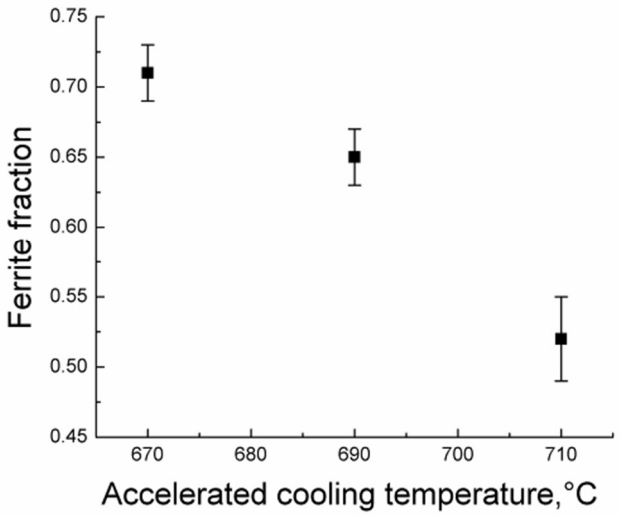

Figure 6.2 Effect of interrupted cooling temperature on ferrite fraction.

6.3.2 Effect of isothermal bainite transformation temperature on microstructure evolution

For comparison, the sample with a dual phase microstructure was produced by direct quenching from 710 °C to room temperature (indicated via a dash line in Fig. 6.1) and referred to as TD Q in the following sections. It displayed the microstructure consisting of polygonal ferrite, second phase regions and a small amount of Widmänstatten ferrite (Fig. 6.3(a)). The second phase regions included martensite

and some bainite (Fig. 6.3(b)). In addition, a layer of polygonal ferrite was observed near the sample surfaces (Fig. 6.3(a)).

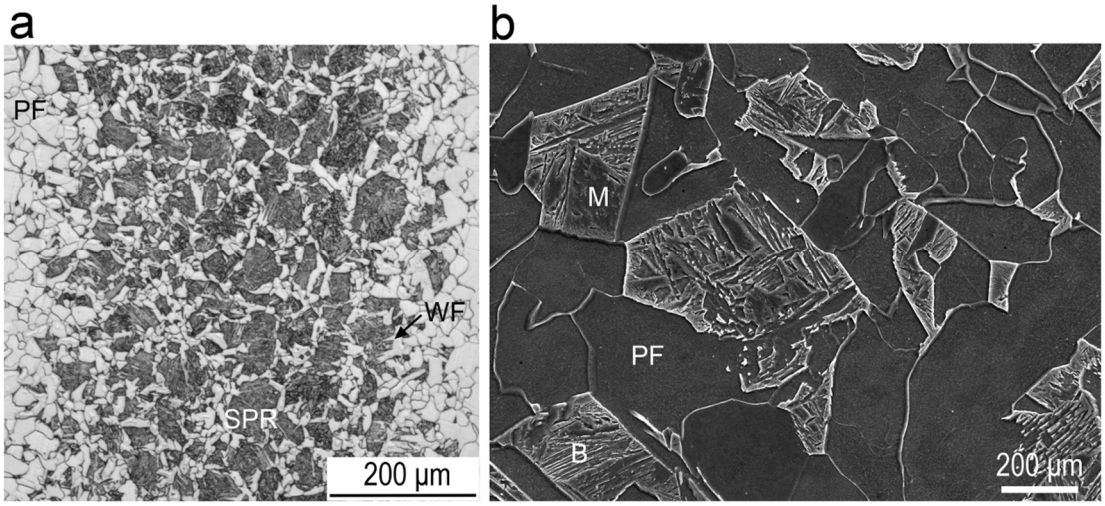

Figure 6.3 (a) Optical and (b) SEM images of the sample directly quenched from 710 °C. *PF* is polygonal ferrite, *WF* is Widmänstatten ferrite, *SPR* is second phase region, *M* is martensite and *B* is bainite.

After fast cooling from the ferrite formation temperature (710 °C), the samples were held at 350, 400, 450 and 500 °C for 900 s. They were denoted as TD 350, TD 400, TD 450 and TD 500, respectively. The optical microscopy of IBT samples showed a similar distribution of second phase regions to those in the TD Q sample (Fig. 6.3(a)). All the IBT samples had ~ 0.55 ferrite fraction.

After holding at 350 °C (TD 350), the microstructure consisted of polygonal ferrite, bainitic ferrite, granular bainite, martensite and RA in polygonal ferrite (Fig. 6.4). Bainitic ferrite consists of ferrite laths separated by film RA; whereas, granular bainite includes irregular-shaped ferrite with dispersed blocky martensite and/or retained austenite (M/RA) constituent [36, 37]. Fig. 6.4(b) shows an example of a second phase region with a size of ~ 1.2 µm included bainitic ferrite. On the contrary, as an example, the M/RA island with a size of smaller than 1 µm after quenching to room temperature was observed in Fig. 6.4(c). Fig. 6.5 (a) demonstrates film RA between bainitic ferrite laths in a small second phase region. Fig. 6.5 (b) shows one example of martensite island adjacent to the interface between polygonal ferrite and second phase region.

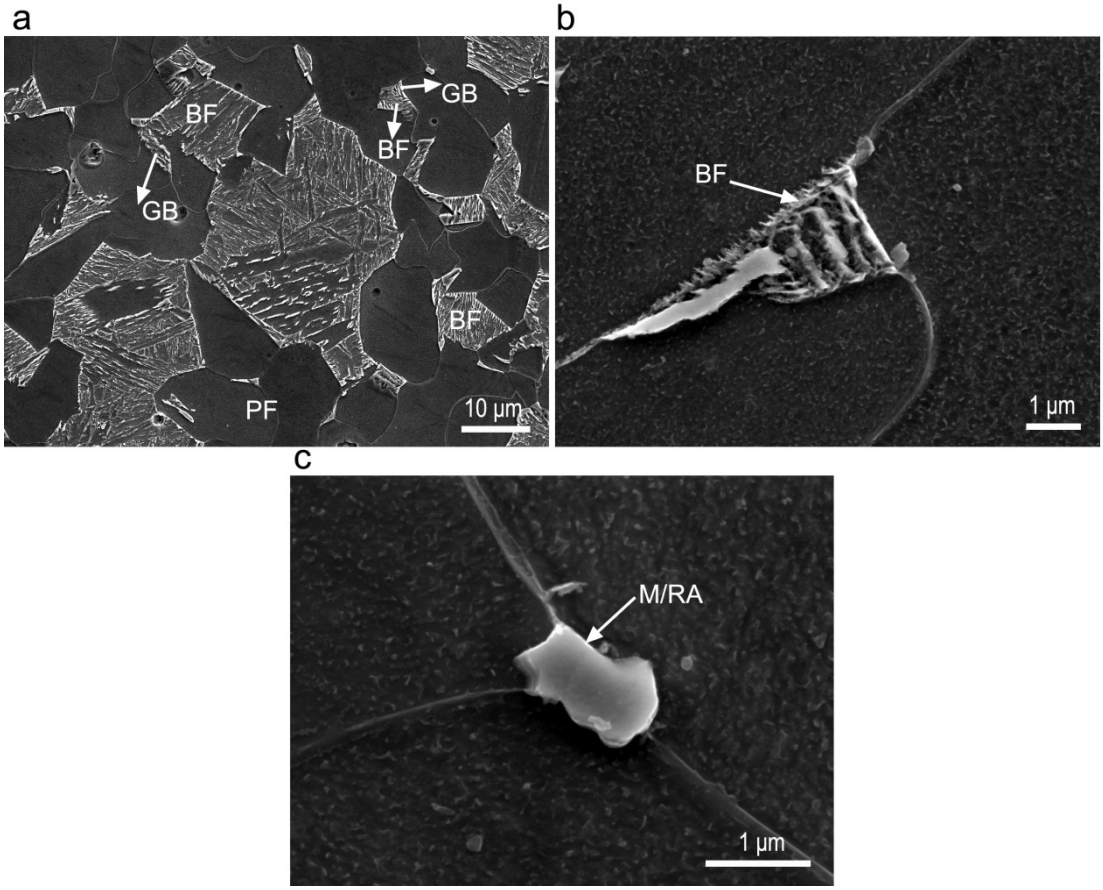

Figure 6.4 Selected SEM images of the sample after holding at 350 °C (TD 350): (a) overview; (b) bainitic ferrite; (c) martensite and/or retained austenite island. *PF* is polygonal ferrite, G*B* is granular bainite, *BF* is bainitic ferrite and *M/RA* is martensite and/or retained austenite.

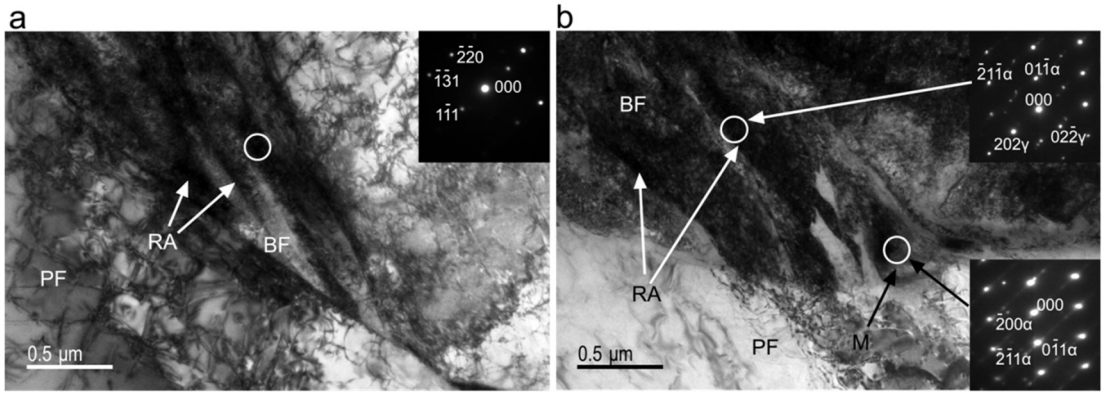

Figure 6.5 TEM images of TD 350 sample: (a) film retained austenite between bainitic ferrite laths in a small second phase region (the zone axis of inset is $[\bar{1}12]_{\gamma}$); (b) martensite island adjacent to polygonal ferrite (the zone axis of insets is $[\bar{1}11]_{\gamma}$ and $[011]_{\alpha}$). *PF* is polygonal ferrite, *BF* is bainitic ferrite, *M* is martensite and *RA* is retained austenite. Diffraction patterns were taken from circled areas.

With an increase in IBT temperature to 400 °C (TD 400), the phase balance in the TRIP steel was similar to that in the TD 350 sample, as shown in Fig. 6.6. In addition, a little amount of Widmänstatten ferrite was observed. Some small islands of granular bainite were observed (Fig. 6.6(b)). The M/RA islands with sizes smaller than ~ 3.5 μm were preserved instead of transforming to bainite during the IBT holding (Fig. 6.6(b)). Some second phase regions shown in Fig. 6.6(c) included many bainite packets. The bright and dark field TEM imaging proved the presence of RA between the bainitic ferrite laths (Figs. 6.7(a, b)). On the other hand, the micrograph in Fig. 6.7(c) was taken from the centre of a large second phase region such that file RA was not observed between bainitic ferrite laths due to lower carbon content as discussed in *Section 6.4.1.2*. An example of a martensite island adjacent to the interface between the polygonal ferrite and the second phase region is also given in (Fig. 6.7(d)).

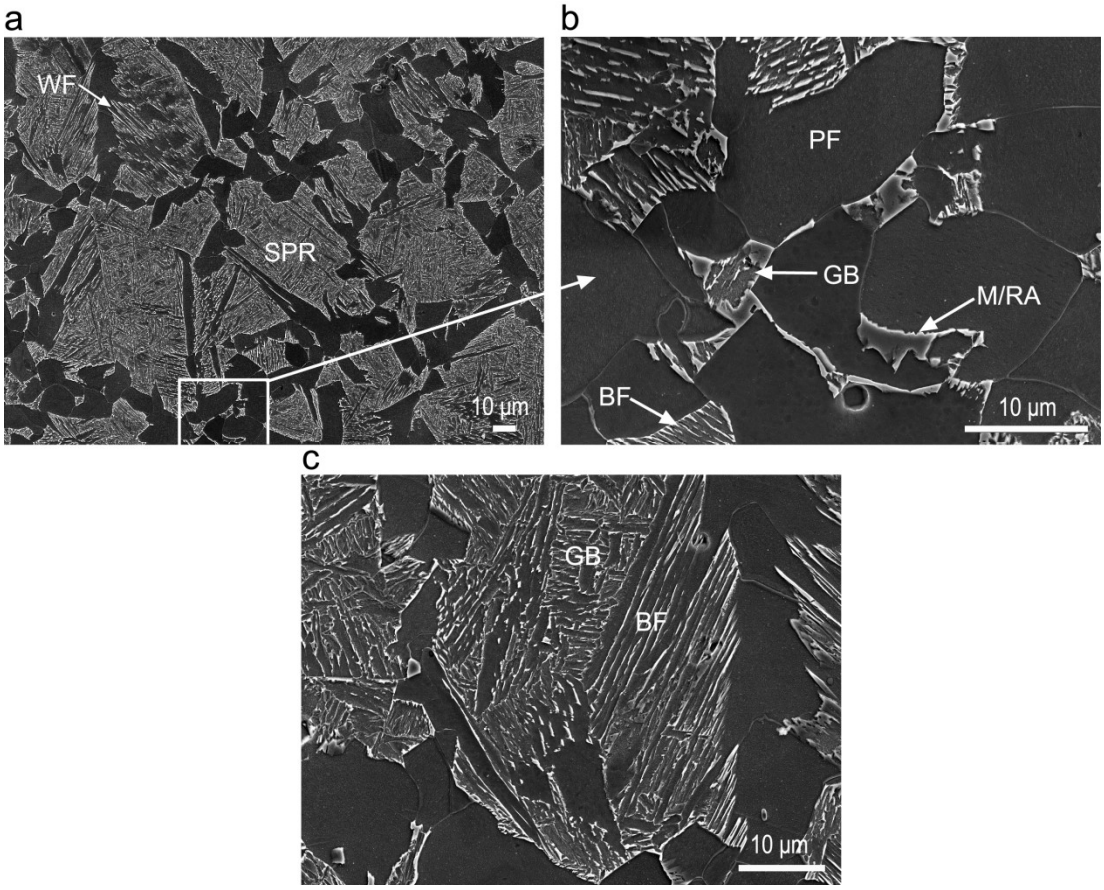

Figure 6.6 Selected SEM images of the sample after holding at 400 °C (TD 400): (a) overview; (b) small second phase regions; (c) large second phase regions. *SPR* is second phase region, *PF* is polygonal ferrite, *WF* is Widmänstatten ferrite, G*B* is granular bainite, *BF* is bainitic ferrite and *M/RA* is martensite and/or retained austenite.

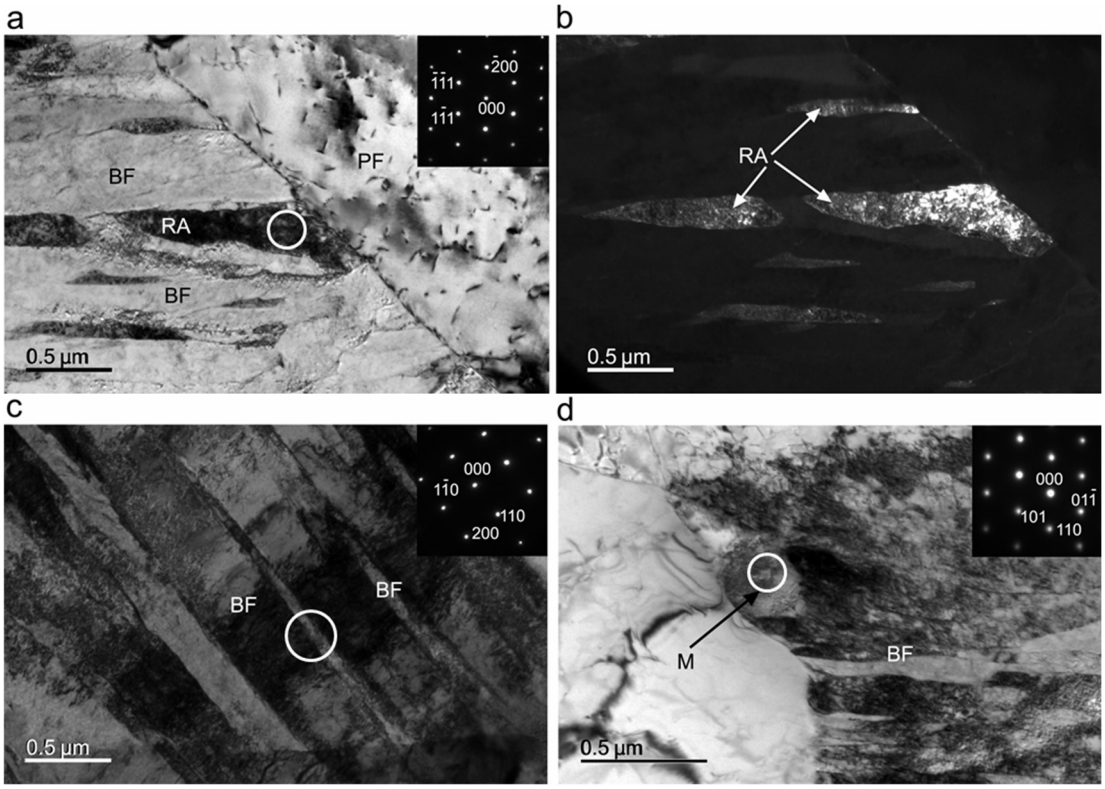

Figure 6.7 TEM images of TD 400 sample: (a) bright and (b) dark (from $(200)_\gamma$) field images of retained austenite between bainitic ferrite laths (the zone axis is $[011]_\gamma$); the zone axis of inset in (c, d) is $[001]_\alpha$ and $[\bar{1}11]_\alpha$, respectively. *PF* is polygonal ferrite, *BF* is bainitic ferrite, *M* is martensite and *RA* is retained austenite. Diffraction patterns were taken from circled areas.

After holding at 450 °C (TD 400), the microstructure also consisted of polygonal ferrite, bainitic ferrite, granular bainite, and M/RA islands in polygonal ferrite (Fig. 6.8). Some second phase regions contained more of granular bainite than bainitic ferrite such as in Fig. 6.8(b). In addition, some coarse M/RA islands adjacent to bainitic ferrite were observed in the large second phase regions (Fig. 6.8(c)). Figs. 6.9 (a, b) show the RA and martensite formed near the interface between polygonal ferrite and second phase region. The observed twins in martensite, showed by arrows in Fig. 6.9 (b), indicate a relatively high carbon content, which is responsible for this twinned martensite. Several cementite particles between bainitic ferrite laths were observed via the selected area diffraction technique and dark field imaging (Figs. 6.9 (c, d)), indicating upper bainite formation. Similar formation of a limited upper bainite amount together with carbide-free bainite morphologies was reported in thermo-mechanically processed TRIP steel with IBT of 470 °C [38].

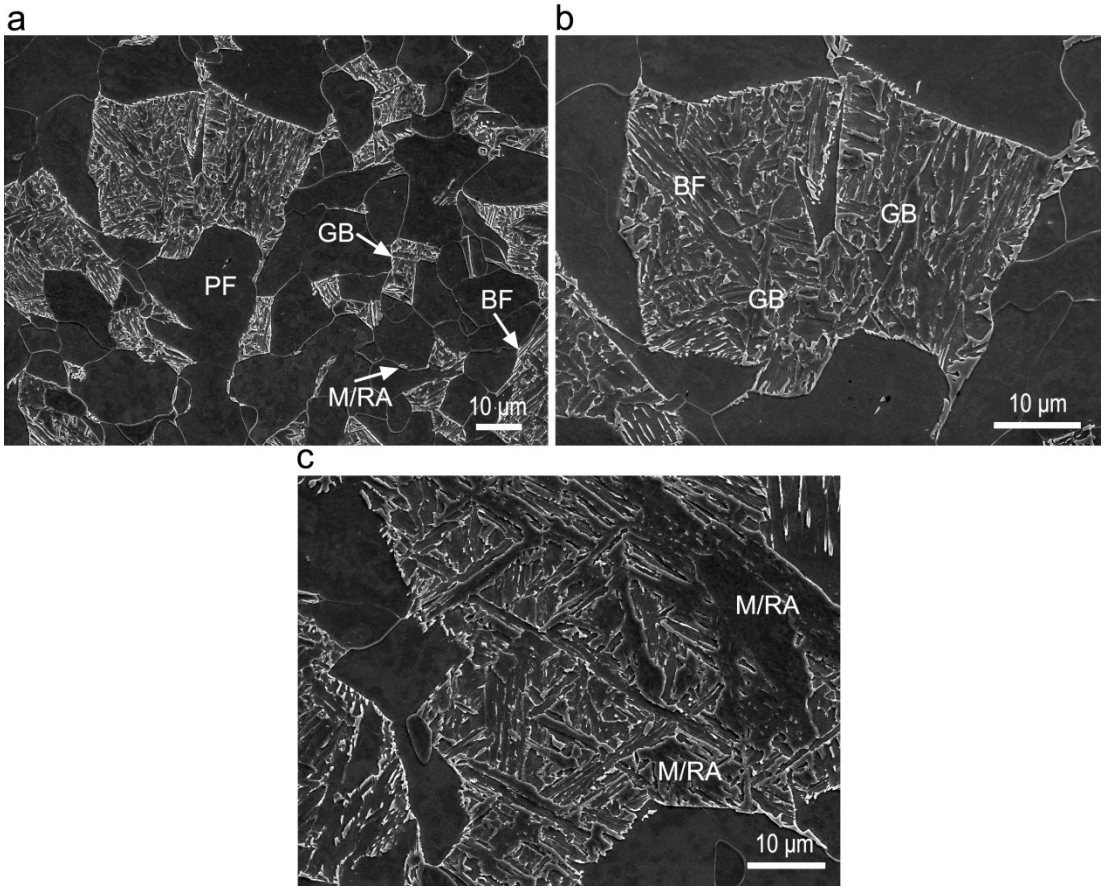

Figure 6.8 Selected SEM images of the sample after holding at 450 °C (TD 450). *PF* is polygonal ferrite, G*B* is granular bainite, *BF* is bainitic ferrite and *M/RA* is martensite and/or retained austenite.

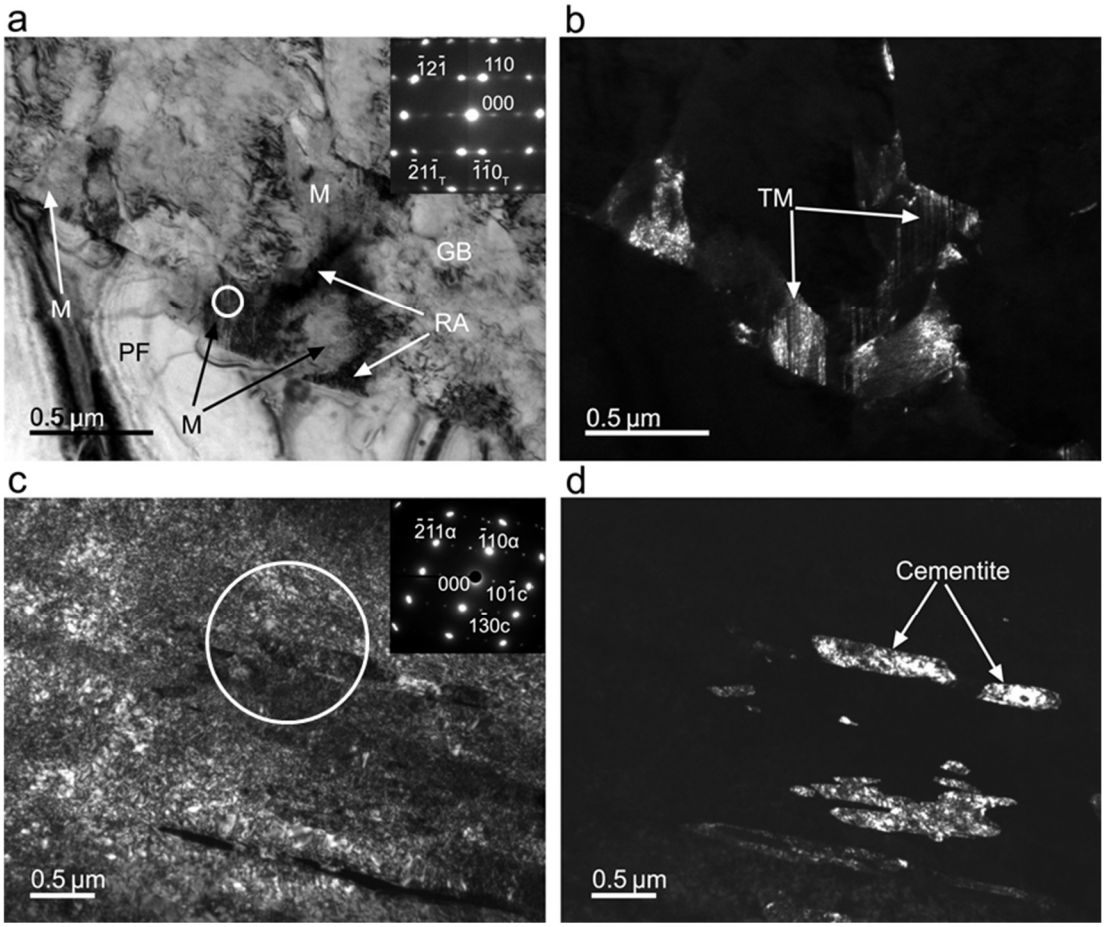

Figure 6.9 TEM images of TD 450 sample: (a) bright and (b) dark (from $(1\bar{2}1)_{\alpha}$) field images of martensite adjacent to the interface between polygonal ferrite and second phase region (the zone axis is near $[\bar{1}13]_{\alpha}$); (c) bright and (d) dark (from $(10\bar{1})_{C}$) field images of cementite between bainitic ferrite laths (the zone axis of bainitic ferrite laths and cementite is near $[131]_{\alpha}$ and $[313]_{c}$, respectively). *PF* is polygonal ferrite, *GB* is granular bainite, *M* is martensite and *RA* is retained austenite. Diffraction patterns were taken from circled areas.

With a further increase in the IBT temperature to 500 °C (TD 500), the microstructure was changed significantly with appearance of many pearlite grains (Fig. 6.10). The pearlite formation is known to be harmful to the TRIP steel properties, due to the carbon consumption resulting in a decreased amount of RA [34, 39]. Thus, the further analysis of microstructure and measurements of mechanical properties for this condition were not carried out.

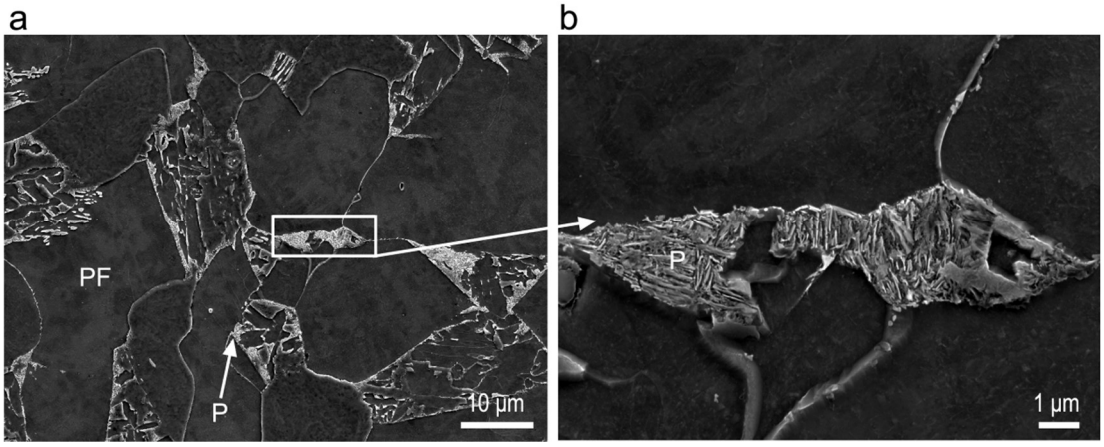

Figure 6.10 Selected SEM images of the sample after holding at 500 °C (TD 500). *PF* is polygonal ferrite and *P* is pearlite.

6.3.3 Detailed characterisation of the TD 400 sample

The distributions of ferrite grain size and the size of second phase region in TD 400 sample are shown as a representative in Fig. 6.11; the other samples (TD Q, TD 350, TD 400 and TD 450) had similar distributions due to the similar ferrite fraction. The distributions are of normal shape, i.e. they have a single maximum, however, a broaden one for the second phase regions. In TD 400 sample, the average grain size of ferrite was 13±7 μm and the average size of second phase regions was 18±16 μm; the maximum sizes for ferrite and second phase regions were 48 and 95 μm, respectively.

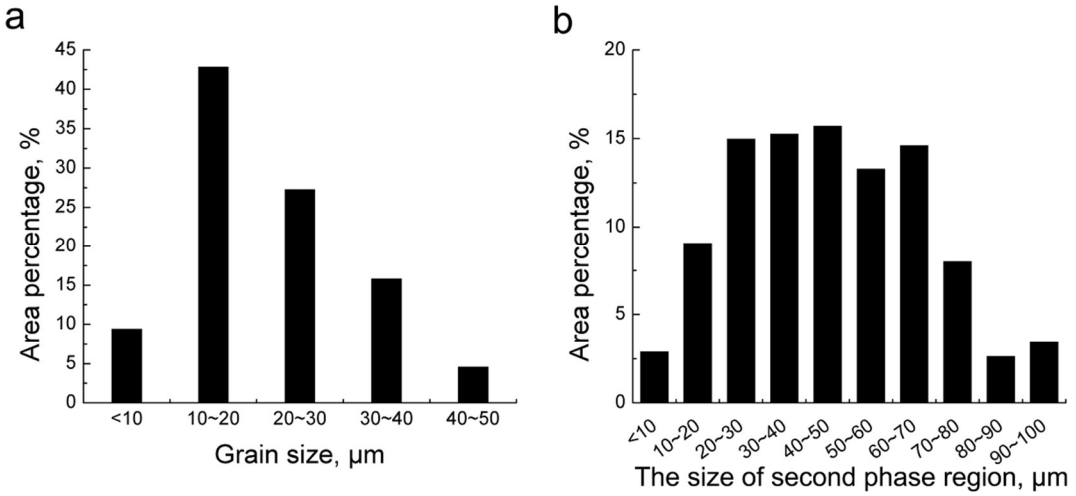

Figure 6.11 (a) The ferrite grain size distribution and (b) the size distribution of second phase region in the TD 400 sample.

In order to assess the deformation effect, three additional samples were produced in a dilatometer using the same austenitising and cooling schedule in Fig. 6.1, which, instead of deformation, contained a period of holding at 670 °C for 300 s in order to obtain 0.55 fraction of ferrite. These samples are denoted as T 350, T 400 and T 450, corresponding to isothermal holding temperatures of 350, 400 and 450 °C, respectively. They are discussed in details elsewhere [28]. As shown in Table 6.1, deformation resulted in a decrease in the average ferrite grain size from 17±10 to 13±7 μm and the average size of second phase regions from 21±24 to 18±16 μm, indicating a refined and more homogenised microstructure after deformation.

Table 6.1 Summary of microstructure statistics.

	Ferrite fraction	Average size, μm		Maximum, μm		Minimum, μm	
		Ferrite	Second phase region	Ferrite	Second phase region	Ferrite	Second phase region
T 400	0.55±0.06	17±10	21±24	51	136	3	3
TD 400	0.52±0.03	13±7	18±16	48	95	3	3

Due to its largest product of ultimate tensile strength and total elongation (discussed in *Section 6.3.4* below) and in order to investigate the effect of second phase region size on the RA fraction, the microstructure of TD 400 sample was further studied using EBSD (Fig. 6.12). In Fig. 6.12 (a), the second phase region A transformed from one remaining austenite grain after polygonal ferrite formation (referred to as remaining austenite) and the second phase region B also transformed from one remaining austenite grain, which is demonstrated by the pole figures in Figs. 6.12 (e) and (f), respectively. As can be seen in Fig. 6.12 (b), the smaller second phase region A had a higher RA fraction than that in the larger second phase region B. Most of the RA was distributed along the remaining austenite/polygonal ferrite interfaces (Fig. 6.12 (b)). Whereas, only a small amount of RA retained inside the second phase regions, i.e. film RA between bainitic ferrite laths and blocky RA between bainite packets (Fig. 6.12 (b)). The carbon enriched area corresponded to this RA distribution (Fig. 6.12 (c)). The polygonal ferrite was depleted in carbon compared to the second phase regions. The manganese distribution looks to be homogeneous (Fig. 6.12 (d)) due to the low diffusion rate of substitutional alloying elements [40] and probably due to a difficulty to detect the small variations in manganese content using this technique. On the other hand, the difference in carbon content in polygonal

ferrite and RA was detected (c.f. Figs. 6.12 (b) and (c)), which is a result of more than an order of magnitude variation in the carbon content between ferrite and RA [32].

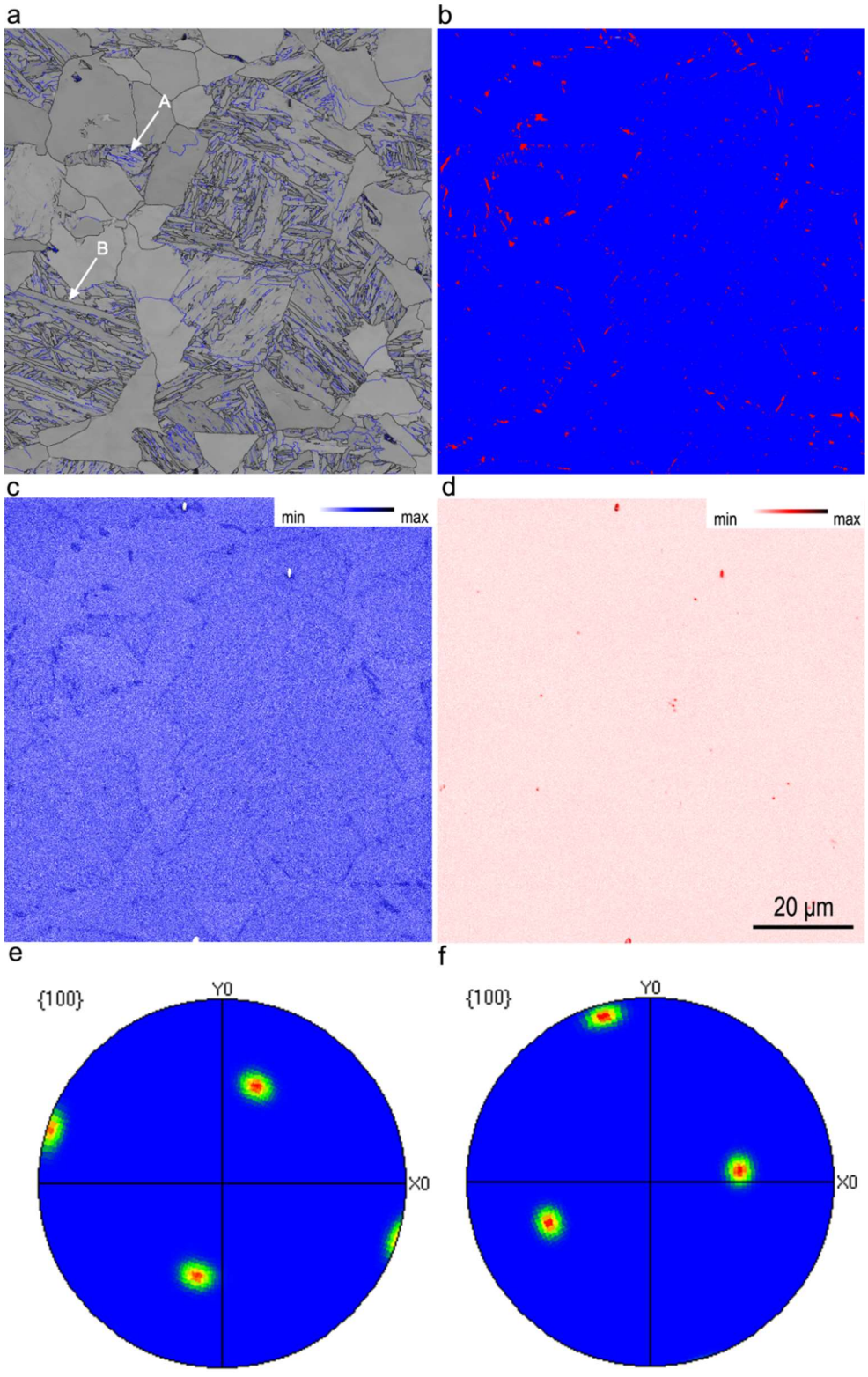

Figure 6.12 EBSD maps in TD 400 sample of the (a) band contrast with grain boundaries (2 ° < low angle grain boundaries < 15° = blue lines and high angle grain boundaries ≥ 15° = black lines) and (b) phase distribution (FCC = red and BCC = blue), EDS elements maps of (d) carbon and (e) manganese, and (e, f) {001} pole figures of the experimental orientation spread of the retained austenite grain corresponding to A and B second phase regions marked in (a), respectively.

6.3.4 Mechanical properties

The engineering stress – engineering strain curves of different thermo-mechanically processed samples are shown in Fig. 6.13, and corresponding mechanical properties are listed in Table 6.2. The yield stress (YS) was determined using 0.2% offset because of continuous yielding behaviour. As expected, TD Q sample had the largest YS and ultimate tensile strength (UTS) with the lowest uniform elongation (UE) and total elongation (TE) due to its ferrite-martensite microstructure. After holding at different IBT temperatures, the TD 400 sample showed the highest UTS of 696 MPa and TE of 0.26, resulting in the largest product of UTS and TE, namely 18096 MPa%. With an increase or a decrease in the IBT temperature, the UTS and TE decreased.

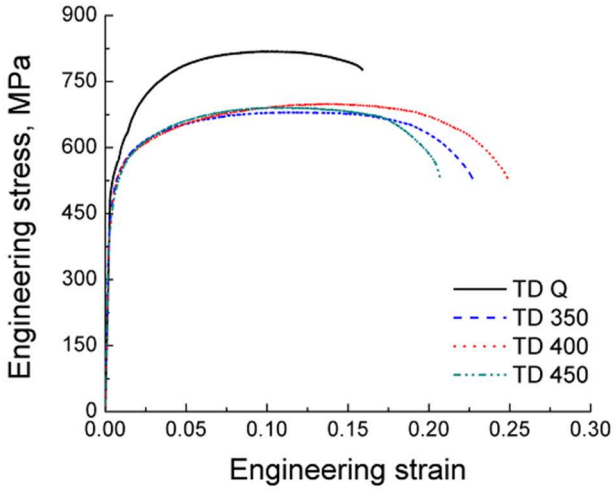

Figure 6.13 Engineering stress – engineering strain curves of different thermo-mechanically processed samples.

Table 6.2 Summary of mechanical properties for different processing schedules.

	Deformation	Ferrite fraction	Yield strength, MPa	Ultimate tensile strength, MPa	Uniform elongation	Total elongation	Product of ultimate tensile strength and total elongation, MPa%
TD Q	0.41±0.02	0.53±0.05	535±13	791±30	0.11±0.017	0.18±0.023	14238
TD 350		0.54±0.01	457±27	675±7	0.12±0.027	0.25±0.029	16875
TD 400		0.52±0.03	447±16	696±6	0.14±0.002	0.26±0.008	18096
TD 450		0.56±0.01	458±11	688±5	0.11±0.020	0.22±0.013	15136

Compared to the samples produced using dilatometer without deformation, with an increase in the amount of deformation the YS and UTS increased while the UE and TE decreased (Figs. 6.14(a, b)). In addition, the product of UTS and TE also increased after deformation (Fig. 6.14(c)). For example, after holding at 400 °C the UTS increased by 106 MPa while the elongation decreased by 0.01 with an increase in reduction from 0 to 0.41. As a result, the product of UTS and TE increased from 159350 to 18096 MPa%. Although the difference in thickness of non-deformed (~ 1 mm) and deformed samples (~ 0.6 mm) was not taken into consideration for its effect on mechanical properties, the ratio of thickness to ferrite grain size was around 50 in both conditions. The similarity of this ratio allows to disregard the effect of specimen thickness on the measurements of mechanical properties [41].

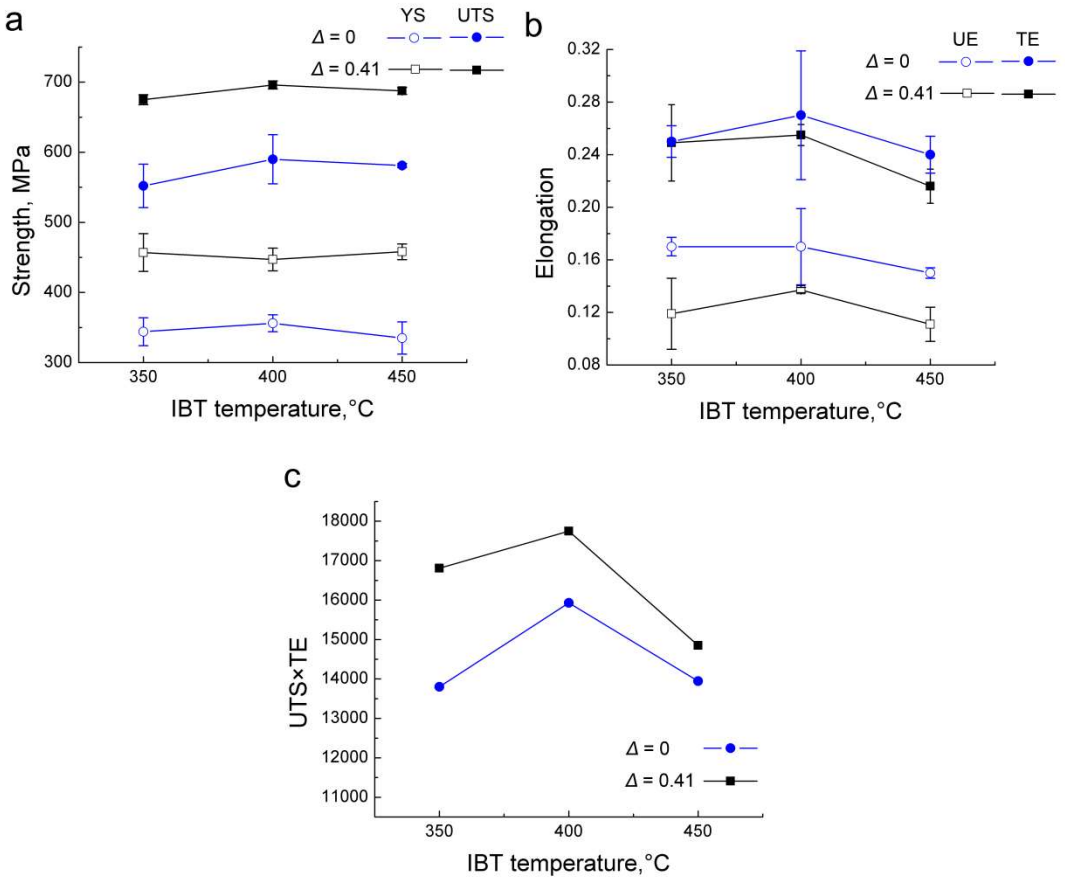

Figure 6.14 The dependence of (a) yield stress (YS) and ultimate tensile strength (UTS), (b) uniform elongation (UE) and total elongation (TE), and (c) the product of UTS and TE on isothermal bainite transformation temperature and the amount of deformation.

6.4 Discussion

6.4.1 Microstructure evolution during thermo-mechanical processing

A typical microstructure similar to a conventional TRIP steel, comprising polygonal ferrite, bainitic ferrite, granular bainite, RA and martensite, was produced via the strip casting technology simulated in the laboratory. The holding of the samples at 1250 °C for 300 s resulted in a prior austenite structure (with an average grain size of 80±27 μm) similar to that after strip casting. Although the deformation temperature of 1050 °C was above the non-recrystallisation temperature (T_{nr}) for this steel grade (around 950 °C [4, 33, 42]), the dynamic recrystallisation should not have happened, due to the small amount of deformation. This can be supported by a result published in Ref. [31], which stated that completion of the dynamic recrystallisation had required a strain of 0.99 when the PAGS was 120 μm and the sample (0.05 C, 0.28 Si, 0.54 Mn, 0.01 P, 0.005 S and balance Fe, all in wt. %) was deformed at 1100 °C at a strain rate of 1 s^{-1}. However, during cooling of our samples from 1050 to 950 °C, the static recrystallisation took place, leading to the refinement of prior austenite structure. On further cooling to the interrupted cooling temperature of 710 °C, polygonal ferrite predominantly nucleated at prior austenite grain boundaries but not inside the austenite grains, because the dislocation substructures might have recovered due to the high deformation temperature [43]. With an increase in reduction from 0 to 0.41, the ferrite grain size decreased from 17±10 to 13±7 μm (Table 6.2), due to an increase in the number of ferrite nucleation sites following the prior austenite grain refinement. A small amount of Widmänstatten ferrite was still observed (Figs. 6.3(a) and 6.6(a)) probably due to the large PAGS and fast cooling. After ~ 0.55 polygonal ferrite formation, the samples were quickly cooled to the IBT temperature in order to avoid pearlite formation [13]. During the holding at IBT temperatures, bainite transformed from austenite and at the same time carbon was rejected to the remaining austenite. During water quenching from the IBT temperature to room temperature, some remaining austenite transformed to martensite and some was preserved as RA, depending on the austenite stability.

6.4.1.1 Effect of isothermal bainite transformation temperature on microstructure evolution

Holding at 500 °C was found to be not suitable for TRIP steel production due to pearlite formation (Fig. 6.10) [34, 39]. With a decrease in IBT temperature from 450 to 350 °C, bainitic ferrite and/or granular bainite were observed in smaller second phase regions (Figs. 6.4(b) and 6.6(b)). It could be explained using the thermodynamics. The critical driving force for bainite formation in the steel (0.19C-1.5Mn-1.6Si-0.2Mo, wt. %) with similar chemical composition to the studied steel can be expressed as [44]:

$$G_{Critical} = 3.64T - 2840 \quad (6.1)$$

where $G_{Critical}$ is the critical driving energy for bainite formation ($J \cdot mol^{-1}$) and T is the holding temperature (°C). Different steels require different coefficients in Eq. (6.1), whereas, the driving force is proportional to the IBT temperature [12, 45, 46]. With a decrease in IBT temperature, the critical driving force decreases. This means an easier transformation of remaining austenite to bainite with a decrease in temperature.

From the above discussion, the RA fraction in TD 350 sample should be smaller than that in TD 400 sample because more remaining austenite was consumed by bainite formation, which was also reported in Ref. [4]. When the IBT temperature increased to 450 °C, the RA fraction should also be smaller than that in TD 400 sample because cementite was observed by TEM (Figs. 6.9(c, d)). Cementite formation consumed carbon which should enrich austenite, leading to a decrease in the amount of RA [38, 47, 48].

6.4.1.2 Effect of second phase region size on retained austenite retention

The carbon map (Fig. 6.12(c)) shows that the carbon content near the interfaces between polygonal ferrite/second phase regions was higher than that inside the second phase regions. In contrast, the manganese content showed a homogenous distribution, despite of few contamination dots or MnS inclusions (Fig. 6.12(d)). These phenomena could be explained via thermodynamics. The volume diffusivities of manganese and carbon in austenite are respectively expressed as following [32, 49]:

$$D_l^{Mn} = 1.78 \times 10^{-5} \exp(-264000 / RT) \quad (6.2)$$

$$D_l^C = 1.75\times10^{-5}\exp(-143320/RT) \quad (6.3)$$

where R is the gas constant (8.314 $J\cdot mol^{-1}\cdot K^{-1}$) and T is the temperature in Kelvin. The diffusion distance (d) is calculated as follows [47]:

$$d = \sqrt{Dt} \quad (6.4)$$

where t is the holding time in seconds. The austenite-to-ferrite transformation temperature (Ar_3) is around 810 °C according to a TRIP steel with similar chemical compositions and a PAGS between 45 and 80 μm [34]. It took 10 s to cool the sample at 10 Ks^{-1} from the assumed Ar_3 to the interrupted cooling temperature of 710 °C; thus, the holding time t for element diffusion can be set as the maximum of 10 s. If a medium value of 760 °C is chosen as the diffusion temperature T and the time is set between 5 and 10 s, the calculated diffusion distances of carbon and manganese would be 2.2 – 3.1 μm and 2.0 – 2.8 nm, respectively. This carbon diffusion range resulted in a layer of high carbon content adjacent to the remaining austenite grain boundaries (Fig. 6.12(c)), which was also demonstrated in Refs. [47, 50]. Manganese diffused much shorter distances which led to its homogenous distribution compared to carbon (c.f. Figs. 6.12(c) and (d)).

A higher carbon content near the remaining austenite grain boundaries, compared to that inside the remaining austenite grains, led to more RA grains adjacent to the polygonal ferrite/second phase region interfaces after quenching to room temperature from the IBT temperatures. In addition, some tiny RA grains were inside the second phase region due to the carbon enrichment during the bainite formation (Fig. 6.12(b)). As a result, the RA fraction in a larger second phase region was lower than that in a smaller one (Fig. 6.12 (b)). This corresponds to Hanzaki *et al.* [17] who also showed the RA fraction decreased from 0.071 to 0.051 when PAGS increased from 45 to 350 μm.

The second phase region was only refined from 21±24 to 18±16 μm with an increase in reduction from 0 to 0.41. Based on the above discussion, it means that the RA fraction after deformation may only change marginally in the studied TRIP steel; the RA fraction in the non-deformed samples was reported to be between 0.02 and 0.05 [28].

6.4.2 Effect of isothermal bainite holding temperature and deformation on mechanical properties

As shown in Fig. 6.14, the combination of strength and ductility after holding at 400 °C was the highest, whether the deformation was applied or not. Without deformation, the best combination of properties after holding at 400 °C was ascribed to the highest RA fraction in the previous study [28]. This phenomenon after holding at different IBT temperatures was reported by many researchers [1, 51, 52]. It was also explained by the largest fraction of RA with suitable carbon content after holding at 400 °C [1, 51, 52]. Based on the discussion in *Section 6.4.1.1*, it is probable that the largest RA fraction was also obtained in TD 400 sample and this was responsible for the best combination of strength and ductility.

The strengthening with deformation, observed in this study (Fig. 6.14), could be predominantly explained by grain refinement and dislocation strengthening. Due to the same processing condition for polygonal ferrite formation, all three samples (TD 350, TD 400 and TD 450) had similar average polygonal ferrite grain sizes. Besides, the dislocation densities for TD 350, TD 400 and TD 450 samples were similar because of low holding temperatures, namely $10.4\pm0.75\times10^{13}$, $9.8\pm0.56\times10^{13}$ and $9.4\pm0.67\times10^{13}$ m^{-2}, respectively, although the dislocation recovery was different due to different IBT temperatures. Thus, as a representative example, the TD 400 sample was used for the analysis of the strengthening mechanism. After holding at 400 °C, with an increase in reduction from 0 to 0.41, the YS and UTS respectively increased by 91 and 106 MPa, while the TE decreased by 0.01. This resulted in an increase in the product of UTS and TE, which indicated an increase in formability [53]. Three aspects should be considered for the strengthening. First of all, after deformation the ferrite grain size decreased from 17±10 to 13±7 μm, which increased the grain refinement contribution to YS by 52 MPa according to the Hall – Petch equation [54]:

$$\sigma = \sigma_0 + kd^{-1/2} \tag{6.5}$$

where the σ_0 and k are material constants, and k is equal to 1500 $MPa \cdot \mu m^{-1/2}$ based on ~ 0.45 fraction of the second phases [55]. Secondly, the deformation increased the dislocation density in the polygonal ferrite. As shown in Fig. 6.15, the dislocation density in the TD 400 sample ($9.8\pm0.56\times10^{13}$ m^{-2}) was higher than that in the T 400

sample ($5.1\pm0.42\times10^{13}$ m^{-2}). This increase in dislocation density accounts for 58 MPa increase in YS according to the Bailey – Hirsch relationship [56]:

$$\sigma_{dis} = M\alpha Gb\rho^{1/2} \quad (6.6)$$

where M is the Taylor factor (M = 2.75 for random textured bcc metals), α is a constant (α = 0.38 in bcc iron), G is shear modulus (G = 81.6 GPa), b is the Burgers vector (b = 0.248 nm) and ρ is the average dislocation density in polygonal ferrite. Thirdly, the size of the second phase region was refined from 21±24 to 18±16 μm, which also could increase the strength: the smaller second phase regions had more interfaces with polygonal ferrite, resulting in a local increase in the dislocation density in ferrite, and a more pronounced interaction between the polygonal ferrite and second phases during deformation [4]. Thus, the grain refinement and dislocation strengthening was ascribed to be the main reasons for the improvement of mechanical properties after deformation. To this end, the variation in the RA contribution to strength is expected to be low due to a marginal change in RA fraction after deformation (as discussed in *Section 6.4.1.2*).

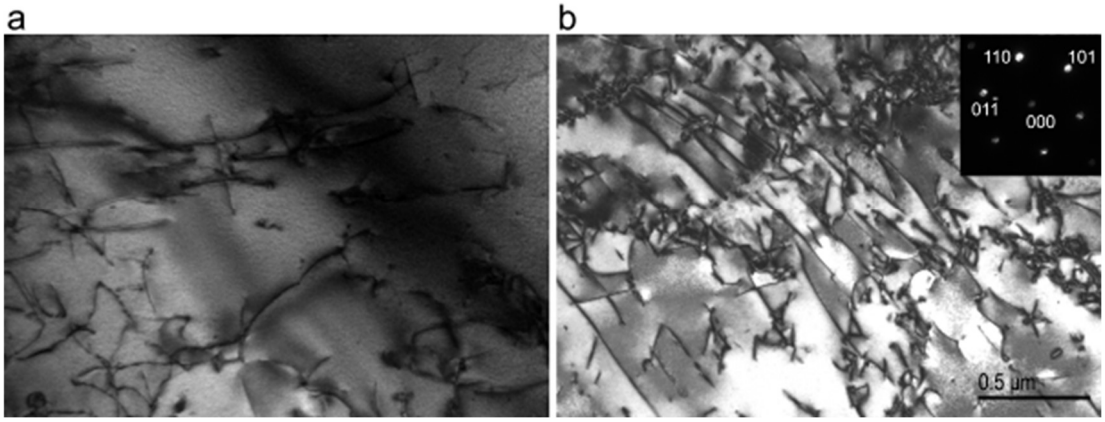

Figure 6.15 Dislocations in polygonal ferrite of (a) T 400 and (b) TD 400 samples. The zone axis in (a, b) is $[\bar{1}11]_{\alpha}$.

The mechanical properties of the investigated TRIP steel produced by strip casting were compared with the ones commercially produced using hot rolling [57]. As can be seen in Fig. 6.16, the studied steels treated without deformation, especially the T 400 sample, exhibited the comparable mechanical properties with TRIP 590. The studied deformed TRIP steels, especially for the TD 400 sample, had comparable mechanical properties with TRIP 690. In the future, the mechanical properties can be further improved by deformation in the non-recrystallisation temperature region and

micro-alloying with additions of molybdenum, vanadium or niobium. Alternatively, the cold rolling and annealing following the strip casting could be another route to improve the mechanical properties of TRIP steel.

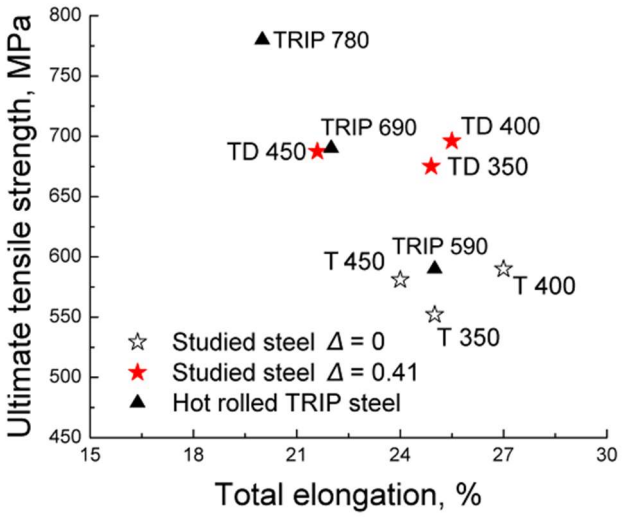

Figure 6.16 Comparison of mechanical properties for the studied steels and hot rolled TRIP steels from Nippon Steel & Sumitomo Metal Corporation's brochure [57].

6.5 Conclusions

A conventional TRIP steel (0.17C-1.52Si-1.61Mn-0.03Al wt. %) was produced using the strip casting technique simulated in the laboratory. The conclusions of the present study are as follows:

(1) A typical microstructure of TRIP steels, consisting of ~ 0.55 fraction of polygonal ferrite with bainitic ferrite, granular bainite, RA and martensite, was obtained. Noticeably, a very little amount of Widmänstatten ferrite was also observed.

(2) The distribution of the RA was non-uniform. It was predominantly located at the interfaces between the polygonal ferrite and second phase regions, while some RA grains, in the form of films and blocky islands, located inside the second phase regions. These RA locations corresponded to the carbon enriched areas identified using EDS.

(3) Larger second phase regions had a lower RA fraction than the smaller second phase regions.

(4) As a result of deformation, the ultimate tensile strength increased by 106 MPa while the total elongation decreased by 0.01 after holding at 400 °C. The strengthening was mainly ascribed to the microstructure refinement.

(5) The mechanical properties of studied TRIP steels produced using simulated deformation during strip casting were comparable to the industrially manufactured TRIP 690 steel.

Acknowledgements

This project was supported by the Australian Research Council (DP130101887). The JEOL JSM-7001F FEG-SEM and JEOL JEM-ARM200F were funded by the Australian Research Council (LE0882613 and LE120100104, respectively). The authors thank Drs. A.A. Gazder and A.A. Saleh University of Wollongong for modification of the tensile stage and EBSD mapping, respectively. The authors also thank Associate Professor N.E. Stanford, Monash University, for casting of the flat samples.

References

[1] A. Mertens, E.M. Bellhouse, J.R. McDermid, Mater. Sci. Eng. A 608 (2014) 249-257.

[2] R. Kuziak, R. Kawalla, S. Waengler, Arch. Civ. Mech. Eng. 8 (2008) 103-117.

[3] A.F. Mark, X. Wang, E. Essadiqi, J.D. Embury, J.D. Boyd, Mater. Sci. Eng. A 576 (2013) 108-117.

[4] R. Ranjan, H. Beladi, S.B. Singh, P.D. Hodgson, Metall. Mater. Trans. A 46A (2015) 3232-3247.

[5] H.X. Yin, A.M. Zhao, Z.Z. Zhao, X. Li, S.J. Li, H.J. Hu, W.G. Xia, Int. J. Min. Metall. Mater. 22 (2015) 262-271.

[6] E.V. Pereloma, A.A. Gazder, I.B. Timokhina, Mater. Sci. Forum 738 (2013) 212-216.

[7] E.V. Pereloma, H. Beladi, L. Zhang, I.B. Timokhina, Metall. Mater. Tran. A 43 (2012) 3958-3971.

[8] I.B. Timokhina, P. Hodgson, E.V. Pereloma, Metall. Mater. Tran. A 35 (2004) 2331-2341.

[9] E.V. Pereloma, P. Hodgson, Mater. Sci. Eng. A 251 (1998) 30-39.

[10] K. Sugimoto, N. Usui, M. Kobayashi, S. Hashimoto, ISIJ Int. 32 (1992) 1311-1318.

[11] E.V. Pereloma, I.B. Timokhina, P. Hodgson, Mater. Sci. Eng. A 273 (1999) 448-452.

[12] S. Li, R. Zhu, I. Karaman, R. Arroyave, Acta Mater. 61 (2013) 2884-2894.

[13] S. Li, R. Zhu, I. Karaman, R. Arroyave, Acta Mater. 60 (2012) 6120-6130.

[14] P.J. Jacques, J. Ladriere, F. Delannay, Metall. Mater. Trans. A 32 (2001) 2759-2768.

[15] R. Nooning Jr, C. Killmore, H. Kaul, A. Phillips, D. Edelman, P. Campbell, J. Williams, in: International Conference on Microalloyed Steels, 2007, pp. 16-19.

[16] K. Mukunthan, P.D. Hodgson, L. Strezov, N. Stanford, ISIJ Int. 53 (2013) 2152-2159.

[17] A.Z. Hanzaki, P.D. Hodgson, S. Yue, Metall. Mater. Trans. A 28 (1997) 2405-2414.

[18] A.B. Cota, C.A.M. Lacerda, F.L.G. Oliveira, F.A. Machado, F.G.D. Araujo, Scr. Mater. 51 (2004) 721-725.

[19] M. Arribas, B. Lopez, J.M. Rodriguez-Ibabe, Mater. Sci. Eng. A 485 (2008) 383-394.
[20] S. Kang, S. Yoon, S.J. Lee, ISIJ Int. 54 (2014) 997-999.
[21] S.J. Lee, J.S. Park, Y.K. Lee, Scr. Mater. 59 (2008) 87-90.
[22] M. Umemoto, K. Horiuchi, I. Tamura, Tetsu-to-Hagane 22 (1982) 854-861.
[23] S. Ge, M. Isac, R.I.L. Guthrie, ISIJ Int. 52 (2012) 2109-2122.
[24] N. Zapuskalov, ISIJ Int. 43 (2003) 1115-1127.
[25] M. Daamen, C. Haase, J. Dierdorf, D.A. Molodov, G. Hirt, Mater. Sci. Eng. A 627 (2015) 72-81.
[26] Z.P. Xiong, A.G. Kostryzhev, N.E. Stanford, E.V. Pereloma, Mater. Sci. Eng. A 651 (2016) 291-305.
[27] Z.P. Xiong, A.G. Kostryzhev, N.E. Stanford, E.V. Pereloma, Mater. Des. 88 (2015) 537-549.
[28] Z.P. Xiong, A.G. Kostryzhev, A.A. Saleh, L. Chen, E.V. Pereloma, Mater. Sci. Eng. A 664 (2016) 26-42.
[29] T. Dorin, N. Stanford, A. Taylor, P. Hodgson, Metall. Mater. Tran. A 46 (2015) 5561-5571.
[30] L. Strezov, J. Herbertson, ISIJ Int. 38 (1998) 959-966.
[31] H.Y. Gao, Z.X. Xie, Y. Yu, Y. Fang, J. Wang, B.D. Sun, ISIJ Int. 49 (2009) 546-552.
[32] Z.D. Li, Z.G. Yang, C. Zhang, Z.Q. Liu, Mater. Sci. Eng. 527 (2010) 4406-4411.
[33] M. El Mehtedi, S. Spinarelli, J. Zrnik, Metall. Ital. (2010) 5-10.
[34] A. Zarei-Hanzaki, S. Yue, ISIJ Int. 37 (1997) 583-589.
[35] S.J. Kim, C.G. Lee, I. Choi, S. Lee, Metall. Mater. Trans. A 32 (2001) 505-514.
[36] A.A. Gazder, F. Al-Harbi, H.T. Spanke, D.R. Mitchell, E.V. Pereloma, Ultramicroscopy 147 (2014) 114-132.
[37] M. Takahashi, H. Bhadeshia, Mater. Trans. JIM 32 (1991) 689-696.
[38] E.V. Pereloma, I.B. Timokhina, M.K. Miller, P.D. Hodgson, Acta Mater. 55 (2007) 2587-2598.
[39] S.M.K. Hosseini, A. Zaeri-Hanzaki, S. Yue, Mater. Sci. Eng. A 618 (2014) 63-70.
[40] S. Yoon, S.J. Lee, ISIJ Int. 54 (2014) 1453-1455.

[41] J. An, Y.F. Wang, Q.Y. Wang, W.Q. Cao, C.X. Huang, Mater. Sci. Eng. A 651 (2016) 1-7.
[42] S.M.K. Hosseini, A. Zarei-Hanzaki, E. Essadiqi, S. Yue, Mater. Sci. Technol. Lond. 24 (2008) 1354-1361.
[43] K. Park, M. Nishiyama, N. Nakada, T. Tsuchiyama, S. Takaki, Mater. Sci. Eng. A 604 (2014) 135-141.
[44] F. Fazeli, M. Militzer, ISIJ Int. 52 (2012) 650-658.
[45] F. Fazeli, T. Jia, M. Militzer, Solid State Phenom. 172-174 (2011) 1183-1188.
[46] D. Gaude-Fugarolas, P.J. Jacques, ISIJ Int. 46 (2006) 712-717.
[47] F. Fazeli, X. Wang, ISIJ Int. 47 (2007) 1341-1350.
[48] F.G. Caballero, M.K. Miller, S.S. Babu, C. Garcia-Mateo, Acta Mater. 55 (2007) 381-390.
[49] M. Kumar, R. Sasikumar, P.K. Nair, Acta Mater. 46 (1998) 6291-6303.
[50] N.M. Xiao, M.M. Tong, Y.J. Lan, D.Z. Li, Y.Y. Li, Acta Mater. 54 (2006) 1265-1278.
[51] Y. Zhao, Q. Yan, L. Chen, X. Yuan, Acta Metall. Sin. 27 (2014) 389-394.
[52] I.B. Timokhina, E.V. Pereloma, P.D. Hodgson, Mater. Sci. Technol. Lond. 17 (2001) 135-140.
[53] Z.Z. Zhao, T.T. Tong, J.H. Liang, H.X. Yin, A.M. Zhao, D. Tang, Mater. Sci. Eng. A 618 (2014) 182-188.
[54] S. Takaki, Mater. Sci. Forum 654-656 (2010) 11-16.
[55] P.H. Chang, A.G. Preban, Acta Metall. 33 (1985) 897-903.
[56] N. Kamikawa, K. Sato, G. Miyamoto, M. Murayama, N. Sekido, K. Tsuzaki, T. Furuhara, Acta Mater. 83 (2015) 383-396.
[57] http://www.nssmc.com/en/.

CHAPTER 7 SITE-SPECIFIC ATOMIC SCALE CHARACTERISATION OF RETAINED AUSTENITE IN A STRIP CAST TRIP STEEL

Z.P. Xiong[1*], A.A. Saleh[1], R.K.W. Marceau[2], A.S. Taylor[2], N.E. Stanford[3], A.G. Kostryzhev[1], E.V. Pereloma[1, 4]

[1]*School of Mechanical, Materials and Mechatronic Engineering, University of Wollongong, Wollongong, NSW 2522, Australia*

[2]*Deakin University, Institute for Frontier Materials, Geelong, VIC 3216, Australia*

[3]*Department of Materials Science and Engineering, Monash University, Clayton, Victoria 3800, Australia*

[4]*Electron Microscopy Centre, University of Wollongong, Wollongong, NSW 2519, Australia*

Abstract: Knowledge of carbon content in retained austenite (RA) with different neighbouring phases is essential to understand the chemical stability of RA, which is useful for microstructure tuning. This study investigated morphologies and chemical compositions of RA site-specifically by correlating electron backscattering diffraction, transmission electron microscopy and atom probe tomography. The effect of neighbouring phases, such as polygonal ferrite, bainitic ferrite lath, ferrite in granular bainite and carbides, on the carbon content in the RA was investigated. The results demonstrated that the film RA did not always had a higher carbon content than the blocky ones; coarse RA sometimes displayed a higher carbon content than the fine RA depending on the neighbouring phases. The diffusion of carbon and manganese between RA and ferrite in bainitic ferrite/granular bainite was explained according to either diffusionless and/or diffusional mechanism of bainitic ferrite formation followed by tempering.

Keywords: Retained austenite; Carbon content; Atom probe tomography; Isothermal bainite transformation; Morphology; Neighbouring phases.

7.1 Introduction

Transformation-induced plasticity (TRIP) steels exhibit microstructure comprising polygonal ferrite (PF), bainitic ferrite (BF), granular bainite (GB), retained austenite (RA) and martensite (M). BF comprises ferrite laths with interlath RA films; whereas, GB consists of irregular-shaped ferrite with dispersed blocky RA and/or M/RA constituent [1, 2]. TRIP steels display an outstanding combination of strength and formability due to the multi-phase microstructure and the TRIP effect, which arises from RA-to-martensite transformation during straining [2, 3].

Therefore, the resistance of RA transformation to martensite, namely its stability, is a key factor for mechanical property improvement [3-6]. The RA stability has been intensely studied with respect to its carbon (C) content [2, 7], morphology [5], size [8], orientation [9, 10] and neighbouring phases [11, 12] using step-wise straining electron backscattering diffraction (EBSD) [8], electron probe microanalysis [13], neutron diffraction [14], synchrotron X-ray diffraction [15, 16], transmission electron microscopy (TEM) and atom probe tomography (APT) [17, 18]. The general results are concluded in the following. First, a certain intermediate C content in RA should be maintained to obtain a maximum contribution of the TRIP effect to elongation because a too high C content leads to an incomplete transformation during straining and a too low C content results in an earlier RA transformation to martensite [2, 7, 19, 20]. Second, blocky RA transforms to martensite in the earlier stage of deformation and film RA shows a low tendency for martensite transformation even until fracture [4, 6, 8]. Third, an increase in the RA grain size leads to an earlier transformation due to availability of a greater number of martensite nucleation sites (such as slip steps and stacking faults) [8]. Fourth, when the RA exhibits an orientation facilitating the RA deformation, it will result in the earlier RA-to-martensite transformation [9, 10, 21]. Lastly, there is contradictory evidence with respect to the effect of neighbouring phases on the RA stability. It was stated that the film RA between BF laths is more stable than the one surrounded by PF, because of a high C content in RA and stress shielding by BF laths [22, 23]; whereas, Tomota *et al.* [14] pointed out that the RA enclosed by PF is more stable because of stress relaxation.

It is noted that neighbouring phases not only determine RA morphology but also affect its C content and stress partitioning. Thus, a careful attention should be paid to the effect of neighbouring phases, which has not been systematically investigated [4, 9, 11, 19, 22]. APT being a powerful characterisation technique for the chemical composition analysis has been applied for determination of C content in RA. However, in majority of cases, unless correlative APT and TEM were carried out [24, 25], the RA morphology and its neighbouring phases could not be directly determined from APT but are assumed based on the comparison with TEM observations [7, 8, 17, 26]. In addition to this drawback, RA and martensite cannot be distinguished in APT experiments because RA transforms to martensite due to the low testing temperature [17, 26]. To solve these two problems, a site-specific investigation was carried out in this study by correlation of EBSD, TEM and APT.

On the other hand, APT also can give an insight into the element redistributions across the interfaces and thus provide an indication of the mechanisms of phase transformations. For example, the observed substitutional solute spikes (such as Mn and Si) at the interface between RA and BF lath in a high-carbon TRIP steel, was explained by the local equilibrium, negligible partitioning (LENP) mode where substitutional solute elements are allowed redistribution [18]. Alternatively, the absence of substitutional elements redistribution between BF lath and RA was attributed to the diffusionless mechanism of BF formation [27, 28].

It is well known that for a long time the transformation mechanism of bainite is debated being diffusional or diffusionless. During the growth of bainite, the theory of diffusionless transformation suggests that there is no C diffusion [29], while the diffusional transformation considers C redistribution at migrating austenite/ferrite interface [30, 31]. However, both of these two mechanisms assume that substitutional solutes do not redistribute at the austenite/ferrite interface during the growth of bainite [29, 30]. Recently, Chen *et al.* proposed a so-called Gibbs energy balance (GEB) approach in order to evaluate the effect of alloying elements on the bainite growth [32, 33]. The approach considers Gibbs energy dissipation due to the alloying element diffusion inside the interface.

According to this GEB approach, depending on the time of BF formation during isothermal bainite transformation (IBT), three growth modes in the sequence of paraequilibrium (PE), negligible partitioning (NP) and partitioning (P) are predicted [32-35]. When the transformation kinetics of austenite-to-bainite is a fast growth mode at an early stage, there is no substitutional solute diffusion and the transformation is controlled by C diffusion under PE condition. When the kinetics turns to a slow growth mode due to the C enrichment in austenite and in turn a reduced driving force, the bainite forming at this stage follows NP condition where the substitutional solute diffusion inside the austenite/ferrite interface is promoted, resulting in solute segregation formation. The bainite transformation at the very late stage proceeds under the P condition where the growth of bainite requires substitutional solute diffusion inside the RA, leading to the formation of solute segregations [18, 32, 36]. However, the corresponding experimental observations of these three modes are not provided. In the current study, several interfaces between RA and BF laths or ferrite in GB were investigated using site-specific APT characterisation in order to elucidate the diffusion behaviour of substitutional solute elements correlated with this GEB approach.

Specifically, the aim of this study is to experimentally clarify and systematically analyse the effect of neighbouring phases on RA morphology and its C content in a strip cast TRIP steel. Following this, some general conclusions made by previous researches with respect to RA carbon content and its size were overthrown and the new explanations were provided. Based on GEB approach, the analysis of substitutional solute element distributions across the interfaces between RA and BF laths or ferrite in GB, suggests PE growth model for GB and BF, and NP or P growth model for BF formed at later stages. Diffusionless model of BF formation followed by tempering is also able to explain the observed substitutional elements partitioning with the exception of one case.

7.2 Experimental details

As-cast samples were produced at Deakin University using a dip tester, which can simulate rapid cooling during solidification when liquid steels contact twin rolls in strip casting [37, 38]. The chemical composition of used steel in weight and atomic percent is listed in Table 7.1.

Table 7.1 The chemical composition of the studied steel.

	C	Si	Mn	Al	Cu	Cr	P
wt.%	0.172	1.520	1.610	0.0266	0.0153	0.195	0.00440
at.%	0.782	2.957	1.601	0.0539	0.0132	0.205	0.00776

The quench-deformation dilatometer Theta was used for the heat treatment. The samples were heated to 1250 ˚C and held for 300 s in order to simulate the prior austenite grain structure (80±27 μm) inherent in strip casting. During cooling at 30 Ks^{-1} to 670 ˚C and 90 s holding formation of 0.55±0.06 ferrite fraction occurred. After cooling at 50 Ks^{-1} to 400 ˚C and holding for 900 s the samples were quenched to room temperature. 0.045±0.003 fraction of RA with an average C content of 1.23±0.01 wt.% (5.39 at. %) was measured using X-ray diffraction (XRD). The detailed description of this heat treatment is given elsewhere [39].

The thin foil (3 mm disc) was produced by wire-cutting the sample through the thickness, mechanical polishing to 80 μm thickness and electropolishing using an electrolyte containing 10 vol. % perchloric acid in methanol. EBSD experiments were carried out on these thin foils using a JEOL JSM-7001F field emission gun – scanning electron microscopy (FEG – SEM) fitted with a Nordlys-II(S) EBSD detector, which operated at 15 kV accelerating voltage and ~ 5.1 nA probe current using a step size 0.04 μm. The microstructures were also characterised using a JEOL JEM-ARM200F scanning transmission electron microscope operating at 200 kV. Electron energy loss spectroscopy (EELS) was carried out using a step size of 11 nm, a collection semi-angle of 8.0 mrad and a convergence semi-angle of 24.5 mrad. The size of PF, second phase region and blocky RA was calculated as equivalent circle diameter (ECD). Noticeably, the ECD and thickness of film RA were determined based on the two-dimensional maps due to the absence of three-dimensional information, although they could be changed into the values in three-dimensional space because of a proportional relationship between two-dimensional values and three-dimensional ones [40].

Correlated to the EBSD maps, atom probe specimens were prepared by the site-specific lift-out method [41, 42] as briefly presented in Figs. 7.1(a, b), using a dual-beam focused ion beam (FIB)/SEM instrument (FEI Quanta 3D), with the final annular FIB milling stage operating at 8 kV and 25 pA. APT experiments were

undertaken using a local electrode atom probe (LEAP 4000HR, Cameca Instruments) operating at a pulse repetition rate of 200 kHz, 20% pulse fraction, temperate set-point of 60 K and target evaporation rate of 0.5%. The data reconstruction and analysis were carried out using the IVAS 3.6.8 software (Cameca Instruments). The compositions of various phases were determined from the regions without any visible clusters, precipitates and interfaces. Interfaces were visually shown using the iso-concentration surfaces with the threshold iso-concentration value chosen as the midpoint of difference in C content between the adjacent phases. A minimum of 20 atoms was used for cluster detection to eliminate random fluctuations. The maximum separation distance method was used for the cluster with a maximum distance of 1 nm and a grid spacing of 0.1 nm [43]. The Guinier radii (r_G) of clusters were calculated from gyration radii (l_g) using the following equation [43]:

$$r_G = \sqrt{\frac{5}{3}} l_g \tag{7.1}$$

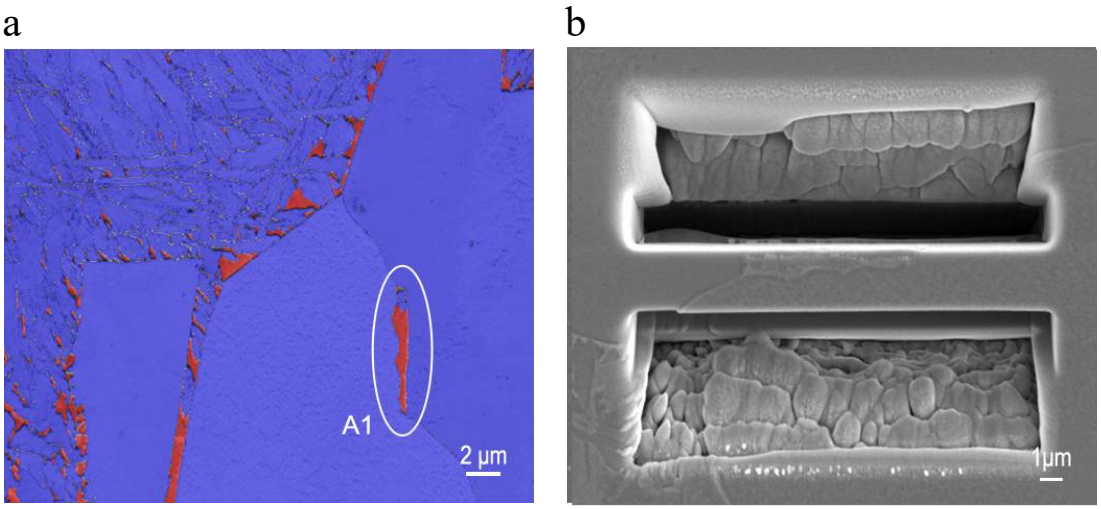

Figure 7.1 Specific microstructure characterisation by correlation of EBSD and APT: (a) EBSD phase map with band contrast (red is fcc and blue is bcc); (b) lift-out preparation from the corresponding circled area in (a).

7.3 Results

7.3.1 Correlation of microstructure using transmission electron microscopy and electron backscattering diffraction

A detailed microstructure characterisation for the studied processing condition has been reported elsewhere [39]. Here, it is worth reminding that the microstructure after holding at 400 ˚C for 900 s comprised 0.55±0.06 fraction of PF, 0.045±0.003 fraction of RA, GB, BF and a small amount of martensite and Widmanstätten ferrite (Figs. 7.2(a-c)). The average sizes of PF and second phase region were 17±10 and 21±24 μm, respectively [39].

The EBSD (Figs. 7.1(a), 7.2(a) and 7.3) and corresponding TEM observation (Figs. 2(b-e)) were used to characterise face-centred cubic (fcc) and body-centred cubic (bcc) phases. Various morphologies of RA, defined by its shape and neighbouring phases, were found in this studied steel: (1) blocky RA enclosed by PF (Fig. 7.3(a)); (2) blocky RA within GB or adjacent to the PF/second phase region interface (Figs. 7.2(a) and 7.3); (3) blocky RA between bainitic packets which were delineated by dashed lines in Fig. 7.2(e); (4) blocky RA present in an austenite/martensite constituent (Fig. 7.2(b)); (5) film RA between BF laths (Figs. 7.2(c, d) and 7.3(a, b)). These five types of RA were also reported by other researchers [2, 9, 22]. In addition, the Kurdjumov–Sachs orientation relationship ($\{110\}_{bcc}//\{111\}_{fcc}$, $\langle 111\rangle_{bcc}//\langle 101\rangle_{fcc}$) [44] was observed between RA and martensite (Fig. 7.2(b)) or BF lath (Fig. 7.2(c)). Some nano-sized RA laths were not resolved in EBSD map (c.f. Figs. 7.2(a) and (d)) due to their small thickness compared to the step size used in the mapping, but are clearly defined using TEM.

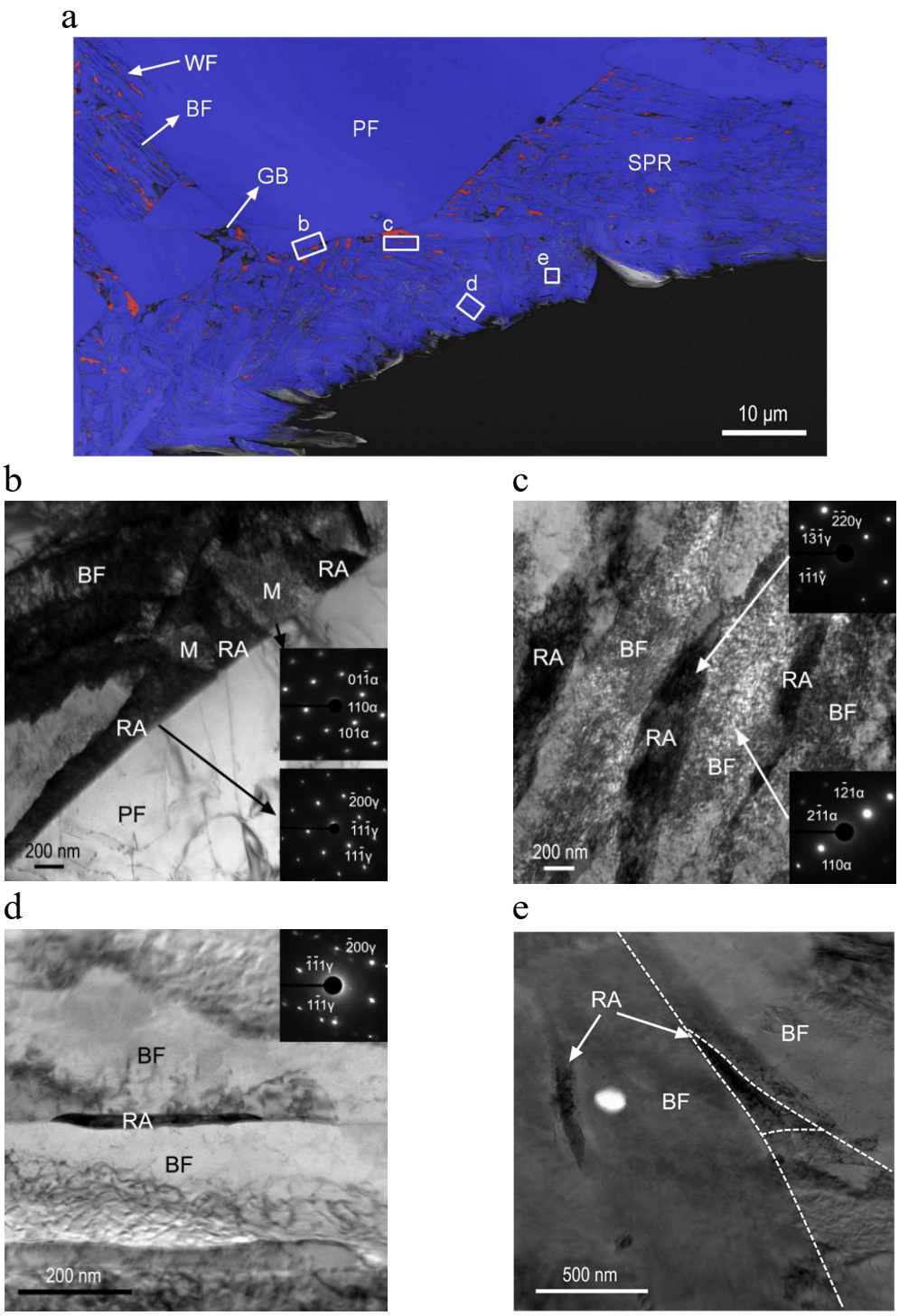

Figure 7.2 (a) (a) EBSD phase map with band contrast (blue = bcc, red = fcc and right lower corner is the disc hole) and (b, c, d, e) correlated TEM microstructures. (b) Blocky retained austenite and martensite adjacent to the polygonal ferrite/second phase region interface (the zone axis of insets is $(011)_\gamma$ and $(111)_\alpha$, respectively); (c, d) film retained austenite between bainitic ferrite laths (the zone axis of (c) insets is $(\bar{1}12)_\gamma$ and $(\bar{1}13)_\alpha$; the zone axis of (d) inset is $(011)_\gamma$); (e) small blocky retained austenite between bainitic packets (the dashed lines showed the boundaries of three bainitic packets). *PF* is polygonal ferrite, *WF* is Widmanstätten ferrite, *SPR* is second phase region, G*B* is granular bainite, *BF* is bainitic ferrite, *M* is martensite and *RA* is retained austenite.

7.3.2 Atom probe tomography study correlated with electron backscattering diffraction

Figs. 7.1(a) and 7.3 show the representative EBSD maps, which were used for APT tips lift-outs. “F”, “B” and “A” stand for film RA between BF laths (F1 – F3), blocky RA adjacent to PF (B1, B2, B4 and B5) or present in GB (B3), and blocky RA among PF (A1 and A2), respectively. Examples of RA atom maps are shown in Figs. 7.4 – 7.7. Based on the total number of ions collected from the volume free of any visible solute segregation, the chemical compositions of RA were calculated and are listed in Table 7.2. The observed C contents in RA are consistent with those published by many researchers [7, 8, 17, 26, 27]. For example, Timokhina *et al.* reported 3.8 at. % C in blocky RA and 6.5 at. % C in film RA in Fe-1.2C-3.8Si-1.9Mn-0.17Mo (at.%) TRIP steel [26], and 1.5 – 7.5 at. % C in film RA in bainitic steel (3.5 C–2.9 Si–1.9 Mn–1.0 Cr–0.13 Mo–2.1 Al–1.4 Co (at.%)) [7].

On one hand, the C content in the film RA (F1 – F3) increased from ~ 3 to 6.36 at. %, with a decrease in the size of second phase region from 83.8 to 25.6 μm (Table 7.2). In the blocky RA adjacent to the PF (B1, B2 and B4) or present in GB (B3), the C content also increased from 5.10 to 6.08 at.% with a decrease in the size of second phase region from > 50.8 to 7.4 μm. On the other hand, the B5 sample exhibited a lower C content of 5.73 at. % with a further decrease in the size of second phase region down to 1.3 μm. The C contents (6.23 – 6.78 at.%) in the blocky RA among PF (A1 and A2) were relatively higher than those in the blocky RA adjacent to the PF (B1, B2 and B4) or present in the GB (B3). Noticeably, film RA did not always have a higher C content than blocky RA (such as F2 and B1 – B5). With a decrease in RA grain size, the C content did not always increase (such as in A1 and A2).

In addition, the Mn content in film RA (F1 – F3) was between 1.68 and 1.95 at. %. For blocky RA (B1 – B4), the Mn concentration increased from 1.53 to 2.15 at. % with a decrease in the second phase region size from > 50.8 to 7.4 μm. This trend is similar to that for C content. When the size of the second phase region was 1.3 μm, the Mn content in the B5 RA decreased to 1.68 at. %. Besides, the Cr content was between 0.37 and 0.41 at.% in film RA and was between 0.23 and 0.46 at.% in the blocky ones. Si content varies around 3.70 at. %. Compared to the nominal steel

composition, this value was a little high in RA probably due to the preferential evaporation of Si [45].

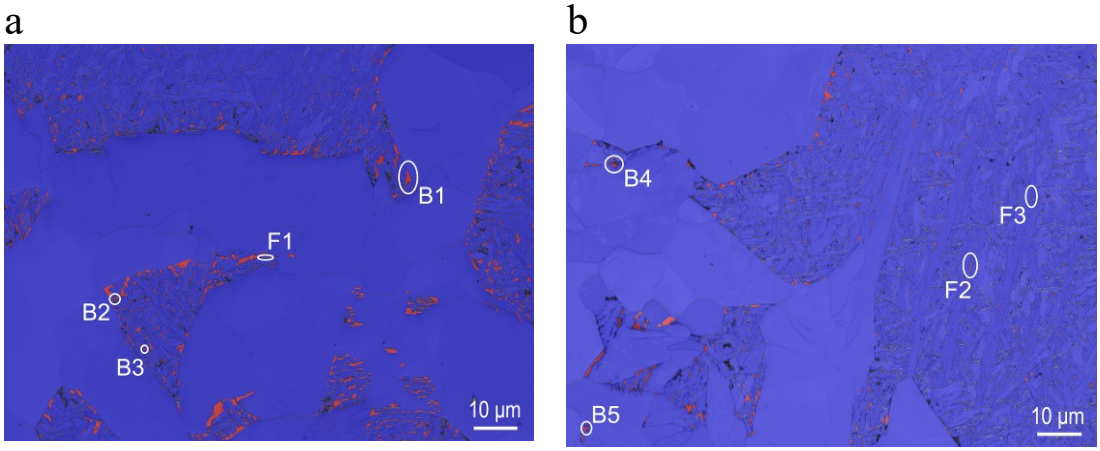

Figure 7.3 (a, b) Representative EBSD phase maps with band contrast showing the regions (white markers) used for correlative APT study. Red is fcc and blue is bcc.

Table 7.2 Chemical compositions of retained austenite (at. %) determined from atom probe tomography data based on the number of atoms, and the equivalent circle diameter (ECD)/thickness of retained austenite together with the ECD of the second phase region corresponding to its location. Iron is balance.

No.	C	Mn	Si	Cr	*Ms*, °C	Thickness, µm	ECD, µm	Second phase region size, µm
F1	6.36±0.02	1.85±0.02	3.72±0.02	0.38±0.01	-179	0.28	--	25.6
F2	2.17±0.05	1.95±0.08	3.70±0.09	0.41±0.04	241	0.24	--	83.8
F3	3.19±0.02	1.76±0.02	3.85±0.03	0.37±0.01	147	0.16	--	83.8
B1	5.10±0.03	1.53±0.05	3.69±0.03	0.31±0.03	-34	--	1.9	>50.8
B2	5.45±0.01	1.60±0.02	2.98±0.04	0.23±0.01	-57	--	1.1	25.6
B3	5.89±0.01	1.87±0.01	3.84±0.01	0.39±0.01	-131	--	0.6	25.6
B4	6.08±0.06	2.15±0.06	3.58±0.07	0.46±0.03	-161	--	1.3	7.4
B5	5.73±0.02	1.68±0.01	3.62±0.02	0.35±0.01	-101	--	1.1	1.3
A1	6.23±0.01	1.68±0.01	3.55±0.01	0.38±0.01	-153	--	2.3	--
A2	6.78±0.01	1.87±0.01	3.83±0.01	0.40±0.01	-226	--	2.5	--

7.3.2.1 Film retained austenite between bainitic ferrite laths

A representative film RA between two BF laths (location F1 in Fig. 7.3(a)), is shown in Fig. 7.4. The atom maps of C, Mn and Cr clearly show the interfaces between RA and BF laths (Figs. 7.4(a, b, d)), due to the variations in their concentrations in RA and BF laths, although Si was more homogenously distributed (Fig. 7.4(c)). On average, a much higher C content of 6.36±0.02 at. % was measured in RA and a much lower C content of 0.53±0.02 at.% was characteristic for the BF laths (Figs. 7.4(a, e, f)). The Mn and Cr contents (Figs. 7.4(e, f)) were slightly higher in RA

(1.85±0.02 at. % Mn and 0.38±0.01 at. % Cr) compared to those in BF laths (1.68±0.07 at. % Mn and 0.28±0.03 at. % Cr). As C, Mn and Cr elements are austenite stabilisers [2, 18, 33], they partition from BF to RA leading to their higher contents in RA than in BF laths.

Chemical gradients across interfaces were revealed using proximity histograms at iso-concentration surfaces of 3.0 at. % C (Figs. 7.4(e, f)). The proximity histogram across the upper interface (Fig. 7.4(e)) shows the C, Mn and Cr concentration peaks of 7.50, 3.09 and 0.67 at.% at 1.1, 0.1 and 0.1 nm, respectively, from the RA/BF lath interface on the RA side. Whereas, the proximity histogram across the lower interface (Fig. 7.4(f)) shows the C, Mn and Cr concentration peaks of 6.82, 2.71 and 0.5 at.% at 1.3, 0.5 and 0.5 nm, respectively, from the RA/BF lath interface on the RA side. The pronounced Mn and Cr enrichments at the RA/ferrite interface (Figs. 7.4 (e, f) and 7.5(e)) are beyond the limits of $\pm 2\sigma_r$ interval. Therefore, these fluctuations can be regarded as real effects but not APT reconstruction artefacts. Noticeably, the Mn segregation adjacent to the interface could lead to local straining due to the substitution of Fe for Mn [13], which would deteriorate RA stability.

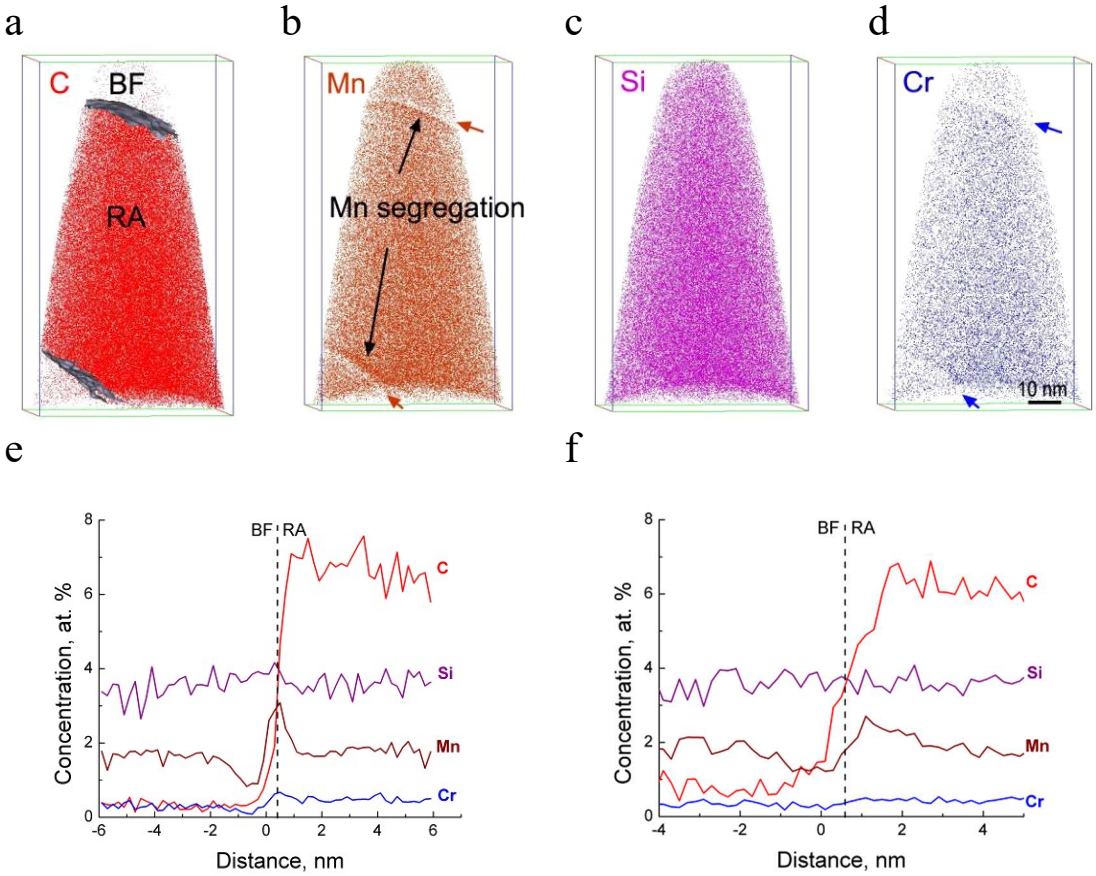

Figure 7.4 (a) Carbon (3.0 at. % C iso-concentration surface is visually shown as the upper and lower interfaces with the removal of isolated fragments for clarity), (b) manganese, (c) silicon and (d) chromium atom maps (brown and blue arrows indicate the interfaces between retained austenite and bainitic ferrite laths); (e, f) proximity histograms across the (e) upper and (f) lower interfaces (dashed lines indicate the interfaces between retained austenite and bainitic ferrite laths). *RA* is retained autenite and *BF* is bainitic ferrite lath. The total number of analysed atoms is 72584277.

7.3.2.2 Blocky retained austenite in granular bainite

A representative blocky RA in GB (location B4 in Fig. 7.3(b)) is shown in Fig. 7.5. The atom maps of C, Mn and Cr clearly show the interface between the RA and ferrite in GB, due to their concentrations varying across the interface (Figs. 7.5(a, b, d)). Si was homogenously distributed in both the RA and ferrite of GB as seen in Figs. 7.5 (c, e). On average, higher C, Mn and Cr contents of 6.08±0.06, 2.15±0.06 and 0.46±0.03 at. %, respectively, were measured in the RA; lower C, Mn and Cr contents of 0.54±0.02, 1.40±0.04 and 0.22±0.02 at. %, respectively, were observed in the ferrite of GB. The proximity histograms calculated across the iso-concentration surface of 3.0 at. % C (Fig. 7.5(e)) show the C, Mn and Cr concentration peaks of

6.80, 2.66 and 0.53 at. % at 1.4, 0.8 and 0.8 nm, respectively, from the RA/ ferrite interface on the RA side. In addition, C clusters were present in ferrite of GB as shown in Fig. 7.5(f). The number of C atoms in the clusters was between 21 and 41.

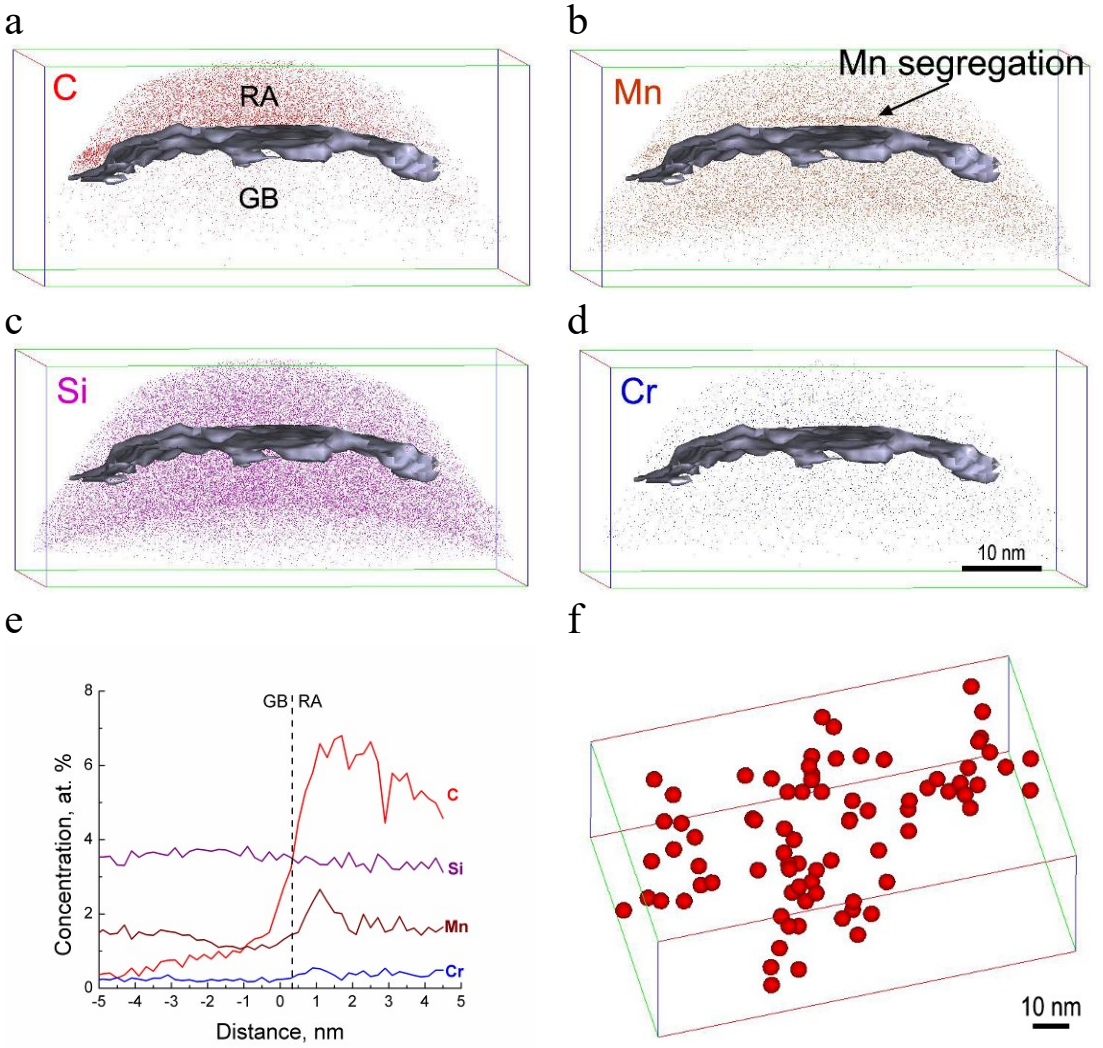

Figure 7.5 (a) Carbon, (b) manganese, (c) silicon and (d) chromium atom maps of granular bainite (3.0 at. % C iso-concentration surface is visually shown as the interface between retained austenite and ferrite of GB with the removement of isolated fragments for clarity); (e) proximity histogram across the interface; (f) carbon clusters in ferrite of granular bainite (the matrix atoms were suppressed with the maximum separation distance of 1 nm). *RA* is retained autenite and *GB* is ferrite in granular bainite. The total number of analysed atoms is 2079655.

7.3.2.3 Blocky retained austenite adjacent to cementite in granular bainite

A representative blocky RA adjacent to the cementite (location B5 in Fig. 7.3(b)) is shown in Fig. 7.6. The C atom map has three distinct regions: the lowest C content region corresponding to ferrite in GB; the highest C content relating to carbide; and

the intermediate C content region presenting the RA. The average C content was 5.73±0.02, 26.07±0.18 and 0.39±0.01 at.% while the Mn content was 1.68±0.01, 2.93±0.08 and 1.40±0.06 in RA, cementite and ferrite of GB, respectively. The concentration profile (Fig. 7.6(b)) along the black arrow allowed to identify that the type of carbide was cementite according to the ~ 25 at. % C content inherent to cementite stoichiometry [46]. In the core, cementite was enriched in Mn and Cr but depleted in Si because of its low solubility in cementite and high driving force for its removal [18, 47]. Although no silicon depletion was observed in cementite during 180 s holding at 500 °C for bainite formation in 0.3C-0.25Si-1.22Mn-0.14Cr steel (wt. %) [48] and after tempering at 200 °C for 240 hours in 0.98C-1.46Si-1.89Mn-0.26Mo-1.26Cr-0.09V steel (wt. %) [27], similar to the current work a significant reduction in Si content in cementite cores was detected in APT studies of cementite formation in 0.22C-1.19Si-1.53Mn-0.57Al-0.037Nb steel (wt. %) during 1800 s holding at 500 °C [17] and in 0.98C-1.46Si-1.89Mn-0.26Mo-1.26Cr-0.09V steel after tempering at 450 °C for 1800 s [49]. As pointed out by Caballero *et al.* [49], during the early stage of cementite formation, there was no redistribution of substitutional solutes between cementite and ferrite, suggesting that cementite was formed by PE growth; with an increase in the holding temperature/time, Si diffused out of the carbide, reaching an equilibrium concentration at the cementite/ferrite interface. This indicates the transition from PE to local equilibrium condition.

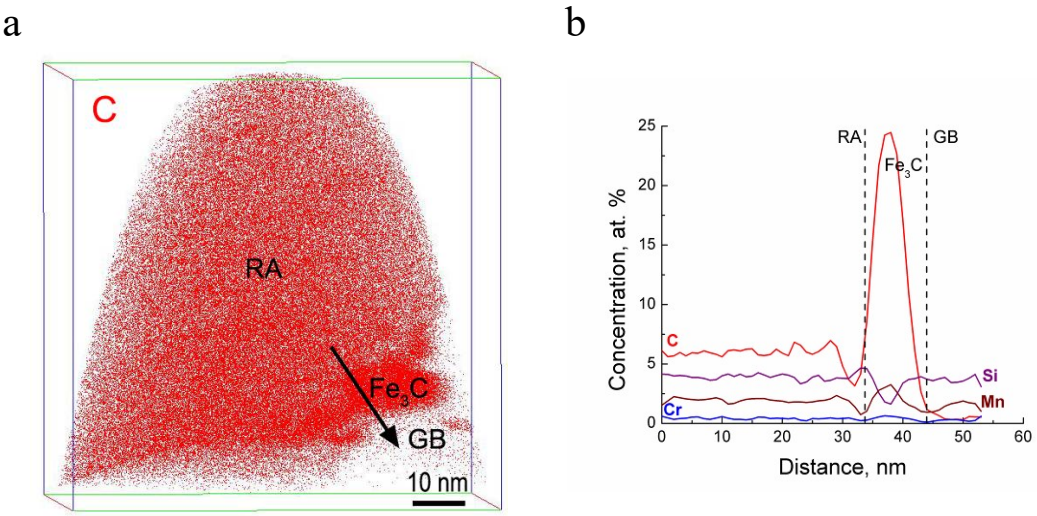

Figure 7.6 (a) Carbon atom map and (b) concentration profiles along the arrow in (a). *RA* is retained austenite, *GB* is ferrite in granular bainite and *Fe_3C* is cementite. The total number of analysed atoms is 11437692.

7.3.2.4 Blocky retained austenite enclosed by polygonal ferrite

A representative blocky RA enclosed by PF (location A1 in Fig. 7.1(a)) is shown in the form of 8.0 at. % C iso-concentration surfaces (Fig. 7.7(a)). The linear feature with significant level of C indicated by the black arrow (Fig. 7.7(a)) was a Cottrell atmosphere. The concentration profiles perpendicular to this atmosphere along the arrow are shown in Fig. 7.7(b). As seen, the dislocation only trapped C atoms but not substitutional solute atoms (Mn, Si and Cr). These phenomena were also suggested by Kalish *et al.* [50]. The average C content of this Cottrell atmosphere was around 7.5 at. %. It corresponds to the saturation C concentration of 6 – 7 at.% in the region of one Burgers vector around the core, which was predicted by Cochardt *et al*. [51]. Similarly, Timokhina *et al.* [52] also revealed a Cottrell atmosphere in RA using an iso-concentration surface of 7.0 at. % C.

Fig. 7.7(c) depicts the C atom map of PF adjacent to the blocky RA shown in Fig. 7.7(a). The atom maps of Mn, Si and Cr are not presented here as these elements have shown homogeneous distributions in PF. C clusters in this PF, indicated by two black arrows in Fig. 7.7(c), were clearly visible in Fig. 7.7 (d). Cottrell atmosphere where C atoms trapped along the dislocation line can also be seen in the PF (Fig. 7.7 (e)), nearly parallel to the blue arrow (Fig. 7.7 (c)). The C content was measured to be 6.23±0.01 and 0.03±0.002 at.% while Mn content was 1.68±0.01 and 1.62±0.01 at .%, and Cr content was 0.37±0.01 and 0.26±0.01 at. % in RA and PF, respectively.

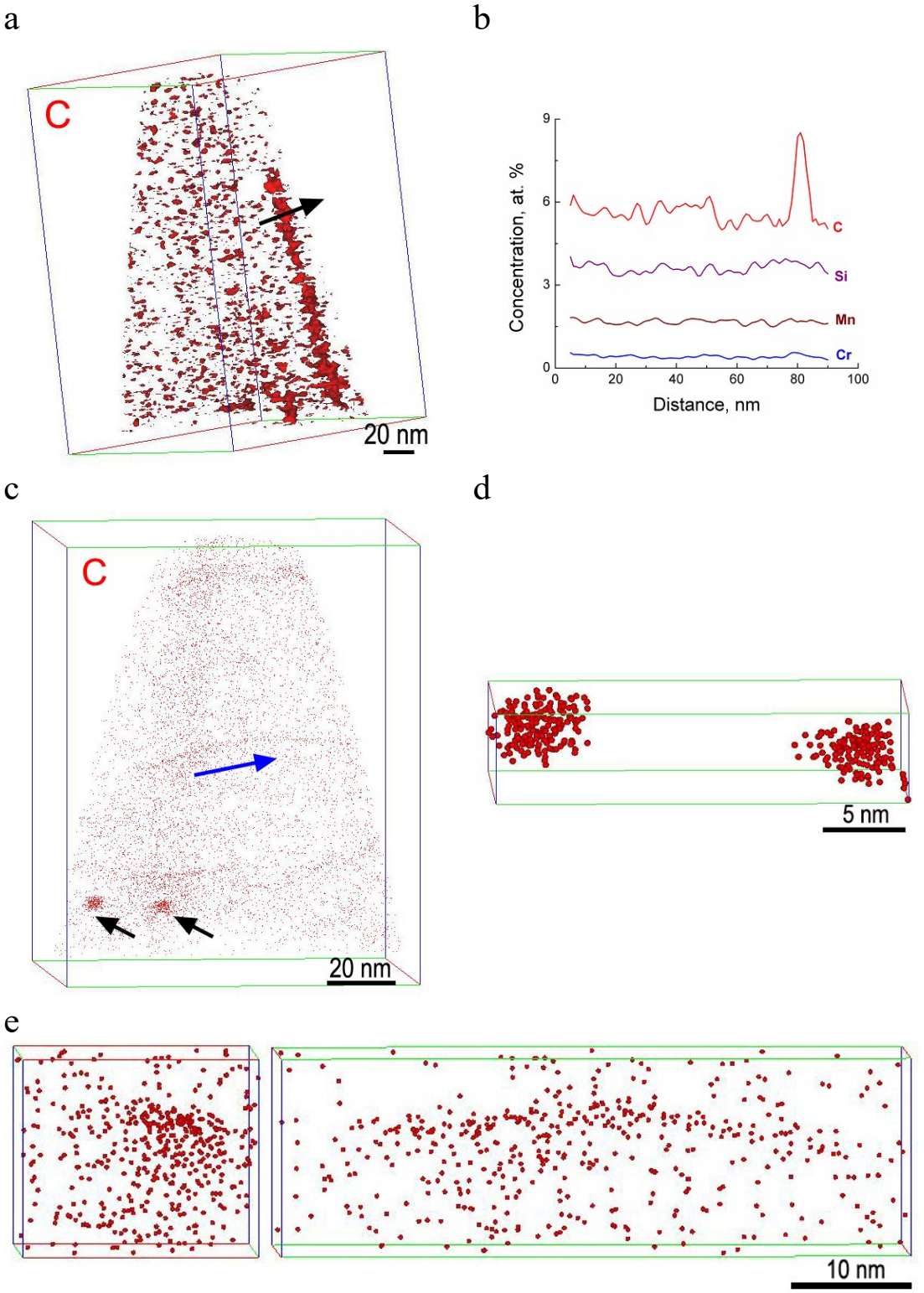

Figure 7.7 (a) Carbon iso-concentration surfaces at 8.0 at. % in blocky retained austenite and (b) concentration profiles along the dark arrow in (a); (c) carbon atom map of polygonal ferrite adjacent to the blocky retained austenite shown in (a), (d) clusters indicated by dark arrows in (c) and (e) atom maps of Cottrell atmosphere parallel to the blue arrow in (c) taken in two perpendicular directions showing its rod-like shape. The matrix atoms for (d) were suppressed with the maximum separation distance of 1 nm. The total number of analysed atoms is 30017388 in (a) and 23583341 in (c).

7.3.2.5 Carbon clusters

C clusters were observed in PF (Fig. 7.7(d)), ferrite of GB (Fig. 7.5(f)) and BF lath (Fig. 7.8(a)). Only limited number of nanoscale cementite (~ 2.7 nm thickness) in BF lath was found and an example is indicated by the arrow in Fig. 7.8(a), which contained 23.67±0.11 at. % C. Similar to the concentration profiles shown in Fig. 7.6(b), the Si content in this cementite was also depleted. Nevertheless, the cementite was not observed in PF and ferrite of GB in this study among at least five APT runs for each phase. Fig. 7.8(b) shows a tendency that the Guinier radius increased with a decrease in C content, which is similar for reported trends in Refs [7, 53]. The number density of C clusters was $4.0\pm2.1\times10^{21}$, $1.7\pm1.4\times10^{23}$ and $4.5\pm4.1\times10^{23}$ m^{-3} in PF, ferrite of GB and BF lath, respectively.

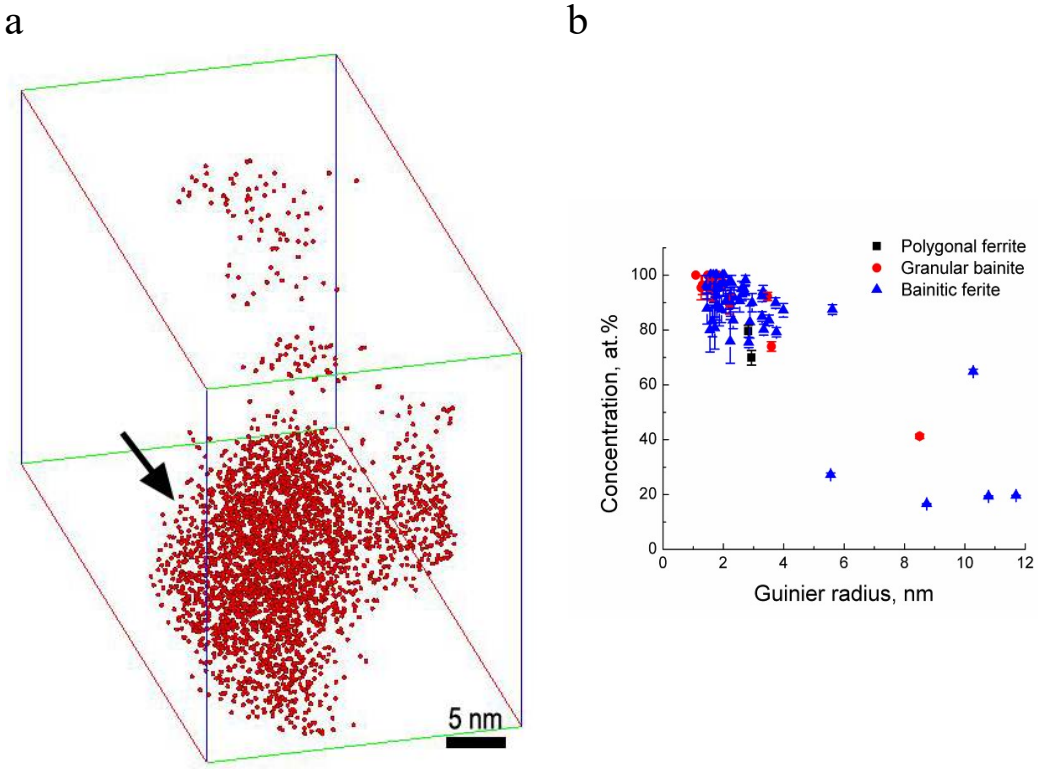

Figure 7.8 (a) Carbon clusters observed in bainitic ferrite lath; (b) variation of Guinier radius with carbon content in clusters observed in polygonal ferrite, ferrite in granular bainite and bainitic ferrite lath.

7.3.2.6 Solute redistribution across the interface

Solute segregations across the interfaces between RA and BF laths (Fig. 7.4) or ferrite in GB (Fig. 7.5) were characterised using the following steps. The proximity

histogram (similar to Fig. 7.4(e)) was calculated in a selected cylinder perpendicular to the iso-concentration surface of 3.0 at. % C (Fig. 7.9(a)). Then the curves of cumulative number of solute atoms as a function of cumulative number of all atoms were plotted in Fig. 7.9(b). Following this, the segregation region was determined according to the change of linear relationship, which was illustrated in Fig. 7.9(b) using an example of Mn.

Fig. 7.9(c) shows the segregation regions determined using C, Mn and Cr, respectively (refer to C/Mn/Cr segregation region). The C segregation region is defined as the interface region because of rapid diffusion of C atoms. The relative diffusion distance of the Mn/Cr segregation region with respect to the C interfacial region was listed in Table 7.3. As can be seen, for the upper interface between RA and BF lath (Fig. 7.4), Mn segregation region contains the C interface region; for the lower interface between RA and BF lath (Fig. 7.4), Mn segregation region moves a distance of 1.0 nm into the RA side; for the interface between RA and ferrite in GB (Fig. 7.5), Mn interfacial region also moves into the RA side but to a large distance of 1.1 nm. Toji *et al.* [25] also reported a diffusion distance of Mn below 2 nm during 300 s holding at 400 ˚C in a quenching and partitioning steel. The Cr interface regions had similar ranges to those determined using Mn element (Fig. 7.9(c) and Table 7.3). It should be noted that the distances listed in Table 7.3 slightly differ from those determined based on proxigram analysis in *Sections 7.3.2.1* and *7.3.2.2* The former are used in subsequent analysis and we believe this approach for determination of diffusion distance is more accurate.

The Gibbs interfacial excess of Mn and Cr (Table 7.3) is calculated as follows [54],

$$\Gamma_i = N_i^{excess} / \eta A \tag{7.2}$$

where N_i^{excess} is determined as shown in Fig. 7.9 (b), η is atom probe's detection efficiency (η = 0.42), and A is the selected interfacial area. The interface between RA and ferrite in GB (Fig. 7.5) exhibits the lowest Γ_i of Mn and Cr, while the upper interface between RA and BF lath (Fig. 7.4) has the highest Γ_i of Mn and Cr. An increase in the diffusion lengths of Mn and Cr corresponds to a decrease in Gibbsian interfacial excess. It gives a support for the diffusion of Mn and Cr.

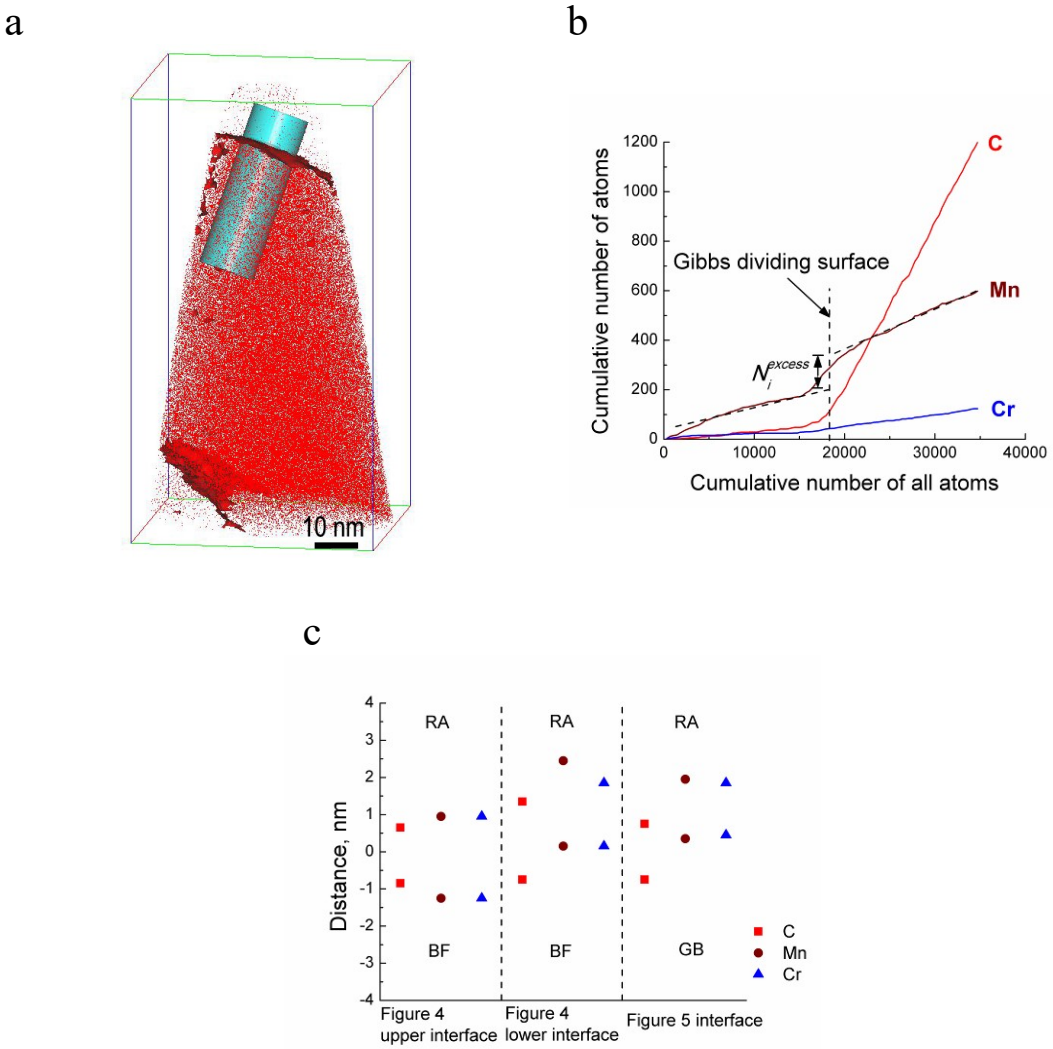

Figure 7.9 (a) A representative selected cylinder volume perpendicular to the iso-concentration surface of 3.0 at. % carbon (Figure 7.4(a)); (b) corresponding integral profiles across the interface showing the cumulative number of carbon, manganese and chromium atoms as a function of cumulative number of all atoms, which was calculated from the corresponding proximity histogram in the selected cylinder (a); (c) interface regions determined by carbon, manganese and chromium. *RA* is retained austenite, *BF* is bainitic ferrite lath and *GB* is ferrite in granular bainite.

Table 7.3 The relative diffusion distance of manganese/chromium segregation region with respect to C interface region and the Gibbsian interfacial excess of solutes (atoms/cm^2). *RA* is retained austenite, *BF* is baintic ferrite and *GB* is granular bainite.

	The diffusion distance with respect to carbon interface region, nm		Gibbsian interfacial excess, atoms/cm^2	
	Mn	Cr	Mn	Cr
Upper interface between RA and BF lath (Figure 4)	0.1	0.1	$2.1\pm0.4\times 10^{14}$	$0.3\pm0.08\times 10^{14}$
Lower interface between RA and BF lath (Figure 4)	1.0	0.7	$1.5\pm0.3\times 10^{14}$	$0.2\pm0.07\times 10^{14}$
The interface between RA and ferrite in GB (Figure 5)	1.1	1.1	$1.4\pm0.4\times 10^{14}$	$0.2\pm0.08\times 10^{14}$

7.4 Discussion

7.4.1 Carbon partitioning

The PF, GB and BF formations during the two-stage heat treatment of studied TRIP steel are responsible for the C enrichment in RA. At first, C was rejected into austenite from the PF forming during cooling to 670 ˚C and 90 s holding at this temperature. Following this, the C enrichment in the austenite continued because of GB and BF formations during cooling to the IBT temperature of 400 ˚C and 900 s holding at this temperature. According to the APT data analysis of volumes free of any visible segregations, the average C content in PF and ferrite in GB/BF lath was calculated as 0.025±0.003 and 0.43±0.099 at.%, respectively. The C content of 0.43±0.099 at.% was about 6 times higher than the expected value (~ 0.075 at. % [17]) calculated based on the PE condition between austenite and ferrite. This high C content in ferrite in GB and BF lath possibly resulted from C atoms trapped in the octahedral interstices from diffusionless transformation [55] and/or C-Mn dipoles formation [56]. Thus, the contribution of C atoms rejected into RA from PF was much higher than that from ferrite in GB and BF lath.

In addition, other three factors can further reduce the capability of ferrite in GB and BF lath to enrich the RA with C atoms. First, the dislocation density in the ferrite in GB and BF lath (10^{14} – 10^{15} m^{-2} [7, 27, 28]) is higher than that in the PF ($5.1\pm0.42\times10^{13}$ m^{-2} [57]), leading to more C atoms being trapped at the dislocations and less C atoms for RA enrichment. Second, the number density of C clusters in ferrite in GB and BF lath (1.7±1.4 and $4.5\pm4.1\times10^{23}$ m^{-3}, respectively) were two orders of magnitude higher than that in PF ($4.0\pm2.1\times10^{21}$ m^{-3}). Third, the observed nanoscale cementite in BF (Fig. 7.8(a)) could reduce the available C atoms for enrichment in the austenite as the C partitioning into austenite and carbide precipitation are competitive processes [29].

7.4.2 The dependence of carbon content of retained austenite on its neighbours

The neighbouring phases of RA affected its morphology. As shown in Fig. 7.2, the RA surrounded by PF and/or in GB exhibited blocky shape; the RA between the BF laths displays film shape; the RA located between the BF packets is characterised by blocky one [2, 5, 18]. In addition, the neighbouring phases of RA also affected its C

partitioning according to *Section 7.4.1*. The PF formation rejected much more C atoms into RA than that of ferrite in GB and BF lath. Thus, the fraction of neighbouring PF around second phase regions should be first considered. For easy comparison, the fraction of neighbouring PF is defined as the ratio of PF area and second phase region area by drawing a circle in the centre of second phase region using a certain radius. In reality, the ratio of volumes should be considered rather than the ratio of the areas. However, only the two-dimensional EBSD maps were obtained in this project. According to this ratio of the areas, obviously with a decrease in the size of second phase region, its fraction of neighbouring PF increased, resulting in more C atoms enriched in RA. This corresponds to the C content in RA increasing with a decrease in the size of second phase region (Table 7.2), regardless of the RA being in the form of film (F1 and F2, F3) or of blocky shape (B1 – B4).

When the fraction of neighbouring PF is similar, GB and BF should be further considered because the RA is further enriched by their formations. F1, B2 and B3 RA were in the same second phase region (Fig. 7.3) and thus they had the same fraction of neighbouring PF. B3 RA had a higher C content than B2 RA, although B2 RA was near the PF/second phase region interface, leading to a short C diffusion distance from PF. This could be explained as follows. The B3 RA was present in GB, compared to the B2 RA, which was adjacent to ferrite in GB from one side and to PF from another side. Therefore, a larger interface area with ferrite in GB for B3 RA than that for B2 RA, led to more C atoms being rejected to B3 RA during GB formation. In addition, the size of B3 RA (0.6 μm) is twice smaller than that of B2 RA (1.1 μm), which further resulted in a higher C concentration in B3 RA. Comparison of film F1 and blocky B3 RA, shows F1 RA exhibiting higher C content. It was ascribed to a higher fraction of interface area for F1 RA surrounded by BF laths than that for the B3 RA present in GB, resulting in more C atoms rejected to the F1 RA.

Moreover, when the carbide is a neighbouring phase of RA, it will act as a C sink, leading to a decrease in RA carbon content. Comparison of B4 and B5 RA shows B5 RA having a lower C content even though its second phase region was smaller (Table 7.2). It results from the carbide formation adjacent to B5 RA (Fig. 7.6).

In addition to C enrichment, the RA was also enriched with Mn. However, the tendency for Mn enrichment in relation to the neighbouring phases was not as clear as for C (Table 7.2). For blocky RA, the Mn content had the same tendency as that for the C content with respect to the size of second phase region. The Mn content increased with a decrease in the size of second phase region because of more Mn atoms being rejected to RA from a larger fraction of neighbouring polygonal ferrite. When the cementite formed, the Mn content decreased in RA (Fig. 7.6) because of Mn being a carbide-forming element. For film RA, the Mn content was between 1.68 and 1.95 at.%, and showed no tendency with respect to the size of second phase region and RA thickness. The Cr was also enriched in RA compared with other phases (Table 7.2) but without any tendency in relation to neighbouring phases. More experimental study and analysis are required in the future.

Following the above discussion with respect to the effect of neighbouring phases (PF, ferrite in GB, BF lath and carbides) on C content in RA, two general conclusions reported in the literature are overthrown. First, many researchers have made a conclusion that film RA has a higher C content than the blocky RA [18, 27, 58]. However, in this site-specific atom scale characterisation, film F2 and F3 RA had a lower C content than all observed blocky RA (Table 7.2). This unexpected low C content was due to the small fraction of neighbouring PF. Besides, film F1 RA exhibited a higher C content than the blocky RA (B1 – B5 and A1) but a lower C content than the blocky A2 RA due to different fraction of neighbouring PF. Second, many researchers also have commented that with a decrease in RA thickness/size, the C content in RA increased [2, 9, 26, 27]. However, for example in this study, even though B4 RA had a larger ECD than B1 – B3 RA, the B4 RA had a higher C content (Table 7.2) due to a larger fraction of neighbouring PF. Whereas, when the RA grains were in the same second phase region having the same fraction of neighbouring PF, comparison of F2 and F3, and B2 and B3, showed smaller thickness and grain size leading to a higher C content. Fig. 7.10 shows the EELS scanning across two film RA grains in the same second phase region, also indicating a relatively higher C content in the thinner film RA (~ 44 nm) than in a thicker one (~ 55 nm). Noticeably, this difference in C content of these two neighbouring film

RA suggests that C distribution was very heterogeneous at the nanoscale in the studied steel. Based on the APT studies, Garcia-Mateo *et al.* [59] also reported the wide variations in the C content of film RA in nanostructured bainitic steel depending on the film thickness. For 1 – 50 nm thick film RA, C content ranged from 4.79 to 14.4 at. %, while for film RA exceeding 50 nm the range was narrower from 4.77 to 6 at. %.

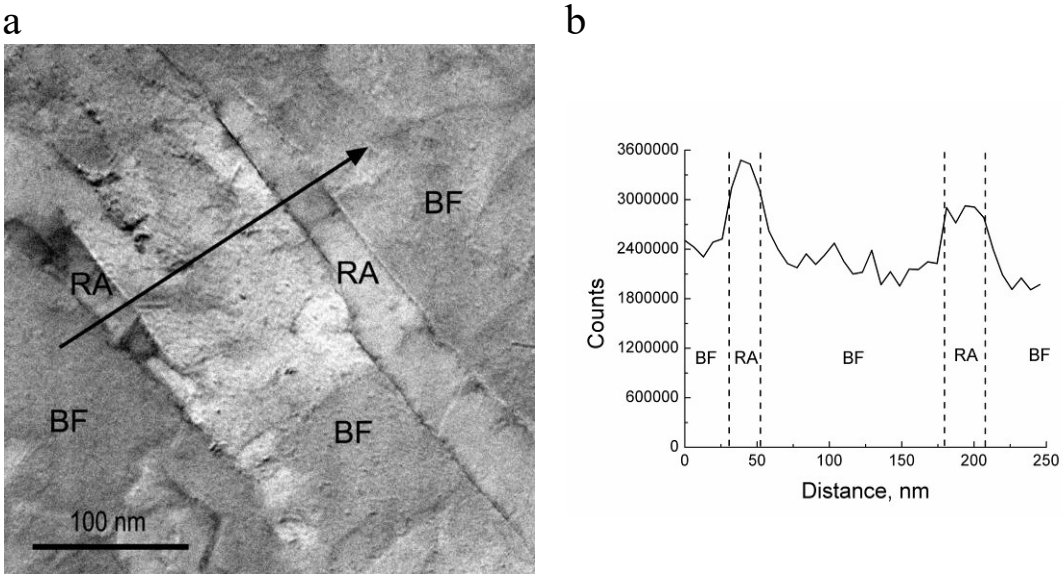

Figure 7.10 (a) TEM showing two film retained austenite and (b) corresponding carbon profile along the dark arrow in (a) using electron energy loss spectroscopy. *RA* is retained austenite and *BF* is bainitic ferrite lath.

It is also well known that the neighbouring phases affect the RA stability [2, 14, 19, 60]. The martensite start transformation temperature (M_s) of investigated RA crystals was calculated using the Andrew's equation as follows [61],

$$M_s = 539 - 423[C\%] - 30.4[Mn\%] - 11[Si\%] - 12.1[Cr\%] \quad (7.3)$$

where [C%], [Mn%], [Si%] and [Cr%] represent weight percentages of C, Mn, Si and Cr, respectively. All calculated M_s (Table 7.2) were below the room temperature except for F2 and F3 RA. The existence of these two film RA at room temperature could be explained by three-dimensional hydrostatic pressure which restricts the volume expansion and shear deformation from austenite-to-martensite transformation [22, 62]. This observation gives a substantial support to the idea that BF lath can strongly stabilise RA. In addition, the formation of Cottrell atmospheres and C clusters in RA (Fig. 7.7(a)) also could contribute to its stabilisation by increasing the

resistance of austenite transformation to martensite [60]. Noticeably, a high C content observed in blocky RA enclosed by polygonal ferrite (A1 and A2 in Table 7.2) gave an alternative support to the high stability of this RA during straining, which has been explained by stress relaxation delaying its transformation [14].

7.4.3 Bainite transformation mechanisms

As well known, a long time debate on the bainite transformation mechanism still has not been solved. According to the displacive mechanism, T_o curve is defined based on the condition of the same free energy of ferrite and austenite having the same chemical composition; T_o' has a similar definition to T_o but additionally, considering the stored energy of the BF lath due to the displacive transformation (400 $J \cdot mol^{-1}$); austenite-to-ferrite transformation line (Ae_3') is calculated based on PE model [29]. Fig. 7.12 shows C contents observed using APT and XRD with respect to T_o', T_o and Ae_3'. The C content measured using XRD was an average value and also included C clusters and Cottrell atmospheres. Based on Fig. 7.12(b), the C content can be categorized into three groups. The C content in F2 film RA was lower than T_o', indicating that this RA could further transform to ferrite. The C content in F3 film RA was between T_o' and T_o, which means the cessation of austenite-to-ferrite transformation. The rest of RA contains a C content of 5.10 – 6.78 at. %, which is much higher than expected from the cessation at the locus of the thermodynamic T_o' (2.65 at. %). It probably resulted from the carbon partitioning during the tempering after completion of bainite transformation. Another reason could be inhomogeneous distribution of C between different RA caused by different neighbouring phases (discussed in *Section 7.4.2*), which may allow transformation to continue to a larger extent than defined by the thermodynamic conditions based on the assumption of uniform carbon distribution [29, 63]. However, the C content in RA cannot reach the Ae_3' line due to the presence of Cottrell atmospheres, C clusters (Fig. 7.7(a)) and carbide (Fig. 7.6). In addition, the C contents in BF lath (0.53±0.02 at.%) and ferrite in GB (0.54±0.02, wt. %) were smaller than T_o' limit, indicating carbon diffusion from ferrite to RA during 900 s holding. Based on the above discussion, a conclusion can be made that higher C content in RA and lower C content in BF lath/ferrite in GB than T_o' could be explained based on diffusionless transformation following by the tempering.

a b

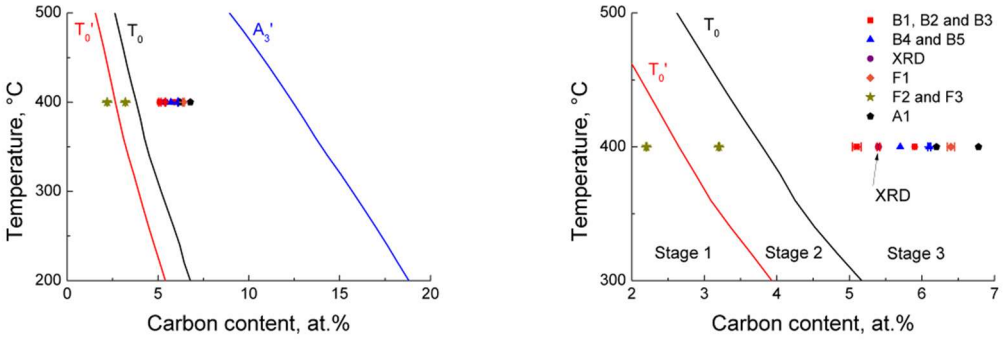

Figure 7.11 (a) Carbon content in retained austenite measured by atom probe tomography and X-ray diffraction and (b) a magnification of (a). T_o, T_o' and Ae_3' are calculated according to http://www.msm.cam.ac.uk/map/steel/programs/mucg46-b.html.

However, in APT study not only C partitioning between RA and ferrite in GB/BF was detected, but also the one of Mn and to a lesser extent of Cr (Figs. 7.4 and 7.5). Only Mn segregation will be discussed in the following because of its clearly observed spike. Recently, a developed GEB approach is promoted to analyse the bainite transformation based on the diffusional transformation mechanism, involving the substitutional solute partitioning [32, 33]. This approach predicts three growth models in the sequence of PE, NP and P modes depending on the time of bainite nucleation during the IBT process [36]. These three growth models are schematically shown in the present dilation curve during 900 s holding at 400 ˚C (Fig. 12(a)) with the corresponding graphic representation of substitutional solute partitioning (Fig. 12(b)). The kinetics of austenite-to-bainite transformation was fast at first within the first 200 s holding and then turned to a slower mode continued up to ~ 400 s (corresponding to PE condition where the segregation forms only during subsequent tempering), and finally reaching a plateau (corresponding to NP and P conditions where the segregation forms during the growth of bainite). If ferrite in GB/BF formed under NP condition (Fig. 12 (a)), then substitutional element partitioning will also continue during tempering, which will be manifested by the slight shift of the peak formed at the interface to the RA side. As formation under P condition takes place at a later time, the time for such a shift will be much less than for NP case and location of the peak will be much closer to the interface, as depicted in Fig. 7.12(b).

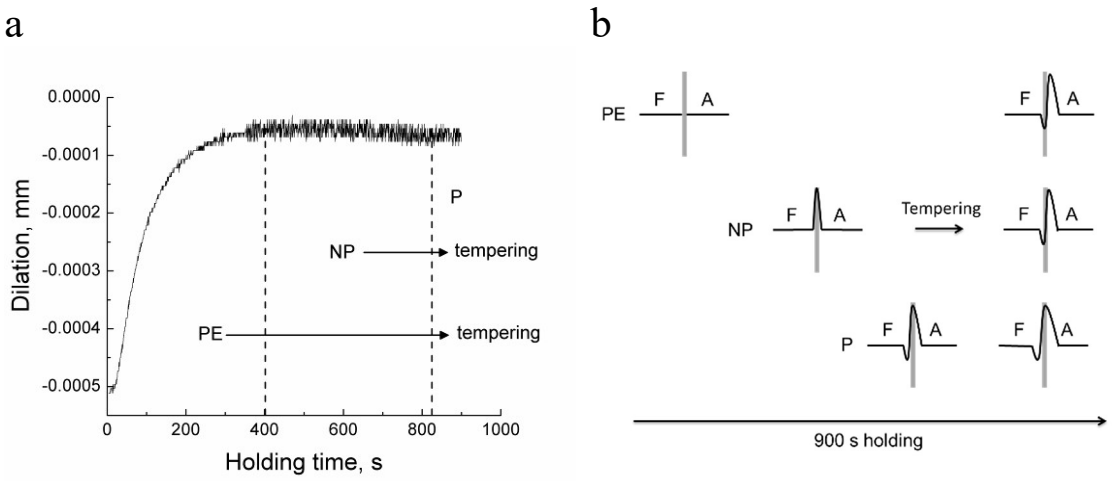

Figure 7.12 (a) The dilation as a function of holding time at 400 ˚C and (b) the corresponding evolution of segregation across the interface between austenite and ferrite after completion of growth (left diagrams) and after tempering (right schematics). *PE* is paraequilibrium, *NP* is negligible partitioning, *P* is partitioning, *F* is ferrite and *A* is austenite.

According to the GEB model, the GB in the location B4 (Fig. 7.3(b)) should form under PE condition because of its early formation during the cooling to IBT temperature. However, the Mn segregation across the interface between RA and ferrite in GB was observed in this study (Fig. 7.5(e)). The ferrite nucleated in the PE transformation stage would grow without any substitutional solute segregation at/in the vicinity of the migrating austenite/ferrite interface [36]. Consequently, the observed segregations are expected to occur at the stationary austenite/ferrite interfaces on tempering after its growth completion under PE condition (as illustrated in Fig. 7.12(b)). Similarly, the Mn segregation forming during the tempering at 300 °C for 9 h was reported in a CMnSiAl TRIP steel [64].

The mean diffusion distance of Mn atoms can be calculated as [65]:

$$d = \sqrt{Dt} \tag{7.4}$$

where t is holding time in seconds and D is diffusion coefficient. The volume diffusion coefficient of Mn atoms in fcc iron matrix is expressed as follows [66]:

$$D = 1.78 \times 10^{-5} \exp(-Q / RT) \tag{7.5}$$

where Q is the activation energy (264000 J·mol^{-1}), R is the universal gas constant and T is the temperature (Kelvin). At 400 ˚C in this study, the volume diffusion coefficient of Mn is calculated as 5.7×10^{-26} m^2·s^{-1} using the Eq. (7.5), which has the

same order of magnitude to that in Ref. [67]. It is noted that the GB formed during the cooling to the holding temperature. The build-up of Mn atoms at the interface between RA and ferrite in GB is also assumed forming during this cooling and subsequent isothermal holding after the growth of GB due to a higher diffusion coefficient in ferrite than austenite by two orders of magnitude, leading to atomic jumps of Mn from the interface into the austenite [18, 67]. Thus, the diffusion time is set as 900 s. According to Eq. (7.4), the mean diffusion path of Mn atoms in the RA is only 0.01 nm. It is a pretty small diffusion distance compared with the distance of 1.1 nm measured by the APT (Table 7.3).

However, the pipe diffusion of Mn along dislocations should be considered due to the high dislocation density of ferrite lath/plate as a result of shear transformation [27]. For instance, Dmitrieva *et al.* [24] reported an increase in the Mn diffusion coefficient by a factor of 45 during holding at 450 ˚C because of a pipe diffusion resulting from a high defect concentration in martensite lath. In addition, the diffusion along grain boundary also could accelerate the diffusion process [65]. Data on the Mn diffusion along dislocations or grain boundary at low temperatures are scarce. Accordingly, the activation energy of Mn diffusion, which yields the measured diffusion distances of 1.1 nm, was back calculated and the result was $0.79Q$. Similarly, it was reported that the activation energy for Cu and Nb pipe diffusion is $0.73Q$ [68] and $0.78Q$ [69], respectively. Moreover, the activation energy for grain boundary diffusion is even smaller than that for pipe diffusion, such as $0.65Q$ for Nb [53]. Thus, it is possible that Mn atoms could diffuse over the measured distance of 1.1 nm during 900 s holding at 400 ˚C by a combination of bulk, pipe and grain boundary diffusion.

As shown in Fig. 7.12(a), the PE condition finished at ~ 400 s. Then the minimum time for Mn diffusion is ~ 500 s. Based on the activation energy of $0.79Q$, the corresponding minimum diffusion distance of Mn is calculated as 0.8 nm. Therefore, the Mn diffusion distance of 1.0 nm on the RA side across the lower interface between RA and BF lath (Fig. 7.4 and Table 7.3) suggests this BF lath also formed under PE condition. It is reasonable because this BF lath nucleated from the austenite grain boundary (as shown in Fig. 7.3(a)), which occurred at the beginning of the

transformation. However, for the case of the upper interface between RA and BF lath (Fig. 7.4), the diffusion length of Mn on the RA side is only 0.1 nm, which is much shorter than the minimum diffusion distance for PE condition. Thus, this BF lath could have formed under NP condition followed by tempering or just under P condition. Furthermore, it means this BF lath nucleated from the primary BF lath during the holding [36], although it cannot be seen in Fig. 7.3(a) probably due to its limited growth and in turn tiny size. Seol *et al.* [18] also suggested the formation of Mn segregation across the interface between RA and BF lath in Fe-0.71C-1.50Mn-1.5Si-0.5Al steel under LENP condition (which is similar to NP condition [36]).

It is noticed that whatever the transformation mode of bainite is, the substitutional solute segregation after tempering exhibits the similar profile (Fig. 7.12(b)). Therefore, the observed segregation by Seol *et al.* [18] also could be ascribed to the tempering after BF lath forming under PE model instead of LENP model. Consequently, when the transformation model is determined only based on the segregation profile and corresponding modelling using DICTRA and Thermo-Calc, these similar segregation profiles after tempering should be taken into consideration.

Noticeably, according to the diffusionless model and dilation curve (Fig. 7.12(a)), only diffusionless growth could take place during first ~ 400 s holding followed by tempering during subsequent holding, which corresponds to the PE condition in the GEB approach based on diffusional mode. In both conditions, substitutional solutes do not partition during the growth of bainite but only partition during the tempering after the completion of growth. For example, Pereloma *et al.* [28] and Caballero *et al.* [27] did not detect the segregation of substitutional solutes between RA and BF lath, which was taken as evidence of diffusionless mechanism of carbide-free bainite formation. Thus, the redistribution of Mn across the interface between RA and ferrite in GB (Fig. 7.5) and between RA and BF lath (lower interface in Fig. 7.4), which was ascribed to the ferrite forming under PE condition followed by the tempering, also could be explained by the diffusionless growth followed by tempering. Importantly, the segregation of Mn across the RA/BF lath interface (upper interface in Fig. 7.4) can only be explained by the ferrite forming under NP or P model. This indicates that bainite formation can be at least locally controlled by a diffusional

mechanism, even though this kind of segregation was observed only in one APT data set. Furthermore, there is a degree of uncertainty in determination of RA/BF interface in APT data set. To reach a more convincing answer, a series of further experiments on segregation of Mn across the interface between RA and ferrite in GB/BF during both early and late stages of bainite transformation are required.

7.5 Conclusions

Site-specific RA characterisation carried out by correlating EBSD, TEM and APT gave an insight into the effect of neighbouring phases on RA carbon content and substitutional solute segregation across the interfaces.

(1) PF formation contributed more carbon to neighbouring RA than BF and GB formations. Carbon rejection to RA was more efficient during BF formation than during GB formation due to a higher ratio of ferrite/RA interface area to the RA volume for BF lath. However, adjacent to RA carbide acting as a carbon sink, resulted in a decrease in carbon content of RA.

(2) Two general believes are overthrown: the blocky RA has a lower carbon content than the film RA; the RA with a smaller size/thickness has a higher carbon content than the coarser ones. Both of them are not always right and instead the neighbouring phases of RA should be first taken into consideration.

(3) Even though the calculated martensite transformation start temperatures (147 - 241˚C) of film RA were much higher than the room temperature, they were still stabilised at room temperature due to high hydrostatic pressure from BF laths.

(4) The diffusion of C and Mn could be explained based on either diffusional mechanism under the PE, NP or P condition and/or diffusionless mechanism followed by tempering. The bainite formation under NP or P condition suggests at least locally controlled diffusion of substitutional solutes across the RA/BF lath interface.

Acknowledgements:

This project was supported by the Australian Research Council (DP130101887). The JEOL JSM-7001F FEG-SEM and JEOL JEM-ARM200F were funded by the Australian Research Council (LE0882613 and LE120100104, respectively). The authors thank Drs. G. Casillas and D.R.G. Mitchell, the University of Wollongong, for TEM and EELS observation, and Dr. A.V. Ceguerra, the University of Sydney, AMMRF, for the Gibbsian interfacial excess discussion. The authors also are grateful to Dr. M.K. Miller, ORNL for the provision of the programme for cluster analysis.

References

[1] M. Takahashi, H. Bhadeshia, Mater. Trans. JIM 32 (1991) 689-696.

[2] E. Pereloma, A. Gazder, I. Timokhina, in: R. Colas, G.E. Totten (Eds.), Retained austenite: Transformation-Induced Plasticity, in Encyclopedia of Iron, Steel and their Alloys, Taylor and Francis, Inc. New York, 2016, pp. 3088-3103.

[3] B.C. De Cooman, Curr. Opin. Solid State Mater. Sci. 8 (2004) 285-303.

[4] I.B. Timokhina, P.D. Hodgson, E.V. Pereloma, Metall. Mater. Trans. A 35 A (2004) 2331-2341.

[5] F.G. Caballero, C. GarcíA-Mateo, J. Chao, M.J. Santofimia, C. Capdevila, C.G. De Andres, ISIJ Int. 48 (2008) 1256-1262.

[6] Y.F. Shen, L.N. Qiu, X. Sun, L. Zuo, P.K. Liaw, D. Raabe, Mater. Sci. Eng. A 636 (2015) 551-564.

[7] I. Timokhina, H. Beladi, X.Y. Xiong, Y. Adachi, P. Hodgson, Acta Mater. 59 (2011) 5511-5522.

[8] H.S. Park, J.C. Han, N.S. Lim, J.B. Seol, C.G. Park, Mater. Scie. Eng. A 627 (2015) 262-269.

[9] W. Li, H. Gao, H. Nakashima, S. Hata, W. Tian, Mater. Charact. 118 (2016) 431-437.

[10] S. Kruijver, L. Zhao, J. Sietsma, S. Offerman, N. van Dijk, E. Lauridsen, L. Margulies, S. Grigull, H. Poulsen, S. van der Zwaag, J. Phys. IV 104 (2003) 499-502.

[11] C. Wang, H. Ding, M. Cai, B. Rolfe, Mater. Sci. Eng. A 610 (2014) 65-75.

[12] E.V. Pereloma, A.A. Gazder, I.B. Timokhina, Mater. Sci. Forum 738-739 (2013) 212-216.

[13] G.K. Tirumalasetty, M.A. van Huis, C. Kwakernaak, J. Sietsma, W.G. Sloof, H.W. Zandbergen, Scripta Mater. 71 (2014) 29-32.

[14] Y. Tomota, H. Tokuda, Y. Adachi, M. Wakita, N. Minakawa, A. Moriai, Y. Morii, Acta Mater. 52 (2004) 5737-5745.

[15] K. Yan, K. Liss, I.B. Timokhina, E.V. Pereloma, Mater. Sci. Eng. A 662 (2016) 185-197.

[16] R. Blondé, E. Jimenez-Melero, L. Zhao, J.P. Wright, E. Brück, S. van der Zwaag, N.H. van Dijk, Mater. Sci. Eng. A 618 (2014) 280-287.

[17] E. Pereloma, I.B. Timokhina, M.K. Miller, P.D. Hodgson, Acta Mater. 55 (2007) 2587-2598.

[18] J. Seol, D. Raabe, P. Choi, Y. Im, C. Park, Acta Mater. 60 (2012) 6183-6199.
[19] X.C. Xiong, B. Chen, M.X. Huang, J.F. Wang, L. Wang, Scripta Mater. 68 (2013) 321-324.
[20] G. Reisner, E. Werner, P. Kerschbaummayr, I. Papst, F. Fischer, JOM 49 (1997) 62-65.
[21] G.K. Tirumalasetty, M.A. van Huis, C. Kwakernaak, J. Sietsma, W.G. Sloof, H.W. Zandbergen, Acta Mater. 60 (2012) 1311-1321.
[22] K. Sugimoto, M. Misu, M. Kobayashi, H. Shirasawa, ISIJ Int. 33 (1993) 775-782.
[23] J. Chiang, J.D. Boyd, A.K. Pilkey, Mater. Sci. Eng. A 638 (2015) 132-142.
[24] O. Dmitrieva, D. Ponge, G. Inden, J. Millán, P. Choi, J. Sietsma, D. Raabe, Acta Mater. 59 (2011) 364-374.
[25] Y. Toji, H. Matsuda, M. Herbig, P. Choi, D. Raabe, Acta Mater. 65 (2014) 215-228.
[26] I.B. Timokhina, M.K. Miller, H. Beladi, P.D. Hodgson, J. Mater. Res. 31 (2016) 806-818.
[27] F.G. Caballero, M.K. Miller, S.S. Babu, C. Garcia-Mateo, Acta Mater. 55 (2007) 381-390.
[28] E. Pereloma, H. Beladi, L. Zhang, I. Timokhina, Metall. Mater. Trans. A 43 (2012) 3958-3971.
[29] H.K.D.H. Bhadeshia, D.V. Edmonds, Acta Metall. 28 (1980) 1265-1273.
[30] M. Hillert, L. Höglund, J. Ågren, Metall. Mater. Trans. A 35 (2004) 3693-3700.
[31] H.I. Aaronson, The Mechanism of Phase Transformations in Crystalline Solids, Institute of Metals, London, 1969.
[32] H. Chen, A. Borgenstam, J. Odqvist, I. Zuazo, M. Goune, J. Ågren, S. van der Zwaag, Acta Mater. 61 (2013) 4512-4523.
[33] H. Chen, K. Zhu, L. Zhao, S. van der Zwaag, Acta Mater. 61 (2013) 5458-5468.
[34] H. Chen, S. van der Zwaag, Metall. Mater. Trans. A 45 (2014) 3429-3437.
[35] H. Chen, Z. Yang, C. Zhang, K. Zhu, S. van der Zwaag, Acta Mater. 104 (2016) 62-71.
[36] H. Chen, S. van der Zwaag, JOM 68 (2016) 1320-1328.
[37] L. Strezov, J. Herbertson, ISIJ Int. 38 (1998) 959-966.
[38] M. Ramajayam, N. Stanford, Mater. Sci. Eng. A 671 (2016) 147-157.

[39] Z.P. Xiong, A.G. Kostryzhev, A.A. Saleh, L. Chen, E.V. Pereloma, Mater. Sci. Eng. A 664 (2016) 26-42.
[40] L.C. Chang, H.K.D.H. Bhadeshia, Mater.Sci. Technol. 11 (1995) 874-882.
[41] K. Thompson, D. Lawrence, D. Larson, J. Olson, T. Kelly, B. Gorman, Ultramicroscopy 107 (2007) 131-139.
[42] P.J. Felfer, T. Alam, S.P. Ringer, J.M. Cairney, Microsc. Res. Tech. 75 (2012) 484-491.
[43] M.K. Miller, Atom probe tomography: Analysis at the atomic level, Kluwer Academic/Plenum press, New York (NY), 2000.
[44] N. Takayama, G. Miyamoto, T. Furuhara, Acta Mater. 60 (2012) 2387-2396.
[45] F. Meisenkothen, E.B. Steel, T.J. Prosa, K.T. Henry, R. Prakash Kolli, Ultramicroscopy 159 (2015) 101-111.
[46] F.G. Caballero, M.K. Miller, C. Garcia-Mateo, Mater. Sci. Technol. 30 (2014) 1034-1039.
[47] W. Owen, Trans. Am. Soc. Metals 46 (1954) 812-829.
[48] F.G. Caballero, Carbide-free bainitic steels, in: E.V. Pereloma, D.V. Edmonds (Eds.), Phase Transformations in Steels: Diffusionless Transformations, High Strength Steels, Modelling and Advanced Analytical Techniques, Woodhead Publishing Limited, 2012, pp. 436-467.
[49] F.G. Caballero, M.K. Miller, C. Garcia-Mateo, C. Capdevila, S.S. Babu, Acta Mater. 56 (2008) 188-199.
[50] D. Kalish, M. Cohen, Mater. Sci. Eng. 6 (1970) 156-166.
[51] A.W. Cochardt, G. Schoek, H. Wiedersich, Acta Metall. 3 (1955) 533-537.
[52] I. Timokhina, H. Beladi, X. Xiong, P.D. Hodgson, Metall. Mater. Trans. A 44 (2013) 5177-5191.
[53] I.B. Timokhina, M. Enomoto, M.K. Miller, E.V. Pereloma, Metall. Mater. Trans. A 43 (2012) 2473-2483.
[54] B.W. Krakauer, D.N. Seidman, Phys. Rev. B 48 (1993) 6724.
[55] E. Pereloma, Mater. Sci. Technol. 32 (2016) 99-103.
[56] K. Tagashira, N. Sumita, H. Hayakawa, Mater. Trans. JIM 30 (1989) 10-18.
[57] Z.P. Xiong, A.G. Kostryzhev, L. Chen, E.V. Pereloma, Mater. Sci. Eng. A 677 (2016) 356-366.

[58] F.G. Caballero, M.J. Santofimia, C. García-Mateo, J. Chao, C.G. de Andrés, Mater. Des. 30 (2009) 2077-2083.
[59] C. Garcia-Mateo, F.G. Caballero, M.K. Miller, J.A. Jimenez, J. Mater. Sci. 47 (2012) 1004-1010.
[60] E.R. Morgan, T. Ko, Acta Metall. 1 (1953) 36-48.
[61] K.W. Andrews, J. Iron Steel Inst. London 203 (1965) 721-727.
[62] T. Sakaki, K. Sugimoto, T. Fukuzato, Acta Metall. 31 (1983) 1737-1746.
[63] F.G. Caballero, C. Garcia-Mateo, M.J. Santofimia, M.K. Miller, C. García de Andrés, Acta Mater. 57 (2009) 8-17.
[64] H. Park, J. Seol, N. Lim, S. Kim, C. Park, Mater. Des. 82 (2015) 173-180.
[65] S.V. Divinski, F. Hisker, Y. Kang, J. Lee, C. Herzig, Interface Sci. 11 (2003) 67-80.
[66] Z. Li, Z. Yang, C. Zhang, Z. Liu, Mater. Sci. Eng. A 527 (2010) 4406-4411.
[67] J. Miettinen, Metall. Mater. Trans. B 28 (1997) 281-297.
[68] P.J. Othen, M.L. Jenkins, G.D.W. Smith, Philos. Mag. A 70 (1994) 1-24.
[69] B. Dutta, E.J. Palmiere, C.M. Sellars, Acta Mater. 49 (2001) 785-794.

CHAPTER 8 CONCLUSIONS AND RECOMMONDATIONS

This study investigated a possibility to manufacture DP and TRIP steels using the strip casting technology. The investigation was conducted in the laboratory, using simulation of thermo-mechanical processing, microstructure characterisation and mechanical property testing. This chapter summarises the main conclusions, highlights the main contributions to the original knowledge and outlines a few suggestions for future work.

8.1 Conclusions

8.1.1 Thermo-mechanical processing schedule design

The processing schedules, which simulate the strip casting technology in the laboratory, were successfully designed for DP (0.08C-0.81Si-1.47Mn-0.03Al wt. %) and TRIP (0.17C-1.52Si-1.61Mn-0.03Al, wt. %) steels, resulting in typical, albeit coarser and more inhomogeneous, microstructures inherent for the hot rolled DP and TRIP steels.

- The similar prior austenite structures to those after strip casting for DP (average grain size: 117±44 μm) and TRIP (average grain size: 80±27 μm) steels were obtained after holding at 1300 °C for 180 s and holding at 1250 °C for 300 s, respectively. Compared to DP steel, smaller PAGS obtained in TRIP steel is due to its higher weight percentage of alloying elements, leading to the restriction of PAGB migration.

- The CCT diagrams were obtained and the nose temperatures of ferrite formation field were determined being around 650 °C for both studied steels.

- With an increase in reduction from 0 to ~ 0.4 at the deformation temperature of 1050 °C, the polygonal ferrite grain size was refined from ~ 20 to ~ 10 μm for both studied steels. It is due to the static recrystallization of austenite resulting in decreased austenite grain size and increased prior austenite grain boundary area, which stimulates ferrite nucleation.

- With a decrease in interrupted cooling temperature, the polygonal ferrite fraction increased for both studied steels, due to more time for ferrite nucleation and growth.

- For DP steel, the ferrite nucleation and growth were found to be dependent on the deformation temperature ranging from 1050 to 700 °C. After deformation up to a reduction of ~ 0.4, the ferrite formation was analysed with respect to the condition of prior austenite (recrystallised austenite or pancaked austenite) and strain-induced ferrite (SIF) formation. Importantly, the minimum ferrite grain size (3.1±2.3 μm) was obtained after deformation at 750 °C as a result of the SIF formation.

- For non-deformed TRIP steel, with an increase in IBT temperature from 350 to 450 °C, the RA fraction reached the maximum value of 4.5±0.3 % with corresponding average carbon content of 1.23±0.01 wt. % at 400 °C. The RA fraction decreased towards the centre of second phase region due to the carbon inhomogeneity arising from its rejection from the neighbouring polygonal ferrite, resulting in most of RA locating along the polygonal ferrite/second phase region interfaces. It implies further study should focus on the microstructure refinement in order to increase the RA fraction.

- With an increase in reduction from 0 to ~ 0.4 at deformation temperature of 1050 °C, the RA fraction may have only changed marginally due to the similar average sizes of second phase regions.

8.1.2 Mechanical properties

- The mechanical properties of strip cast DP steel were improved by a larger amount of deformation at lower deformation temperature. The corresponding strengthening was ascribed to dislocation strengthening and grain refinement. The largest product of UTS and TE was obtained after deformation at a reduction of ~ 0.4 in the SIF formation temperature range of 750 – 800 °C. These products (16000 – 18000 MPa%) were much higher than those in industrially manufactured hot/cold rolled DP 600 steel (12760 – 14740 MPa%).

- The modified iso-work modelling indicated that SIF could enhance strength while only slightly decreasing the ductility.

- For strip cast TRIP steel, the best combination of strength and ductility was obtained after holding at 400 °C due to the highest RA fraction. The strengthening of steel after imposed deformation at 1050 °C is predominantly ascribed to an increase in dislocation density and grain refinement; the variation in the RA contribution to strength is expected to be low due to a marginal change in RA fraction after deformation. The studied non-deformed and deformed TRIP steels had comparable tensile properties with industrially produced TRIP 590 and TRIP 690 steels, respectively.

8.1.3 Transformation mechanisms analysis

- In DP steel, the application of EBSD allowed separation of microstructure constituents (polygonal ferrite, SIF and second phase region), which helped to understand the SIF formation mechanism. The polygonal ferrite and SIF did not exhibit the peak of high misorientation angles (~ 49 – 60°) originated from crystallographic variants pairing observed in the second phase region. In contrast to second phase region, a similar distribution of the deviation from the theoretical K–S and N–W orientation relationships was observed between SIF and polygonal ferrite. In addition, similar dislocation substructures were observed in polygonal ferrite and SIF using TEM. All these observations gave a support for the similarity in the SIF and polygonal ferrite transformation mechanisms, namely the diffusional transformation mechanism, in contrast to the diffusionless mechanism of formation of the second phases.

- In TRIP steel, the carbon content in RA was affected by its morphology and neighbouring phases. Polygonal ferrite formation rejected more carbon atoms to neighbouring RA, compared to bainitic ferrite and granular bainite formations. Bainitic ferrite formation rejected carbon more efficiently to RA than granular bainite formation due to a higher ratio of interface area to

volume in bainitic ferrite lath. However, carbide formed adjacent to RA acted as a carbon sink, resulting in decreased carbon content in the RA.

- By the correlated EBSD and APT, it was found that carbon content in the film RA was not always higher than that in blocky RA, and the coarser RA did not always have a lower carbon content than a finer RA unless they had a similar fraction of neighbouring polygonal ferrite. The observed partitioning of C and Mn between RA and ferrite in bainitic ferrite/granular bainite could be explained according to either diffusional mechanism under the PE, NP or P conditions and/or diffusionless mechanism followed by tempering.

8.2 Contributions to Original Knowledge

In the literature, DP and TRIP steels produced using hot rolling and cold rolling followed by intercritical annealing have been intensively studied. However, the application of strip casting technology to produce these steels was not previously reported. Strip casting differs from conventional processing routes by a very coarse initial austenite grain size resulted from direct solidification from liquid and by the limited possible reduction of strip thickness. This study is a trial to produce DP and TRIP steels using strip casting technique on the laboratory scale. The effect of processing parameters on microstructure and mechanical properties of thin cast DP and TRIP steels was investigated here for the first time. In addition, to-date there is no consensus on the effect of morphology, grain size and neighbouring phases on RA carbon content. Thus, a combined application of EBSD, TEM and APT was used to analyse these relationships. The original contributions of this present study are listed as follows:

- This is the first study that details the production of DP steel using strip casting technique. The effects of the amount of deformation, deformation temperature and interrupted cooling temperature on ferrite formation and mechanical properties were clearly explained. The tensile properties of the strip cast DP steel exceeded those of the industrially manufactured DP 600 steel.

- This is one of the first studies to separate the microstructure constituents of polygonal ferrite, SIF and second phase regions based on the mean angular deviation and grain size using EBSD. Following this, the texture, misorientation angle distribution and the deviation from the theoretical orientation relationships for each constituent were analysed. The contribution of each constituent to tensile properties was also analysed using modified iso-work modelling, indicating that SIF could increase strength with only small decrease in ductility.

- This is one of the first studies that suggests the possibility for SIF formation via diffusional transformation based on its similar features to polygonal

ferrite, such as misorientation angle distributions, the distribution of deviations from theoretical K–S and N–W orientation relationships and dislocation substructures.

- This is the first study that designed the processing route for the production of TRIP steel using strip casting technique. The effects of deformation, interrupted cooling temperature and IBT temperature on microstructure evolution and mechanical properties were intensively investigated. The tensile properties obtained in strip cast TRIP steel reach the level of the industrially produced TRIP 590 and TRIP 690 steels.

- This is first study to systematically demonstrate using a combination of EBSD, TEM and APT that the previously accepted believes of film RA always having a higher carbon content than the blocky one and of coarser RA having a lower carbon content compared to the finer RA do not valid. It highlighted a significant role of neighbouring phases.

- This is the first study to provide some experimental evidence indicating the possibility of the bainitic ferrite formation by diffusional mechanism under NP or P condition.

8.3 Future work

In this study, DP and TRIP steels were produced using laboratory simulated strip casting. The challenge for this process is to refine the microstructure from a very coarse prior austenite grain structure. Micro-alloying with additions of molybdenum, vanadium or niobium is a useful way to refine prior austenite grains and in turn final microstructure [1, 2]. Thus, further research would benefit of composition modifications.

The current work was focused only on the determination of tensile properties. However, in service the automotive steels require to satisfy standards for dent resistance, formability, surface quality and dimensional accuracy [3]. Thus, for example, further investigations with respect to forming limits, hole expansion, galvanising and paint baking of strip cast DP and TRIP steels could be undertaken.

Alternatively, the cold rolling and intercritical annealing following the strip casting could be another processing route to improve the microstructure and mechanical properties of DP and TRIP steels. Thus, it is suggested to develop this route and study the effect of processing parameters on the microstructure and mechanical properties.

To gain a stronger experimental evidence with regards to the transformation mode of SIF, in the future, a systematic research by quenching after different amounts of deformation at different deformation temperatures could be carried out.

To clarify the possibility of bainitic ferrite growth with substitutional elements partitioning during the slow growth stage according to Gibbsian energy balance model [4], a systematic site-specific APT study of bainitic ferrite laths formed at various locations and at different holding times at 400 °C needs to be conducted.

References

[1] E.J. Pavlina, C.J. van Tyne, J.G. Speer, Mater. Charact. 102 (2015) 35-46.

[2] M.G. Akben, B. Bacroix, J.J. Jonas, Acta Metall. 31 (1983) 161-174.

[3] T.B. Hilditch, T. de Souza, P.D. Hodgson, Properties and automotive applications of advanced high-strength steels (AHSS), in M. Shome and M. Tumuluru (Eds.), Welding and Joining of Advanced High Strength Steels (AHSS), Woodhead Publishing, 2015, pp. 9-28.

[4] H. Chen, S. van der Zwaag, JOM 68 (2016) 1320-1328.